

SOLAR ENERGY HARVESTING FOR PHOTOVOLTAIC CELLS AND PHOTOCATALYSIS

A thesis submitted to the College of Graduate Studies and Research
In partial fulfillment of the requirements for the degree of

Doctor of Philosophy

In the Department of Chemistry
University of Saskatchewan
Saskatoon

By

Mahesh Kumar Gangishetty
Supervisors: Dr. Timothy L. Kelly & Dr. Robert W.J. Scott

Permission to Use

In presenting this thesis in partial fulfillment of the requirements for a Postgraduate degree from the University of Saskatchewan, I agree that the Libraries of this University may make it freely available for inspection. I further agree that permission for copying of this thesis in any manner, in whole or in part, for scholarly purposes may be granted by the professors who supervised my thesis work or, in their absence, by the Head of the Department or the Dean of the College in which my thesis work was done. It is understood that any copying or publication or use of this thesis or parts thereof for financial gain shall not be allowed without my written permission. It is also understood that due recognition shall be given to me and to the University of Saskatchewan in any scholarly use which may be made of any material in my thesis.

Requests for permission to copy or to make other uses of materials in this thesis/dissertation in whole or part should be addressed to:

Head of the Department of Chemistry
University of Saskatchewan
Saskatoon, Saskatchewan (S7N 5C9)
Canada.

Abstract

In recent years, alternative energy resources have gathered tremendous attention due to an increase in energy demand and overcome the global effects of burning fossil fuels. Solar energy is an abundant and clean resource of energy and is one of the most promising alternatives to fossil fuels. This thesis investigates the various approaches to harvesting the solar energy and transforming it into electrical and chemical energy.

The primary focus of this thesis is employing plasmonic metal nanoparticles as light harvesting elements in photovoltaic cells and photocatalytic materials. Triangular metal nanoparticles (Au, Ag) exhibit strong plasmonic effects due to the presence of sharp features, and their optical properties are tunable based on their size. By integrating Ag@SiO₂ nanotriangles in dye-sensitized solar cells (DSSCs), *ca.* 30% enhancement in the power conversion efficiency (PCE) was achieved. However, the sharp features of Ag nanotriangles are not stable, and the Ag nanotriangles are oxidized at elevated temperatures. The changes in the morphology of these Ag@SiO₂ nanoparticles at different annealing temperatures and in different environments (dry air and N₂) was studied by X-ray absorption spectroscopy (XAS). Upon annealing in air, the silver nanotriangles decomposed to small (~2 nm) Ag particles, whereas in a N₂ atmosphere, they formed truncated triangles. To overcome this stability issue, Ag@SiO₂ nanotriangles were replaced by Au@SiO₂ nanotriangles. By integrating these nanomaterials in DSSCs, panchromatic light harvesting in the device was achieved. Plasmonic light harvesting was also explored as a route to promote Pd catalysis using AuPd nanotriangles. Upon light illumination, the energy from excited plasmons in Au is transferred to Pd, and this resulted in an enhancement in the rates of the reactions.

Recently, another new light harvesting material based on organic-inorganic hybrid perovskites ($\text{CH}_3\text{NH}_3\text{PbX}_3$; X= Cl, I, Br) has been explored in solar cells. In perovskite solar cells, to determine the optimum conditions for efficient light harvesting and charge collection, the perovskite layer thickness and relative humidity (RH) in the atmosphere were investigated. Results showed ~ 300 nm thick perovskite layers and 40% atmospheric RH are the best conditions for achieving efficient devices.

Acknowledgements

This work would not be possible without the support from many people, both within and outside the lab. First and foremost, I would like to express my gratitude to my supervisors, Dr. Timothy L. Kelly, and Dr. Robert W. J. Scott. You both are fantastic persons; I am very thankful for the motivation, encouragement, and guidance that has been provided at each stage in my Ph.D. I can confidently say that you both are successful in supervising me and making me better knowledgeable person compared to my first year. Your supervision is very positively influenced both my professional career and personal life.

I would like to thank my advisory committee Dr. Ronald P. Steer, Dr. Lee D. Wilson, and Dr. Michael P. Bradley for their valuable suggestions during the meetings. I am grateful to all the faculty members; particularly, to Dr. Matthew Paige for providing me access to his Laser facility along with his encouragement. I have used the synchrotron facility at Canadian Light Source; I am thankful to all the staff at HXMA and SXRMB beam lines.

Over the period of Ph.D., I have been teaching several labs in the department. The support and feedback from Alex, Val are very helpful in improving my presentation skills; I sincerely acknowledge their support. I am thankful to all the departmental staff; particularly to Leah for her all time reminders in arranging the committee meetings and etc.

All the past and present group members of Drs. Kelly and Scott's group are very cooperative and helpful. It is a big list of people; I am thankful to each and every person in these two groups. Outside the lab, I had a lot of fun and amusement from friends; I sincerely appreciate the time I have spent with them.

Finally, I am incredibly grateful to my parents, my brother, my sweet sister, and other family members; nothing would have been possible without their love and care.

Dedications

I would like to dedicate this thesis to my parents, and my supervisors, Drs. Tim Kelly
and Robert Scott

Table of Contents

Permission to Use.....	i
Abstract	ii
Acknowledgements	iv
Dedications	v
Table of Contents.....	vi
List of Figures	xi
List of Schemes	xviii
List of Tables.....	xix
List of Abbreviations.....	xxi
CHAPTER 1.....	1
Introduction.....	1
1.0. Solar Energy	1
1.1. Plasmonic Nanoparticles	2
1.1.1. Properties of plasmonic nanoparticles	3
1.1.2. Synthesis	7
1.1.3. Applications	11
1.2. Photovoltaic Cells	12
1.2.1. Overview.....	12
1.2.2. Dye-sensitized solar cells.....	17
1.2.3. Perovskite solar cells.....	25

1.3. Photocatalysis.....	35
1.3.1. Overview.....	35
1.3.2. Plasmonic light harvesting for photocatalysis	36
1.4. Research Objectives	42
1.5. References.....	44
CHAPTER 2.....	62
Plasmonic Enhancement of Dye Sensitized Solar Cells in the Red-to-NIR Region using Triangular Core-Shell Ag@SiO₂ Nanoparticles.....	62
2.1. Abstract	63
2.2. Introduction	63
2.3. Experimental Section	66
2.3.1. Materials	66
2.3.2. Characterization	67
2.3.3. Synthesis of silver nanoprisms.....	67
2.3.4. Synthesis of Ag@SiO ₂ core-shell nanoprisms.....	67
2.3.5. Preparation of TiO ₂ and Ag@SiO ₂ /TiO ₂ pastes	68
2.3.6. Cell fabrication and characterization	68
2.4. Results and Discussion	70
2.5. Conclusions.....	85
2.6. References.....	87
CHAPTER 3.....	91
Thermal Degradation Mechanism of Triangular Ag@SiO₂ Nanoparticles..	91
3.1. Abstract	92
3.2. Introduction	92
3.3. Experimental.....	95
3.3.1. Materials and methods	95
3.3.2. Synthesis of Ag and Ag@SiO ₂ nanotriangles.....	95
3.3.3. Thermal annealing studies	96
3.3.4. Characterization	96
3.4. Results and Discussion	97
3.4.1. Thermal degradation study of Ag@SiO ₂ using UV-Vis and TEM	98

3.4.2. Thermal degradation study of Ag@SiO ₂ using XANES and EXAFS analysis.....	103
3.5. Conclusions.....	108
3.6. References.....	109
CHAPTER 4.....	113
Panchromatic Enhancement of Light Harvesting Efficiency in DSSCs using Thermally Annealed Au@SiO₂ Triangular Nanoprisms.....	113
4.1. Abstract	114
4.2. Introduction	114
4.3. Experimental Section	117
4.3.1. Materials	117
4.3.2. Synthesis of triangular Au and Au@SiO ₂ nanoparticles	117
4.3.3. Thermal annealing studies	118
4.3.4. Fabrication of DSSCs	118
4.3.5. Characterization	119
4.4. Results and Discussion	119
4.4.1. Thermal degradation of Au@SiO ₂ nanoparticles	123
4.4.2. Overlap between the UV-Vis spectra of the dye and the Au@SiO ₂ nanoparticles	125
4.4.3. Device characteristics	127
4.5. Conclusions.....	132
4.6. References.....	133
CHAPTER 5.....	137
Effect of CH₃NH₃PbI₃ Thickness on Device Efficiency in Planar Heterojunction Perovskite Solar Cells.....	137
5.1. Abstract	138
5.2. Introduction	138
5.3. Experimental.....	141
5.3.1 Cell fabrication procedures	141
5.3.2 Device characterization.....	142
5.3.3 Thin film characterization.....	143
5.4. Results and Discussion	143
5.4.1. Comparison of solution- and vapour-phase PbI ₂ deposition.....	143

5.4.2. Effect of PbI ₂ film thickness on CH ₃ NH ₃ PbI ₃ composition and morphology	147
5.4.3. Device performance as a function of perovskite film thickness	154
5.5. Conclusions.....	162
5.6. References.....	164
CHAPTER 6.....	168
Effect of Relative Humidity on Crystal Growth, Device Performance and Hysteresis in Planar Heterojunction Perovskite Solar Cells	168
6.1. Abstract	169
6.2. Introduction	169
6.3. Experimental Section	171
6.3.1. Materials	171
6.3.2. Device fabrication.....	172
6.3.3. Characterization	172
6.4. Results and Discussion.....	173
6.4.1. Effect of humidity on perovskite crystal growth	173
6.4.2. Effect of humidity on device performance	178
6.4.3. Effect of humidity on device hysteresis.....	181
6.5. Conclusions	185
6.6. References.....	186
CHAPTER 7.....	190
Improving the Rates of Pd-Catalyzed Reactions by Exciting the Surface Plasmons of AuPd Bimetallic Nanotriangles.....	190
7.1. Abstract	191
7.2. Introduction	191
7.3. Experimental Section	194
7.3.1. Materials	194
7.3.2. Characterization	194
7.3.3. Methods.....	195
7.3.4. Catalytic reactions.....	196
7.4. Results and Discussion	197
7.4.1. AuPd bimetallic nanotriangles.....	197

7.4.2. Plasmon enhanced Suzuki-coupling reactions.....	199
7.4.3. Catalyst stability and recyclability.....	204
7.4.4. Plasmon enhanced hydrogenation reaction.....	206
7.5. Conclusions.....	208
7.6. References.....	210
CHAPTER 8.....	214
8.1. Summary	214
8.2. Future Outlook	218
8.2.1. Plasmonic heating effects vs. plasmonic hot electron effects in Pd-catalyzed reactions	219
8.2.2. Plasmonic near-field effect vs plasmonic light scattering effect in DSSCs.....	222
8.3. References.....	223

List of Figures

Figure 1.1. Schematic representation of localized surface plasmon resonance in metal nanoparticles.	3
Figure 1.2. Calculated (by Discrete Dipole Approximation) optical spectra for metal (Ag) nanoparticles of different shapes: (a) a sphere, (b) a cube, (c) a tetrahedron, (d) an octahedron, (e) a triangular plate. Here the spectral color represents extinction (black), absorption (red), and scattering spectra. Figure (f) represents the extinction spectra of nanobars with different aspect ratios; 2 (black), 3 (red), and 4 (blue). Figures are reprinted from Reference (18). Copyright (2009) Annual Reviews.	4
Figure 1.3. Schematic representation of surface plasmon decay pathways; (a) radiative decays in the form of local electric field, (b) showing hot electrons excited above the Fermi level and (c) hot electron transfer mechanism at metal/semiconductor interface. Reprinted from Reference (30). Copyright (2014) Nature Publishing Group.	5
Figure 1.4. Schematic illustration of nucleation and growth pathways to different shapes of metal nanoparticles. Here, green, orange and purple represent (100), (111) and (110) facets, respectively. Reprinted from Reference (18). Copyright (2009) Annual Reviews.	9
Figure 1.5. (a) A typical current-voltage (I-V) curve for a solar cell (b) the equivalent circuit diagram of a typical solar cell; here, I_L is photocurrent, R_s is series resistance, R_{sh} is shunt resistance and V is voltage.	15
Figure 1.6. The structures of some of the champion Ru dyes, here TBA is the tetrabutylammonium ion.	19
Figure 1.7. (a) A schematic of DSSCs showing the key components and (b) the charge transfer and recombination kinetics. Figure (a) Reprinted from Reference (107) and figure (b) is reprinted from (108). Copyright (2005, 2010) American Chemical Society.	19
Figure 1.8. Standard AM 1.5G (Air mass) solar spectrum	21
Figure 1.9. Plasmonic effects using spherical nanoparticles in silicon solar cells; (a) plasmonic light scattering effect and (b) plasmonic near-field enhancement. Here, the orange layer is <i>n</i> -type silicon, and blue layer is <i>p</i> -type silicon. Reprinted from Reference (114). Copyright (2010) Nature Publishing Group.	22
Figure 1.10. Various architectures of perovskite solar cells; mesoscopic solar cells (a) Al_2O_3 scaffold, (b) TiO_2 mesoscopic layer and planar heterojunction solar	

cells; (c) n-i-p type and (d) p-i-n type architectures. Here, FTO is fluorine doped tin oxide and ITO is indium doped tin oxide Reprinted from Reference (151). Copyright (2015) Royal Society of Chemistry.	27
Figure 1.11. The top panel (a & b) shows the one-step deposition method; (a) direct deposition of perovskite precursor on TiO ₂ , (b) solvent engineering by dripping toluene solvent. The bottom panel (c, d, e & f) shows the two step deposition technique; (c) two-step deposition by dipping PbI ₂ in MAI solution, (d) physical vapor deposition (dual source co-deposition) of PbCl ₂ and MAI, (e) two-step spin coating (inter-diffusion) method, and (f) vapor assisted solution process (two-step). Reprinted from References (170, 174, 158, 177 and 176). Copyright (2013, 2014) Nature Publishing Group, (2015, 2016) Royal Society of chemistry, and (2014) American Chemical Society.....	31
Figure 1.12. Plasmon energy transfer mechanisms for photocatalysis; (a) Plasmonic near-field effect, (b) Plasmonic charge transfer to a semiconductor (crossing the Schottky junction), and (c) plasmonic charge transfer to the adsorbate molecule. Reprinted from Reference (206). Copyright (2013) The Royal Society of Chemistry.	36
Figure 2.1. a) & b) TEM images of the as-prepared silver nanoprisms, (c) UV/Vis/NIR spectra of the as-prepared silver nanoprisms (black line) and the nanoprisms after functionalization with 16-mercaptohexadecanoic acid (red line).	71
Figure 2.2. Size distributions of the as-prepared silver nanoprisms, (a) edge length, and (b) thickness.	71
Figure 2.3. TEM micrographs of Ag@SiO ₂ core-shell particles synthesized with different TEOS concentrations: (a) 0.8 mM, (b) 1.8 mM, (c) 9 mM, and (d) 16 mM.	72
Figure 2.4. (a) Normalized UV/Vis/NIR spectra of Ag nanoprisms functionalized with 16-mercaptohexadecanoic acid (black line), and Ag@SiO ₂ nanoprisms synthesized using various TEOS concentrations: 0.8 mM (red line), 1.8 mM (blue line), 9 mM (green line), and 16 mM (pink line). (b) Peak position of the LSPR band (λ_{LSPR}) as a function of both TEOS concentration (black triangles) and shell thickness (blue squares).....	73
Figure 2.5. Schematic depiction of the device architecture, showing the Ag@SiO ₂ nanoparticles embedded in the TiO ₂ photoanode.	74
Figure 2.6. (a) <i>J-V</i> characteristics of the highest performing DSSC for each Ag@SiO ₂ /TiO ₂ ratio: 0.00% (purple line), 0.01% (blue line), 0.05% (green line), 0.10% (yellow line), 0.33% (orange line), 0.50% (red line), 1.00% (dark red line). (b) Mean fill factor, short circuit current density, open circuit voltage, and PCE plotted as a function of Ag@SiO ₂ loading. The error bars show plus or minus one standard deviation from the mean.....	76

Figure 2.7. (a) Incident photon-to-current efficiency spectra of DSSCs made using various Ag@SiO ₂ /TiO ₂ ratios: 0.0% (black line), 0.05% (red line), 0.10% (cyan line), 0.33% (green line) and 0.5% (blue line). (b) The relative IPCE enhancement ((IPCE _{Ag@SiO₂} – IPCE _{control}) / IPCE _{control}) for the device with a 0.05% Ag@SiO ₂ (black line) loading and the absorption spectrum of the Ag@SiO ₂ nanoprisms (blue line).....	80
Figure 2.8. (a) Incident photon-to-current efficiency spectra of DSSCs made using 0.0% (black line) and 0.05% (red line) Ag@SiO ₂ loadings. The difference spectrum is also shown (blue line). (b) The relative IPCE enhancement ((IPCE _{Ag@SiO₂} – IPCE _{control}) / IPCE _{control}) for the device with a 0.05% Ag@SiO ₂ loading (blue line) and the original IPCE spectrum (black line).	81
Figure 2.9. TEM image of the Ag@SiO ₂ nanoparticles with the thickest SiO ₂ shells after sintering.	83
Figure 2.10. Average PCE for DSSCs prepared using 0.05% (w/w) of Ag@SiO ₂ nanoprisms with different shell thicknesses, as well as for the control devices without any Ag@SiO ₂ . The thickness of the photoanode in all devices was 3 – 4 μm. The error bars show plus or minus one standard deviation from the mean.	84
Figure 2.11. (a) UV/Vis/NIR spectra of the Ag@SiO ₂ nanoprisms with a 33 nm thick shell: in acetonitrile (black line), 30 min after adding the I ⁻ /I ₃ ⁻ electrolyte (red line), and 20 h after addition of the electrolyte solution (blue line). (b) UV/Vis/NIR spectra of the Ag@SiO ₂ nanoprisms with a 7 nm thick shell: in acetonitrile (black line), and 30 min after adding the I ⁻ /I ₃ ⁻ electrolyte (red line).	85
Figure 3.1. (a) UV-Vis spectrum of Au@SiO ₂ nanotriangles suspended in EtOH (b) TEM image of as-synthesized triangular Ag@SiO ₂ nanoparticles.	98
Figure 3.2. Normalized UV-Vis absorption spectra of Ag@SiO ₂ nanotriangles after annealing in either an (a) air or (b) N ₂ atmosphere.	99
Figure 3.3. TEM images of the Ag@SiO ₂ nanotriangles after annealing in either (a-d) air, or (e-h) N ₂ atmospheres. The samples were annealed at: (a,e) 150 °C, (b,f) 300 °C, (c,g) 450 °C, and (d,h) 600 °C. The scale bars in the main images are 100 nm, while those in the insets are 20 nm.	100
Figure 3.4. TEM images of SiO ₂ @Ag control samples annealed a) at 450 °C and (b) at 600 °C.	102
Figure 3.5. Ag <i>K</i> -edge (a,b) XANES and (c,d) FT-EXAFS spectra of Ag@SiO ₂ nanotriangles annealed in (a,c) air and (b,d) N ₂ . All spectra were collected at room temperature.	104

Figure 3.6. EXAFS fitting of Ag@SiO ₂ nanotriangles annealed in (a) air and (b) N ₂ at different temperatures. All spectra were collected at room temperature after annealing.....	106
Figure 3.7. Proposed thermal degradation mechanism of Ag nanotriangles in air and N ₂ . The silica shell is omitted for clarity.	108
Figure 4.1. (a) TEM image, (b) size distribution, and (c) UV-Vis spectrum of the as-synthesized Au nanoprisms.	120
Figure 4.2. Normalized UV-Vis spectra of Au@SiO ₂ nanoparticles after annealing at indicated temperatures. As-prepared (black), 150 °C (red), 250 °C (blue), 350 °C (pink), 450 °C (purple) and the absorption spectrum of Black Dye (dashed green).	120
Figure 4.3. TEM images of Au@SiO ₂ nanoparticles synthesized using different concentrations of TEOS: (a) 0.46 mM, (b) 0.92mM, (c) 1.38 mM, (d) 1.84mM, (e) 2.76 mM, and (f) 4.6 mM.....	122
Figure 4.4. (a) Normalized UV-Vis spectra of Au nanoparticles functionalized with 16-mercaptohexadecanoic acid (black line), and Au@SiO ₂ nanoparticles synthesized using different concentrations of TEOS: 0.46 mM, 0.92 mM, 1.38 mM, 1.84 mM, 2.76 mM and 4.6 mM. The spectra normalized to the maximum optical density (b) LSPR peak position (λ_{LSPR}) as a function of both TEOS concentration and SiO ₂ shell thickness.....	122
Figure 4.5. Normalized UV-Vis spectra of Au@SiO ₂ nanoparticles after annealing at different temperatures, as-prepared (black line), 150 °C (red line), 250 °C (blue line), 350 °C (orange line), 450 °C (purple line). The spectra were normalized to the in-plane dipole plasmon peak (second peak of each spectrum).	123
Figure 4.6. TEM images of Au@SiO ₂ nanoparticles after annealing at different temperatures in air, (a) 150 °C, (b) 250 °C, (c) 350 °C, (d) 450 °C.	125
Figure 4.7. (a) Product of the dye absorption spectrum and the LSPR bands of the Au@SiO ₂ nanoparticles: as-synthesized (black line), and after annealing at 150 °C (red line), 250 °C (blue line), 350 °C (orange line), and 450 °C (purple line). (b) Overlap integral (area under the curve in (a)) as a function of annealing temperature.	126
Figure 4.8. <i>J-V</i> curves of control (red line) and plasmon-enhanced (black line, 0.05% (w/w) Au@SiO ₂) devices. In both cases, the active layer thickness was measured to be 4 μm. Here, the layer thickness was measured by profilometry.	130
Figure 4.9. (a) IPCE spectra of control (red line) and plasmon-enhanced (black line, 0.05% (w/w) Au@SiO ₂) devices. In both cases, the active layer thickness was measured to be 4 μm. (b) Relative IPCE enhancement ((IPCE _{Au@SiO₂} -	

IPCE _{control}) / IPCE _{control}) spectrum (black line) for the data shown in (a) and the absorption spectrum of the Au@SiO ₂ nanoparticles annealed at 450 °C (purple line).....	131
Figure 5.1. (a) Powder X-ray diffraction patterns of PbI ₂ films deposited by spin coating (S-PbI ₂) and thermal evaporation (E-PbI ₂), and the corresponding CH ₃ NH ₃ PbI ₃ films after dipping in methylammonium iodide solution. All films were deposited on ITO/glass substrates. The * denotes PbI ₂ peaks and O denotes the characteristic peaks of CH ₃ NH ₃ PbI ₃ . (b) SEM micrograph of a perovskite film produced from a spin coated PbI ₂ film; (c) SEM micrograph of a perovskite film produced from an evaporated PbI ₂ film.	145
Figure 5.2. (a) <i>J-V</i> curves and (b) IPCE spectra for the highest-performing ITO/ZnO/CH ₃ NH ₃ PbI ₃ /P3HT/Ag devices prepared from both solution-processed (black line) and thermally evaporated (red line) PbI ₂ films.....	147
Figure 5.3. (a) Perovskite film thickness as a function of the thickness of the precursor PbI ₂ film, as determined by profilometry; (b) Absorbance spectra of the films from (a). Error bars represent plus-or-minus one standard deviation from the mean.....	149
Figure 5.4. The unit cells and cell volumes of lead iodide and tetragonal CH ₃ NH ₃ PbI ₃ : Pb (grey), I (purple), C (brown) and N (grey). The unit cell of CH ₃ NH ₃ PbI ₃ contains four CH ₃ NH ₃ PbI ₃ units, and so the volume per CH ₃ NH ₃ PbI ₃ repeat unit is 248 Å ³	149
Figure 5.5. Powder X-ray diffraction patterns. All samples were prepared and measured on ITO/ZnO substrates. (a) Bare ITO/ZnO; (b) PbI ₂ ; (c) Calculated diffraction pattern for the tetragonal phase of CH ₃ NH ₃ PbI ₃ (peak widths arbitrarily broadened to 0.2° 2θ). Where more than one reflection contributes to an unresolved peak, only the most intense reflection is labelled; (d) 61 nm CH ₃ NH ₃ PbI ₃ ; (e) 200 nm CH ₃ NH ₃ PbI ₃ ; (f) 280 nm CH ₃ NH ₃ PbI ₃ ; (g) 400 nm CH ₃ NH ₃ PbI ₃ ; (h) 560 nm CH ₃ NH ₃ PbI ₃	150
Figure 5.6. SEM images of (a-c) evaporated PbI ₂ films and (d-f) the corresponding CH ₃ NH ₃ PbI ₃ films after dipping in CH ₃ NH ₃ I. Films were (a) 50, (b) 150, (c) 300, (d) 110, (e) 330 and (f) 580 nm thick, as determined by profilometry.....	151
Figure 5.7. Williamson-Hall plots for CH ₃ NH ₃ PbI ₃ films of various thicknesses.	152
Figure 5.8. (a) Particle size as measured by SEM (blue triangles) and minimum grain size as determined by a Williamson-Hall analysis of powder X-ray diffraction data (red squares) as a function of perovskite layer thickness. The linear fits are a guide to the eye. (b) Microstrain (as calculated by a Williamson-Hall analysis of powder X-ray diffraction data) as a function of perovskite layer thickness.	153
Figure 5.9. AFM images of CH ₃ NH ₃ PbI ₃ films of various thicknesses on ITO/ZnO substrates: (a) 200 nm, (b) 280 nm, (c) 400 nm, and (d) 560 nm. All images	

were of a $15 \mu\text{m} \times 15 \mu\text{m}$ area. The samples had root-mean-squared surface roughnesses (R_{rms}) of: (a) 33, (b) 29, (c) 23, and (d) 49 nm, respectively.....	154
Figure 5.10. (a) J - V curves and (b) IPCE spectra for ITO/ZnO/CH ₃ NH ₃ PbI ₃ /P3HT/Ag devices with perovskite layers of 110 (black line), 210 (blue line), 330 (purple line), 410 (dark brown line), 490 (red line) and 580 nm (orange line).....	155
Figure 5.11. (a) Open circuit voltage, (b) short circuit current density, (c) fill factor and (d) PCE as a function of perovskite film thickness. Error bars represent plus-or-minus one standard deviation from the mean. Data are derived from measurements on 8, 17, 34, 12, 11 and 14 separate devices for 110, 210, 330, 410, 490, and 580 nm thick films, respectively.....	156
Figure 5.12. Nyquist plots for ITO/ZnO/CH ₃ NH ₃ PbI ₃ /P3HT/Ag devices with different CH ₃ NH ₃ PbI ₃ thicknesses: (a) 110 nm, (b) 330 nm, (c) 580 nm. Experimental data (black squares) and theoretical fit (red line). (d) Equivalent circuit model used to fit the data.....	157
Figure 5.13. Schematic of the ITO/ZnO/CH ₃ NH ₃ PbI ₃ /P3HT/Ag devices tested in this work, showing the effect of the roughened CH ₃ NH ₃ PbI ₃ /P3HT interface on the hole-extraction efficiency.	161
Figure 5.14. (a) J - V curves for a representative ITO/ZnO/CH ₃ NH ₃ PbI ₃ /P3HT/Ag device, measured from forward-bias (FB) to short-circuit (SC), and from short-circuit to forward-bias. (b) Ratio of the PCEs measured from FB to SC and from SC to FB as a function of perovskite film thickness. Measurements were the average of at least 6 devices, and the error bars represent plus or minus one standard deviation from the mean.....	162
Figure 6.1. Schematic of the apparatus used to control the RH inside an atmospheric bag containing a spin coater. PbI ₂ films are converted into CH ₃ NH ₃ PbI ₃ by immersion in a solution of CH ₃ NH ₃ I, spin dried at 3000 r.p.m. for 30 s, and allowed to dry for a further 10 min.....	173
Figure 6.2 (a) UV-Vis absorption spectra for vapor deposited PbI ₂ thin films (yellow line), and CH ₃ NH ₃ PbI ₃ thin films prepared at 1% (black line), 33% (blue line), 40% (red line), and 60% (green line) RH. (b) Photographs of CH ₃ NH ₃ PbI ₃ thin films prepared at various RH values. (c) Powder X-ray diffraction patterns for ITO/PbI ₂ /CH ₃ NH ₃ PbI ₃ thin films prepared at various RH values. Peaks due to ITO and PbI ₂ are marked with an asterisk (*) and dagger (†), respectively.....	175
Figure 6.3. (a) SEM images of (a) PbI ₂ , and CH ₃ NH ₃ PbI ₃ films prepared at (b) 1%, (c) 20%, (d) 30%, (e) 40%, and (f) 60% RH.....	177
Figure 6.4 (a) J - V curves of the highest performance devices measured at a scan rate of 0.83 V/s. (b) IPCE spectra of the same devices.....	179

Figure 6.5. (a) J - V curves measured at 0.1 V/s for the best device prepared at 40% RH. (b) Ratio of PCEs determined from forward (SC-FB) and reverse (SC-FB) scans as a function of RH. The linear fit is a guide to the eye.....	182
Figure 6.6. J - V curves measured at 0.1 V/s for devices prepared at: (a) 1%, (b) 20%, (c) 30%, (d) 40%, and (e) 60% RH.	183
Figure 6.7. (a) Average device performance characteristics (measured at a scan rate of 0.1 V/s) as a function of relative humidity. Error bars represent plus or minus one standard deviation from the mean. (b) Steady-state current densities for representative devices at each relative humidity.	184
Figure 7.1. (a) Normalized UV-Vis spectra of Au and AuPd bimetallic nanotriangles; the spectra are normalized to the maximum of the plasmon band. TEM images of (b) as-synthesized Au nanotriangles, (c) AuPd bimetallic nanotriangles and (d) magnified image of AuPd nanotriangles.	198
Figure 7.2. a) The LED light source with an array of green LEDs mounted on heat sinks, b) percent conversions calculated from ^1H NMR are plotted against time; the reaction is between <i>p</i> -iodobenzoic acid and phenylboronic acid. The green triangles indicate the control dark reaction performed in a hot water bath and the inverted blue triangles indicate the light reaction performed in a 25 °C water bath. The solid lines are a best-fit using a first-order kinetic model.	200
Figure 7.3. The normalized power vs wavelength for several LEDs including green LED source that was used to study the plasmonic catalysis. This is taken from the seller's (LUXEON) website.	201
Figure 7.4. (a) UV-Vis absorption spectra of AuPd nanotriangles before and after cross-coupling reactions performed between <i>p</i> -iodobenzoic acid and phenylboronic acid. (b) Recyclability of AuPd nanotriangles and final temperature of the same coupling reaction performed under light illumination, and (c) TEM image showing aggregation of the AuPd nanotriangles, recorded after one cycle of the light reaction.	206
Figure 7.5. Percent conversion of hydrogenation reactions performed on 2-methyl-3-buten-2-ol using AuPd nanotriangles in the presence and absence of light. The black squares show the reaction performed at 23 °C under ambient conditions, the red circles show the reaction performed under illumination that achieved a final temperature of 30 °C, and the green triangles show the dark reaction performed at 30 °C using hot water bath. The solid lines are a best-fit using a first-order kinetic model.	208
Figure 8.1. (a) TEM image of Au@SiO ₂ @Pd core-shell-shell nanoparticles, and (b) percent conversions of a cross-coupling reaction between <i>p</i> -iodobenzoic acid and phenyl boronic acid at ambient temperatures; substrate to catalyst loading ratio was (2.5mmol: 0.002mmol). The conversions are calculated from ^1H NMR	221

List of Schemes

Scheme 2.1. Synthesis of the Ag@SiO ₂ triangular nanoprisms.....	71
Scheme 4.1. Synthesis of Au@SiO ₂ nanoprisms.	120
Scheme 7.1. Schematic representation of a model Suzuki reaction used to test the AuPd nanotriangles as catalysts.....	200
Scheme 8.1. Representation of controlling the plasmonic hot electron effect vs plasmonic heating effect using three different types of nanoparticles.....	220

List of Tables

Table 2.1. Mean V_{oc} , J_{sc} , FF and PCE, along with their associated standard deviations, for DSSCs with different Ag@SiO ₂ loadings. The number of devices tested (N) for each loading is shown.	77
Table 2.2. ANOVA analysis of PCE as a function of Ag@SiO ₂ loading carried out at the 95% confidence level. The calculated F-value (13.3) is larger than the critical F-value (2.3) required for 95% confidence, and the P-value is less than 0.05. Therefore, the results show a statistically significant variation in PCE with Ag@SiO ₂ loading.	78
Table 2.3. Pairwise t-tests (assuming unequal variances, 95% confidence) comparing the PCEs of devices made with various Ag@SiO ₂ loadings with pure TiO ₂ controls. In all cases, the absolute value of the t-statistic is larger than the critical t-value required for 95% confidence in a two-tailed test, and the P-value is less than 0.05. Therefore, each sample shows a statistically significant increase in PCE relative to the TiO ₂ controls.	79
Table 2.4. Device performance characteristics for DSSCs prepared using 0.05% (w/w) of Ag@SiO ₂ nanoprisms with different shell thicknesses, as well as for the control devices without any Ag@SiO ₂ . The thickness of the photoanode in all devices was 3 – 4 μm.	84
Table 3.1. EXAFS fitting parameters of Ag@SiO ₂ nanotriangles annealed in air and N ₂ at different temperatures, the amplitude factor for the fittings was kept at fixed value of 0.973	107
Table 4.1. Average Voc, Jsc, FF, and PCE, along with their standard deviations, for DSSCs with different Au@SiO ₂ loadings.	128
Table 4.2. t-test for PCE (pairwise, two-tailed, assuming unequal variances).	128
Table 4.3. t-test for active layer thickness (pairwise, two-tailed, assuming unequal variances).	129
Table 5.1. Device performance parameters for perovskite solar cells. ^a Averages derived from measurements on 29 separate devices. ^b Averages derived from measurements on 34 separate devices.	146
Table 5.2. Average series (R_s) and shunt (R_{sh}) resistances for perovskite solar cells.	159
Table 5.3. Tabulated fit parameters for the EIS data.	159

Table 6.1. Average device characteristics for perovskite solar cells measured at a scan rate of 0.1 V/s. Values shown in parentheses are for the highest performance devices measured at a scan rate of 0.83 V/s.	181
Table 7.1. Percent conversions measured by ¹ H NMR for different Suzuki reactions performed in both the dark and the light.	204

List of Abbreviations

AFM	Atomic force microscope
ANOVA	Analysis of variance
APTES	3(-aminopropyl)triethoxysilane
CB	Conduction band
CIGS	Copper indium gallium selenide
CLS	Canadian light source
CTAB	Cetyltrimethylammonium bromide
CTAC	Cetyltrimethylammonium chloride
DSSCs	Dye-sensitized solar cells
EC	Ethyl cellulose
EIA	Energy information administration
EIS	Electrochemical impedance spectroscopy
ETL	Electron transport layer
EXAFS	Extended X-ray absorption fine spectra
FAI	Formamidinium
FB	Forward bias
FF	Fill factor
FT-EXAFS	Fourier-transformed radial distribution function
FTO	Fluorine doped tin oxide
GO	Graphene oxide

HTL	Hole transport layer
HXMA	Hard X-ray Micro Analysis
IPCE	Incident photon to current-conversion efficiency
ITO	Indium-doped tin oxide
LHE	Light harvesting efficiency
Li-TFSI	Lithium-bis(trifluoromethanesulfonyl)imide
LSPR	Localized surface plasmon resonance
MAI	Methylammonium
MHA	Mercaptohexadecanoic acid
NIR	Near-infrared
P(E/B)-PEO	Poly(ethylene-co-butylene)-b-poly(ethylene oxide)
P3HT	Poly(3-hexylthiophene)
PCBM	Phenyl-C61-butyric acid methyl ester
PCE	Power conversion efficiency
PEDOT:PSS	Poly(3,4-ethylenedioxythiophene):polystyrene sulfonate
PHJ	Planar heterojunction
PL	Photoluminescence
PRET	Plasmon resonance energy transfer
PSSS	Poly(sodium styrenesulphonate)
PVA	Polyvinyl alcohol
PVP	Polyvinylpyrrolidone
PVs	Photovoltaics

pXRD	Powder X-ray diffraction
RH	Relative humidity
SC	Short circuit
SEM	Scanning electron microscope
spiro-OMETAD	2,2',7,7'-tetrakis-(N,N-di-p-methoxyphenylamine)-9,9'-bifluorene
TEM	Transmission electron microscope
TEOS	Tetraethoxysilane
TSC	Trisodium citrate
VB	Valence band
XANES	X-ray absorption near-edge spectra
XAS	X-ray absorption spectroscopy

CHAPTER 1

Introduction

1.0. Solar Energy

Global energy consumption has been increasing steadily due to continuous population growth. If we continue consuming energy at the current rate, the energy requirement will increase tremendously in the immediate future. The US Energy Information Administration (EIA) projects that global energy consumption will increase by 48% from 2012 to 2040.¹ The current energy resources that share a large part of world energy production are oil, coal, and natural gas. From the climate-model standpoint, if we remain using these fossil fuels as our major energy resources, there will be a further rise in global temperatures by 1.7 - 4.8 °C by the end of the 21st century due to the emission of greenhouse gases.² To prevent the detrimental effects of these gases and simultaneously fulfill future energy demands there is an urgent need for alternative green, renewable and sustainable energy resources.

The current alternative renewable resources are wind, hydroelectric, geothermal and solar energy. However, they contribute only 19.2% to the overall global energy supply.³ Among these, solar energy is one of the most abundant and desirable alternative energy resources. In 2001, calculations demonstrated that the amount of solar energy received by the earth in one and a half hours could supply the overall global energy consumed in that year.⁴ However, the solar constant (solar power per area) is low (1.36 kW/m^2);⁵ thus to meet the increasing demand for global energy large area photovoltaic cells are required. On the other hand, the growth of photovoltaics in the last decade is very promising; in 2001 the solar energy contribution to the global energy supply

was 0.1%, which increased to 1.8% in 2015 and is predicted to grow further to 16% by 2050.⁶ In addition to the generation of electricity, solar energy has been used in solar water heaters and to accelerate and drive chemical reactions. This thesis investigates several strategies of transforming solar energy efficiently into electrical and chemical energy. One of the approaches is employing plasmonic metal nanoparticles as energy transfer systems in solar cells and photocatalysis. In addition to this, several device engineering techniques are studied to improve the performance of perovskite solar cells.

1.1. Plasmonic Nanoparticles

Metal nanoparticles show unique optical properties when they interact with light. Due to the presence of continuous energy levels in their conduction band (CB), the free electrons in the CB oscillate in resonance with the incoming light. This phenomenon is called localized surface plasmon resonance (LSPR) (Figure 1.1).⁷ Several factors can determine the frequency of the plasmon oscillations, such as the effective mass of electrons in the metal, the size and shape of the nanoparticles, and the surrounding dielectric material.⁸⁻¹⁰ Among all metal nanoparticles, Au, Ag, and Cu are attractive due to the presence of their LSPR band in the visible region. However, Cu nanoparticles are less studied since they easily oxidize to Cu₂O or CuO under atmospheric conditions, which results in a loss of their optical properties.¹¹ Ag nanoparticles do oxidize to Ag_xO_y under ambient atmosphere, but with a slower rate compared to the Cu. Other plasmonic metal nanoparticles such as Pd and Pt are also known, but they are less explored in light harvesting applications as their SPR band is typically in the UV-region. However, they are widely used as catalysts in heterogeneous reactions. Recently, Al has been found to have its plasmon band in the visible region.^{12, 13} Several other non-metal plasmonic nanoparticles including transition metal nitrides and Cu₂S have been explored as alternatives to metal nanoparticles.¹⁴⁻¹⁶

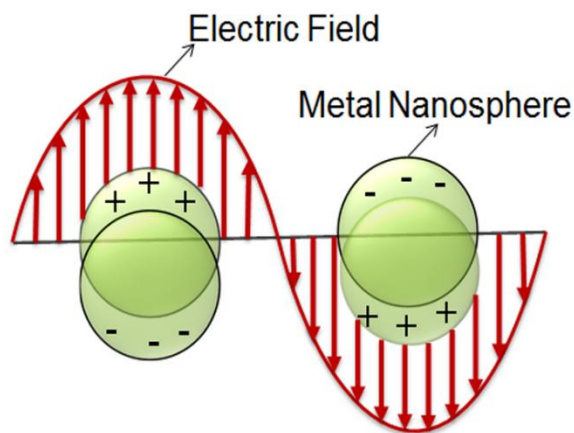


Figure 1.1. Schematic representation of localized surface plasmon resonance in metal nanoparticles.

1.1.1. Properties of plasmonic nanoparticles

In 1908, Gustave Mie discovered the origin of the red color in Au nanoparticles.¹⁷⁻²⁰ To describe the optical properties of metal nanoparticles, Mie presented a solution of Maxwell's equations.²⁰ According to Mie theory, the extinction cross section of a spherical metal nanoparticle is a sum of absorption and scattering cross sections. It is proportional to r^6 , where r is the diameter of the particle. The extinction cross section in particles with size < 30 nm is dominated by the absorption cross section. With an increase in the size of the nanoparticle, light scattering becomes the dominating factor.²⁰⁻²² When a metal nanoparticle interacts with photons, the free electrons in the CB oscillate in resonance with the incoming light (LSPR). Due to continuous displacement of negative charges (free electrons), a polarization takes place within the nanoparticle. This displacement is confined within the boundaries of the nanoparticle surface; hence, the polarization depends on the diameter of the nanoparticle. Small particles can accommodate only dipoles and show only a dipole plasmon mode. As the size of the particle increases, the particle can accommodate multiple plasmon modes including quadrupole or multipole plasmon modes. All the plasmon modes are present in the optical spectra. The intensity and width of the plasmon peaks vary depending on the geometry and dimension of the nanoparticle.¹⁰

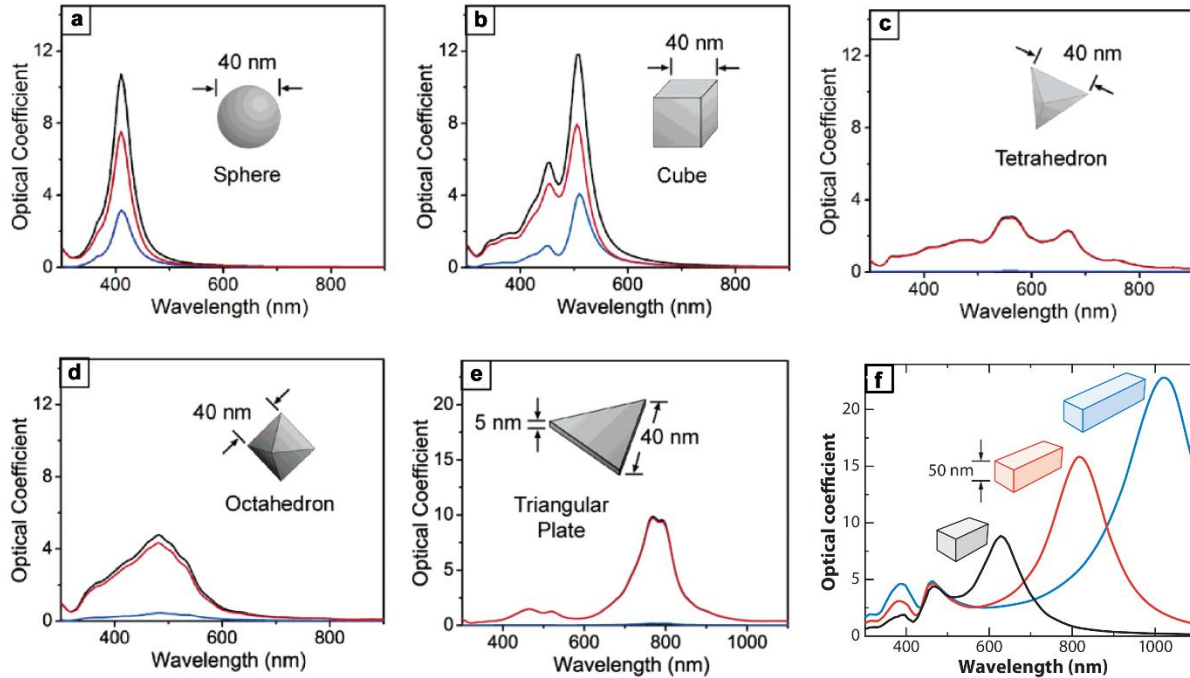


Figure 1.2. Calculated (by Discrete Dipole Approximation) optical spectra for metal (Ag) nanoparticles of different shapes: (a) a sphere, (b) a cube, (c) a tetrahedron, (d) an octahedron, (e) a triangular plate. Here the spectral color represents extinction (black), absorption (red), and scattering spectra. Figure (f) represents the extinction spectra of nanobars with different aspect ratios; 2 (black), 3 (red), and 4 (blue). Figures are reprinted from Reference (18). Copyright (2009) Annual Reviews.

In an anisotropic nanoparticle, the surface plasmons are unevenly distributed throughout the particle.^{23, 24} Due to the anisotropy, the particle displays additional plasmon modes along with the dipole and quadrupole modes; hence, often the anisotropic nanoparticles exhibit a broad SPR.²⁴ The plasmon modes are dependent on the shape and aspect ratio of the nanoparticle (Figure 1.2). For example, Au nanorods exhibit two different types of plasmon oscillations: one is the longitudinal mode, and the other is transverse mode (Figure 1.2f).^{25, 26} The longitudinal mode (low energy/high wavelength) corresponds to the plasmonic oscillations along the length of the nanorod. The transverse mode (high energy/low wavelength) corresponds to the plasmonic oscillations perpendicular to the length.²⁵ In the case of nanotriangles, due to their plate like structure, the plasmon oscillations are distributed both within the plane and out of the plane. Based on the aspect

ratios they exhibit in-plane dipole and in-plane quadrupole, out-of-plane dipole and out-of-plane quadrupole modes. However, the main plasmon peak of nanotriangles always arises from the in-plane dipole oscillations; the intense peak at ~ 800 nm in Figure 1.2e is due to these in-plane dipole oscillations. The other modes do appear in the absorption spectrum, but with a lower intensity. All these plasmon modes are distinguishable depending on the aspect ratio of the nanoparticle. In a similar way, several other shapes (nanocubes, nanowires, and nanotetrahedra) show multiple plasmon modes, as well as tunable optical properties.^{10, 27} Along with the shape and size, the dielectric medium around the nanoparticles can also influence the optical properties of the plasmonic nanoparticle.^{18, 28} The dipoles/quadrupoles generated in the nanoparticle induce a polarization in the surrounding dielectric medium.^{10, 29} The induced opposite poles in the surrounding medium then affect the frequency of plasmon oscillations, which leads to a shift in the plasmon band. The magnitude of the shift depends on the polarizability (dielectric constant) of the surrounding material.

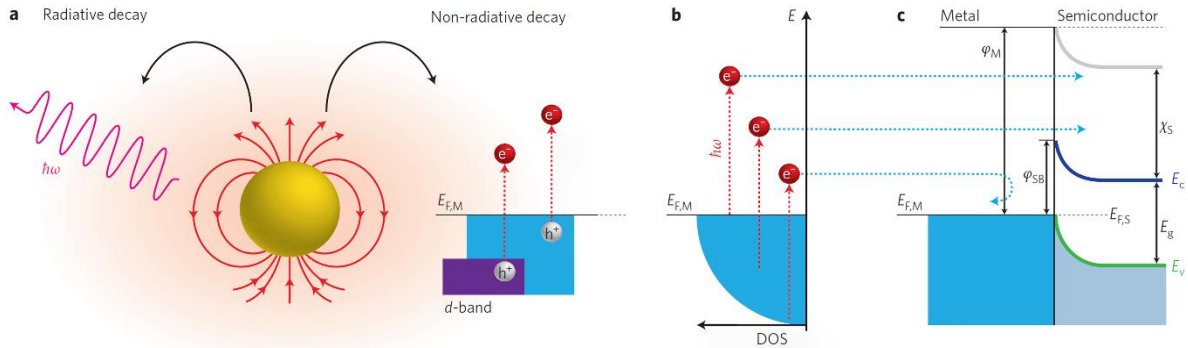


Figure 1.3. Schematic representation of surface plasmon decay pathways; (a) radiative decays in the form of local electric field, (b) showing hot electrons excited above the Fermi level and (c) hot electron transfer mechanism at metal/semiconductor interface. Reprinted from Reference (30). Copyright (2014) Nature Publishing Group.

The energy accumulated by absorption of light by the surface plasmons is dissipated through various radiative and non-radiative relaxation pathways (Figure 1.3a).³⁰ As a consequence of the radiative relaxation process, the energy is released either in the form of near-fields or far-

fields by electron-photon scattering.³¹ Electron-photon scattering causes re-emission of the energy in the form of photons (i.e., light scattering), and it depends on the shape and size of the particle (Figure 1.2).¹⁰ The near-fields are the local electric fields generated around the metal nanoparticles. Due to the oscillation of free electrons (negative charges), dipoles are generated in the nanoparticles. These dipoles lead to the development of intense electric fields around the nanoparticle. This local field concentrates the incoming light in the nanoscale domains around of the nanoparticle; this phenomenon is called the near-field effect. Non-radiative plasmon decay occurs *via* generation of hot electrons in the metal nanoparticle; the term “hot electrons” implies that the electrons are not in thermal equilibrium with the metal.^{30,32} The energy of the hot electrons depends on the power of the incoming light source; the energy can go high enough to overcome the Schottky barrier present at metal/semiconductor interfaces (Figure 1.3b and c).^{30,33} In some cases, these electrons are ejected (photoemission) from the nanoparticle; however, this requires a high power (GW) light source.^{34,35} Such high energy could be attributed to the multiphoton absorption by the CB electrons. Some of the energy of the hot electrons is immediately redistributed among the many low energy electrons in the nanoparticles through electron-electron scattering.³⁶ Some of these hot electrons relax by releasing energy in the form of heat; this is called electron-phonon scattering. The local heat generated on the surface of the nanoparticle is estimated to increase the temperature to 500 °C in the vicinity of a spherical Au nanoparticle;²² this heat was found to be sufficient enough to weld two nanoparticles together.^{37,38} All of these excitation and relaxation pathways in the metal nanoparticles lead to their exceptional optical and electronic properties.

1.1.2. Synthesis

The amplitude and frequency of surface plasmon oscillations are determined by the shape and size of the nanoparticle. Particularly, various shapes of Au and Ag nanoparticles have drawn attention because of their tunable SPR bands in the visible region. Therefore, different shapes of nanoparticles, such as nanorods, triangular nanoprisms, nanostars, nanocubes, and nanowires have been synthesized.³⁹⁻⁴⁸ There are many methods available for the synthesis of these shapes; these methods include wet chemical synthesis,¹⁸ lithography,^{49, 50} and laser ablation techniques.⁵¹ Wet chemical synthesis is one of the most common approaches, where the size and morphology of the nanoparticles are controlled by varying the reaction conditions such as solvent, stabilizing agent and temperature.¹⁸ The wet chemical synthesis can be a single-step or a two-step synthesis; the famous single step method used for synthesizing Au nanoparticles is the Turkevich/Ferns method.⁵² In this method, spherical Au nanoparticles are synthesized by using citrate as both the reducing and stabilizing agent in one step. For synthesizing different shapes and sizes of nanoparticles, stabilizing agents play a critical role. Common stabilizing agents include polyvinylpyrrolidone (PVP), trisodium citrate (TSC), cetyltrimethylammonium chloride (CTAC), and cetyltrimethylammonium bromide (CTAB). They selectively bind to a specific crystal plane and allow the growth of the particle in the other planes. For example, PVP binds to (100) planes and allows growth in the [110] and [111] directions.⁴² By using PVP as the stabilizing agent, Xia and coworkers introduced a shape-selective synthesis of Ag nanocubes.⁴⁶ Here, ethylene glycol was used as a reducing agent (polyol synthesis). After this report, the polyol method using PVP as the stabilizing agent was explored to synthesize various shapes (nanobars, nanobipyramids, and nanocubes) of Ag and Pd nanoparticles.¹⁸ In a similar way, other stabilizing agents such as CTAB and CTAC have also been shown to bind to (100) planes; however, unlike PVP, they have higher

binding affinity to these planes, which could be advantageous in achieving monodisperse nanoparticles.⁵³ By using CTAB as the shape-directing agent, Murphy and coworkers developed a seed-mediated wet chemical synthesis for different shapes of Au nanoparticles.^{43, 54} Here, ascorbic acid was used as a reducing agent; the relative concentrations of CTAB and ascorbic acid determine the final shape of the nanoparticle.⁴³ Apart from modifying stabilizing agents, anisotropic nanoparticles can also be synthesized by plasmonic excitation. Mirkin and Schatz devised a photo-driven synthesis of Ag nanoprisms by exciting surface plasmons using a monochromatic light source.⁵⁵ Here, in the first step the Ag nanoparticles dissociate into small Ag nanoprisms upon illumination, which then grow to nanoprisms depending on the wavelength of the incoming light. However, this method was useful for synthesizing only triangular nanoparticles. Duyne and coworkers pioneered another technique called nanosphere lithography for patterning nanotriangles and nanorods on a glass substrate.⁵⁶ All of the above methods are used for making monometallic nanoparticles. To synthesize bimetallic nanoparticles, either the two metal precursors are simultaneously reduced or one metal salt is reduced on already synthesized metal nanoparticle from the other metal salt.⁵⁷

Regardless of the synthetic method, the growth of metal nanoparticles to any shape begins from the nucleation process. The nuclei formed in this step grow to form seeds (small nanoparticles); these seeds then grow further to form nanocrystals. Evolution of the final shape and size of the metal nanocrystals is governed by crystal twinning in the seeds (Figure 1.4). The seeds can be single crystals, singly twinned crystals or multiply twinned crystals. The crystal twinning depends on the reaction conditions employed during the formation of the seeds.^{18, 58, 59} Nanocubes, nano-octahedra and nanobars originate from a single crystal seed. If the seed contains singular twinning then it produces a pyramidal shape. If it contains multiply twinned planes, then

it results in a hexagonal nanorod.¹⁸ For nanotriangles, the seed contains stacking faults parallel to the (111) planes as shown in the Figure 1.4.⁶⁰ However, stabilizing agents also play a key role in the growth of a seed to a specific shape.

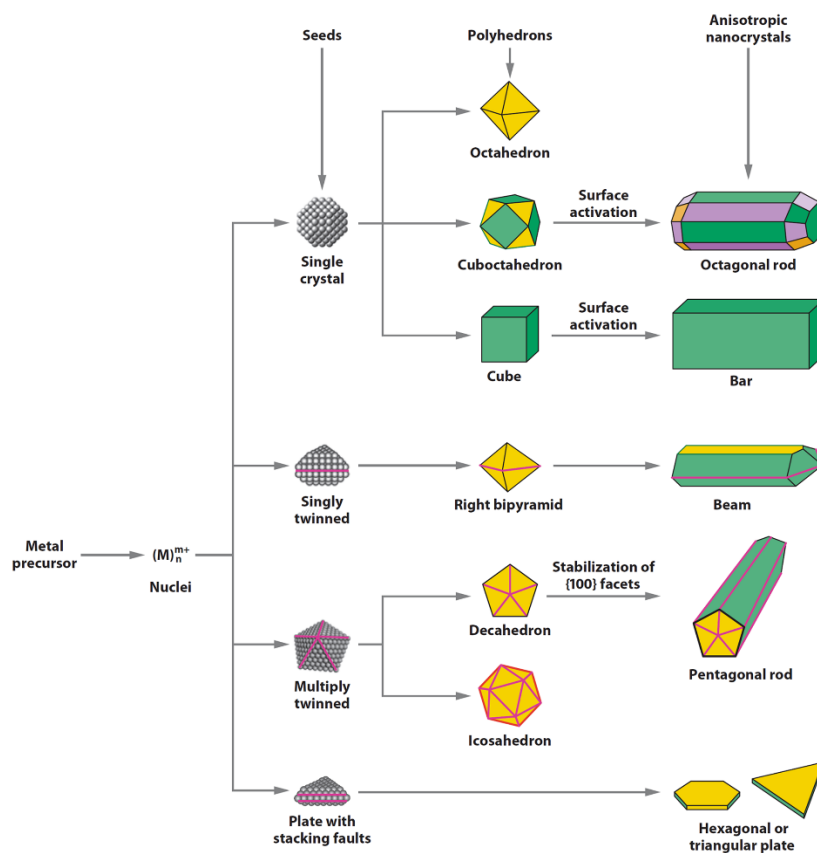


Figure 1.4. Schematic illustration of nucleation and growth pathways to different shapes of metal nanoparticles. Here, green, orange and purple represent (100), (111) and (110) facets, respectively. Reprinted from Reference (18). Copyright (2009) Annual Reviews.

In this thesis, Au and Ag nanotriangles (also referred to nanoprisms) are used as light harvesting materials in DSSCs and photocatalysis. In this paragraph different methods that are reported for the synthesis of nanotriangles are discussed. The nanotriangles are plate-like structures, containing three sharp edges. They adopt a face centered cubic structures enclosed by (111) planes on the basal facets and (110) or (100) planes on the sides. There are numerous reports on the synthesis of Ag and Au nanoprisms, which are largely based on photo-driven and wet

chemical synthetic methods.^{55, 60-63} In photo-driven syntheses, the nanotriangles are grown by selectively exciting the plasmon modes using a monochromatic light source. Chen and coworkers devised a photo-induced approach to synthesize Au nanotriangles by irradiating H₂AuCl₄ salt in the presence of polyvinyl alcohol (PVA).⁶⁴ Here, PVA acts as a stabilizing agent. However, this method produced Au nanoparticles of various shapes. Recently, Wei and co-workers demonstrated that the concentrations of stabilizing agents (PVA, PVP, or citrate) and the wavelength of the incoming light source play a critical role in achieving monodisperse Au nanotriangles.^{63, 65} Mirkin and co-workers used this photo-driven approach for synthesising Ag nanotriangles using trisodium citrate as a reducing agent.⁵⁵ Here, monodisperse Ag nanotriangles were achieved when monochromatic light was used, and also the edge length was controlled by the illumination time.⁵⁵

In the case of wet chemical synthesis, there are two-different approaches to synthesize Ag or Au nanotriangles. One is seed-mediated synthesis (two-step), and the other is one step synthesis.¹⁸ The most common stabilizing agents explored in these methods are poly(sodium styrenesulphonate) (PSSS), PVP, CTAB, CTAC, and TSC. Aherne *et al.* devised a simple seed-mediated method for producing silver nanoprisms with tunable edge lengths and sizes.⁶⁰ This method involves a synthesis of a separate solution of Ag seeds using PSSS as a stabilizer. These seeds were then mixed with another (growth) solution, where the actual growth of nanotriangles takes place. In this method, the edge length of the nanotriangles was easily tunable by varying the relative volumes of seed and growth solutions;⁶⁰ but the downside of this method is that it produces polydisperse nanotriangles. Mirkin and coworkers reported a three step seed-mediated synthesis of Au nanotriangles using CTAB as the stabilizing agent.⁶⁶ This method produces uniform sizes of the nanotriangles, however, along with the nanotriangles a significant population of spherical

nanoparticles was observed. In addition to this, nanotriangles with edge lengths below 100 nm could not be prepared by this method.

To synthesize monodisperse triangular Ag nanoparticles, Zhang *et al.* adopted a one-step method using PVP and TSC as the stabilizing and reducing agents, respectively.⁶⁷ Here, they used hydrogen peroxide as an oxidative etchant; it plays a critical role in the formation of planar twinned seeds, which yield monodisperse triangular nanoparticles. However, this method can only produce one size of nanotriangle; the edge lengths are not tunable. Chen *et al.* reported a seedless procedure for the synthesis of highly monodisperse Au nanotriangles. They used an oxidative etching method using ascorbic acid and sodium iodide in the presence of CTAC as the stabilizing agent. By this process, Au nanotriangles with tunable edge lengths were prepared.⁶⁸

1.1.3. Applications

Due to their unique tunable optical properties, plasmonic nanoparticles have been explored in a wide range of applications such as in biomedical fields,^{19, 69-72} photovoltaic (PV) cells and photocatalysis.³² In the biomedical field, they have been employed in both diagnosis and therapeutic applications.⁷³ Due to their strong light scattering cross section, they are used to provide high contrast images in various microscopy techniques such as dark-field imaging of cancer cells using a confocal microscope,⁷⁰⁻⁷² and surface enhanced Raman spectroscopy.⁶⁹ The optical properties of these materials are highly sensitive to the surrounding dielectric medium, which make them promising materials for biosensors⁷⁴ and biomarkers.^{75, 76} The local heat generated on the surface has been useful for destroying malignant tumors and cancer cells, which is widely known as photodynamic therapy.^{77, 78} This thesis investigates applications of plasmonic nanoparticles in photovoltaic cells and photocatalysis which are discussed in Sections 1.2.2.2 and 1.3.2, respectively.

1.2. Photovoltaic Cells

1.2.1. Overview

The phenomenon of converting light into electricity is called the photovoltaic effect; it was first discovered by Alexander Becquerel in 1839.^{79, 80} A large area photovoltaic cell using selenium was prepared in 1894; it produced a *ca.* 1% efficiency.⁸¹ In the 1950s, the field of photovoltaics (PVs) was revolutionized by the development of silicon-based solar cells, and in the early 90s Green *et al.* report the highest efficiency of ~20% in these silicon solar cells, which was a record at that time.⁸² In the last few decades, several different types of solar cells have been developed, which are categorized into different generations in the following section.

First generation solar cells: These are traditional solar cells based on crystalline silicon. Monocrystalline and polycrystalline silicon solar cells fall into this category. The best-reported efficiencies for monocrystalline and polycrystalline solar cells are 27.1% and 21.3%, respectively.⁸³ The band gap of silicon is 1.1 eV, and the maximum efficiency these silicon solar cells can reach is 32% (the Shockley-Queisser limit). Monocrystalline silicon solar cells are expensive compared to polycrystalline silicon solar cells; their cost is associated with the production of pure single crystals of silicon. About 80% of the current commercial market is occupied by crystalline silicon solar cells.⁸⁴

Second generation solar cells: These are thin film solar cells, which consist of an active layer that is a few micrometers thick. Amorphous silicon, copper indium gallium selenide (CIGS) and cadmium telluride (CdTe) are widely known active layers in these solar cells. The highest efficiency reported for amorphous silicon solar cells was *ca.* 13.6%,^{85, 86} and they can be manufactured at low cost compared to crystalline silicon. Although they are cheap, their stability is a major issue; they degrade upon long-term exposure to light.⁸⁷ CIGS and CdTe solar cells have

shown promising efficiencies of *ca.* 22 % in recent years,^{83, 88} but the toxicity of Cd is a problem for CdTe solar cells.

Third generation solar cells: Third-generation solar cells are designed to overcome the disadvantages of first and second generation solar cells. The most common third generation solar cells are multi-junction (tandem) solar cells; they have the potential to overcome the Shockley-Queisser limit by harvesting different regions of light with different semiconductors. Further, many other emerging solar cells are included in this generation; these are nanostructured dye-sensitized, and quantum dot solar cells, organic small molecule and polymer solar cells and perovskite solar cells. Nanostructured solar cells are already showing promising performances, with the best reported efficiencies being 13 -14 %^{89, 90} and 10 - 11%^{91, 92} for dye-sensitized, and quantum dot sensitized solar cells, respectively. Moreover, the performance of organic solar cells is growing steadily; the highest efficiencies reported to date are *ca.* 9% for small organic molecules and *ca.* 11% for polymer-based solar cells.^{93, 94} Recently, new solid state perovskite-based solar cells have been introduced in the PV field, with remarkable progress in a short period of time, and a highest reported efficiency of 22%.⁸⁸ Perovskite solar cells are promising, cheap, alternatives to crystalline silicon solar cells. Most of these emerging solar cells have an additional advantage in that they can be fabricated on flexible substrates.

1.2.1.2. Solar Cell Characterization

Characteristics of Current-Voltage (I-V) Curves

Upon shining light on a solar cell, an electron-hole pair (exciton) is generated in its active layer (light absorber). The electrons move in one direction, and the holes move in the other direction when there is an external bias applied. This results in a generation of current from the device, which is called the *photocurrent* (I_L). The device also produces some current in the absence

of light, just by an external voltage; this is called the *dark current* (I_D). In this case, the device acts as a diode and the output current depends on the applied voltage. The dark current always acts in the opposite direction to the light current. The I - V (current-voltage) curve of a solar cell is given in Figure 1.5a, and its characteristic equation can be written in terms of I_L and I_D as shown in Eq. (1.1).

$$I(V) = I_L - I_D(V) \quad (1.1)$$

Assuming the solar cell acts as an ideal diode in the absence of light, then the dark current equation can be written as Eq.1.2. By placing this in Eq. 1.1, we will get Eq. 1.3:

$$I_D = I_o \left[\exp \left(\frac{qV}{k_B T} \right) - 1 \right] \quad (1.2)$$

$$I = I_L - I_o \left[\exp \left(\frac{qV}{k_B T} \right) - 1 \right] \quad (1.3)$$

where I_o is a constant, q is the elementary charge, k_B is the Boltzmann constant, and T is the temperature.

The device also contains parasitic resistances, which are called the series (R_s) and shunt (R_{sh}) resistance. These two resistances arise from interfacial contacts, poor charge transporting materials, and current leakage through pinholes present in either the active layer or the electron or hole transport layers. A simple circuit diagram of a solar cell after including the two resistance terms is shown in Figure 1.5b. The resulting mathematical expression after considering R_s and R_{sh} is given in Eq. 1.4. Here, an extra term ‘ m ’ is included in the equation. It is an ideality factor and determines the non-ideal behavior of the device. Generally, the value lies between 1 and 2.

$$I = I_L - I_o \left[\exp q \left(\frac{V + IR_s}{mk_B T} \right) - 1 \right] - \frac{V + IR_s}{R_{sh}} \quad (1.4)$$

From this equation (Eq. 1.4), all the characteristics of a solar cell are derived. These characteristics are shown in Figure 1.5a and discussed in the following section.

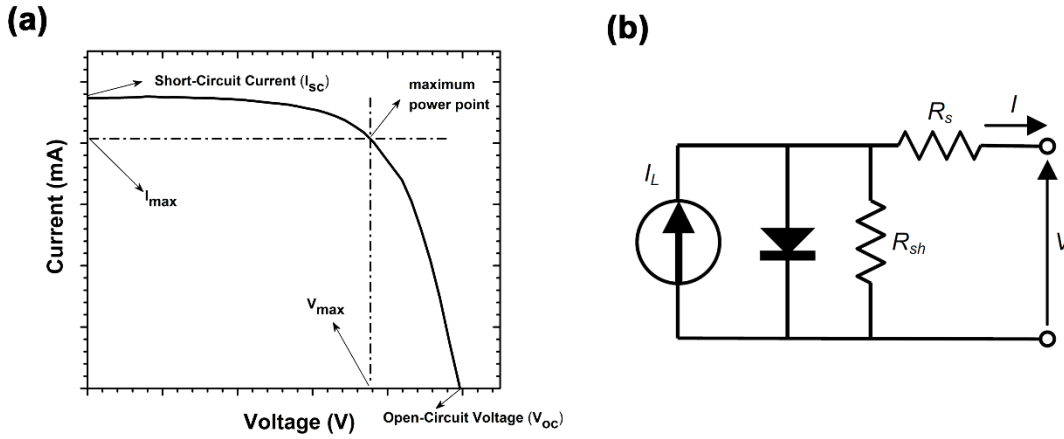


Figure 1.5. (a) A typical current-voltage (I-V) curve for a solar cell (b) the equivalent circuit diagram of a typical solar cell; here, I_L is photocurrent, R_s is series resistance, R_{sh} is shunt resistance and V is voltage.

Short-Circuit Current (I_{sc}): The dark current I_D always acts against the light current I_L . The maximum photocurrent is generated only when there is no external bias is applied to the device. Under this condition, the contribution of the dark current is zero, and the current obtained from the device is only due to the photocurrent. This current is called the short-circuit current, and the equation for I_{sc} is shown as Eq. 1.5. Several factors can influence the short-circuit current, such as carrier generation and carrier mobility in the sensitizer, film morphology, and device architecture.

$$I(V) = I_L - I_D(V)$$

$$I_{sc} = I_L \quad (1.5)$$

Open-Circuit Voltage (V_{oc}): At a particular applied voltage, the device generates the same amount of dark current (I_D) as that of light current (I_L). Since I_D and I_L act in the opposite direction, the resulting net current from the device is zero. This applied voltage is called the open circuit voltage; the equation is shown as Eq. 1.6.

$$V_{oc} = \frac{mk_B T}{q} \ln \left(\frac{I_{sc}}{I_o} + 1 \right) \quad (1.6)$$

Fill Factor (FF): The fill factor is a measure of the quality of a solar cell. It is the ratio of the maximum power to the product of I_{sc} and V_{oc} . The maximum power point is shown in Figure 1.5a. The fill factor measures the ‘squareness’ of the I - V curve as shown in Figure 1.5a. It is always less than one (or 100%). The corresponding equation for the FF is given in Eq. 1.7.

$$FF = \frac{I_{max} V_{max}}{I_{sc} V_{oc}} \quad (1.7)$$

Power Conversion Efficiency (PCE): The PCE is the ratio of the maximum output power to the input power; it is denoted by η . It determines the overall performance of the device. When the input power is taken as one sun (100 mW/cm^2), the PCE is written as Eq. 1.8.

$$\begin{aligned} \eta &= \frac{P_{max}}{P_{in}} \\ \eta &= \frac{J_{max} \times V_{max}}{100 \text{ mW/cm}^2} \\ \eta &= \frac{J_{sc} V_{oc} \times FF}{100 \text{ mW/cm}^2} \end{aligned} \quad (1.8)$$

Here, J_{sc} is the short-circuit current density, and J_{max} is maximum current density. The current density is defined as the current per unit area.

Series (R_s) and Shunt Resistance (R_{sh}): As discussed earlier, the device contains two parasitic resistances: the series and the shunt resistance. The series resistance arises from bulk resistance (within the semiconductor or the active layer), and interfacial resistance (resistance to charge injection). The major contributions to the shunt resistance are impurities or pinholes in the active layer; they create a current leakage in the device.

Incident Photon to Current-conversion Efficiency (IPCE):

IPCE is defined as the probability of one electron will be generated from a solar cell per incident photon as a function of wavelength. It provides information on the fraction of photons that are utilized by the device at a given wavelength. It depends on the extinction coefficient of the active material at that wavelength, charge transport within the active layer and interfacial charge transport. By integrating the IPCE spectrum, we can determine the short-circuit current density (J_{sc}) of the device. The mathematical relation between J_{sc} and IPCE is shown in equation (1.10).

$$IPCE \% = \frac{\text{number of electrons, } n}{\text{number of incident photons, } N} \quad (1.9)$$

$$J_{sc} = q \int \Phi(\lambda) \times IPCE(\lambda) \times d\lambda \quad (1.10)$$

here, q is an elementary charge, $\Phi(\lambda)$ is the AM 1.5G (Air Mass 1.5 Global Spectrum) incident photon flux at a wavelength λ ,

$$\Phi(\lambda) = \frac{\# \text{ of photons}}{\text{sec} \times \text{cm}^2}$$

1.2.2. Dye-sensitized solar cells

1.2.2.1. Overview

The foundation of dye-sensitized solar cells came from the concept of sensitization in early photography.⁹⁵ Hauffe *et al.* and Gerischer took these principles to design photoelectrochemical cells.^{96,97} Dye-sensitized solar cells are regenerative photoelectrochemical cells, where ideally no net chemical changes in the cell components occur during solar energy conversion. DSSCs were extensively studied in the 1990s,⁹⁸ but the efficiencies could not reach more than 1% due to poor

dye-sensitization on the smooth surface of the bulk metal oxide.⁹⁹ Here, the metal oxide is a semiconductor, and it transports the electrons that are injected from the dye to the electrode through its conduction band. In the late 1990s, O'Regan and Grätzel published a seminal work on replacing the smooth metal oxide electrode with a mesoscopic metal oxide (TiO₂).¹⁰⁰ The mesoscopic electrode was made by depositing a thin layer of 25 nm TiO₂ nanoparticles; the resulting layer contained mesoscopic (2-50 nm diameter) pores arising from the voids between the nanoparticles. The dye was infiltrated through these pores and coated the nanoparticles, this eventually resulted in a large surface area of the metal oxide sensitized by the dye. This novel approach produced a promising efficiency of 7.9%. After this study, many different dyes were explored in DSSCs. During the 1990s and early 2000s, inorganic complexes based on ruthenium were reported as high performing dyes in DSSCs. Some of the champion ruthenium-based dyes are N3, N719, N712 and N749 (also known as black dye) and their structures are shown in Figure 1.6. These dyes allowed for efficiencies of 10 -11% in DSSCs.¹⁰¹⁻¹⁰⁴ The best efficiencies were achieved only when iodide/triiodide solutions (I₂ and KI dissolved in acetonitrile) was used as the redox couple.¹⁰⁵ In 2011, Grätzel and coworkers set a new record efficiency of 12.3% by using a Zn-porphyrin based donor- π -acceptor dye with a Co²⁺/Co³⁺ redox couple.¹⁰⁶ In the past, this redox couple suffered from fast recombination rates by interacting with the dye molecule.¹⁰⁵ To minimize this, they introduced insulating groups on the dye molecule.¹⁰⁶ In 2014, by modifying the donor- π -acceptor dye, the efficiency was further improved to 13%.⁹⁰

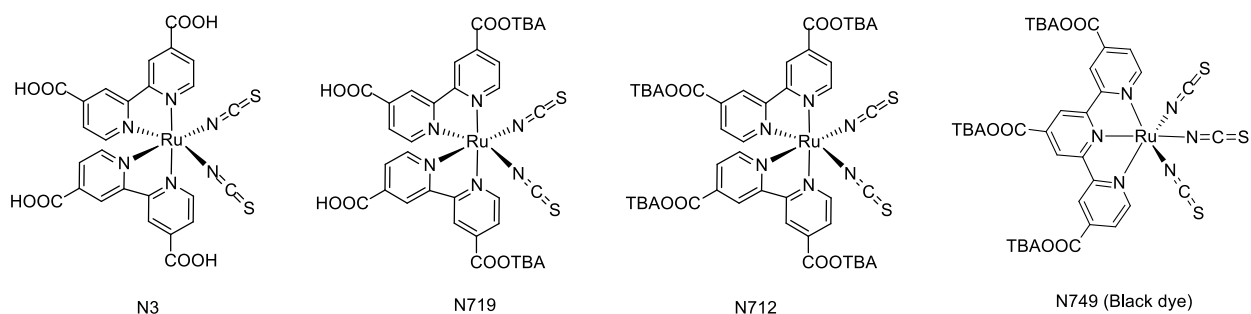


Figure 1.6. The structures of some of the champion Ru dyes, here TBA is the tetrabutylammonium ion.

1.2.2.2. Working principle of DSSC

A diagram of a traditional DSSC or Grätzel Cell is depicted in Figure 1.7a and the corresponding energy level (Jablonski) diagram with characteristic timescales of various processes is shown in Figure 1.7b.^{107, 108} The key components of a DSSC are a dye (sensitizer), a mesoporous semiconducting metal oxide (electron transport layer), a redox couple (for the dye regeneration) and two metal electrodes (where the charge is collected). In Figure 1.7b, the kinetics are based on the iodide/triiodide redox couple. The generation of photocurrent from the device occurs in several steps.

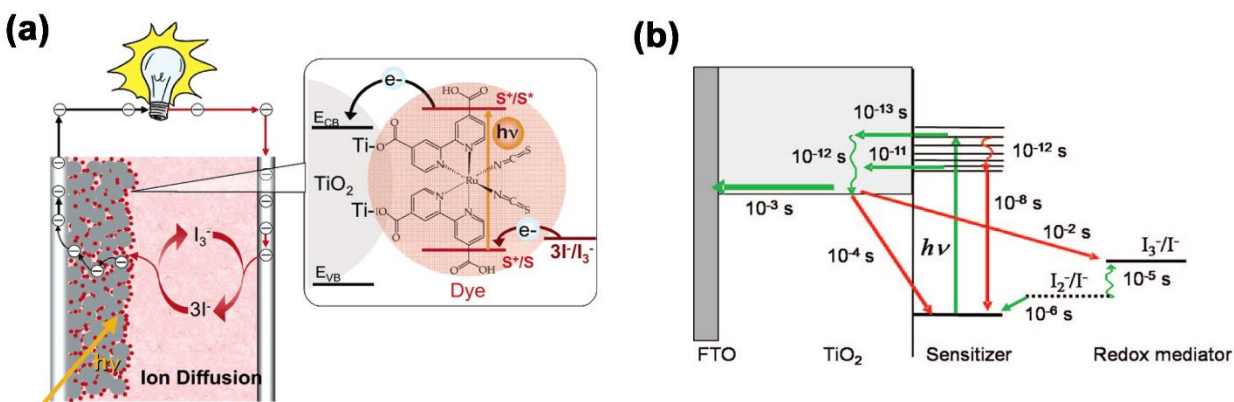


Figure 1.7. (a) A schematic of DSSCs showing the key components and (b) the charge transfer and recombination kinetics. Figure (a) Reprinted from Reference (107) and figure (b) is reprinted from (108). Copyright (2005, 2010) American Chemical Society.

Step 1: In this step, the dye absorbs a photon and undergoes excitation. An electron-hole pair (exciton) is generated as a result of this excitation. The lifetime of this excited state is critical for achieving high performance. The excited state lifetimes of the most common Ru-based dyes are on the order of tens of nanoseconds.¹⁰⁸

Step 2: After the dye excitation, the electrons are injected into the CB of the semiconducting metal oxide (e.g., TiO₂, ZnO) as shown in Figure 1.7b. There is always a competition between the charge injection process and dye relaxation (via recombination). However, in most of the Ru-based dyes, the electron transfer to the metal oxide (on the order of ps) is relatively fast compared to the dye relaxation (on the order of ns).¹⁰⁸ To achieve an efficient electron transfer from the dye to the semiconductor, the dye must be adsorbed on the surface of the semiconductor. Often the dyes are functionalized with -COOH groups, since these groups have a tendency to bind with the semiconductor oxide surface.

Step 3: After charge injection, the electrons are transported through the mesoscopic structure of the semiconductor until they reach the electrode. To achieve efficient charge transport, the semiconductor nanoparticles in the mesoporous layer are often sintered by annealing at elevated temperatures. The charge transport in the semiconductor is a relatively very slow process. Here, the loss of photocurrent is mainly due to recombination of the electrons with either the oxidized dye or the iodide electrolyte.

Step 4 & 5: In these steps, the oxidized dye is regenerated by taking an electron from the iodide in the electrolyte. After regeneration, the redox couple returns to its original state (I⁻) as I₃⁻ is reduced back to I⁻ at the Pt electrode.

1.2.2.3. Plasmon-enhanced DSSCs

The solar energy that reaches the Earth is spread over a wide wavelength range (Figure 1.8). Harvesting a broad region of this light is essential for achieving high-performance solar cells. In DSSCs, the dye plays a key role; it must have a large extinction coefficient over a broad region. The performance of DSSCs is often limited by the narrow region of light absorption of the dye. Several efforts have been dedicated to the synthesis of panchromatic dyes, which include introducing another chromophore on existing dyes, and by making donor-acceptor conjugated molecules.¹⁰⁹⁻¹¹¹ Further, to harvest light in multiple regions of the visible spectrum, co-sensitizers such as quantum dots have been used along with existing dyes.^{112, 113} However, the problem with multiple sensitizers is there is often a competition between the sensitizers to adsorb on the surface of the semiconductor. Another promising approach is employing plasmonic nanoparticles to improve light harvesting in DSSCs. The plasmonic nanoparticles have unique optical properties (*cf.* Section 1.2.2), which are easily tunable based on the particle size and morphology. They can act as nanoscale antennas by concentrating the incoming light into small domains. They can be integrated in the mesoscopic layer or the iodide electrolyte. In both cases, they enhance the performance of DSSCs.³²

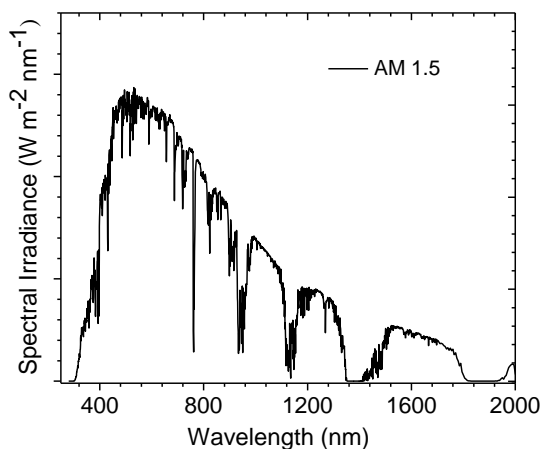


Figure 1.8. Standard AM 1.5G (Air mass) solar spectrum

Energy transfer processes:

Atwater and Polman reviewed plasmonic light trapping mechanisms in silicon solar cells; the two major mechanisms are shown in Figure 1.9.¹¹⁴ As discussed earlier (*cf.* Section 1.1.1), the excited plasmons release the trapped light energy *via* radiative and non-radiative pathways. The radiative energy can be in the form of either far-fields (light scattering) or near-fields (local electric field). These two effects contribute to produce an overall enhancement of light harvesting efficiency (LHE) in the device. Upon shining light on this plasmonic device, the integrated plasmonic nanoparticles scatter the light (far-field effect) in all directions. This leads to an increase in the path length of light within the device. As a result, the active material (dye or Si) gets multiple chances to absorb the light, which ultimately improves the overall light harvesting in the device. Here, the energy of the scattered light must still fall within the absorption spectrum of the active material. In addition to the light scattering effect, the local electric field generated on the surface of the nanoparticle can enhance the charge carrier separation in the surrounding medium.^{22, 32, 115} This ultimately results in an enhancement of the overall photocurrent in the device.

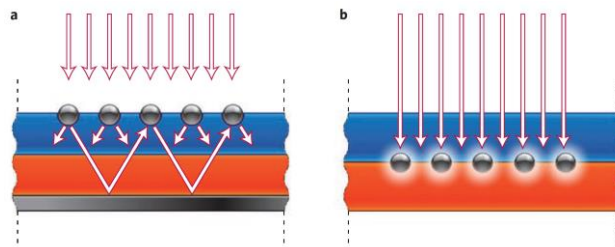


Figure 1.9. Plasmonic effects using spherical nanoparticles in silicon solar cells; (a) plasmonic light scattering effect and (b) plasmonic near-field enhancement. Here, the orange layer is *n*-type silicon, and blue layer is *p*-type silicon. Reprinted from Reference (114). Copyright (2010) Nature Publishing Group.

Non-radiative relaxation results in either the generation of hot electrons or plasmon resonance energy transfer (PRET) to the surrounding medium. Kamat and coworkers observed plasmonic hot electron transfer from Au to TiO₂ in DSSCs; such hot electrons altered the Fermi energy level in TiO₂, resulting in a significant change in the V_{oc} .¹¹⁶ The other mechanism is PRET;

while this mechanism was observed in single molecule fluorescence enhancement (energy transfer from an Au nanoparticle to a fluorophore),¹¹⁷ it is poorly understood how much it might contribute to DSSCs. All these radiative and non-radiative energy transfer processes are highly dependent on the size, morphology, and composition of the plasmonic nanoparticles.

Effect of Size, Shape, and Morphology:

According to Mie theory, the extinction cross section of a spherical metal nanoparticle is proportional to r^6 , where 'r' is the diameter of the nanoparticle. Thus the size of the metal nanoparticle plays a significant role in plasmonic enhancement effects. If the size is less than 30 nm, absorption dominates over light scattering. Ultra-small metal nanoparticles (often called clusters, which have sizes of *ca.* 1 nm) do not show any light scattering effects, as they do not support LSPR modes but rather have discrete HOMO-LUMO transitions. Thus, they can be directly used as light absorbers in solar cells. Chen *et al.* achieved a *ca.* 2% efficiency power conversion by using Au₂₅ clusters (~1 nm) as active materials.¹¹⁸ With an increase in size, plasmonic nanoparticles tend to exhibit surface plasmon oscillations. As a result of this, they show light scattering and absorption effects (*cf.* Section 1.2.2). Au nanoparticles of ~5 nm in size have been shown to transfer plasmonic hot electrons from Au to TiO₂; this resulted in a slight increase in the photocurrent current from the device.¹¹⁶ Further, by employing different sizes of Au nanoparticles between 5-100 nm in DSSCs, an increase in PCE was observed.^{119, 120} In both reports, the enhancement in PCE was due to an increase in J_{sc} and V_{oc} ; these changes were dependent on the size of the nanoparticles. Particles that were 5-50 nm in size showed enhancements in both J_{sc} and V_{oc} , whereas the sizes between 80-100 nm only led to an increase in J_{sc} .

Morphology is another important factor that governs the optical properties of plasmonic nanoparticles. Many reports on plasmonic DSSCs have used spherical nanoparticles with core-

shell morphologies, where the core is the metal and the shell is a metal oxide.¹²¹⁻¹²⁶ For example, Jeong *et al.* integrated Ag@TiO₂ core@shell nanoparticles in DSSCs and achieved *ca.* 25% enhancement of the overall performance.¹²⁶ Here, the metal oxide shell protects the nanoparticles from the corrosive action of the iodide electrolyte.^{125, 124} However, the thickness of the TiO₂ shell plays a critical role in the plasmonic enhancement. Thicker shells attenuate the local electric fields generated on the surface of the plasmonic nanoparticles,¹²⁷ resulting in a reduction in the overall plasmonic enhancement. Plasmonic near-fields generated on the surface are available only a small away distance from the surface. Standridge *et al.* found that a ~ 7 nm thick TiO₂ shell is the optimum thickness for preventing near-field attenuation while simultaneously protecting the nanoparticle.¹²⁸ However, the semiconductor metal oxide (TiO₂) shell leads to interference with charge transport in the mesoscopic TiO₂ layer. To prevent this interference, Snaith and coworkers replaced the TiO₂ shells with insulating SiO₂ shells on Au nanoparticles.¹²³ In a similar way, various shapes of plasmonic nanoparticles have been employed in DSSCs; these shapes include, nanorods,^{129, 130} nanocubes,¹³¹ nanoprisms,^{127, 132} nanostars,¹³³ nanowires,^{134, 135} and other complex morphologies.¹³⁶ The advantage of using anisotropic nanoparticles is they have broad plasmon bands which are tunable in the desired region. For example, harvesting light in the near-IR region is very challenging in DSSCs, since most dyes absorb weakly in this region. In addition to the tunable properties, anisotropic nanoparticles exhibit intense local electric fields compared to spherical nanoparticles. By integrating Au@Ag₂S nanorods in DSSCs, Chen *et al.*¹³⁰ achieved a *ca.* 10 % enhancement in the IPCE in the 600-720 nm region. Dong *et al.*¹²⁹ and Zaric *et al.*,¹³¹ observed enhanced IPCE in the red region using Ag@Au nanorods and Au nanocubes, respectively. In a similar way, a plasmonic enhancement in light harvesting has also been explored in other solar cells, such as organic photovoltaic cells,¹³⁷ quantum-dot-sensitized solar cells,¹³⁸ and

perovskite solar cells.¹³⁹ However, in perovskite solar cells, no notable plasmonic enhancement was observed. The lead halide perovskite that is used in perovskite solar cells itself is a strong light absorber over a broad region. Therefore, to improve the device efficiency, other approaches such as controlling the perovskite layer thickness and improving perovskite crystal growth and connectivity are investigated in this thesis. Perovskite solar cells are discussed in more detail in the following Section.

1.2.3. Perovskite solar cells

1.2.3.1. Overview

Organic-inorganic lead halide perovskites are excellent semiconductor materials for solar cells. Miyasaka and co-workers pioneered these perovskite solar cells in 2009; they achieved an efficiency of 3.2% by using an architecture similar to DSSCs (*cf.* Section 1.2.2.2).¹⁴⁰ Further, by replacing the liquid iodide redox couple with a solid-state hole-transport material, Snaith and co-workers produced a high performing perovskite solar cell with an efficiency of *ca.* 12%. In the last few years, there have been numerous articles and reviews published on perovskite solar cells.¹⁴¹⁻
¹⁵¹ The best efficiency so far reported for perovskite solar cells is 22.1%, which makes these solar cells potential candidates for commercialization.⁸⁸ Besides the high performance, the cost associated with these solar cells is orders of magnitude cheaper than crystalline silicon solar cells. Here, the perovskite is an organic-inorganic hybrid halide, and it adopts the crystal structure of a natural mineral, CaTiO₃. The chemical formula of this perovskite is ABX₃, and in lead halide perovskites, A is a monovalent organic or inorganic cation such as methylammonium (MA, CH₃NH₃⁺), formamidinium (FA, CH(NH₂)₂⁺) or Cs⁺, B is a divalent metal (Pb²⁺, Sn²⁺) and X is a halide (Cl⁻, Br⁻, I⁻) ion.

The optoelectronic properties of these hybrid perovskites were extensively studied in the early 1990s by Mitzi and co-workers.⁷³ However, no solar cell was fabricated using perovskite materials at that time. All these optoelectronic properties depend on the identity of A, B, and X. The valence band is derived from the orbitals of the halide ions (X), and the conduction band is derived from the orbitals of the divalent metal (B). The major role of the monovalent cation (A) is to stabilize the perovskite crystal structure.¹⁴¹ Among all lead halide perovskites, methylammonium lead iodide ($\text{CH}_3\text{NH}_3\text{PbI}_3$) is the most studied perovskite in solar cells. $\text{CH}_3\text{NH}_3\text{PbI}_3$ is a direct bandgap semiconductor with a reported band gap of 1.50 - 1.61 eV.¹⁴¹ The absorption coefficient of $\text{CH}_3\text{NH}_3\text{PbI}_3$ is $1.5 \times 10^4 \text{ cm}^{-1}$ at 550 nm; this value was estimated using a mesoscopic TiO_2 architecture. The band gap of this $\text{CH}_3\text{NH}_3\text{PbI}_3$ perovskite changes when the I^- is replaced by other halide ions. For example, Seok and co-workers observed a change in the band gap from 1.6 - 2.2 eV by varying the ratios of I^-/Br^- in $\text{MAPbI}_{3-x}\text{Br}_x$.¹⁴² Among the devices they made, the best efficiency was observed for MAPbI_2Br perovskites. The band gap is also tunable based on the identity of the monovalent cation (A in ABX_3). Although the orbitals associated with these cations do not contribute to either the VB or CB, changing this cation influences the Pb-I bond angles resulting in an overall change in the perovskite crystal structure, which eventually alters the band gap of the perovskite. Grätzel and co-workers observed a narrowing of the band gap to 1.4 eV by replacing MA with FA;¹⁴³ the $\text{MA}_{0.4}\text{FA}_{0.6}\text{PbI}_3$ perovskite produced a high-performing device.

In addition to having tunable optical properties, these perovskites have excellent electronic properties such as low exciton binding energies,^{144, 145} large dielectric constants,¹⁴⁶ high charge carrier mobilities, and slow carrier recombination kinetics.^{147, 148} The carrier diffusion lengths in mixed halide ($\text{MAPbI}_x\text{Cl}_{3-x}$) perovskites were reported to be in the micrometer range.¹⁴⁸ A

millimeter length single perovskite crystal exhibits even longer carrier diffusion lengths; which are in the order of hundreds of micrometers.¹⁴⁹ Due to these promising properties, this class of perovskite materials shows significant efficiencies even on insulating Al₂O₃ scaffolds.¹⁵⁰

1.2.3.2. Architectures of perovskite solar cells

The architecture of a perovskite solar cell greatly affects the performance of the device. It governs the growth of the perovskite crystallites, the rate of charge carrier extraction and hence the efficiency of the device. Along with the performance, the stability of the perovskite also depends on the device architecture. Perovskite solar cells can be constructed in two major architectures, (1) mesoscopic, and (2) planar heterojunction as shown in Figure 1.10. The device can also be fabricated in two different ways, one with the electron transport layer below the perovskite layer and the other with the electron transport layer above the perovskite layer. These two configurations are denoted as (i) n-i-p and (ii) p-i-n, where the n-type contact layer is the electron transport layer (ETL), i- is the active (perovskite) layer and the p-type contact layer is the hole transport layer (HTL) as shown in Figure 1.10.¹⁵¹

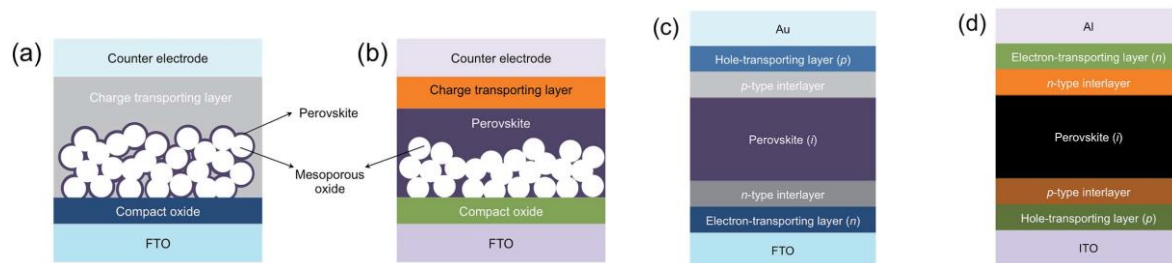


Figure 1.10. Various architectures of perovskite solar cells; mesoscopic solar cells (a) Al₂O₃ scaffold, (b) TiO₂ mesoscopic layer and planar heterojunction solar cells; (c) n-i-p type and (d) p-i-n type architectures. Here, FTO is fluorine doped tin oxide and ITO is indium doped tin oxide Reprinted from Reference (151). Copyright (2015) Royal Society of Chemistry.

Mesoscopic perovskite solar cells: In mesoscopic perovskite solar cells, the n-type contact layer consists of a mesoporous thin film. This film is made by depositing a thin layer of metal oxide

nanoparticles. Upon annealing this layer at elevated temperatures, the film produces mesoscopic pores from the void spaces between the particles. The perovskite precursors are infiltrated into the pores, and the crystallites are grown. The first report of perovskite solar cells used this mesoscopic architecture.¹⁴⁰ The common configuration of mesoscopic perovskite solar cells is FTO/compact-TiO₂/mesoscopic-layer/perovskite/HTL/electrode; here, FTO is fluorine doped tin oxide; it is a transparent conductive oxide. The mesoscopic layer is composed of either a semiconducting or an insulating metal oxide. Snaith and co-workers produced a *ca.* 12% efficient device by using an Al₂O₃ (insulating) scaffold and *ca.* 9% efficient device using a TiO₂ scaffold.¹⁵⁰ The thickness of this mesoporous layer is critical; thinner layers accommodate less perovskite, resulting in a reduction of light absorption, while thicker layers suffer from insufficient pore filling.^{152, 153} However, the pore filling also depends on the perovskite deposition method. Grätzel and co-workers used a two-step sequential deposition technique to achieve efficient pore filling.¹⁵⁴ Here, they reported an efficiency of *ca.* 15% using a TiO₂ mesoscopic scaffold. Later, several other metal oxide nanoparticles such as ZrO₂ and SiO₂ were used in this mesoscopic layer.^{155, 156} Recently, Seok and co-workers produced an efficiency of 20.1% using the mesoscopic architecture with mixed (MA and FA) perovskites as the light absorbing material.¹⁵⁷

Planar heterojunction (PHJ) solar cells: In planar heterojunction solar cells, the junction at the ETL/perovskite and perovskite/HTL interface is planar. Here, the perovskite layer is sandwiched between the flat ETL and HTL. Due to the low exciton binding energy and excellent charge carrier diffusion lengths in these perovskite materials, the charge carriers are easily transported within the perovskite until they reach the planar interfaces. However, uniform surface coverage and a smooth perovskite layer are essential for efficient charge transport within the perovskite as well as transport across the interface. Unlike mesoscopic architectures, some of the planar films are

fabricated at room temperature. Due to this low temperature processing, PHJ cells can be made on flexible plastic substrates. There are two configurations of PHJ solar cells; one is with the electron transport layer below the perovskite layer (regular: n-i-p), and the other is with the electron transport above the perovskite layer (inverted: p-i-n).

In regular PHJ solar cells, thin films of TiO₂ or ZnO nanoparticles are generally used as electron transport layers. By using planar TiO₂ films, Snaith and co-workers achieved a PCE of *ca.* 15% when the perovskite was deposited by a physical vapor deposition method.¹⁵⁸ However, the compact TiO₂ layer used here still required high-temperature annealing. Yella *et al.* used relatively low temperature processed rutile TiO₂ as an electron transport layer and achieved a high V_{oc} of 1.11 V, which ultimately resulted in an efficiency of about 13%.¹⁵⁹ From our group, Liu *et al.* employed a room temperature-processed planar ZnO nanoparticle layer and achieved an efficiency of *ca.* 16%.¹⁶⁰ The device also showed a promising efficiency of 10.2% on flexible substrates. In a similar way, other electron transport layers such as SnO₂ nanoparticles and CdSe nanoparticles have also been explored in this regular PHJ configuration.^{161, 162}

In the inverted architecture, the electron transport layer is located above the perovskite layer. The most widely studied inverted configuration is ITO/PEDOT:PSS/perovskite/PCBM/electrode. Here, ITO (indium doped tin oxide) is a transparent conductive oxide, PEDOT:PSS (poly(3,4-ethylenedioxythiophene) polystyrene sulfonate) is the hole transport layer, and the PCBM (phenyl-C61-butyric acid methyl ester) is the electron transport layer. In early work, this configuration produced very poor performing devices with a maximum efficiency of 3.9%.¹⁶³ The low efficiencies were attributed to poor film morphology. By employing a mixed halide perovskite (MAPbI_xCl_(3-x)), the efficiency was improved to *ca.* 11%.^{164, 165} However, the perovskite domain size and the layer coverage still

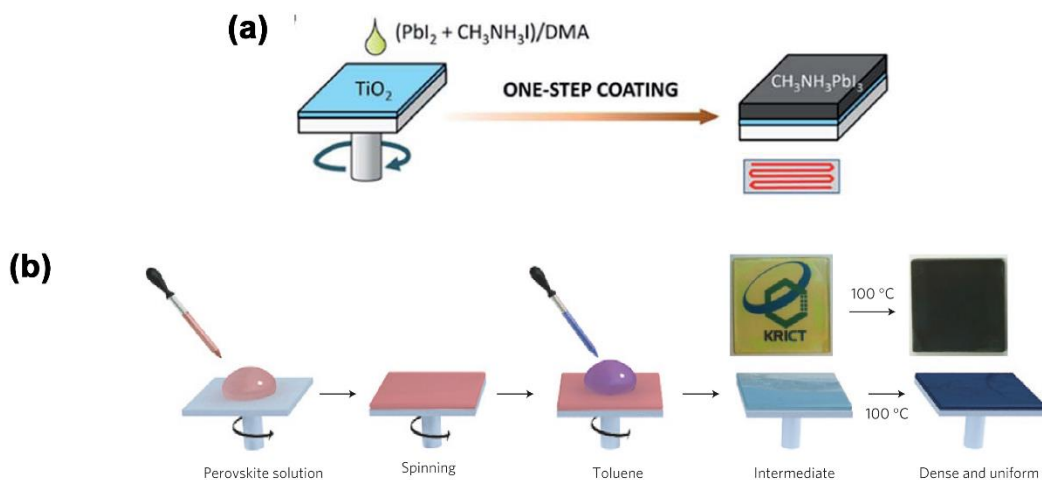
limited the performance of the device. By employing solvent annealing, Huang and co-workers improved the perovskite crystallite size and the film coverage on the PEDOT:PSS layer. This ultimately resulted in an overall enhancement of the device performance, with a peak efficiency of *ca.* 15%.¹⁶⁶ Further, You *et al.* studied moisture-assisted crystallite growth; they produced a device with 17.1% efficiency.¹⁶⁷ By casting the perovskite on a hot substrate, Nie *et al.* produced millimeter scale perovskite crystals and the device made from these crystals produced a high efficiency of *ca.* 18%. Along with PEDOT:PSS, there have been many other hole transport layers studied in this inverted configuration, such as graphene oxide (GO), spiro-OMETAD (2,2',7,7'-tetrakis-(N,N-di-p-methoxyphenylamine)-9,9'-bifluorene), NiO_x, V₂O₅ and CuSCN.^{151, 168} Recently, by using NiO_x as a p-type contact layer, Yang and his co-workers produced a device with *ca.* 16% efficiency in a perovskite solar cell. They further improved the moisture stability of the device by depositing a ZnO n-type contact layer on top of the perovskite layer.¹⁶⁹

1.2.3.3. Perovskite deposition techniques and the film morphology

Regardless of the architecture, the performance of perovskite solar cells is influenced by the perovskite crystallinity, grain size, film morphology, and surface coverage. All these factors are dependent on the deposition techniques used and the atmospheric conditions (e.g., relative humidity, ambient air or N₂ atmosphere).¹⁷⁰ The deposition techniques are classified into two major categories: (1) one-step deposition, (2) two-step deposition (sequential deposition) (Figure 1.11).

One-step deposition technique: The one-step deposition technique is a single step process, in which the perovskite precursors are co-deposited on the desired substrate. The precursors are typically the organic (MA or FA) halide and the inorganic metal (Pb or Sn) halide. In this method, the formation of the perovskite crystallites occurs in two consecutive stages; one is solvent

One-step deposition techniques



Two-step deposition techniques

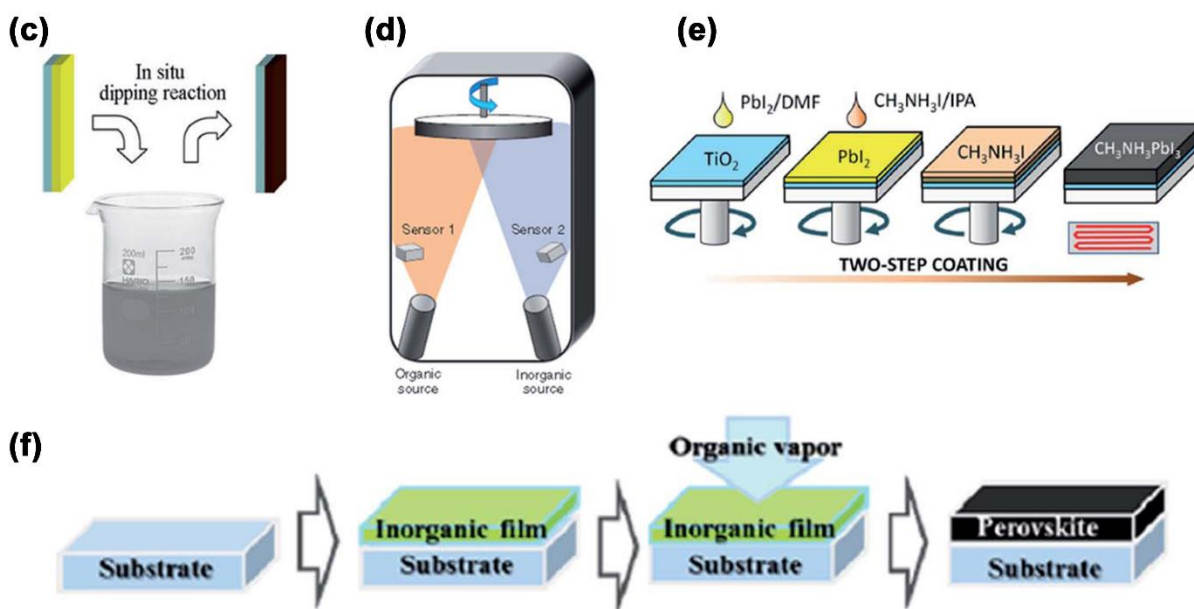


Figure 1.11. The top panel (a & b) shows the one-step deposition method; (a) direct deposition of perovskite precursor on TiO_2 , (b) solvent engineering by dripping toluene solvent. The bottom panel (c, d, e & f) shows the two step deposition technique; (c) two-step deposition by dipping PbI_2 in MAI solution, (d) physical vapor deposition (dual source co-deposition) of PbCl_2 and MAI, (e) two-step spin coating (inter-diffusion) method, and (f) vapor assisted solution process (two-step). Reprinted from References (170, 174, 158, 177 and 176). Copyright (2013, 2014) Nature Publishing Group, (2015, 2016) Royal Society of chemistry, and (2014) American Chemical Society.

evaporation, and the other is crystallization. This method works well for mesoscopic architectures; the pores slow the rate of solvent evaporation and enhance the rate of perovskite crystallization. However, by using this method, pore filling becomes a major concern in mesoscopic solar cells. In the case of planar architectures, this deposition method produces poor surface coverage due to the slow nucleation and rapid crystallization due to the fast evaporation of the solvent in the spin-coating process. To overcome this rapid crystallization, often the solutions are prepared by adding a co-solvent, such as DMSO or DMF. The DMSO coordinates with the PbX_2 salt and suppresses the rate of crystallization.^{171, 172} The rate of crystallization can also be controlled by changing the perovskite composition. By using a mixture of MAI and PbCl_2 , Snaith and co-workers controlled the perovskite coverage on a planar TiO_2 layer.¹⁷³ Here, the presence of Cl^- ions causes lattice distortions resulting in prolonged crystallization of the perovskite. The change in nucleation and growth of the perovskite upon Cl^- inclusion was attributed to the rapid formation of MAPbCl_3 intermediates. Seok *et al.* achieved an exceptionally uniform perovskite layer by solvent engineering during the perovskite formation stage of the one-step deposition method (Figure 1.11b).¹⁷⁴ Here, they used a mixture of solvents (γ -butyrolactone and DMSO) to deposit $\text{CH}_3\text{NH}_3\text{PbI}_x\text{Br}_{(3-x)}$, and during the spin-drying step, another solvent (toluene) was dripped on top of the film. The addition of DMSO impedes the reaction between MAI(Br) and $\text{PbI}_2(\text{Br})$ by forming a MAI- PbI_2 -DMSO intermediate phase, and toluene dripping accelerates the formation of this intermediate phase *via* removal of excess DMSO in the film. As a result of the formation of this stable intermediate phase, the perovskite nucleation and crystallization were controlled. This method produced an efficient device with a remarkable performance of 17.5%.

Two-step deposition (sequential deposition) technique: A general concern with the one-step deposition technique is achieving complete perovskite formation and uniform crystal growth.

To overcome these issues, a two-step deposition method was introduced. In this method, the first step is the deposition of a PbI_2 layer. After preparing the PbI_2 film, the perovskite is produced by either dipping the substrate in a solution of methylammonium iodide (MAI) or by spin-casting a MAI solution in the second step. The two-step deposition was first reported by Mitzi and co-workers.¹⁷⁵ Grätzel and co-workers adopted this method for the fabrication of mesoscopic perovskite solar cells.¹⁵⁴ By using this sequential deposition method, they produced an efficient device with *ca.* 15% power conversion efficiency. This method has since been used by many other groups for both types of architecture. However, the major concern with this method is the reproducibility of the film morphology, which varies from group to group, and depends on many other factors such as pre and post-annealing temperatures and atmospheric conditions (relative humidity). Several modifications to the two-step deposition method have been reported including an inter-diffusion method (two-step spin coating), and vapor assisted solution processed method.¹⁷⁶ By using the two-step spin-coating process on mesoscopic substrates, Park and co-workers were able to grow perovskite crystals of up to $\sim 1 \mu\text{m}$ in size and achieved a PCE of 17%.¹⁷⁷ Here, the MAI solution was spin-coated on top of a PbI_2 layer; the growth of the perovskite crystals was controlled by varying the concentration of MAI and the spinning speed. Yang and co-workers introduced a vapor assisted solution process to construct the polycrystalline perovskite layer.¹⁷⁶ In this method, MAI vapor was used instead of a solution. Using this method, they produced a uniform perovskite layer on a planar TiO_2 layer, which led to a device with PCE of 12.1%. Recently, Seok and coworkers achieved a *ca.* 20% PCE by a two-step spin coating technique on a mesoscopic layer; they used a $\text{PbI}_2(\text{DMSO})$ complex solution instead of only PbI_2 .¹⁷⁸ By depositing formamidinium iodide (FAI) on the $\text{PbI}_2(\text{DMSO})$ layer, they achieved high-quality

FAPbI₃ films, and demonstrated that the direct intermolecular exchange of DMSO with FAI produced large-grained microstructures of the perovskite.

1.2.3.4. Device Issues

Although the performance of perovskite solar cells is promising, there are many concerns associated with these solar cells. The major issues are hysteresis in the J - V curves (unstable photocurrents), irreproducibility of the device fabrication, and device stability.¹⁷⁹⁻¹⁸¹ Unlike many other solar cells, perovskite solar cells show an unusual hysteresis in their J - V curves; this hysteresis depends on the sweep rate and the sweep direction of the applied bias. In general, reverse sweeping (scanning from open circuit voltage to short-circuit current) produces higher efficiencies than a forward sweep. The origin of this unusual behavior has been attributed to several factors including the capacitive behavior of lead halide perovskites,¹⁸²⁻¹⁸⁴ intrinsic trap states, grain boundaries,^{185, 186} and ion migration (ferroelectric behavior) in the perovskite.¹⁸⁷⁻¹⁸⁹ Regular planar heterojunction solar cells that consist of TiO₂ and spiro-OMETAD show pronounced J - V hysteresis compared to both inverted and mesoscopic solar cells. It has been demonstrated that due to high capacitive nature of TiO₂ and spiro-OMETAD, the charge is accumulated at the ETL/perovskite and perovskite/HTL interfaces.¹⁸⁰ Upon replacing TiO₂ and spiro-OMETAD with low capacitance materials, such as PCBM and PEDOT:PSS or NiO_x, a decrease in the hysteresis was observed.¹⁸² Several reports demonstrated that, the presence of intrinsic trap states within the perovskite layer and the traps created by grain boundaries could also contribute to the hysteresis in the device.^{183, 186} To passivate these traps, Huang *et al.* spin coated a PCBM capping layer on top of the perovskite layer, which resulted in a hysteresis-free device with 14.9% efficiency.¹⁸⁶ By carefully considering all the factors that are causing the hysteresis many recent reports have produced hysteresis-free perovskite solar cells.^{190, 191}

Another major issue with perovskite solar cells is their stability; the perovskite layer degrades upon exposure to humidity, heat, and light. Lead halide perovskites are highly hygroscopic in nature; by exposing the perovskite film to moisture (>50% RH), the color of the perovskite changes from dark brown to yellow or colorless within a short period of time, which ultimately results in detrimental effects on the device performance.¹⁴² An early study on perovskite degradation reported the formation of a colorless monohydrate lead iodide salt ($\text{CH}_3\text{NH}_3\text{PbI}_3 \cdot \text{H}_2\text{O}$) as an intermediate phase,¹⁹² and later the structure was demonstrated by Hao *et al.*¹⁹³ However, some of the recent reports on perovskite degradation assigned the intermediate phase as a dihydrate perovskite ($\text{CH}_3\text{NH}_3\text{PbI}_3 \cdot 2\text{H}_2\text{O}$).^{194, 195} Finally, by using time-resolved X-ray diffraction, Leguy *et al.* resolved this intermediate phase as a monohydrate product ($\text{CH}_3\text{NH}_3\text{PbI}_3 \cdot \text{H}_2\text{O}$).¹⁹⁶ They found that upon exposure to moisture, the perovskite first forms a reversible monohydrate product, which eventually degrades to the dihydrate product upon exposure to humidity for a long time. In addition to moisture, light and heat have been shown to accelerate perovskite degradation. Most recently, several reports demonstrated that the mixed FA–cesium perovskites such as $\text{FA}_{0.9}\text{Cs}_{0.1}\text{PbI}_3$ and $\text{Cs}_5\text{MA}_{0.16}\text{FA}_{0.79}\text{PbI}_{2.49}\text{Br}_{0.51}$ undergo slower decomposition in the presence of both humidity and light compared to MAPbI_3 .^{197, 198} However, these issues still need to be completely addressed before the commercialization of perovskite solar cells can be realized.

1.3. Photocatalysis

1.3.1. Overview

The transformation of solar energy into chemical energy is another expanding field. For many years, semiconductor nanoparticles such as TiO_2 , ZnO , and ZrO_2 have been used as photocatalysts to drive chemical reactions. However, due to their wide band gaps, they show

catalytic activity only in the UV region. To make these catalysts active in the visible region, their bandgap can be altered by doping with different elements such as N, S, and Mn.¹⁹⁹⁻²⁰¹ However, upon doping, their catalytic activity was affected; they showed decreased activities compared to the undoped nanoparticles.²⁰² Alternatively, various other visible light absorbing nanomaterials such as WO₃, and CdS have been studied as photocatalysts.³³ Similarly, plasmonic nanoparticles have been used to harvest visible light for driving (or improving) the rates of these chemical reactions.

1.3.2. Plasmonic light harvesting for photocatalysis

Plasmonic nanoparticles are promising materials for light harvesting due to their strong extinction cross sections and tunable optical properties in the visible region. During the early 2000s, Kamat and coworkers used Au nanoparticles to improve the photocatalytic activity of TiO₂ in the visible region.²⁰³ Although plasmonic nanoparticles were used in photocatalysis applications in the early 2000s, the word plasmonic catalysis was introduced by Awazu *et al.* in 2008,²⁰⁴ who used plasmonic Ag nanoparticles to improve the catalytic activity of TiO₂ in methylene blue degradation. Since then, plasmonic nanoparticles have been employed for various chemical reactions such as dye degradation, water splitting, oxidation and reduction reactions, and cross-coupling reactions.²⁰⁵

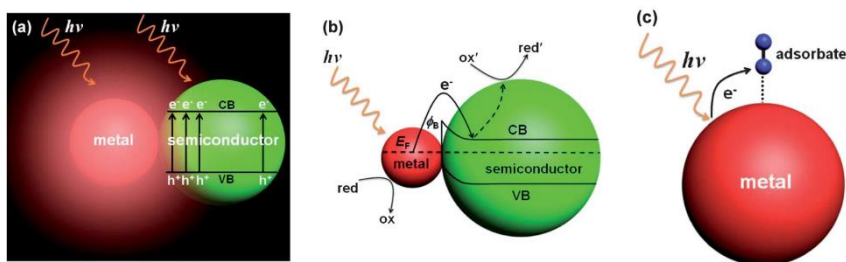


Figure 1.12. Plasmon energy transfer mechanisms for photocatalysis; (a) Plasmonic near-field effect, (b) Plasmonic charge transfer to a semiconductor (crossing the Schottky junction), and (c) plasmonic charge transfer to the adsorbate molecule. Reprinted from Reference (206). Copyright (2013) The Royal Society of Chemistry.

Plasmonic nanoparticles can be used to drive chemical transformations in several ways (Figure 1.12).^{32, 206} (i) plasmonic hot electron injection, (ii) plasmonic near-field effects, (iii) plasmonic local heating and (iv) plasmonic resonance energy transfer. In some cases, the plasmonic nanoparticles directly catalyze the reactions (plasmon-mediated catalysis), and in other cases, they enhance the activity of existing catalysts connected to the plasmonic particles (plasmon-enhanced catalysis). These mechanisms are discussed in the following section.

1.3.2.1. Mechanisms of plasmonic enhancement

Plasmonic local fields: Due to surface plasmon oscillations, a dipole is generated in the nanoparticles. This dipole causes the generation of an electric field (near-field effect) on the surface of the particle. By using finite-difference time-domain simulations, Mizeikis *et al.* demonstrated that the local electric field intensity at a Au/TiO₂ interface could be up to 10⁴ times greater than the incident electric field.²⁰⁷ However, the magnitude of these local fields is highly dependent on the morphology of the plasmonic nanoparticles.²⁰⁸ These local fields can enhance carrier separation in metal oxides and these free carriers can then participate in the chemical reaction; this eventually leads to an enhanced catalytic activity of the metal oxide nanoparticles. In particular, the near-field effect is helpful in materials like Fe₂O₃, where carrier recombination is a major issue. For example, upon embedding Au nanoparticles in a Fe₂O₃ photoelectrode, an enhanced photocurrent was observed in the presence of visible light; this improved the activity of Fe₂O₃ for the water splitting reaction.^{209, 210} Duan *et al.* reported enhanced electron-pair generation in CdS nanoparticles due to the generation of near-fields at the Ag/CdS interface.²¹¹ Here, the enhancement was observed even after using an insulating SiO₂ spacer between the Ag and CdS nanoparticle. In a similar way, using pump-probe studies Cushing *et al.* observed an increase in charge carrier separation in Cu₂O by exciting the surface plasmons in Au@SiO₂@Cu₂O

core@shell@shell nanoparticles.²¹² They demonstrated that the enhanced carrier separation is due to electromagnetic field mediated plasmonic resonance energy transfer (RET) from Au to Cu₂O.

Charge transfer from metal to the catalyst: This mechanism is observed in metal/semiconductor catalysts; here the semiconductor catalyzes the chemical reactions. One of the consequences of the plasmonic relaxation process is a generation of high-energy plasmonic ‘hot’ electrons in the metal nanoparticle. The energy of these hot electrons can be sufficient enough to cross the Schottky barrier at the metal/metal oxide (e.g., TiO₂ or ZrO₂) interface. Therefore, upon exciting the plasmon band in a metal nanoparticle, the hot electrons are transferred from the metal to the semiconductor metal oxide. As a result of this transfer, the metal oxide gains high energy electrons in its conduction band, leading to an improvement in the overall catalytic activity in the visible region.^{33, 205} Plasmonic hot electron transfer was also observed in bimetallic (e.g., AuPd and AuCu) nanoparticles.^{22, 213} Unlike the metal oxide examples there is no Schottky junction at the interface for these AuPd and AuCu systems; the charge is transferred from Au to the other metal.²¹³

Plasmon-induced heating for catalysis: Plasmonic nanoparticles have been used as heat sources in several heterogeneous reactions. The excited plasmons generate heat by electron-phonon scattering during the relaxation process. The magnitude of heat depends on the power of the incoming light source; generally, such heating effects are observed when high power (power density on the order of tens of W/cm²) laser sources are used. Recently, by exciting the surface plasmon band in Ag nanowires, Garnet *et al.* observed a welding of the two nanowires at their junctions due to plasmon heating.²¹⁴ By using plasmonic heating, Adleman and co-workers reported the combustion of ethanol to CO₂, and H₂O.²¹⁵ Plasmonic-heating has been explored in several other reactions such as cross-coupling reactions, epoxidation, decomposition of peroxides and decomposition of organometallic molecules.^{216 217}

Direct charge transfer to the adsorbate: Upon illumination, the hot electrons in the metal nanoparticles can transiently occupy the LUMO of an adsorbed molecule. This direct charge transfer can induce a chemical transformation in the adsorbed molecule. This was first observed in 1988 by Trager *et al.*,²¹⁸ who studied the laser-induced desorption of Na atoms from Na nanoparticles. The rate of desorption was found to be a maximum when the Na nanoparticles were illuminated with a light source whose wavelength matches their plasmon peak; they claimed that desorption was both phonon-driven and hot-electron driven. Over the past few years, there has been an increase in the number of reports on this plasmonic charge transfer-driven photochemistry.^{21, 22, 219-223} For example, as a result of plasmonic electron transfer, an enhanced dissociation of O-O bonds in adsorbed O₂ molecules was observed on the surface of a Ag nanocube/Al₂O₃ nanocomposite, using a ~250 mW/cm² visible light source.^{222, 223} The authors demonstrated that plasmonic local heating accelerated the rate of O-O dissociation. In a similar way, the dissociation of H₂ molecules was observed when metal (Au, Al) nanoparticles was illuminated by a kW power laser source in the presence of H₂ gas by Halas and co-workers;^{224, 225} the bond dissociation was attributed to the plasmon hot electron transfer from the metal (Au, Al) surface to adsorbed H₂.

1.3.2.2. Plasmonic Photocatalysis

Decomposition of organic contaminants: Organic dyes, such as methyl orange, methylene blue, and rhodamine are widely used as model compounds to study the degradation of organic molecules using a photocatalyst. Often wide bandgap semiconductor metal oxides are used to catalyze their decomposition. Semiconductor nanoparticles generate reactive oxygen species (oxygen radicals: ·OH, ·O, ·O₂⁻) upon UV illumination; these radicals can decompose the dye by oxidation.²⁰⁵ Harnessing visible light for this decomposition can be achieved by using plasmonic nanoparticles.

For example, Awazu *et al.* embedded Ag@SiO₂ nanoparticles in TiO₂ films to make the catalyst active in visible light. They observed a 7-fold enhancement in the decomposition of methylene blue in the presence of visible light. Here, a SiO₂ shell was used to prevent the oxidation of Ag. The thickness of the SiO₂ shell is critical; Kumar and co-workers observed a decrease in the rate of methylene blue decomposition with an increase in the silica shell thickness.²²⁶ They demonstrated that the reduction in the decomposition rate could be due to the decrease in the near-field available in the surrounding medium. Christopher *et al.* employed various shapes of Ag nanoparticles (nanowires, nanocubes, and nanoparticles) on TiO₂ for the decomposition of methylene blue.²²⁷ Higher decomposition rates were obtained for Ag nanocube/TiO₂ nanocomposites; increased decomposition was attributed to the enhanced generation of e⁻/h⁺ pairs in TiO₂.

Solar water splitting: Using solar energy for water splitting is a potential approach for the generation of H₂ fuel. Several groups have employed plasmonic nanoparticles to harvest visible light for water splitting.^{205, 206, 228} By depositing Au nanoparticles on TiO₂, Silva *et al.* observed an enhanced generation of hydrogen in photoelectrochemical water splitting when the catalyst was illuminated by a 532 nm laser.²²⁹ In the absence of Au, TiO₂ showed poor catalytic activity regardless of light illumination. Here, the enhancement was attributed to direct electron transfer from Au to TiO₂. Recently, Duchene *et al.* verified the plasmonic hot electron transfer from Au NPs to TiO₂ by *in situ* monitoring of the open circuit voltage of a Au/TiO₂ photoanode.²³⁰ They used a 300 W Xenon light source for panchromatic illumination. On the other hand, by using a similar photoelectrochemical cell, Liu *et al.* demonstrated that the enhancement in H₂ generation is due to plasmonic near-field effects rather than plasmonic hot-electron transfer process.²²⁸ In agreement with previous results, Ingram and Linic have shown that plasmonic near fields led to

enhanced rates of water splitting using a Au/N-TiO₂ (nitrogen doped TiO₂) photoanode.²³¹ Further, Torimoto *et al.* showed evidence for the effect of plasmonic near-fields on water splitting by exciting the surface plasmons in Au@SiO₂@CdS core@shell@shell nanostructures using a Xe lamp source (power ~100 mW/cm²).²³² They observed that the plasmonic enhancement in H₂ production was dependent on the thickness of the silica spacer between the Au and the CdS. Recently, by probing the valence orbitals in Zn in Ag/ZnO nanocomposite using X-ray absorption spectroscopic studies at the Zn K-edge, Chen *et al.* have drawn conclusions that there is a contribution of both plasmonic hot-electron injection and plasmonic near-field effects in the enhancement of H₂ production.²³³ Finally, a review by Zhang *et al.* has recently summarized all of the plasmonic effects that contribute to solar water splitting.²³⁴

Organic reactions: Organic substrates such as alcohols, aldehydes, anilines, and hydrocarbons have been successfully oxidized by plasmonic nanoparticles supported on TiO₂, ZrO₂ and CeO₂ in the presence of an O₂ atmosphere.²³⁵ By using a Au/TiO₂ photocatalyst, Naya *et al.* observed the transformation of cinnamyl alcohol to cinnamaldehyde in the presence of visible light. However, the reaction also produced a significant amount of cinnamic acid. Tsukamoto *et al.* also employed Au nanoparticles on various supports (TiO₂ and CeO₂) for the oxidation of benzaldehyde.²³⁶ The maximum conversion was achieved by depositing Au on a mixture of rutile/anatase TiO₂. Zhao *et al.* studied the aerobic oxidation of aromatic amines using plasmonic metal nanoparticles (Au and Ag); they demonstrated that the oxidation is driven by the direct hot electron transfer in Ag or Au to the 2π* orbitals of adsorbed oxygen.²³⁷ In a similar way, plasmonic nanoparticles have been used for light harvesting in Pd-catalyzed reactions such as the hydrogenation of nitrophenols to anilines and cross-coupling reactions.^{238, 217} The most studied catalysts for these reactions are AuPd bimetallic nanoparticles. Wang *et al.* used Pd-tipped Au nanorods to harvest light in cross-

coupling reactions catalyzed by Pd.²¹⁷ Zhang *et al.* observed an enhanced rate of cross-coupling between aryl chlorides and phenylboronic acid using Au@Pd bimetallic nanoparticles supported on ZrO₂.²³⁹ In this thesis, Au@Pd bimetallic nanotriangles were employed to make use of visible light for Pd-catalyzed reactions.

1.4. Research Objectives

The primary objective of the thesis is to improve the harvesting of solar energy in photovoltaic cells and photocatalytic processes. Here, two types of photovoltaic cells are investigated; one is DSSCs, and the other is perovskite solar cells. In DSSCs, one of the key components is the dye; the efficiency of DSSCs is often limited by weak dye absorption. This thesis takes advantage of the plasmonic properties of metal nanoparticles to improve light harvesting in DSSCs. Specifically, plasmonic M@SiO₂ (M = Au, Ag) nanotriangles are used. Due to their anisotropy, these nanotriangles show broad plasmonic peaks from multiple plasmon modes, and they offer intense near-fields from their sharp tips. In Chapter 2, the plasmonic enhancement was studied by integrating different quantities of Ag@SiO₂ in DSSCs. It was found that the Ag@SiO₂ nanotriangles are unstable; they are easily oxidized at higher temperatures. However, after annealing in air, they showed interesting changes in their morphology. In Chapter 3, these morphological changes were systematically studied by using X-ray absorption spectroscopy. Here, the nanotriangles are annealed in different atmospheric conditions (N₂ and air), and at different temperatures. Alternatively, more stable Au@SiO₂ nanotriangles were also employed in DSSCs. In Chapter 4, the thermal stability of Au@SiO₂ nanotriangles and their effect on the performance of DSSCs are discussed.

In the case of perovskite solar cells, the perovskite MAPbI₃ is already a strong light absorber; it has a large extinction coefficient over a broad range of visible spectrum. Due to the

excellent optoelectronic properties of this perovskite material, employing external light harvesting materials such as plasmonic nanoparticles is likely not required in these solar cells. However, alternative approaches to improving light harvesting efficiency and device performance are still needed. Chapter 5 demonstrates the effect of perovskite layer thickness on the performance of perovskite solar cells. In Chapter 6, the growth of perovskite crystallites was studied by controlling the relative humidity in the surrounding atmosphere.

The last project (Chapter 7) is focused on harvesting solar energy to drive chemical reactions. Here, the rate of Pd-catalyzed reactions was improved by using plasmonic nanoparticles. The Pd itself does not absorb in the visible region, thus to utilize solar energy for these reactions, Au@Pd core@shell bimetallic nanotriangles were employed. Plasmonic enhancements were observed for both a Suzuki coupling reaction and the hydrogenation of 2-methyl-3-butene-2-ol. Finally, Chapter 8 summarizes the accomplishments of all the projects that are described in this thesis and also lays out future work that could be done in these areas.

1.5. References

1. U. S. E. I. A. (EIA), International Energy Outlook 2016 <http://www.eia.gov/>, Accessed May 12, 2016.
2. C. Intergovernmental Panel on Climate, *Climate Change 2013 – the Physical Science Basis: Working Group I Contribution to the Fifth Assessment Report of the Intergovernmental Panel on Climate Change*, Cambridge University Press, Cambridge, 2014.
3. REN21, Renewables 2016 Global Status Report, <http://www.ren21.net/>, Accessed June 8, 2016.
4. J. Y. Tsao, N. S. Lewis and G. W. Crabtree, *U.S. Department of Energy*, 2006, 1-24.
5. G. Kopp and J. L. Lean, *Geophys. Res. Lett.*, 2011, **38**, L01706.
6. I. E. A. (IEA), Technology Roadmap: Solar Photovoltaic Energy - 2014 Edition, <https://www.iea.org/>, Accessed September, 2014.
7. U. Kreibig and M. Vollmer, *Optical Properties of Metal Clusters*, Springer, Berlin ; New York, 1995.
8. S. Underwood and P. Mulvaney, *Langmuir*, 1994, **10**, 3427-3430.
9. P. Mulvaney, *Langmuir*, 1996, **12**, 788-800.
10. K. L. Kelly, E. Coronado, L. L. Zhao and G. C. Schatz, *J. Phys. Chem. C*, 2002, **107**, 668-677.
11. G. H. Chan, J. Zhao, E. M. Hicks, G. C. Schatz and R. P. Van Duyne, *Nano Lett.*, 2007, **7**, 1947-1952.
12. M. W. Knight, N. S. King, L. Liu, H. O. Everitt, P. Nordlander and N. J. Halas, *ACS Nano*, 2014, **8**, 834-840.

13. C. Langhammer, M. Schwind, B. Kasemo and I. Zorić, *Nano Lett.*, 2008, **8**, 1461-1471.
14. U. Guler, V. M. Shalaev and A. Boltasseva, *Mater. Today*, 2015, **18**, 227-237.
15. J. M. Luther, P. K. Jain, T. Ewers and A. P. Alivisatos, *Nat. Mater.*, 2011, **10**, 361-366.
16. G. V. Naik, V. M. Shalaev and A. Boltasseva, *Adv. Mater.*, 2013, **25**, 3264-3294.
17. F. Kretschmer, S. Mühlig, S. Hoepfner, A. Winter, M. D. Hager, C. Rockstuhl, T. Pertsch and U. S. Schubert, *Part. Part. Syst. Char.*, 2014, **31**, 721-744.
18. X. Lu, M. Rycenga, S. E. Skrabalak, B. Wiley and Y. Xia, *Annu. Rev. Phys. Chem.*, 2009, **60**, 167-192.
19. M. Hu, J. Chen, Z.-Y. Li, L. Au, G. V. Hartland, X. Li, M. Marquez and Y. Xia, *Chem. Soc. Rev.*, 2006, **35**, 1084-1094.
20. G. Mie, *Ann Phys-Berlin*, 1908, **330**, 377-445.
21. S. Linic, P. Christopher and D. B. Ingram, *Nat. Mater.*, 2011, **10**, 911-921.
22. S. Linic, U. Aslam, C. Boerigter and M. Morabito, *Nat. Mater.*, 2015, **14**, 567-576.
23. E. Hutter and J. H. Fendler, *Adv. Mater.*, 2004, **16**, 1685-1706.
24. E. Hao, G. C. Schatz and J. T. Hupp, *J. Fluoresc.*, 2004, **14**, 331-341.
25. A. Brioude, X. C. Jiang and M. P. Pileni, *J. Phys. Chem. C*, 2005, **109**, 13138-13142.
26. B. M. I. van der Zande, M. R. Böhmer, L. G. J. Fokkink and C. Schönenberger, *J. Phys. Chem. C*, 1997, **101**, 852-854.
27. P. K. Jain, K. S. Lee, I. H. El-Sayed and M. A. El-Sayed, *J. Phys. Chem. B*, 2006, **110**, 7238-7248.
28. B. J. Wiley, S. H. Im, Z.-Y. Li, J. McLellan, A. Siekkinen and Y. Xia, *J. Phys. Chem. C*, 2006, **110**, 15666-15675.
29. V. V. Kresin, *Phys. Rev. B*, 1995, **51**, 1844-1849.

30. C. Clavero, *Nat. Photon.*, 2014, **8**, 95-103.
31. C. Sönnichsen, T. Franzl, T. Wilk, G. von Plessen, J. Feldmann, O. Wilson and P. Mulvaney, *Phys. Rev. Lett.*, 2002, **88**, 077402.
32. W. R. Erwin, H. F. Zarick, E. M. Talbert and R. Bardhan, *Energy Environ. Sci.*, 2016, **9**, 1577-1601.
33. R. Jiang, B. Li, C. Fang and J. Wang, *Adv. Mater.*, 2014, **26**, 5274-5309.
34. P. Dombi, A. Hörl, P. Rácz, I. Márton, A. Trügler, J. R. Krenn and U. Hohenester, *Nano Lett.*, 2013, **13**, 674-678.
35. J. G. Endriz and W. E. Spicer, *Phys. Rev. Lett.*, 1970, **24**, 64-68.
36. M. L. Brongersma, N. J. Halas and P. Nordlander, *Nat Nano*, 2015, **10**, 25-34.
37. E. C. Garnett, W. Cai, J. J. Cha, F. Mahmood, S. T. Connor, M. Greyson Christoforo, Y. Cui, M. D. McGehee and M. L. Brongersma, *Nat. Mater.*, 2012, **11**, 241-249.
38. S. Han, S. Hong, J. Ham, J. Yeo, J. Lee, B. Kang, P. Lee, J. Kwon, S. S. Lee, M.-Y. Yang and S. H. Ko, *Adv. Mater.*, 2014, **26**, 5808-5814.
39. M. R. Langille, M. L. Personick, J. Zhang and C. A. Mirkin, *J. Am. Chem. Soc.*, 2012, **134**, 14542-14554.
40. G. S. Métraux and C. A. Mirkin, *Adv. Mater.*, 2005, **17**, 412-415.
41. P.-J. Chung, L.-M. Lyu and M. H. Huang, *Chem. Eur. J.*, 2011, **17**, 9746-9752.
42. B. Wiley, Y. Sun and Y. Xia, *Acc. Chem. Res.*, 2007, **40**, 1067-1076.
43. T. K. Sau and C. J. Murphy, *J. Am. Chem. Soc.*, 2004, **126**, 8648-8649.
44. F. Kim, S. Connor, H. Song, T. Kuykendall and P. Yang, *Angew. Chem., Int. Ed.*, 2004, **43**, 3673-3677.
45. A. Kedia and P. S. Kumar, *J. Phys. Chem. C*, 2012, **116**, 23721-23728.

46. Y. Sun and Y. Xia, *Science*, 2002, **298**, 2176-2179.
47. D. Aherne, D. M. Ledwith and J. M. Kelly, in *Metal-Enhanced Fluorescence*, John Wiley & Sons, Inc., 2010, pp. 295-362.
48. S. Chen, Z. Fan and D. L. Carroll, *J. Phys. Chem. C*, 2002, **106**, 10777-10781.
49. P.-C. Chen, X. Liu, J. L. Hedrick, Z. Xie, S. Wang, Q.-Y. Lin, M. C. Hersam, V. P. Dravid and C. A. Mirkin, *Science*, 2016, **352**, 1565-1569.
50. L. M. Demers, D. S. Ginger, S.-J. Park, Z. Li, S.-W. Chung and C. A. Mirkin, *Science*, 2002, **296**, 1836-1838.
51. V. Amendola and M. Meneghetti, *Phys. Chem. Chem. Phys.*, 2009, **11**, 3805-3821.
52. J. Kimling, M. Maier, B. Okenve, V. Kotaidis, H. Ballot and A. Plech, *J. Phys. Chem. C*, 2006, **110**, 15700-15707.
53. X. Xia, M. Yang, Y. Wang, Y. Zheng, Q. Li, J. Chen and Y. Xia, *ACS Nano*, 2012, **6**, 512-522.
54. C. J. Murphy, T. K. Sau, A. M. Gole, C. J. Orendorff, J. Gao, L. Gou, S. E. Hunyadi and T. Li, *J. Phys. Chem. B*, 2005, **109**, 13857-13870.
55. R. Jin, Y. Cao, C. A. Mirkin, K. L. Kelly, G. C. Schatz and J. G. Zheng, *Science*, 2001, **294**, 1901-1903.
56. T. R. Jensen, M. D. Malinsky, C. L. Haynes and R. P. Van Duyne, *J. Phys. Chem. C*, 2000, **104**, 10549-10556.
57. K. D. Gilroy, A. Ruditskiy, H.-C. Peng, D. Qin and Y. Xia, *Chem. Rev.*, 2016, **116**, 10414-10472.
58. Y. Xiong and Y. Xia, *Adv. Mater.*, 2007, **19**, 3385-3391.
59. Y. Xia, Y. Xiong, B. Lim and S. E. Skrabalak, *Angew. Chem., Int. Ed.*, 2009, **48**, 60-103.

60. D. Aherne, D. M. Ledwith, M. Gara and J. M. Kelly, *Adv. Funct. Mater.*, 2008, **18**, 2005-2016.
61. J. E. Millstone, S. J. Hurst, G. S. Métraux, J. I. Cutler and C. A. Mirkin, *Small*, 2009, **5**, 646-664.
62. C. Xue, X. Chen, S. J. Hurst and C. A. Mirkin, *Adv. Mater.*, 2007, **19**, 4071-4074.
63. L. Brus, *Nat. Mater.*, 2016, **15**, 824-825.
64. Y. Zhou, C. Y. Wang, Y. R. Zhu and Z. Y. Chen, *Chem. Mater.*, 1999, **11**, 2310-2312.
65. Y. Zhai, J. S. DuChene, Y.-C. Wang, J. Qiu, A. C. Johnston-Peck, B. You, W. Guo, B. DiCiaccio, K. Qian, E. W. Zhao, F. Ooi, D. Hu, D. Su, E. A. Stach, Z. Zhu and W. D. Wei, *Nat. Mater.*, 2016, **15**, 889-895.
66. J. E. Millstone, S. Park, K. L. Shuford, L. Qin, G. C. Schatz and C. A. Mirkin, *J. Am. Chem. Soc.*, 2005, **127**, 5312-5313.
67. Q. Zhang, N. Li, J. Goebel, Z. Lu and Y. Yin, *J. Am. Chem. Soc.*, 2011, **133**, 18931-18939.
68. L. Chen, F. Ji, Y. Xu, L. He, Y. Mi, F. Bao, B. Sun, X. Zhang and Q. Zhang, *Nano Lett.*, 2014, **14**, 7201-7206.
69. S. Nie and S. R. Emory, *Science*, 1997, **275**, 1102-1106.
70. A. Wax and K. Sokolov, *Laser Photon. Rev.*, 2009, **3**, 146-158.
71. X. Cai, W. Li, C.-H. Kim, Y. Yuan, L. V. Wang and Y. Xia, *ACS Nano*, 2011, **5**, 9658-9667.
72. J. Aaron, N. Nitin, K. Travis, S. Kumar, T. Collier, S. Y. Park, M. José-Yacamán, L. Coghlan, M. Follen, R. Richards-Kortum and K. Sokolov, *J. Biomed. Opt.*, 2007, **12**, 034007-034011.
73. D. B. Mitzi, *Chem. Mater.*, 1996, **8**, 791-800.

74. J. N. Anker, W. P. Hall, O. Lyandres, N. C. Shah, J. Zhao and R. P. Van Duyne, *Nat. Mater.*, 2008, **7**, 442-453.
75. S. Kumar, N. Harrison, R. Richards-Kortum and K. Sokolov, *Nano Lett.*, 2007, **7**, 1338-1343.
76. W.-C. Law, K.-T. Yong, A. Baev and P. N. Prasad, *ACS Nano*, 2011, **5**, 4858-4864.
77. X. Huang, P. K. Jain, I. H. El-Sayed and M. A. El-Sayed, *Lasers Med. Sci.*, 2007, **23**, 217-228.
78. J. Oh, H. Yoon and J.-H. Park, *Bio. Med. Eng. Lett.*, 2013, **3**, 67-73.
79. A. E. Becquerel, *C. R. Acad. Sci.*, 1839, **9**.
80. R. Williams, *J. Chem. Phys.*, 1960, **32**, 1505-1514.
81. C. E. Fritts, *Am. J. Sci.*, 1883, **26**.
82. A. W. Blakers and M. A. Green, *Appl. Phys. Lett.*, 1986, **48**, 215-217.
83. M. A. Green, K. Emery, Y. Hishikawa, W. Warta and E. D. Dunlop, *Prog. Photovolt: Res. Appl.*, 2016, **24**, 905-913.
84. Y.-J. Lee, B.-S. Kim, S. M. Ifitiquar, C. Park and J. Yi, *J. Korean Phys. Soc.*, 2014, **65**, 355-361.
85. M. Boccard, C. Battaglia, S. Hänni, K. Söderström, J. Escarré, S. Nicolay, F. Meillaud, M. Despeisse and C. Ballif, *Nano Lett.*, 2012, **12**, 1344-1348.
86. K. Yamamoto, A. Nakajima, M. Yoshimi, T. Sawada, S. Fukuda, T. Suezaki, M. Ichikawa, Y. Koi, M. Goto, T. Meguro, T. Matsuda, M. Kondo, T. Sasaki and Y. Tawada, *Solar Energy*, 2004, **77**, 939-949.
87. D. L. Staebler and C. R. Wronski, *Appl. Phys. Lett.*, 1977, **31**, 292-294.

88. M. A. Green, K. Emery, Y. Hishikawa, W. Warta and E. D. Dunlop, *Prog. Photovolt: Res. Appl.*, 2016, **24**, 3-11.
89. K. Kakiage, Y. Aoyama, T. Yano, K. Oya, J.-i. Fujisawa and M. Hanaya, *Chem. Commun.*, 2015, **51**, 15894-15897.
90. S. Mathew, A. Yella, P. Gao, R. Humphry-Baker, F. E. CurchodBasile, N. Ashari-Astani, I. Tavernelli, U. Rothlisberger, K. NazeeruddinMd and M. Grätzel, *Nat. Chem.*, 2014, **6**, 242-247.
91. Z. Du, Z. Pan, F. Fabregat-Santiago, K. Zhao, D. Long, H. Zhang, Y. Zhao, X. Zhong, J.-S. Yu and J. Bisquert, *J. Phys. Chem. Lett.*, 2016, 3103-3111.
92. X. Lan, O. Voznyy, F. P. García de Arquer, M. Liu, J. Xu, A. H. Proppe, G. Walters, F. Fan, H. Tan, M. Liu, Z. Yang, S. Hoogland and E. H. Sargent, *Nano Lett.*, 2016, **16**, 4630-4634.
93. Q. Zhang, B. Kan, F. Liu, G. Long, X. Wan, X. Chen, Y. Zuo, W. Ni, H. Zhang, M. Li, Z. Hu, F. Huang, Y. Cao, Z. Liang, M. Zhang, T. P. Russell and Y. Chen, *Nat. Photon.*, 2015, **9**, 35-41.
94. W. Zhao, D. Qian, S. Zhang, S. Li, O. Inganäs, F. Gao and J. Hou, *Adv. Mater.*, 2016, **28**, 4734-4739.
95. W. H. Brattain and C. G. B. Garrett, *Bell System Technical Journal*, 1955, **34**, 129-176.
96. H. Gerischer, *J. Electrochem. Soc.*, 1966, **113**, 1174-1182.
97. K. Hauffe, H. J. Danzmann, H. Pusch, J. Range and H. Volz, *J. Electrochem. Soc.*, 1970, **117**, 993-999.
98. M. Grätzel, *Nature*, 2001, **414**, 338-344.
99. N. Alonso V., M. Beley, P. Chartier and V. Ern, *Rev. Phys. Appl. (Paris)*, 1981, **16**, 5-10.

100. B. O'Regan and M. Grätzel, *Nature*, 1991, **353**, 737-740.
101. M. K. Nazeeruddin, A. Kay, I. Rodicio, R. Humphry-Baker, E. Mueller, P. Liska, N. Vlachopoulos and M. Graetzel, *J. Am. Chem. Soc.*, 1993, **115**, 6382-6390.
102. M. K. Nazeeruddin, F. De Angelis, S. Fantacci, A. Selloni, G. Viscardi, P. Liska, S. Ito, B. Takeru and M. Grätzel, *J. Am. Chem. Soc.*, 2005, **127**, 16835-16847.
103. F. Gao, Y. Wang, D. Shi, J. Zhang, M. Wang, X. Jing, R. Humphry-Baker, P. Wang, S. M. Zakeeruddin and M. Grätzel, *J. Am. Chem. Soc.*, 2008, **130**, 10720-10728.
104. M. K. Nazeeruddin, P. Péchy, T. Renouard, S. M. Zakeeruddin, R. Humphry-Baker, P. Comte, P. Liska, L. Cevey, E. Costa, V. Shklover, L. Spiccia, G. B. Deacon, C. A. Bignozzi and M. Grätzel, *J. Am. Chem. Soc.*, 2001, **123**, 1613-1624.
105. B. E. Hardin, H. J. Snaith and M. D. McGehee, *Nat. Photon.*, 2012, **6**, 162-169.
106. A. Yella, H.-W. Lee, H. N. Tsao, C. Yi, A. K. Chandiran, M. K. Nazeeruddin, E. W.-G. Diao, C.-Y. Yeh, S. M. Zakeeruddin and M. Grätzel, *Science*, 2011, **334**, 629-634.
107. M. Grätzel, *Inorg. Chem.*, 2005, **44**, 6841-6851.
108. A. Hagfeldt, G. Boschloo, L. Sun, L. Kloo and H. Pettersson, *Chem. Rev.*, 2010, **110**, 6595-6663.
109. Y. Wu, X. Zhang, W. Li, Z.-S. Wang, H. Tian and W. Zhu, *Adv. Energy Mater.*, 2012, **2**, 149-156.
110. F. M. Jradi, D. O'Neil, X. Kang, J. Wong, P. Szymanski, T. C. Parker, H. L. Anderson, M. A. El-Sayed and S. R. Marder, *Chem. Mater.*, 2015, **27**, 6305-6313.
111. M. Sreenivasu, A. Suzuki, M. Adachi, C. V. Kumar, B. Srikanth, S. Rajendar, D. Rambabu, R. S. Kumar, P. Malleshm, N. V. B. Rao, M. S. Kumar and P. Y. Reddy, *Chem. Eur. J.*, 2014, **20**, 14074-14083.

112. S. Giménez, A. L. Rogach, A. A. Lutich, D. Gross, A. Poeschl, A. S. Susha, I. Mora-Seró, T. Lana-Villarreal and J. Bisquert, *J. Appl. Phys.*, 2011, **110**, 014314.
113. S. Sarkar, A. Makhil, K. Lakshman, T. Bora, J. Dutta and S. Kumar Pal, *J. Phys. Chem. C*, 2012, **116**, 14248-14256.
114. H. A. Atwater and A. Polman, *Nat. Mater.*, 2010, **9**, 205-213.
115. M. A. Green and S. Pillai, *Nat. Photon.*, 2012, **6**, 130-132.
116. H. Choi, W. T. Chen and P. V. Kamat, *ACS Nano*, 2012, **6**, 4418-4427.
117. M. Li, S. K. Cushing and N. Wu, *Analyst*, 2015, **140**, 386-406.
118. Y.-S. Chen, H. Choi and P. V. Kamat, *J. Am. Chem. Soc.*, 2013, **135**, 8822-8825.
119. Q. Wang, T. Butburee, X. Wu, H. Chen, G. Liu and L. Wang, *J. Mater. Chem. A*, 2013, **1**, 13524-13531.
120. N. Chander, A. F. Khan, E. Thouti, S. K. Sardana, P. S. Chandrasekhar, V. Dutta and V. K. Komarala, *Solar Energy*, 2014, **109**, 11-23.
121. C. Hägglund, M. Zäch and B. Kasemo, *Appl. Phys. Lett.*, 2008, **92**, 013113.
122. K. Ishikawa, C.-J. Wen, K. Yamada and T. Okubo, *J. Chem. Eng. Jpn.*, 2004, **37**, 645-649.
123. M. D. Brown, T. Suteewong, R. S. S. Kumar, V. D'Innocenzo, A. Petrozza, M. M. Lee, U. Wiesner and H. J. Snaith, *Nano Lett.*, 2011, **11**, 438-445.
124. J. Qi, X. Dang, P. T. Hammond and A. M. Belcher, *ACS Nano*, 2011, **5**, 7108-7116.
125. S. D. Standridge, G. C. Schatz and J. T. Hupp, *Langmuir*, 2009, **25**, 2596-2600.
126. N. C. Jeong, C. Prasittichai and J. T. Hupp, *Langmuir*, 2011, **27**, 14609-14614.
127. M. K. Gangishetty, K. E. Lee, R. W. J. Scott and T. L. Kelly, *ACS Appl. Mater. Interfaces*, 2013, **5**, 11044-11051.
128. S. D. Standridge, G. C. Schatz and J. T. Hupp, *J. Am. Chem. Soc.*, 2009, **131**, 8407-8409.

129. H. Dong, Z. Wu, A. El-Shafei, B. Xia, J. Xi, S. Ning, B. Jiao and X. Hou, *J. Mater. Chem. A*, 2015, **3**, 4659-4668.
130. S. Chang, Q. Li, X. Xiao, K. Y. Wong and T. Chen, *Energy Environ. Sci.*, 2012, **5**, 9444-9448.
131. H. F. Zarick, O. Hurd, J. A. Webb, C. Hungerford, W. R. Erwin and R. Bardhan, *ACS Photonics*, 2014, **1**, 806-811.
132. M. K. Gangishetty, R. W. J. Scott and T. L. Kelly, *Langmuir*, 2014, **30**, 14352-14359.
133. H. Elbohy, M. R. Kim, A. Dubey, K. M. Reza, D. Ma, J. Zai, X. Qian and Q. Qiao, *J. Mater. Chem. A*, 2016, **4**, 545-551.
134. K. Guo, M. Li, X. Fang, X. Liu, Y. Zhu, Z. Hu and X. Zhao, *J. Mater. Chem. A*, 2013, **1**, 7229-7234.
135. H. Dong, Z. Wu, F. Lu, Y. Gao, A. El-Shafei, B. Jiao, S. Ning and X. Hou, *Nano Energy*, 2014, **10**, 181-191.
136. Q. Xu, F. Liu, Y. Liu, K. Cui, X. Feng, W. Zhang and Y. Huang, *Sci. Rep.*, 2013, **3**, 2112.
137. Q. Gan, F. J. Bartoli and Z. H. Kafafi, *Adv. Mater.*, 2013, **25**, 2385-2396.
138. H. Feng Lu, S. Mokkalapati, L. Fu, G. Jolley, H. Hoe Tan and C. Jagadish, *Appl. Phys. Lett.*, 2012, **100**, 103505.
139. W. Zhang, M. Saliba, S. D. Stranks, Y. Sun, X. Shi, U. Wiesner and H. J. Snaith, *Nano Lett.*, 2013, **13**, 4505-4510.
140. A. Kojima, K. Teshima, Y. Shirai and T. Miyasaka, *J. Am. Chem. Soc.*, 2009, **131**, 6050-6051.
141. M. A. Green, Y. Jiang, A. M. Soufiani and A. Ho-Baillie, *J. Phys. Chem. Lett.*, 2015, **6**, 4774-4785.

142. J. H. Noh, S. H. Im, J. H. Heo, T. N. Mandal and S. I. Seok, *Nano Lett.*, 2013, **13**, 1764-1769.
143. N. Pellet, P. Gao, G. Gregori, T.-Y. Yang, M. K. Nazeeruddin, J. Maier and M. Grätzel, *Angew. Chem., Int. Ed.*, 2014, **53**, 3151-3157.
144. A. Miyata, A. Mitioglu, P. Plochocka, O. Portugall, J. T.-W. Wang, S. D. Stranks, H. J. Snaith and R. J. Nicholas, *Nat. Phys.*, 2015, **11**, 582-587.
145. V. D’Innocenzo, G. Grancini, M. J. P. Alcocer, A. R. S. Kandada, S. D. Stranks, M. M. Lee, G. Lanzani, H. J. Snaith and A. Petrozza, *Nat. Com.*, 2014, **5**, 3586.
146. Q. Lin, A. Armin, R. C. R. Nagiri, P. L. Burn and P. Meredith, *Nat Photon*, 2015, **9**, 106-112.
147. G. Xing, N. Mathews, S. Sun, S. S. Lim, Y. M. Lam, M. Grätzel, S. Mhaisalkar and T. C. Sum, *Science*, 2013, **342**, 344-347.
148. S. D. Stranks, G. E. Eperon, G. Grancini, C. Menelaou, M. J. P. Alcocer, T. Leijtens, L. M. Herz, A. Petrozza and H. J. Snaith, *Science*, 2013, **342**, 341-344.
149. Q. Dong, Y. Fang, Y. Shao, P. Mulligan, J. Qiu, L. Cao and J. Huang, *Science*, 2015, **347**, 967-970.
150. M. M. Lee, J. Teuscher, T. Miyasaka, T. N. Murakami and H. J. Snaith, *Science*, 2012, **338**, 643-647.
151. T. Salim, S. Sun, Y. Abe, A. Krishna, A. C. Grimsdale and Y. M. Lam, *J. Mater. Chem. A*, 2015, **3**, 8943-8969.
152. T. Leijtens, B. Lauber, G. E. Eperon, S. D. Stranks and H. J. Snaith, *J. Phys. Chem. Lett.*, 2014, **5**, 1096-1102.
153. J. M. Ball, M. M. Lee, A. Hey and H. J. Snaith, *Energy Environ. Sci.*, 2013, **6**, 1739-1743.

154. J. Burschka, N. Pellet, S.-J. Moon, R. Humphry-Baker, P. Gao, M. K. Nazeeruddin and M. Grätzel, *Nature*, 2013, **499**, 316-319.
155. D. Bi, S.-J. Moon, L. Haggman, G. Boschloo, L. Yang, E. M. J. Johansson, M. K. Nazeeruddin, M. Grätzel and A. Hagfeldt, *RSC Advances*, 2013, **3**, 18762-18766.
156. S. H. Hwang, J. Roh, J. Lee, J. Ryu, J. Yun and J. Jang, *J. Mater. Chem. A*, 2014, **2**, 16429-16433.
157. W. S. Yang, J. H. Noh, N. J. Jeon, Y. C. Kim, S. Ryu, J. Seo and S. I. Seok, *Science*, 2015.
158. M. Liu, M. B. Johnston and H. J. Snaith, *Nature*, 2013, **501**, 395-398.
159. A. Yella, L.-P. Heiniger, P. Gao, M. K. Nazeeruddin and M. Grätzel, *Nano Lett.*, 2014, **14**, 2591-2596.
160. D. Liu and T. L. Kelly, *Nat. Photon.*, 2014, **8**, 133-138.
161. J. Song, E. Zheng, J. Bian, X.-F. Wang, W. Tian, Y. Sanehira and T. Miyasaka, *J. Mater. Chem. A*, 2015, **3**, 10837-10844.
162. L. Wang, W. Fu, Z. Gu, C. Fan, X. Yang, H. Li and H. Chen, *J. of Mater. Chem. C*, 2014, **2**, 9087-9090.
163. J.-Y. Jeng, Y.-F. Chiang, M.-H. Lee, S.-R. Peng, T.-F. Guo, P. Chen and T.-C. Wen, *Adv. Mater.*, 2013, **25**, 3727-3732.
164. J. You, Z. Hong, Y. Yang, Q. Chen, M. Cai, T.-B. Song, C.-C. Chen, S. Lu, Y. Liu, H. Zhou and Y. Yang, *ACS Nano*, 2014.
165. P. Docampo, J. M. Ball, M. Darwich, G. E. Eperon and H. J. Snaith, *Nat. Com.*, 2013, **4**, 2761.
166. Z. Xiao, Q. Dong, C. Bi, Y. Shao, Y. Yuan and J. Huang, *Adv. Mater.*, 2014, **26**, 6503-6509.

167. J. You, Y. Yang, Z. Hong, T.-B. Song, L. Meng, Y. Liu, C. Jiang, H. Zhou, W.-H. Chang and G. Li, *Appl. Phys. Lett.*, 2014, **105**, 183902.
168. L. Meng, J. You, T.-F. Guo and Y. Yang, *Acc. Chem. Res.*, 2016, **49**, 155-165.
169. J. You, L. Meng, T.-B. Song, T.-F. Guo, Y. Yang, W.-H. Chang, Z. Hong, H. Chen, H. Zhou, Q. Chen, Y. Liu, N. De Marco and Y. Yang, *Nat Nano*, 2016, **11**, 75-81.
170. T.-B. Song, Q. Chen, H. Zhou, C. Jiang, H.-H. Wang, Y. Yang, Y. Liu, J. You and Y. Yang, *J. Mater. Chem. A*, 2015, **3**, 9032-9050.
171. Y. Zhao and K. Zhu, *Chem. Soc. Rev.*, 2016, **45**, 655-689.
172. Y. Wu, A. Islam, X. Yang, C. Qin, J. Liu, K. Zhang, W. Peng and L. Han, *Energy Environ. Sci.*, 2014, **7**, 2934-2938.
173. G. E. Eperon, V. M. Burlakov, P. Docampo, A. Goriely and H. J. Snaith, *Adv. Funct. Mater.*, 2014, **24**, 151-157.
174. N. J. Jeon, J. H. Noh, Y. C. Kim, W. S. Yang, S. Ryu and S. I. Seok, *Nat. Mater.*, 2014, **13**, 897-903.
175. K. Liang, D. B. Mitzi and M. T. Prikas, *Chem. Mater.*, 1998, **10**, 403-411.
176. Q. Chen, H. Zhou, Z. Hong, S. Luo, H. S. Duan, H. H. Wang, Y. Liu, G. Li and Y. Yang, *J. Am. Chem. Soc.*, 2014, **136**, 622-625.
177. J.-H. Im, I.-H. Jang, N. Pellet, M. Grätzel and N.-G. Park, *Nat. Nanotechnol.*, 2014, **9**, 927-932.
178. W. S. Yang, J. H. Noh, N. J. Jeon, Y. C. Kim, S. Ryu, J. Seo and S. I. Seok, *Science*, 2015, **348**, 1234-1237.
179. H. J. Snaith, A. Abate, J. M. Ball, G. E. Eperon, T. Leijtens, N. K. Noel, S. D. Stranks, J. T.-W. Wang, K. Wojciechowski and W. Zhang, *J. Phys. Chem. Lett.*, 2014, **5**, 1511-1515.

180. B. Chen, M. Yang, S. Priya and K. Zhu, *J. Phys. Chem. Lett.*, 2016, **7**, 905-917.
181. J. Yang and T. L. Kelly, *Inorg. Chem.*, 2016.
182. H.-S. Kim, I.-H. Jang, N. Ahn, M. Choi, A. Guerrero, J. Bisquert and N.-G. Park, *J. Phys. Chem. Lett.*, 2015, **6**, 4633-4639.
183. H.-S. Kim and N.-G. Park, *J. Phys. Chem. Lett.*, 2014, **5**, 2927-2934.
184. B. Chen, M. Yang, X. Zheng, C. Wu, W. Li, Y. Yan, J. Bisquert, G. Garcia-Belmonte, K. Zhu and S. Priya, *J. Phys. Chem. Lett.*, 2015, **6**, 4693-4700.
185. K. Wojciechowski, S. D. Stranks, A. Abate, G. Sadoughi, A. Sadhanala, N. Kopidakis, G. Rumbles, C.-Z. Li, R. H. Friend, A. K. Y. Jen and H. J. Snaith, *ACS Nano*, 2014, **8**, 12701-12709.
186. Y. Shao, Z. Xiao, C. Bi, Y. Yuan and J. Huang, *Nat. Com.*, 2014, **5**, 5784.
187. J. M. Azpiroz, E. Mosconi, J. Bisquert and F. De Angelis, *Energy Environ. Sci.*, 2015, **8**, 2118-2127.
188. J. M. Frost, K. T. Butler, F. Brivio, C. H. Hendon, M. van Schilfgaarde and A. Walsh, *Nano Lett.*, 2014, **14**, 2584-2590.
189. J. Haruyama, K. Sodeyama, L. Han and Y. Tateyama, *J. Am. Chem. Soc.*, 2015, **137**, 10048-10051.
190. H. Yoon, S. M. Kang, J.-K. Lee and M. Choi, *Energy Environ. Sci.*, 2016, **9**, 2262-2266.
191. K. Mahmood, B. S. Swain and A. Amassian, *Adv. Energy Mater.*, 2015, **5**, 1500568-n/a.
192. A. Poglitsch and D. Weber, *J. Chem. Phys.*, 1987, **87**, 6373-6378.
193. F. Hao, C. C. Stoumpos, Z. Liu, R. P. H. Chang and M. G. Kanatzidis, *J. Am. Chem. Soc.*, 2014, **136**, 16411-16419.

194. J. A. Christians, P. A. Miranda Herrera and P. V. Kamat, *J. Am. Chem. Soc.*, 2015, **137**, 1530-1538.
195. J. Yang, B. D. Siempelkamp, D. Liu and T. L. Kelly, *ACS Nano*, 2015, **9**, 1955-1963.
196. A. M. A. Leguy, Y. Hu, M. Campoy-Quiles, M. I. Alonso, O. J. Weber, P. Azarhoosh, M. van Schilfgaarde, M. T. Weller, T. Bein, J. Nelson, P. Docampo and P. R. F. Barnes, *Chem. Mater.*, 2015, **27**, 3397-3407.
197. J.-W. Lee, D.-H. Kim, H.-S. Kim, S.-W. Seo, S. M. Cho and N.-G. Park, *Adv. Energy Mater.*, 2015, **5**, 1501310-n/a.
198. M. Saliba, T. Matsui, J.-Y. Seo, K. Domanski, J.-P. Correa-Baena, M. K. Nazeeruddin, S. M. Zakeeruddin, W. Tress, A. Abate, A. Hagfeldt and M. Grätzel, *Energy Environ. Sci.*, 2016, **9**, 1989-1997.
199. R. Asahi, T. Morikawa, T. Ohwaki, K. Aoki and Y. Taga, *Science*, 2001, **293**, 269-271.
200. J. Zhang, J. Xi and Z. Ji, *J. Mat. Chem.*, 2012, **22**, 17700-17708.
201. W. Choi, A. Termin and M. R. Hoffmann, *J. Phys. Chem.*, 1994, **98**, 13669-13679.
202. S. Sakthivel, M. Janczarek and H. Kisch, *J. Phys. Chem. C*, 2004, **108**, 19384-19387.
203. N. Chandrasekharan and P. V. Kamat, *J. Phys. Chem. C*, 2000, **104**, 10851-10857.
204. K. Awazu, M. Fujimaki, C. Rockstuhl, J. Tominaga, H. Murakami, Y. Ohki, N. Yoshida and T. Watanabe, *J. Am. Chem. Soc.*, 2008, **130**, 1676-1680.
205. W. Hou and S. B. Cronin, *Adv. Funct. Mater.*, 2013, **23**, 1612-1619.
206. M. Xiao, R. Jiang, F. Wang, C. Fang, J. Wang and J. C. Yu, *J. Mater. Chem. A*, 2013, **1**, 5790-5805.
207. V. Mizeikis, E. Kowalska and S. Juodkazis, *J. Nanosci. Nanotechnol.*, 2011, **11**, 2814-2822.

208. E. Hao and G. C. Schatz, *J. Chem. Phys.*, 2004, **120**, 357-366.
209. I. Thomann, B. A. Pinaud, Z. Chen, B. M. Clemens, T. F. Jaramillo and M. L. Brongersma, *Nano Lett.*, 2011, **11**, 3440-3446.
210. H. Gao, C. Liu, H. E. Jeong and P. Yang, *ACS Nano*, 2012, **6**, 234-240.
211. H. Duan and Y. Xuan, *Physica E Low Dimens. Syst. Nanostruct.*, 2011, **43**, 1475-1480.
212. S. K. Cushing, J. Li, F. Meng, T. R. Senty, S. Suri, M. Zhi, M. Li, A. D. Bristow and N. Wu, *J. Am. Chem. Soc.*, 2012, **134**, 15033-15041.
213. J. Cheng, X. Gu, X. Sheng, P. Liu and H. Su, *J. Mater. Chem. A*, 2016, **4**, 1887-1894.
214. E. C. Garnett, W. Cai, J. J. Cha, F. Mahmood, S. T. Connor, M. Greyson Christoforo, Y. Cui, M. D. McGehee and M. L. Brongersma, *Nat. Mater.*, 2012, **11**, 241-249.
215. J. R. Adleman, D. A. Boyd, D. G. Goodwin and D. Psaltis, *Nano Lett.*, 2009, **9**, 4417-4423.
216. J. Qiu and W. D. Wei, *J. Phys. Chem. C*, 2014, **118**, 20735-20749.
217. F. Wang, C. Li, H. Chen, R. Jiang, L.-D. Sun, Q. Li, J. Wang, J. C. Yu and C.-H. Yan, *J. Am. Chem. Soc.*, 2013, **135**, 5588-5601.
218. W. Hoheisel, K. Jungmann, M. Vollmer, R. Weidenauer and F. Träger, *Phys. Rev. Lett.*, 1988, **60**, 1649-1652.
219. J. G. Smith, J. A. Faucheaux and P. K. Jain, *Nano Today*, 2015, **10**, 67-80.
220. M. J. Kale, T. Avanesian and P. Christopher, *ACS Catal.*, 2014, **4**, 116-128.
221. X. Zhou, G. Liu, J. Yu and W. Fan, *J. Mat. Chem.*, 2012, **22**, 21337-21354.
222. P. Christopher, H. Xin, A. Marimuthu and S. Linic, *Nat. Mater.*, 2012, **11**, 1044-1050.
223. P. Christopher, H. Xin and S. Linic, *Nat. Chem.*, 2011, **3**, 467-472.
224. L. Zhou, C. Zhang, M. J. McClain, A. Manjavacas, C. M. Krauter, S. Tian, F. Berg, H. O. Everitt, E. A. Carter, P. Nordlander and N. J. Halas, *Nano Lett.*, 2016, **16**, 1478-1484.

225. S. Mukherjee, F. Libisch, N. Large, O. Neumann, L. V. Brown, J. Cheng, J. B. Lassiter, E. A. Carter, P. Nordlander and N. J. Halas, *Nano Lett.*, 2013, **13**, 240-247.
226. M. K. Kumar, S. Krishnamoorthy, L. K. Tan, S. Y. Chiam, S. Tripathy and H. Gao, *ACS Catal.*, 2011, **1**, 300-308.
227. P. Christopher, D. B. Ingram and S. Linic, *J. Phys. Chem. C*, 2010, **114**, 9173-9177.
228. Z. Liu, W. Hou, P. Pavaskar, M. Aykol and S. B. Cronin, *Nano Lett.*, 2011, **11**, 1111-1116.
229. C. Gomes Silva, R. Juárez, T. Marino, R. Molinari and H. García, *J. Am. Chem. Soc.*, 2011, **133**, 595-602.
230. J. S. DuChene, B. C. Sweeny, A. C. Johnston-Peck, D. Su, E. A. Stach and W. D. Wei, *Angew. Chem., Int. Ed.*, 2014, **53**, 7887-7891.
231. D. B. Ingram and S. Linic, *J. Am. Chem. Soc.*, 2011, **133**, 5202-5205.
232. T. Torimoto, H. Horibe, T. Kameyama, K.-i. Okazaki, S. Ikeda, M. Matsumura, A. Ishikawa and H. Ishihara, *J. Phys. Chem. Lett.*, 2011, **2**, 2057-2062.
233. H. M. Chen, C. K. Chen, C.-J. Chen, L.-C. Cheng, P. C. Wu, B. H. Cheng, Y. Z. Ho, M. L. Tseng, Y.-Y. Hsu, T.-S. Chan, J.-F. Lee, R.-S. Liu and D. P. Tsai, *ACS Nano*, 2012, **6**, 7362-7372.
234. P. Zhang, T. Wang and J. Gong, *Adv. Mater.*, 2015, **27**, 5328-5342.
235. A. Tanaka, K. Hashimoto and H. Kominami, *J. Am. Chem. Soc.*, 2012, **134**, 14526-14533.
236. D. Tsukamoto, Y. Shiraishi, Y. Sugano, S. Ichikawa, S. Tanaka and T. Hirai, *J. Am. Chem. Soc.*, 2012, **134**, 6309-6315.
237. L.-B. Zhao, X.-X. Liu, M. Zhang, Z.-F. Liu, D.-Y. Wu and Z.-Q. Tian, *J. Phys. Chem. C*, 2016, **120**, 944-955.

238. M. Hajfathalian, K. D. Gilroy, A. Yaghoubzade, A. Sundar, T. Tan, R. A. Hughes and S. Neretina, *J. Phys. Chem. C*, 2015, **119**, 17308-17315.
239. S. Zhang, C. Chang, Z. Huang, Y. Ma, W. Gao, J. Li and Y. Qu, *ACS Catal.*, 2015, **5**, 6481-6488.

CHAPTER 2

Plasmonic Enhancement of Dye Sensitized Solar Cells in the Red-to-NIR Region using Triangular Core-Shell Ag@SiO₂ Nanoparticles

*Mahesh K. Gangishetty,[†] Kee Eun Lee,[†] Robert W. J. Scott, and Timothy L. Kelly**

Department of Chemistry, University of Saskatchewan, 110 Science Place, Saskatoon, SK, S7N 5C9, Canada

This project investigates the plasmonic enhancement in the efficiency of DSSCs using triangular Ag@SiO₂ nanoparticles. Most of the champion dyes in DSSCs suffer from the limited absorption in the narrow region of the visible light. Harvesting the broad range of light is one of the major challenges in the field. Here, by using triangular nanoparticles, we could harvest the light in red to near-IR region and improve the performance of the device.

This chapter is a near-verbatim copy of a paper published in *ACS Appl. Mater. Interfaces*, **2013**, 5, 11044. It was published with an equal contribution of myself and Dr. Kee Eun Lee. I would like to acknowledge her contribution to this work. My contribution to this article is synthesizing triangular Ag and Ag@SiO₂ nanoparticles, their characterization by UV-Vis and transmission electron microscopy (TEM) and studying their stability toward the iodide redox couple. Dr. Kee Eun Lee fabricated and characterized all the DSSCs. The first draft of the manuscript was written by me and was revised by Prof. Tim Kelly and Prof. Robert Scott prior to publication.

2.1. Abstract

Recently, plasmonic metal nanoparticles have been shown to be very effective in increasing the light harvesting efficiency of DSSCs. Most commonly, spherical nanoparticles composed of silver or gold are used for this application; however, the localized surface plasmon resonances of these isotropic particles have maxima in the 400 – 550 nm range, limiting any plasmonic enhancements to wavelengths below 600 nm. Herein, we demonstrate that the incorporation of anisotropic, triangular silver nanoprisms in the photoanode of DSSCs can dramatically increase the light harvesting efficiency in the red and near-infrared (NIR) regions. Core-shell Ag@SiO₂ nanoprisms were synthesized and incorporated in various quantities into the titania pastes used to prepare the photoanodes. This optimization led to an overall $32 \pm 17\%$ increase in the PCE of cells made using 0.05% (w/w) of the Ag@SiO₂ composite. Measurements of the incident photon-to-current efficiency provided further evidence that this increase is a result of improved light harvesting in the red and near-infrared regions. The effect of shell thickness on nanoparticle stability was also investigated, and it was found that thick (30 nm) silica shells provide the best protection against corrosion by the triiodide-containing electrolyte, while still enabling large improvements in PCE to be realized.

2.2. Introduction

DSSCs have attracted a great deal of scientific and technical interest due to their low cost and ease of fabrication. While the development of new dyes has led to continued improvements in the PCEs of DSSCs in recent years,¹ they are still often limited by the weak absorption of the dye sensitizer. This is exemplified by the commonly used ruthenium (II) polypyridyl dyes (e.g., N719). N719 absorbs strongly at 535 nm, but has drastically reduced extinction coefficients at longer

wavelengths.² Thus, improving the light harvesting efficiency in the 600 – 900 nm wavelength range is one promising way of increasing the PCEs of these devices.^{3, 4} The synthesis of panchromatic sensitizers, such as porphyrin derivatives, has been shown to improve the incident photon-to-current efficiency at longer wavelengths;^{5, 6} however, the overall efficiency of these dyes is often lower than champion ruthenium dyes due to their reduced light harvesting efficiency at shorter wavelengths.

This issue of poor light absorption often necessitates the use of thick photoanodes,⁷ scattering layers,⁸⁻¹⁰ back reflectors,¹¹ or other light trapping elements¹² in order to achieve the LHE required to produce a highly efficient DSSC. An emerging approach to better light harvesting in solar cells utilizes the LSPR of noble metal nanostructures (e.g., Au or Ag).^{13,14} Due to their unique optical properties, plasmonic nanoparticles are finding applications in diverse scientific fields such as catalysis,¹³ electronics,¹⁴ biological imaging,¹⁵ and sensing.¹⁶ When applied to a DSSC, the plasmonic nanoparticles can act as efficient light trapping components, resulting in an enhancement of the light harvesting efficiency of the cell.¹⁷⁻²³ Plasmonic materials can enhance the LHE in one of the several ways. The first is by resonant scattering of the incident light, whereby incident light is scattered off-normal, increasing the effective optical path length of the device. Another possibility is that the excitation of LSPR modes greatly increases the local electric field at the particle surface (near-field enhancement) and that this results in an increase of the absorbance of the dye sensitizer in these regions.

A number of approaches have been explored for the incorporation of metal nanoparticles in a DSSC. In the simplest of these, gold nanoparticles were directly mixed with the TiO₂ nanoparticle paste, resulting in Au/TiO₂ composite electrodes.¹⁸ These electrodes produced a substantial increase in the current density generated at 532 nm, near the absorption maximum of

the gold LSPR. Similarly, an increase in the short circuit current density was observed when silver nanoparticles were embedded in the photoanode of a DSSC by an in situ synthetic procedure.²² Despite these promising results, the use of bare metal nanoparticles is undesirable from a stability perspective, because the bare nanoparticles may suffer from surface corrosion when in direct contact with the dye and iodide/triiodide electrolyte.²⁴ The nanoparticles may also act as electron traps, reducing the electron collection efficiency. To remedy this, the use of core-shell nanoparticles has been explored, where the plasmonic core is protected by a thin metal oxide (e.g., SiO₂, TiO₂) shell.^{19, 20} The insulating shell both protects the underlying particle from oxidative etching and also helps prevent unwanted electron storage effects.²⁵ The effect of multiple shells and particle aggregation has also been explored through the synthesis of Au@SiO₂@TiO₂ nanoparticles.²⁶

Most of these studies on plasmon-enhanced DSSCs have been based on spherical nanoparticles, and the maxima of the LSPR bands for these materials typically lie in the range of 400 – 550 nm.^{19, 20} Conventional ruthenium dyes such as N719 already absorb strongly in these regions, diminishing the need for plasmonic light trapping. In contrast, N719 absorbs much more weakly in the 550 – 700 nm range, and in order to better amplify the light harvesting efficiency in this regime, better spectral match between the LSPR band and the edge of the N719 absorption band is required. The position of the LSPR band depends on factors such as the nanoparticle size, shape, and dielectric environment.²⁷ While spherical silver nanoparticles typically have LSPR absorption bands in the range of 380 – 450 nm, anisotropic nanoparticles such as triangular silver nanoprisms have substantially red-shifted extinction maxima. By changing the aspect ratio of the silver nanoprisms, the position of the LSPR band can be tuned anywhere from the blue-violet to

the near-infrared region of the spectrum.²⁸ Gold nanorods²⁹ and silver nanoprisms³⁰ have both demonstrated the viability of such an approach in polymer bulk heterojunction solar cells.

In this study, we synthesize core-shell nanoparticles consisting of a triangular silver nanoprism core and a silica shell of variable thickness (Ag@SiO₂). The core-shell particles display a broad LSPR band centered at *ca.* 730 nm, which is ideally suited to overlap with the edge of the N719 absorption spectrum. The silica coating was designed to both protect the underlying silver nanoprism from the corrosive I⁻/I₃⁻ redox mediator and to prevent electron transfer from either the TiO₂ or the dye excited state to the metal nanoparticle. We find that the incorporation of 0.05% (w/w) Ag@SiO₂ into the photoanode of a DSSC results in a 32 ± 17% increase in the overall PCE of the device and that this improvement is entirely driven by an increase in the short circuit current density. IPCE measurements suggest that this is due to an improvement in LHE in the 550 – 750 nm range, caused by plasmonic light trapping effects.

2.3. Experimental Section

2.3.1. Materials

Silver nitrate (99%), sodium borohydride (98%), and hydrogen peroxide (30% w/w), glacial acetic acid (99.7%), nitric acid (70%), and *iso*-propanol (99.9%) were purchased from Fisher Scientific. Ethyl cellulose (EC) powders EC-10 (Ethocel standard 10 cP) and EC-45 (Ethocel standard 45 cP) were purchased from Dow Chemicals. α -Terpineol (\geq 96%), sodium citrate tribasic (\geq 96%), poly(*N*-vinylpyrrolidone) (\geq 99%, MW ~ 40,000), 16-mercaptohexadecanoic acid (MHA, 90%), tetraethoxysilane (TEOS, 99%), titanium tetrakisopropoxide (\geq 97%) and *N,N*-dimethylamine (40% w/v) were purchased from Sigma-

Aldrich. All chemicals were used as received without further purification. Deionized water (18.2 M Ω ·cm) was obtained from a Milli-Q water purification system.

2.3.2. Characterization

UV/Vis/NIR spectra were measured in a quartz cell with an optical path length of 1.0 cm using a Varian Cary50 UV-Visible spectrophotometer. TEM analysis was carried out on a Philips 410 microscope operating at 100 kV. TEM samples were prepared by placing a drop of the nanoparticle solution on a carbon-coated 300 mesh Cu grid and allowing it to air dry.

2.3.3. Synthesis of silver nanoprisms

The synthesis of the silver nanoprisms was carried out based on literature procedures.³¹ Briefly, 0.050 M AgNO₃ (50 μ L) was added to deionized water (24.75 mL), to this mixture, 75 mM trisodium citrate (500 μ L), 17.5 mM PVP (100 μ L) and H₂O₂ (60 μ L) were then added sequentially. This mixture was stirred for 2 min, after which 0.1 M NaBH₄ (250 μ L) was added. A change in the color of solution from yellow and to blue was observed after 40 min. The silver nanoprisms were collected by centrifugation at 8,500 rpm (10,000 g) for 3.5 h and were then re-dispersed in 5 mM aqueous trisodium citrate (25 mL).

2.3.4. Synthesis of Ag@SiO₂ core-shell nanoprisms

Ag@SiO₂ core@shell nanoprisms were prepared according to the synthetic protocol of Xue *et al.*³² The nanoprisms were functionalized by the addition of a 5.0 mM ethanolic solution of 16-mercaptohexadecanoic acid; enough solution was added to bring the final thiol concentration to 60 μ M. After stirring for 10 min, the functionalized nanoprisms were collected by centrifugation at 8,500 rpm (10,000 g) for 3.5 h and were re-dispersed in ethanolic tetraethoxysilane, and 0.6 M DMA and stirred for 12h.

2.3.5. Preparation of TiO₂ and Ag@SiO₂/TiO₂ pastes

The TiO₂ nanoparticles were synthesized according to literature procedures.³³ Titanium tetraisopropoxide (13 mL) was mixed with glacial acetic acid (2.5 mL) and stirred for 15 min, after which the mixture was poured into deionized water (64 mL) while stirring. After 1 h, 65% nitric acid (1.2 mL) was added into the solution, which was heated to reflux for 80 min with intense stirring. The prepared colloidal solution was transferred to a 125 mL Teflon-lined autoclave and heated at 220 °C for 15 h. After completing the autoclave reaction, 65% nitric acid (0.53 mL) was added to the colloidal solution, and the solution homogenized using an ultrasonic horn (QSonica Q500, 1/4th of an inch probe) for 15 min. The TiO₂ nanoparticles were then washed three times with ethanol by centrifugation/redispersion cycles to yield a TiO₂ wet cake.

A paste was prepared from the wet cake by adding ethyl cellulose and terpineol. Two kinds of pure ethyl cellulose powders, EC-10 (Ethocel standard 10 cP, Dow) and EC-45 (Ethocel standard 45 cP, Dow) were dissolved in a 9:7 ratio in ethanol to yield 10% (w/w) solutions. The ethyl cellulose solution, terpineol, and ethanol were added to the TiO₂ wet cake in a 5 : 4 : 17.5 : 1 weight ratio. This mixture was then sonicated using an ultrasonic horn for 15 minutes (2 s pulses, with a 2 s rest between pulses). The solvent was removed by evaporation using a rotary evaporator to yield a 13% (w/w) TiO₂ paste.

Ag@SiO₂ incorporated TiO₂ pastes were prepared in the same manner as the pure TiO₂ paste. Ag@SiO₂ particles were added to the TiO₂ wet cake in ratios ranging from 0.01% to 1.0% (w/w). Higher Ag@SiO₂ loadings resulted in more deeply blue colored pastes.

2.3.6. Cell fabrication and characterization

FTO-coated glass (TEC 8, Hartford Glass Co.) was used as a substrate for both the working and the counter electrode. The working electrode was prepared by doctor blading the TiO₂ paste

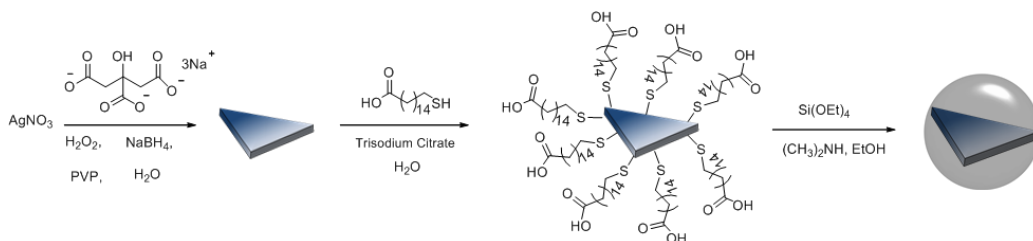
onto a TiCl_4 pretreated (0.2 mM (aq), 30 min at 70 °C) FTO-coated glass substrate, followed by sintering at 450 °C in air for 30 min. The thickness of the resulting films was measured using a KLA Tencor D-120 Stylus profilometer, which was calibrated using a 4.474 μm reference sample (VLSI Standard Incorporated, KTS-4.5 QS). The working electrode was then post-treated with TiCl_4 (0.2 mM_(aq), 30 min at 70 °C) and again sintered in air at 450 °C. After cooling to 80 °C, the electrode was collected and immersed in a dye solution (0.5 mM in EtOH) for 2 days. Counter-electrodes were prepared by spreading two drops of H_2PtCl_6 solution (50 mM in *iso*-propanol) onto a pre-pierced (two holes) piece of FTO-coated glass, followed by heating to 380 °C for 30 min. The TiO_2 anode and the counter-electrode were assembled into a sandwich-type cell and sealed with a thermoplastic sealant (Meltonix 1170-25, Solaronix) of 25 μm thickness by hot-pressing at 150 °C for 20 s. The I^-/I_3^- -based electrolyte (Iodolyte AN-50, Solaronix) was injected through the holes in the counter-electrode and then sealed using the thermoplastic sealant and cover glass.

The $J-V$ testing of the DSSC sample was carried out using a Keithley 2400 source measure unit. Air mass 1.5 global simulated sunlight ($100 \text{ mW}\cdot\text{cm}^{-2}$) was produced by a 450 W solar simulator (Sol3A, Oriel Instruments). The incident light intensity was calibrated to one sun by a photovoltaic reference cell system (91150V, Oriel Instruments). The cell active area was defined as 0.196 cm^2 using a black anodized aluminum aperture mask. IPCE spectra were measured in DC mode using a QE-PV-SI system (Oriel Instruments) equipped with a 300 W xenon arc lamp, filter wheel, and monochromator. The IPCE spectra were calibrated to a silicon reference photodiode (71674, Oriel Instruments).

2.4. Results and Discussion

The synthesis of the core-shell Ag@SiO₂ nanoprisms is shown in Scheme 2.1. The triangular silver nanoprism core is first prepared by the chemical reduction of silver nitrate with NaBH₄ in the presence of sodium citrate, hydrogen peroxide, and poly(*N*-vinylpyrrolidone).³¹ TEM images of the as-prepared nanoprisms are shown in Figure 2.1, and the edge length and thickness of the prisms were found to be 30 ± 8 nm and 2.9 ± 0.6 nm, respectively. This method produced *ca.* 80% nanotriangles and the particle size distributions of the nanotriangles are shown in Figure 2.2. The nanoprisms have a broad LSPR absorption band centered at 693 nm (Figure 2.1c). This peak is strongly red-shifted compared to spherical silver nanoparticles due to the high aspect ratio of the nanoprisms. Previous work has assigned the shoulder at 490 nm to an in-plane quadrupole resonance.^{34, 35} After synthesis, the nanoprisms are functionalized with 16-mercaptohexadecanoic acid, and a silica shell is grown via a sol-gel process using a solution of tetraethylorthosilicate and *N,N*-dimethylamine in ethanol.³² The thickness of the silica shell can be tuned by adjusting the concentration of TEOS in the reaction mixture;³² starting from a single batch of silver nanoprisms, we prepared a series of four samples with shell thicknesses ranging from 7 to 33 nm (Figure 2.3). In all cases, the nanoprism core (which is distinguishable from the silica shell due to the higher electron contrast of silver due to its higher electron density) retains its triangular shape. At the lowest TEOS concentration (0.8 mM), a very thin (7 nm) silica shell is visible on the particle surface; as the concentration of TEOS in the reaction mixture is increased, the shell increases in thickness, and the overall shape of the core-shell particle changes from triangular to roughly spherical. At a TEOS concentration of 16 mM, secondary nucleation of silica particles begins to occur, and SiO₂ nanospheres not containing a silver core are observed alongside

the core-shell particles. At this TEOS concentration, a 33 nm thick shell is produced; due to the issue of secondary nucleation, this was taken as the upper limit of shell thickness in this study.



Scheme 2.1. Synthesis of the Ag@SiO₂ triangular nanoprisms.

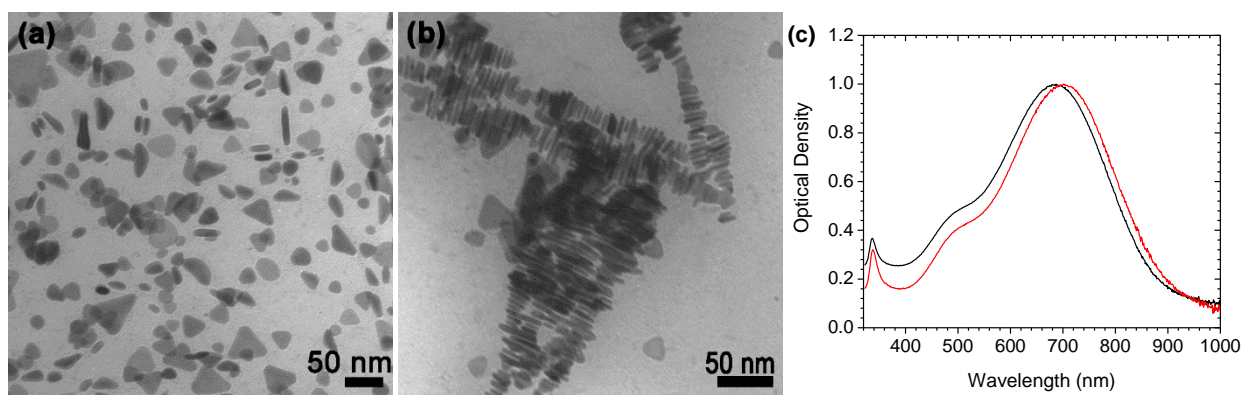


Figure 2.1. a) & b) TEM images of the as-prepared silver nanoprisms, (c) UV/Vis/NIR spectra of the as-prepared silver nanoprisms (black line) and the nanoprisms after functionalization with 16-mercaptohexadecanoic acid (red line).

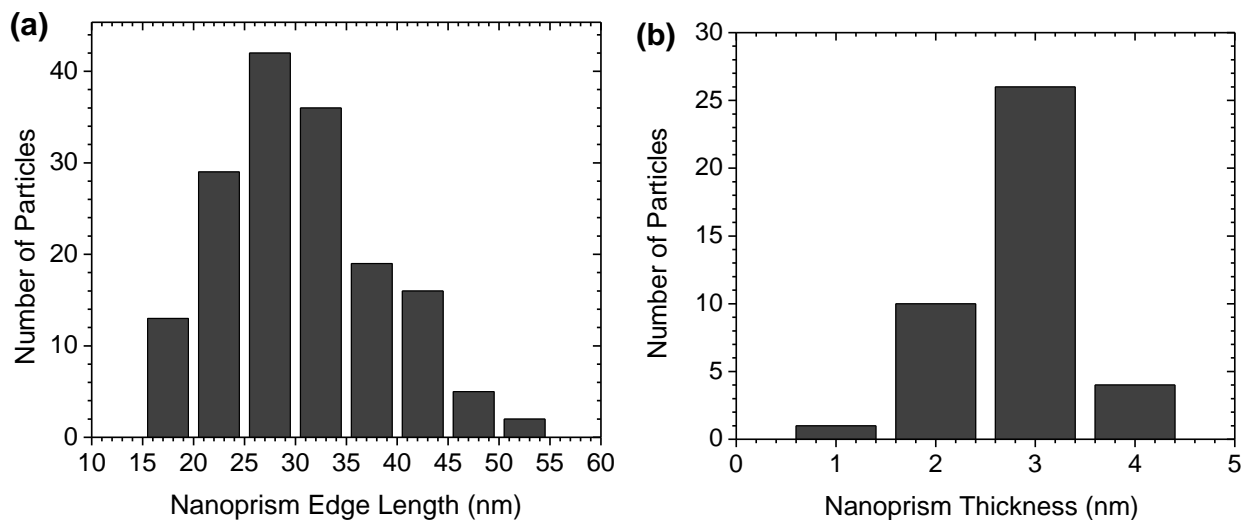


Figure 2.2. Size distributions of the as-prepared silver nanoprisms, (a) edge length, and (b) thickness.

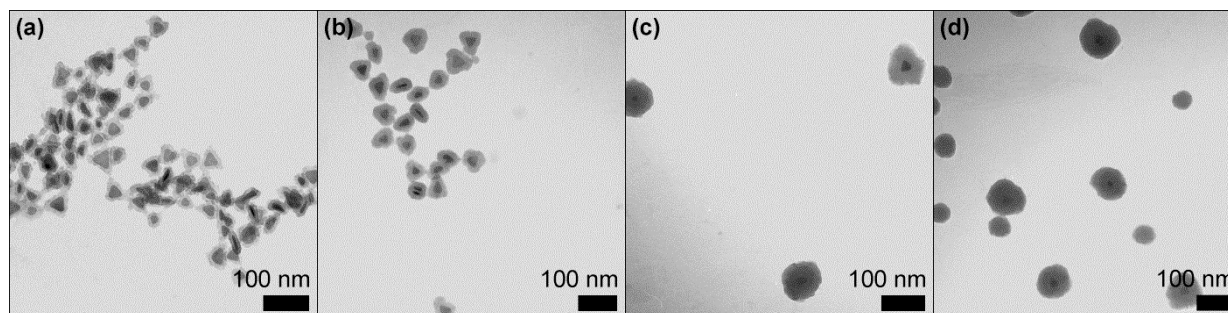


Figure 2.3. TEM micrographs of Ag@SiO₂ core-shell particles synthesized with different TEOS concentrations: (a) 0.8 mM, (b) 1.8 mM, (c) 9 mM, and (d) 16 mM.

The position of the localized surface plasmon resonance depends very strongly on the dielectric environment surrounding the nanoparticle. Compared to the citrate-stabilized nanoprisms, the silver nanoprisms functionalized with 16-mercaptohexadecanoic acid show a 10 nm red-shift in the position of the plasmon band (Figure 2.1c), consistent with thiol-coordination to the surface. After growth of the silica shell, the plasmon peak is further red-shifted with respect to the thiol-functionalized nanoprisms (Figure 2.4). The magnitude of this red-shift was found to increase with the concentration of TEOS in the reaction mixture, and it tracks the silica shell thickness closely, as would be expected for an increase in the refractive index of the surrounding medium. After the shell has reached 24 nm in thickness, there appears to be little further shift in the peak position, even with further increases in shell thickness. The local field generated by localized surface plasmon resonances is strongly dependent on the distance from the nanoparticle surface.^{4, 34, 35} In the case of the Ag@SiO₂ nanoprisms, as the shell thickness increases, the effect of the solvent medium (ethanol) on the LSPR decreases. After the shell thickness has reached a limiting value, the effect of the surrounding medium completely vanishes, and no further red-shift in the LSPR peak is observed. Very similar approaches have been used in the past to measure the distance dependence of the local electromagnetic field,³⁶⁻³⁸ and our results suggest that for the thickest silica shells, the position of the plasmon band will remain constant, regardless of its

inclusion in the matrix of the TiO₂ photoanode. This also provides a unique opportunity to probe the importance of far-field effects on device efficiency, as for silica shell thicknesses greater than 24 nm, near-field effects should be greatly attenuated, and only resonant scattering (far-field) effects should be observed. Also, the triangles with thicker shell shown an increased absorption at lower wavelengths, this could be attributed to the Rayleigh scattering.

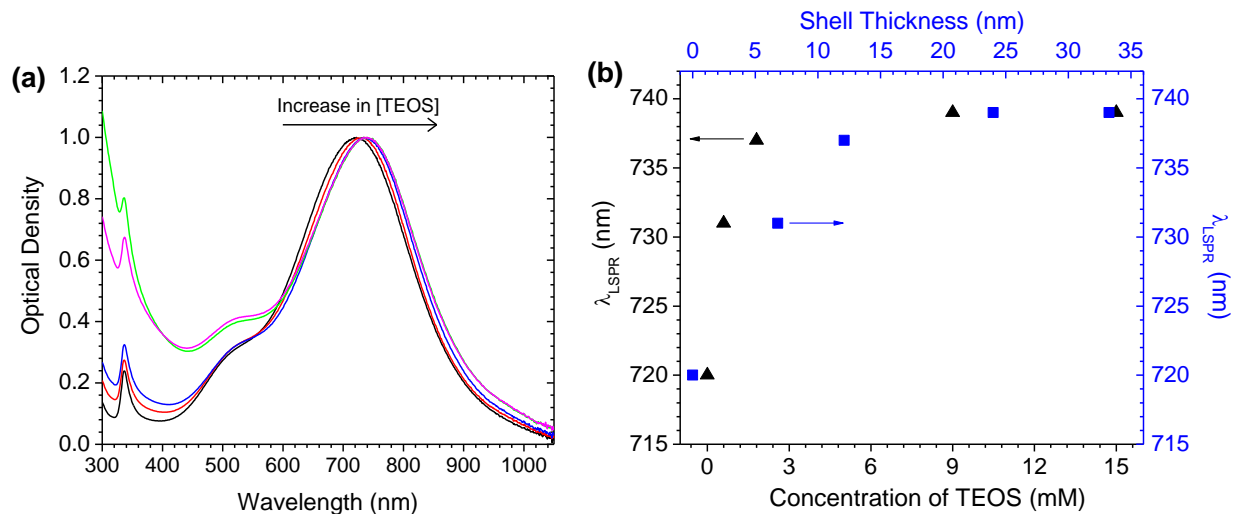


Figure 2.4. (a) Normalized UV/Vis/NIR spectra of Ag nanoparticles functionalized with 16-mercaptohexadecanoic acid (black line), and Ag@SiO₂ nanoparticles synthesized using various TEOS concentrations: 0.8 mM (red line), 1.8 mM (blue line), 9 mM (green line), and 16 mM (pink line). (b) Peak position of the LSPR band (λ_{LSPR}) as a function of both TEOS concentration (black triangles) and shell thickness (blue squares).

In order to carry out optimization studies on the incorporation of Ag@SiO₂ nanoparticles into DSSCs, the nanoparticles with the thickest (33 nm) silica shell were chosen. These particles were found to be ~ 70 nm in diameter (Figure 2.3d), and while somewhat larger in size than the TiO₂ nanoparticles ($d \sim 20$ nm) made via a sol-gel / hydrothermal approach,³³ the two materials could readily be dispersed into a homogeneous paste. This was accomplished by blending the two types of nanoparticles together in various mass ratios, along with ethyl cellulose binders, followed by ultra-sonication for a period of 15 minutes. After the homogenization process, an opaque blue paste was obtained. The concentration of the Ag@SiO₂ nanoparticles in the paste is a key

parameter affecting the PCE of the device, since for very low concentrations of Ag@SiO₂, little to no effect should be observed, while very high concentrations of the insulating nanoprisms will likely prove detrimental to charge transport within the photoanode. Thus, in order to determine the optimum mass ratio of Ag@SiO₂ to TiO₂, different TiO₂ pastes were prepared with varying concentrations of silver nanoprisms. The Ag@SiO₂ to TiO₂ mass ratio of these pastes ranged from 0.01% to 1% (w/w). The pastes were subsequently used to prepare photoanodes that were 8–10 μm in thickness, which were in turn sensitized by N719 dye (Figure 2.5). For comparison, control devices were also prepared without inclusion of the Ag@SiO₂ nanoprisms.

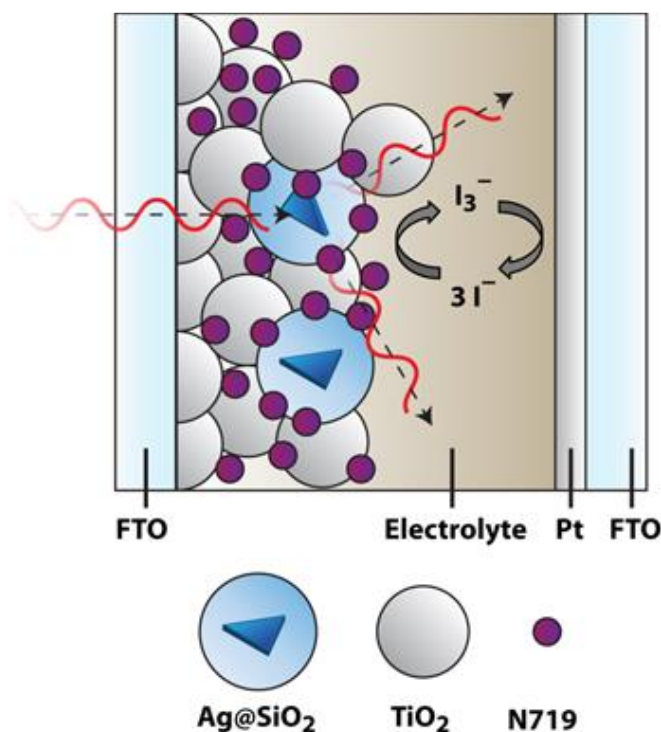


Figure 2.5. Schematic depiction of the device architecture, showing the Ag@SiO₂ nanoparticles embedded in the TiO₂ photoanode.

The *J–V* curves of both the TiO₂ and Ag@SiO₂/TiO₂-based devices are shown in Figure 2.6a, and the average open circuit voltages, short circuit current densities, fill factors, and PCEs are plotted in Figure 2.6b as a function of Ag@SiO₂ loading. The averaged data are also tabulated in Table 2.1, along with the PCE of the highest performing device from each set. The control

devices (with no plasmonic nanoparticles) demonstrated an average PCE of 5.6%. With the addition of 0.01% Ag@SiO₂ to the photoanode, the average PCE increased slightly to 6.3%, and then increased sharply to a maximum of 7.4% with the addition of 0.05% Ag@SiO₂. Thereafter, the average PCE decreased with increased Ag@SiO₂ loading. For the optimized loading of 0.05%, the PCE was improved by $32 \pm 17\%$ relative to the TiO₂ control devices. This is a substantial improvement of device performance, and is especially significant given the very low loading of Ag@SiO₂ required to achieve this performance increase. Even for unoptimized loadings (> 0.1%), the devices still displayed PCEs that were 10% higher than the TiO₂ controls. Compared to previous work on DSSCs enhanced by spherical Ag@TiO₂ nanoparticles,¹⁹ the optimized loading of plasmonic nanoparticles is substantially reduced while maintaining similar improvements in the overall PCE. Past the optimized loading of 0.05%, there is a clear downward trend in PCE with increasing Ag@SiO₂ concentration. At these concentrations, improvements in the PCE due to plasmonic light trapping effects may begin to be offset by a reduction in electron transport pathways within the TiO₂ nanoparticle network.

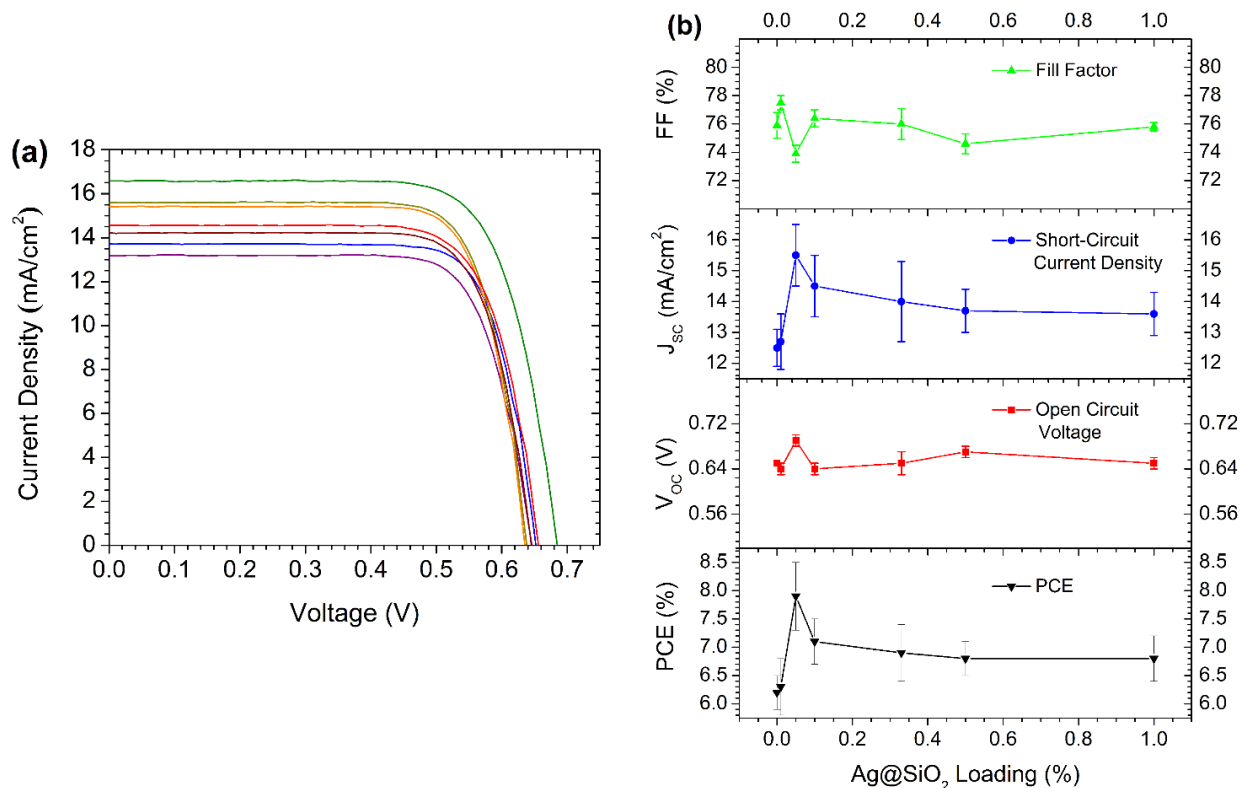


Figure 2.6. (a) J - V characteristics of the highest performing DSSC for each Ag@SiO₂/TiO₂ ratio: 0.00% (purple line), 0.01% (blue line), 0.05% (green line), 0.10% (yellow line), 0.33% (orange line), 0.50% (red line), 1.00% (dark red line). (b) Mean fill factor, short circuit current density, open circuit voltage, and PCE plotted as a function of Ag@SiO₂ loading. The error bars show plus or minus one standard deviation from the mean.

In order to statistically validate the results, the data shown in Table 2.1 was subjected to several statistical tests of significance. In the first of these, an analysis of variance (or ANOVA) test, the data is treated collectively and analyzed for differences between the group means. The results of the ANOVA analysis (at 95% confidence) are shown in Table 2.2. In short, the calculated F-value is larger than the critical F-value required for 95% confidence, meaning that the PCE is affected by the Ag@SiO₂ loading in a statistically significant way. While the ANOVA analysis is perhaps most applicable to data sets containing multiple groups (as in the present case), the results are also in very good agreement with those of pairwise t-tests between the plasmon-enhanced cells and the TiO₂ controls (Table 2.3), with p-values < 0.05. The pairwise t-tests are analogous to the

Z-test advocated by Lubber and Buriak;³⁹ however, for the sample sizes involved ($N < 30$), the t-test is more rigorous.

Table 2.1. Mean V_{oc} , J_{sc} , FF and PCE, along with their associated standard deviations, for DSSCs with different Ag@SiO₂ loadings. The number of devices tested (N) for each loading is shown.

Ag@SiO₂ Loading (%)	Average V_{oc} (V)	Average J_{sc} (mA/cm²)	Average FF (%)	Average PCE (%)	Best PCE (%)	N
0.00	0.65 ± 0.01	11.2 ± 1.2	75.7 ± 1.2	5.6 ± 0.6	6.5	15
0.01	0.64 ± 0.01	12.7 ± 0.9	77.5 ± 0.5	6.3 ± 0.5	6.9	4
0.05	0.70 ± 0.01	14.4 ± 1.4	73.5 ± 0.9	7.4 ± 0.7	8.4	13
0.10	0.64 ± 0.01	14.5 ± 1.0	76.4 ± 0.6	7.1 ± 0.4	7.3	4
0.33	0.66 ± 0.02	13.4 ± 1.3	75.6 ± 1.1	6.7 ± 0.5	7.5	6
0.50	0.67 ± 0.01	13.7 ± 0.7	74.6 ± 0.7	6.8 ± 0.3	7.1	4
1.00	0.65 ± 0.01	13.6 ± 0.7	75.8 ± 0.3	6.8 ± 0.4	7.0	4

Table 2.2. ANOVA analysis of PCE as a function of Ag@SiO₂ loading carried out at the 95% confidence level. The calculated F-value (13.3) is larger than the critical F-value (2.3) required for 95% confidence, and the P-value is less than 0.05. Therefore, the results show a statistically significant variation in PCE with Ag@SiO₂ loading.

Anova: Single Factor

SUMMARY

<i>Ag@SiO₂ Loading</i>	<i>Count</i>	<i>Sum</i>	<i>Average</i>	<i>Variance</i>
0.00%	15	83.2	5.5	0.4
0.01%	4	25.4	6.3	0.3
0.05%	13	95.8	7.4	0.5
0.10%	4	28.5	7.1	0.2
0.33%	6	40.2	6.7	0.3
0.50%	4	27.2	6.8	0.1
1.00%	4	27	6.8	0.1

ANOVA

<i>Source of Variation</i>	<i>SS</i>	<i>df</i>	<i>MS</i>	<i>F</i>	<i>P-value</i>	<i>F crit</i>
Between Groups	25.9	6	4.3	13.3	1.78E-08	2.3
Within Groups	13.9	43	0.3			
Total	39.8	49				

From Figure 2.6b, it is clear that the overall increase in PCE is driven by improvements in J_{sc} . Compared to the TiO₂ control devices, only small changes to the open circuit voltage and fill factor were observed for any of the plasmonic devices (a maximum difference of 6% and 3%, respectively). Furthermore, there is no consistent trend observed for either the V_{oc} or FF, with various Ag@SiO₂ loadings producing both positive and negative changes, and some loadings leading to no change at all. Clearly, neither the V_{oc} nor the FF can be responsible for the $32 \pm 17\%$ increase in PCE. In contrast, when 0.05% Ag@SiO₂ is incorporated into the device, the J_{sc} increases from 11.2 to 14.4 mA/cm², and then drops slowly for large Ag@SiO₂ loadings, mirroring the trends observed in the PCE. These data are entirely consistent with plasmonic light trapping being the primary driving force behind the increase in PCE. Increased light harvesting efficiency

results in improved currents, but should have no effect on either V_{oc} or FF. While previous work on DSSCs incorporating Au@TiO₂ has suggested that electron charging effects may result in shifts of the quasi-Fermi level of the TiO₂ (and hence changes to the V_{oc}),²⁵ the insulating SiO₂ shell used in the present work should only permit changes to the light harvesting efficiency.

Table 2.3. Pairwise t-tests (assuming unequal variances, 95% confidence) comparing the PCEs of devices made with various Ag@SiO₂ loadings with pure TiO₂ controls. In all cases, the absolute value of the t-statistic is larger than the critical t-value required for 95% confidence in a two-tailed test, and the P-value is less than 0.05. Therefore, each sample shows a statistically significant increase in PCE relative to the TiO₂ controls.

<i>Ag@SiO₂ Loading</i>	<i>0.00%</i>	<i>0.01%</i>	<i>0.00%</i>	<i>0.05%</i>	<i>0.00%</i>	<i>0.10%</i>
Mean	5.546	6.339	5.546	7.372	5.546	7.115
Variance	0.368	0.254	0.368	0.466	0.368	0.171
Observations	15	4	15	13	15	4
Hypothesized Mean Difference	0		0		0	
df	6		24		7	
t Stat	-2.670		-7.434		-6.050	
P(T<=t) one-tail	0.019		0.000		0.000	
t Critical one-tail	1.943		1.711		1.895	
P(T<=t) two-tail	0.0370		1.13E-07		0.0005	
t Critical two-tail	2.447		2.064		2.365	

<i>Ag@SiO₂ Loading</i>	<i>0.00%</i>	<i>0.33%</i>	<i>0.00%</i>	<i>0.50%</i>	<i>0.00%</i>	<i>1.00%</i>
Mean	5.546	6.694	5.546	6.802	5.546	6.761
Variance	0.368	0.251	0.368	0.088	0.368	0.128
Observations	15	6	15	4	15	4
Hypothesized Mean Difference	0		0		0	
df	11		11		8	
t Stat	-4.456		-5.826		-5.118	
P(T<=t) one-tail	0.000		0.000		0.000	
t Critical one-tail	1.796		1.796		1.860	
P(T<=t) two-tail	0.0010		0.0001		0.0009	
t Critical two-tail	2.201		2.201		2.306	

In order to confirm the origin of these improvements in PCE, IPCE measurements were carried out on a number of the completed devices (Figure 2.7). Since the current density in a solar cell is governed by the integral of the product of the photon flux and the IPCE, any changes to the

value of J_{sc} should also be reflected in the IPCE spectra. The results agree well with the trends observed in the J - V curves. DSSCs with a 0.05% loading of Ag@SiO₂ nanoprisms displayed notably higher IPCE values in the range of wavelengths from 400 nm to 750 nm compared to the reference device. The IPCE increased from 60% to 76% at 530 nm (the maximum of the IPCE spectrum), and substantial increases were also observed at longer wavelengths as well (e.g., from 23% to 39% at 630 nm). While it is also possible for pure silica nanoparticles to scatter light (and therefore produce higher values of J_{sc} and IPCE), if that were the case one would expect to see dramatically different behavior in the IPCE spectra. Smaller nanoparticles ($d < 0.1 \lambda$) should produce enhancements in the IPCE spectrum that closely follow the $1/\lambda^4$ dependence typical of Rayleigh scattering, while larger nanoparticles ($d \gg 0.1 \lambda$) should lead to scattering that is largely independent of wavelength. The observed differences in the IPCE spectrum (Figure 2.8) are inconsistent with either scenario, but entirely consistent with resonant scattering caused by the nanoparticle.

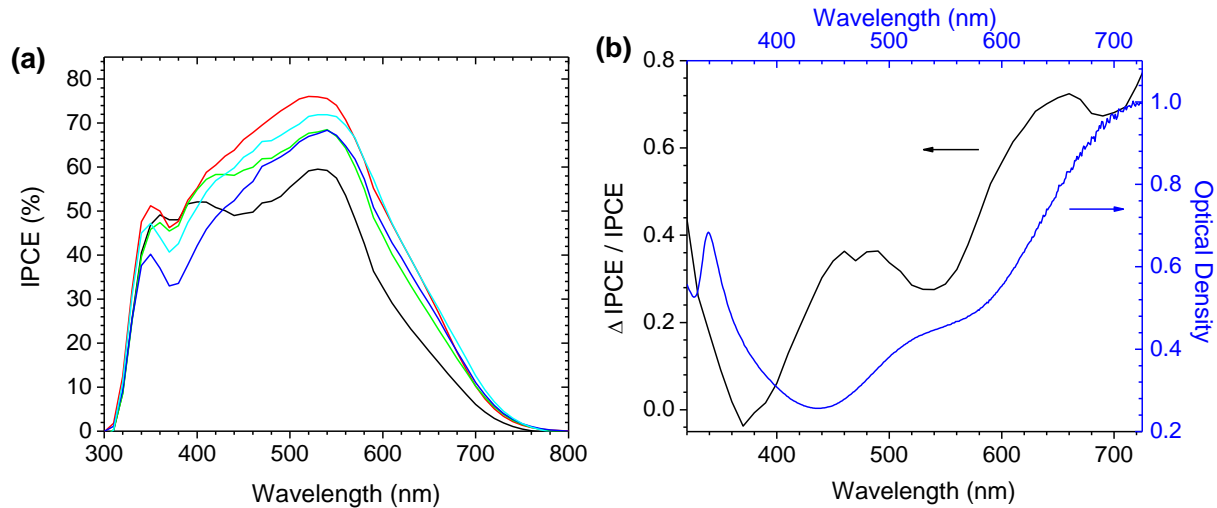


Figure 2.7. (a) Incident photon-to-current efficiency spectra of DSSCs made using various Ag@SiO₂/TiO₂ ratios: 0.0% (black line), 0.05% (red line), 0.10% (cyan line), 0.33% (green line) and 0.5% (blue line). (b) The relative IPCE enhancement $((IPCE_{Ag@SiO_2} - IPCE_{control}) / IPCE_{control})$ for the device with a 0.05% Ag@SiO₂ (black line) loading and the absorption spectrum of the Ag@SiO₂ nanoprisms (blue line).

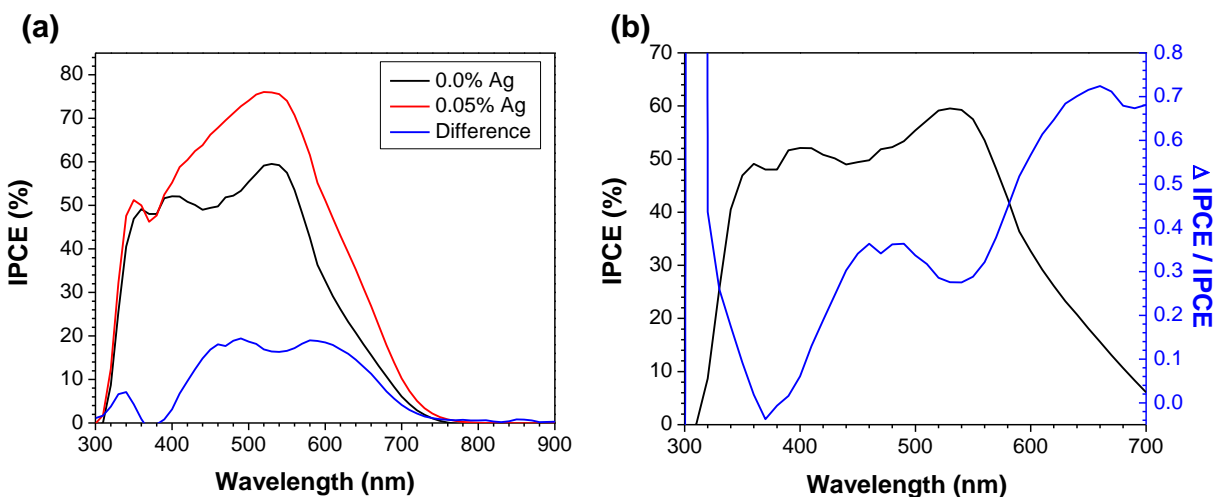


Figure 2.8. (a) Incident photon-to-current efficiency spectra of DSSCs made using 0.0% (black line) and 0.05% (red line) Ag@SiO₂ loadings. The difference spectrum is also shown (blue line). (b) The relative IPCE enhancement ($(\text{IPCE}_{\text{Ag@SiO}_2} - \text{IPCE}_{\text{control}}) / \text{IPCE}_{\text{control}}$) for the device with a 0.05% Ag@SiO₂ loading (blue line) and the original IPCE spectrum (black line).

As the Ag@SiO₂ concentration increases, there continues to be an improvement in IPCE for the long wavelength region of the spectrum, despite a decrease in IPCE at shorter wavelengths. This spectral shift can best be understood by separately considering the various factors that control the IPCE, including the light harvesting efficiency, the efficiency of electron injection from the excited dye molecule to the TiO₂ electrode, and the electron collection efficiency at the anode. The increase in IPCE at wavelengths resonant with the Ag@SiO₂ LSPR band is consistent with an increase in the LHE. For wavelengths off-resonance with the LSPR band, however, the Ag@SiO₂ nanoparticles are expected to have a detrimental impact on the IPCE. Embedding insulating silica particles inside the mesoporous TiO₂ network will disrupt charge percolation networks, forcing the charge carriers to take increasingly convoluted pathways to the electrode as the Ag@SiO₂ concentration is increased. Several reports have clearly demonstrated that straighter, less convoluted electron transport pathways with fewer grain boundaries are critical in maximizing the electron collection efficiency.⁴⁰⁻⁴² As such, the decrease in collection efficiency results in a net

decrease in the IPCE for wavelengths that are off-resonance with the LSPR band, and these effects are particularly pronounced for the devices with the highest Ag@SiO₂ loadings.

Further evidence for the contribution of the silver nanoprisms to the enhanced light harvesting efficiency can be found by comparison of the relative increase in IPCE ($\Delta\text{IPCE}/\text{IPCE}_{\text{control}}$) and the Ag@SiO₂ absorption spectrum (Figure 2.7b). The IPCE enhancement spectrum is dominated by a large feature at 660 nm, with a second, less pronounced peak at 460 nm. This is in reasonable agreement with the Ag@SiO₂ absorption spectrum, which displays an intense peak at 724 nm due to the in-plane dipole LSPR mode, and a shoulder at 515 nm due to the in-plane quadrupole mode (note that the position of this peak is slightly offset from the data shown in Figure 2.4 due to batch-to-batch variability in the preparation of the nanoprisms). This correlation between the nanoparticle LSPR band and the IPCE enhancement spectrum is in agreement with previous reports of plasmon-enhanced DSSCs.^{19, 43} There are two notable differences between the two spectra: first, the location of the IPCE enhancement is blue-shifted with respect to the initial absorption spectrum of the Ag@SiO₂ nanoparticles, and second, there is an additional contribution at 460 nm that is unlikely to be entirely due to the quadrupole mode of the nanoprisms. These discrepancies may be caused by changes in the particle shape during the electrode deposition and/or cell fabrication process (most likely during the sintering step). In order to evaluate their stability, TEM images were acquired after sintering a sample of Ag@SiO₂ nanoparticles (Figure 2.9). The tips of triangular silver nanoprisms are prone to rounding or truncation (thereby blue-shifting the LSPR band),⁴⁴ and various levels of tip rounding can be seen in Figure 2.9. Some particles are still triangular in shape (giving rise to the enhancements observed at wavelengths > 600 nm), while others have been reduced in size to smaller plates or spheres (likely contributing to the extra IPCE enhancement observed at 460 nm). The complete retention

of anisotropic nanoparticle shape under sintering conditions is a challenge for many in this area, and is certainly an area in which further improvements could be made; however, regardless of any small changes in particle morphology, the light harvesting efficiency of the DSSC has been dramatically improved in the vicinity of 660 nm – a spectral region that is very challenging to reach with isotropic, spherical nanoparticles.

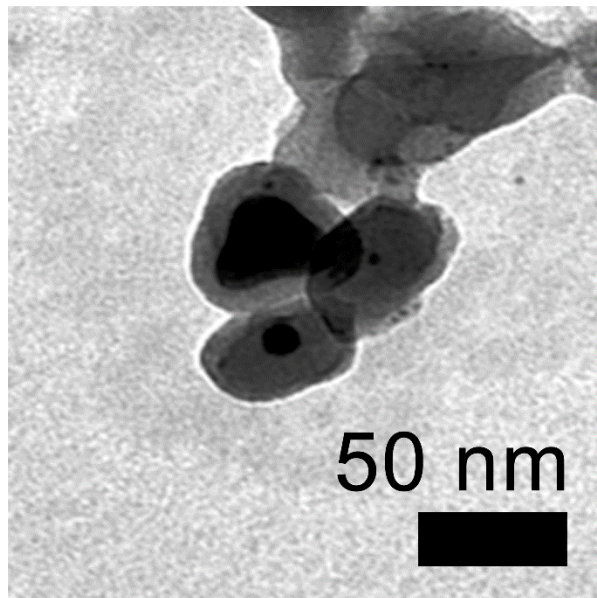


Figure 2.9. TEM image of the Ag@SiO₂ nanoparticles with the thickest SiO₂ shells after sintering.

In order to investigate the effect of silica shell thickness on the plasmon-based efficiency enhancement, Ag@SiO₂ nanoparticles with various shell thicknesses were incorporated into DSSCs. Nanoparticles with SiO₂ shells of 7 nm were chosen in order to provide a contrast with the thick-shelled nanoprisms studied previously; since near-field effects are strongly distance dependent, thin silica shells might be expected to lead to greater overall improvements. Our results indicate that the efficiencies of DSSCs fabricated with the thin-shelled nanoprisms are no different than the PCEs of the TiO₂ controls (Figure 2.10), in stark contrast to the improvements in PCE observed for the thick-shelled nanoprisms. The average device characteristics are tabulated in Table 2.4. To better understand this discrepancy, the stabilities of both types of Ag@SiO₂ core-

shell particles were tested in I^-/I_3^- electrolyte solutions over a period of 20 h. The Ag@SiO₂ nanoparticles with the thickest shells showed no change in either the intensity or the position of the plasmon band after electrolyte exposure; however, the Ag@SiO₂ nanoparticles with the 7 nm silica shells suffered an immediate (within 30 min) disappearance of the LSPR band (Figure 2.11). This clearly indicates that the thinner silica shell is either incomplete or slightly porous, leading to the dissolution of the underlying silver nanoprism core.

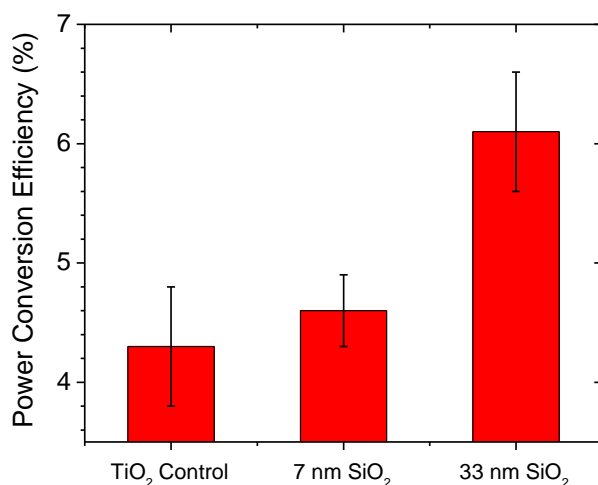


Figure 2.10. Average PCE for DSSCs prepared using 0.05% (w/w) of Ag@SiO₂ nanoprisms with different shell thicknesses, as well as for the control devices without any Ag@SiO₂. The thickness of the photoanode in all devices was 3 – 4 μ m. The error bars show plus or minus one standard deviation from the mean.

Table 2.4. Device performance characteristics for DSSCs prepared using 0.05% (w/w) of Ag@SiO₂ nanoprisms with different shell thicknesses, as well as for the control devices without any Ag@SiO₂. The thickness of the photoanode in all devices was 3 – 4 μ m.

Device Type	Average V _{OC} (V)	Average J _{SC} (mA/cm ²)	Average FF (%)	Average PCE (%)
TiO₂ Control	0.63 ± 0.02	9.3 ± 0.8	72.9 ± 0.2	4.3 ± 0.5
7 nm Ag@SiO₂	0.68 ± 0.01	9.1 ± 0.6	73.3 ± 0.8	4.6 ± 0.3
33 nm Ag@SiO₂	0.65 ± 0.01	12.9 ± 0.9	71.7 ± 0.8	6.1 ± 0.5

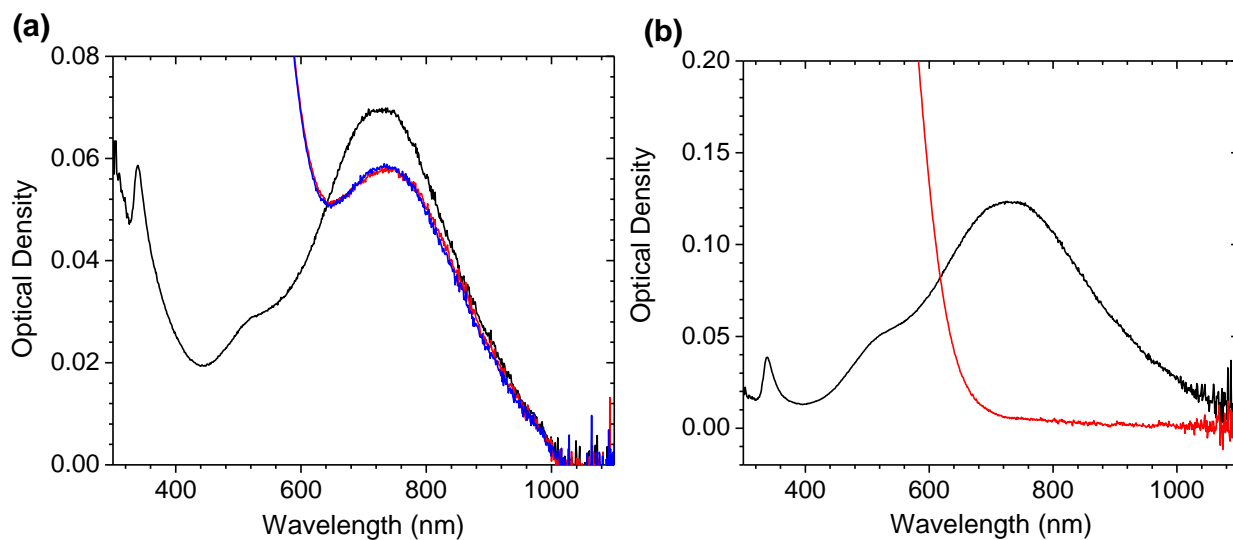


Figure 2.11. (a) UV/Vis/NIR spectra of the Ag@SiO₂ nanoprisms with a 33 nm thick shell: in acetonitrile (black line), 30 min after adding the I⁻/I₃⁻ electrolyte (red line), and 20 h after addition of the electrolyte solution (blue line). (b) UV/Vis/NIR spectra of the Ag@SiO₂ nanoprisms with a 7 nm thick shell: in acetonitrile (black line), and 30 min after adding the I⁻/I₃⁻ electrolyte (red line).

2.5. Conclusions

We have demonstrated the successful utilization of triangular silver nanoprisms as light harvesting elements in a dye-sensitized solar cell. The loading of the silica-capped nanoprisms was optimized, and it was found that a very low loading of 0.05% Ag@SiO₂ in the titania photoanode resulted in a $32 \pm 17\%$ increase in the overall PCE of the device, driven primarily by an increase in the short circuit current density. This plasmonic efficiency enhancement resulted in an 8.4% PCE for the highest performing device in the present study.

IPCE measurements clearly indicate that these increases are due to improvements in the light harvesting efficiency at longer wavelengths (resonant with the Ag@SiO₂ LSPR band), and that further increases in the Ag@SiO₂ loading result in a detrimental effect on the electron collection efficiency. In contrast to previous work on spherical nanoparticle systems, the anisotropic nature, and high aspect ratio of the nanoprism core leads to strongly red-shifted LSPR modes and large improvements in the LHE at longer wavelengths. We expect that the application

of anisotropic metal particles to plasmon-enhanced DSSCs will help fulfill a major role in improving the efficiency of these devices – namely, the improvement of the light harvesting efficiency at red to NIR wavelengths where most dyes absorb very weakly.

2.6. References

1. A. Yella, H. W. Lee, H. N. Tsao, C. Yi, A. K. Chandiran, M. K. Nazeeruddin, E. W. Diau, C. Y. Yeh, S. M. Zakeeruddin and M. Grätzel, *Science*, 2011, **334**, 629-634.
2. A. Hagfeldt, G. Boschloo, L. Sun, L. Kloo and H. Pettersson, *Chem. Rev.*, 2010, **110**, 6595-6663.
3. M. Grätzel, *Acc. Chem. Res.*, 2009, **42**, 1788-1798.
4. T. W. Hamann, R. A. Jensen, A. B. F. Martinson, H. Van Ryswyk and J. T. Hupp, *Energy Environ. Sci.*, 2008, **1**, 66-78.
5. W. M. Campbell, K. W. Jolley, P. Wagner, K. Wagner, P. J. Walsh, K. C. Gordon, L. Schmidt-Mende, M. K. Nazeeruddin, Q. Wang, M. Grätzel and D. L. Officer, *J. Phys. Chem. C*, 2007, **111**, 11760-11762.
6. L.-L. Li and E. W.-G. Diau, *Chem. Soc. Rev.*, 2013, **42**, 291-304.
7. P. Balraju, P. Suresh, M. Kumar, M. S. Roy and G. D. Sharma, *J. Photochem. Photobiol., A*, 2009, **206**, 53-63.
8. S. Hore, C. Vetter, R. Kern, H. Smit and A. Hinsch, *Sol. Energy Mater. Sol. Cells*, 2006, **90**, 1176-1188.
9. Y.-Z. Zheng, X. Tao, L.-X. Wang, H. Xu, Q. Hou, W.-L. Zhou and J.-F. Chen, *Chem. Mater.*, 2009, **22**, 928-934.
10. F. Huang, D. Chen, X. L. Zhang, R. A. Caruso and Y.-B. Cheng, *Adv. Funct. Mater.*, 2010, **20**, 1301-1305.
11. I. K. Ding, J. Zhu, W. Cai, S.-J. Moon, N. Cai, P. Wang, S. M. Zakeeruddin, M. Grätzel, M. L. Brongersma, Y. Cui and M. D. McGehee, *Adv. Energy Mater.*, 2011, **1**, 52-57.

12. D.-H. Ko, J. R. Tumbleston, A. Gadisa, M. Aryal, Y. Liu, R. Lopez and E. T. Samulski, *J. Mat. Chem.*, 2011, **21**, 16293-16303.
13. S. Linic, P. Christopher and D. B. Ingram, *Nat. Mater.*, 2011, **10**, 911-921.
14. E. Ozbay, *Science*, 2006, **311**, 189-193.
15. P. K. Jain, K. S. Lee, I. H. El-Sayed and M. A. El-Sayed, *J. Phys. Chem. B*, 2006, **110**, 7238-7248.
16. P. K. Jain, X. Huang, I. H. El-Sayed and M. A. El-Sayed, *Acc. Chem. Res.*, 2008, **41**, 1578-1586.
17. H. A. Atwater and A. Polman, *Nat. Mater.*, 2010, **9**, 205-213.
18. W. B. Hou, P. Pavaskar, Z. W. Liu, J. Theiss, M. Aykol and S. B. Cronin, *Energy Environ. Sci.*, 2011, **4**, 4650-4655.
19. J. F. Qi, X. N. Dang, P. T. Hammond and A. M. Belcher, *ACS Nano*, 2011, **5**, 7108-7116.
20. M. D. Brown, T. Suteewong, R. S. S. Kumar, V. D'Innocenzo, A. Petrozza, M. M. Lee, U. Wiesner and H. J. Snaith, *Nano Lett.*, 2011, **11**, 438-445.
21. S. D. Standridge, G. C. Schatz and J. T. Hupp, *J. Am. Chem. Soc.*, 2009, **131**, 8407-8409.
22. N. C. Jeong, C. Prasittichai and J. T. Hupp, *Langmuir*, 2011, **27**, 14609-14614.
23. S. Chang, Q. Li, X. D. Xiao, K. Y. Wong and T. Chen, *Energy Environ. Sci.*, 2012, **5**, 9444-9448.
24. S. D. Standridge, G. C. Schatz and J. T. Hupp, *Langmuir*, 2009, **25**, 2596-2600.
25. H. Choi, W. T. Chen and P. V. Kamat, *ACS Nano*, 2012, **6**, 4418-4427.
26. S. W. Sheehan, H. Noh, G. W. Brudvig, H. Cao and C. A. Schmuttenmaer, *J. Phys. Chem. C*, 2012, **117**, 927-934.

27. D. Aherne, D. M. Ledwith and J. M. Kelly, in *Metal-Enhanced Fluorescence*, John Wiley & Sons, Inc., 2010, pp. 295-362.
28. D. Aherne, D. M. Ledwith, M. Gara and J. M. Kelly, *Adv. Funct. Mater.*, 2008, **18**, 2005-2016.
29. V. Janković, Y. Yang, J. You, L. Dou, Y. Liu, P. Cheung and J. P. Chang, *ACS Nano*, 2013, **7**, 3815-3822.
30. A. P. Kulkarni, K. M. Noone, K. Munechika, S. R. Guyer and D. S. Ginger, *Nano Lett.*, 2010, **10**, 1501-1505.
31. Q. Zhang, N. Li, J. Goebel, Z. Lu and Y. Yin, *J. Am. Chem. Soc.*, 2011, **133**, 18931-18939.
32. C. Xue, X. Chen, S. J. Hurst and C. A. Mirkin, *Adv. Mater.*, 2007, **19**, 4071-4074.
33. S. Ito, T. N. Murakami, P. Comte, P. Liska, C. Grätzel, M. K. Nazeeruddin and M. Grätzel, *Thin Solid Films*, 2008, **516**, 4613-4619.
34. K. L. Kelly, E. Coronado, L. L. Zhao and G. C. Schatz, *J. Phys. Chem. C*, 2002, **107**, 668-677.
35. D. D. Evanoff, Jr. and G. Chumanov, *Chem. Phys. Chem.*, 2005, **6**, 1221-1231.
36. D. D. Evanoff, R. L. White and G. Chumanov, *J. Phys. Chem. C*, 2004, **108**, 1522-1524.
37. A. J. Haes, S. Zou, G. C. Schatz and R. P. Van Duyne, *J. Phys. Chem. C*, 2003, **108**, 109-116.
38. J. Rodríguez-Fernández, I. Pastoriza-Santos, J. Pérez-Juste, F. J. García de Abajo and L. M. Liz-Marzán, *J. Phys. Chem. C*, 2007, **111**, 13361-13366.
39. E. J. Lubber and J. M. Buriak, *ACS Nano*, 2013, **7**, 4708-4714.
40. S. H. Kang, S. H. Choi, M. S. Kang, J. Y. Kim, H. S. Kim, T. Hyeon and Y. E. Sung, *Adv. Mater.*, 2008, **20**, 54-58.

41. E. Ghadiri, N. Taghavinia, S. M. Zakeeruddin, M. Grätzel and J.-E. Moser, *Nano Lett.*, 2010, **10**, 1632-1638.
42. D. K.-P. Wong, C.-H. Ku, Y.-R. Chen, G.-R. Chen and J.-J. Wu, *Chem. Phys. Chem.*, 2009, **10**, 2698-2702.
43. X. Dang, J. Qi, M. T. Klug, P.-Y. Chen, D. S. Yun, N. X. Fang, P. T. Hammond and A. M. Belcher, *Nano Lett.*, 2013, **13**, 637-642.
44. L. J. Sherry, R. Jin, C. A. Mirkin, G. C. Schatz and R. P. Van Duyne, *Nano Lett.*, 2006, **6**, 2060-2065.

CHAPTER 3

Thermal Degradation Mechanism of Triangular Ag@SiO₂ Nanoparticles

Mahesh K. Gangishetty, Robert W. J. Scott, and Timothy L. Kelly**

Department of Chemistry, University of Saskatchewan, 110 Science Place, Saskatoon, SK, S7N 5C9, Canada

This project studies the thermal degradation pathways of Ag@SiO₂ nanotriangles by using X-ray absorption spectroscopy. Upon annealing Ag@SiO₂ nanotriangles in air, they showed interesting changes in the morphology (*cf.* Chapter 2). To understand these changes, XANES (X-ray absorption near-edge spectra) and EXAFS (extended X-ray absorption fine spectra) were employed in this study.

This chapter is a near-verbatim copy of work published in *Dalton Transactions*, **2016**, 45, 9827 All the experimental work in this article was performed by me. The first draft of the manuscript was written by me and it was revised by Prof. Tim Kelly and Prof. Robert Scott prior to publication.

3.1. Abstract

Triangular silver nanoparticles are promising materials for light harvesting applications because of their strong plasmon bands; these absorption bands are highly tunable, and can be varied over the entire visible range based on the particle size. A general concern with these materials is that they are unstable at elevated temperatures. When thermally annealed, they suffer from changes in the particle morphology, which in turn affects their optical properties. Because of this stability issue, these materials cannot be used in applications requiring elevated temperatures. In order to address this problem, it is important to first understand the degradation mechanism. Here, we measure the changes in particle morphology, oxidation state, and coordination environment of Ag@SiO₂ nanotriangles caused by thermal annealing. UV-Vis spectroscopy and TEM reveal that upon annealing the Ag@SiO₂ nanotriangles in air, the triangular cores are truncated, and smaller nanoparticles are formed. Ag *K*-edge X-ray absorption spectroscopy (XANES and EXAFS) shows that the small particles consist of Ag(0), and that there is a decrease in the Ag-Ag coordination number with an increase in the annealing temperature. We hypothesize that upon annealing Ag in air, it is first oxidized to Ag_xO, after which it subsequently decomposes back to well-dispersed Ag(0) nanoparticles. In contrast, when the Ag@SiO₂ nanotriangles are annealed in N₂, since there is no possibility of oxidation, no small particles are formed. Instead, the triangular core rearranges to form a disc-like shape.

3.2. Introduction

Localized surface plasmon resonance is a phenomenon unique to metal nanoparticles, and has a wide variety of applications. When metal nanoparticles interact with incoming light, the light drives coherent oscillations of the electrons in their conduction bands, known as localized surface

plasmons. LSPR occurs when the frequency of these oscillations is in resonance with the frequency of the incoming light.¹⁻³ Due to their unique optical properties, they have been used in a variety of applications such as surface-enhanced Raman spectroscopy,^{4, 5} sensing,⁶⁻⁸ photocatalysis⁹⁻¹⁴ and optoelectronics.¹⁵⁻¹⁹ The frequency of the LSPR band depends on both the type of material (e.g., Au, Ag or Cu), and the shape and size of the nanoparticles.^{1, 4}

Triangular Ag nanoparticles have high extinction coefficients, and their optical properties are easily tunable by changing the edge length.²⁰ In addition to this, they exhibit very intense near fields as the charge that arises from the plasmon oscillations is concentrated near the tips. Because of this strong LSPR and the corresponding strong near field effects, they have been efficient materials for light harvesting applications.^{15, 21-23} However, a major concern with these materials is their stability.²⁴ There have been numerous studies, both theoretical and experimental, on the stability of Ag nanotriangles. Any oxidation promoting reagents such as halide ions^{24, 25} and thiols²⁶ attack the tips of the triangles, causing a change in particle morphology which affects their optical properties. In addition to these chemical reagents, UV irradiation^{27, 28} and heating the colloidal solutions²⁸⁻³⁰ also have detrimental effects on the morphology of these triangles. All of the above treatments degrade the tips of the triangle, and similar behaviour is observed for other particles with sharp features, such as nanowires,^{30, 31} nano-tetrahedra,³² and nanocubes.³³ To protect them from chemical etching agents, such particles are often coated with different materials such as SiO₂,^{15, 34} TiO₂³⁵ and Au.^{23, 24, 36} However, protecting the nanotriangles from thermal degradation is quite challenging, and the presence of porous SiO₂ or TiO₂ shells may not be enough to prevent decomposition. Lei *et al.* observed the degradation of Ag nanospheres at elevated temperatures even after coating with a thin silica shell, as oxygen from the atmosphere diffused through the porous silica and led to the oxidation of the Ag core.³⁷

The stability of nanoparticles depends on their surface energy. Ag has a face centered cubic crystal structure, and the triangular nanoparticles are enclosed by low energy (111) planes on their basal surfaces and high energy (110) or (100) planes on their edges.³⁰ The surface energies of these crystal planes follow the order (100) > (110) > (111).³⁸ As per the Gibbs-Thomson effect, the tips are even more unstable than the edges, since they are formed by the intersection of two high energy facets (the edges). Hence, the decomposition of these particles begins with the dissociation of atoms from the tips, followed by the edges.³⁹ The dissociated atoms are either redeposited on the more stable basal planes, leading to the formation of thick nanodiscs, or they completely detach from the nanoparticle resulting in a reduction in the overall particle size.^{29, 39} Tang *et al.* observed dissociation of Ag atoms from the tips of triangles and the formation of circular nanodiscs upon aging Ag nanotriangles at 95 °C.²⁹ Upon irradiating the solution of degraded Ag nanotriangles with a sodium lamp, reconstruction to the original morphology of nanotriangles was observed.²⁸ Many groups have similarly used mild heating in solvent as a route for synthesizing Ag circular nanodiscs from triangular precursors.^{29, 40} Although it is clear that the Ag nanotriangles are forming circular nanodiscs upon decomposition, there are several questions that are left unaddressed about the mechanism of degradation. It has been noted that the overall size of the nanoparticles decreases upon annealing at elevated temperatures,^{24, 29} where the fate of the dissociated atoms needs to be fully understood.

Here, we elucidate the mechanism of thermal degradation of Ag@SiO₂ nanotriangles using XAS. XAS is a powerful tool for understanding changes in oxidation state, atomic environment and first shell coordination number (and thus average particle size) during the shape transformation of the nanotriangles. We synthesized the Ag@SiO₂ nanotriangles and annealed them in air and N₂ atmospheres at different temperatures, ranging from 150 to 600 °C. The Ag *K*-edge spectra were

recorded for all samples before and after annealing. Our analysis showed that upon annealing the Ag@SiO₂ nanotriangles in air, the Ag core breaks up to form multiple smaller Ag particles. We hypothesize that the Ag core is first oxidized to Ag_xO, which then further dissociates to form small Ag nanoparticles in the pores of the silica spheres. Further evidence for this mechanism is found by studying samples annealed in N₂, which do not show such formation of small Ag nanoparticles.

3.3. Experimental

3.3.1. Materials and methods

Silver nitrate (99%), sodium borohydride (98%), and hydrogen peroxide (30% w/w), were purchased from Fisher Scientific. Trisodium citrate dihydrate ($\geq 96\%$), poly (*N*-vinylpyrrolidone) ($\geq 99\%$, MW 40,000 g/mol), 16-mercaptohexadecanoic acid (90%), tetraethoxysilane (99%), and *N,N*-dimethylamine (40% w/v) were purchased from Sigma-Aldrich. All chemicals were used as received without further purification. Deionized water (18.2 M Ω ·cm) was obtained from a Milli-Q water purification system.

3.3.2. Synthesis of Ag and Ag@SiO₂ nanotriangles

Triangular Ag and Ag@SiO₂ nanoparticles were synthesized using existing procedures.^{15,}
⁴¹ To 248 mL of deionized water, aqueous solutions of AgNO₃ (500 μ L, 50 mM), trisodium citrate (5 mL, 75 mM), PVP (1 mL, 17.5 mM) and H₂O₂ (600 μ L) were added. Finally, aqueous NaBH₄ (2.5 mL, 0.1 M) was rapidly injected into the solution. After the formation of a blue colored solution, the nanotriangles were collected by centrifugation (10,000 g, 3.5 h).

After centrifugation, the nanotriangles were dispersed in 100 mL deionized water, followed by the addition of an ethanolic MHA solution (1.5 mL, 5 mM) and stirring for 10 min. The MHA-functionalized Ag nanotriangles were centrifuged (10,000 g, 3.5h) and redispersed in ethanolic

TEOS (20 mL, 16 mM). After 2 min of stirring, aqueous dimethylamine (2 mL, 20% w/v) was added, and the solution was stirred for 12 h. The Ag@SiO₂ nanotriangles were collected by centrifugation (10,000 g, 1 h) and dried at room temperature. To prepare the SiO₂@Ag control samples (triangular Ag nanoparticles adsorbed on SiO₂ spheres), first SiO₂ nanospheres were synthesized by stirring a mixture of TEOS and dimethylamine (using the same concentrations as above) for 12 h in ethanol. After purifying the SiO₂ nanoparticles by centrifugation and redispersion, an aqueous solution of MHA-functionalized Ag nanotriangles was added and stirred for 2 h. The SiO₂@Ag sample was then isolated by centrifugation.

3.3.3. Thermal annealing studies

To study the thermal degradation of the Ag@SiO₂ nanotriangles, they were annealed at different temperatures (150 °C, 300 °C, 450 °C and 600 °C) in either air or N₂ atmosphere. The samples were heated at a rate of 10 °C/min and the dwell time at the final temperature was 15 min. A Lindberg/Blue M tube furnace was used to carry out the annealing studies, and a flow of N₂ was used to generate the N₂ atmosphere.

3.3.4. Characterization

TEM images were collected using a Hitachi HT7700 TEM operating at 100 kV. TEM samples were prepared by drop casting the nanoparticle solution onto a carbon-coated 300 mesh Cu TEM grid. UV-vis spectra were measured using a Varian Cary 50 Bio UV-vis spectrophotometer with an optical path length of 1 cm.

X-ray absorption measurements were performed at the Hard X-ray Micro Analysis (HXMA) beamline 061D-1 (energy range 5–40 keV; resolution, $1 \times 10^{-4} \Delta E/E$) at the Canadian Light Source (CLS, 2.9 GeV storage ring, 250 mA current). A double-crystal Si monochromator

was used for energy selection of the Ag *K*-edge (25514 eV). All samples were in the form of solid powders and were mixed with boron nitride (to give a 5% w/w Ag loading) and then pelletized before analysis. Measurements were taken in both transmission and fluorescence mode concurrently. The data analysis and EXAFS fitting were performed by using the IFEFFIT software package.^{42, 43} We used Ag (Fm-3m) crystallographic data to fit the Ag-foil spectrum. First, fitting was performed on the Ag-foil spectrum, keeping the coordination number fixed (CN = 12) in order to determine the amplitude reduction factor (S_o^2). From this fitting, the amplitude reduction factor determined for the Ag-foil was 0.973 and was used for the subsequent sample fits.

3.4. Results and Discussion

Ag@SiO₂ nanotriangles were prepared by following previously published procedures.¹⁵ Briefly, the Ag nanotriangles were synthesized by reducing AgNO₃ using NaBH₄ in the presence of trisodium citrate and H₂O₂. Subsequently, these nanotriangles were functionalized with 16-mercaptohexadecanoic acid and then used to prepare the Ag@SiO₂ core@shell nanotriangles using a Stöber sol-gel process. The nanoparticles were then characterized by UV-Vis spectroscopy and transition electron microscopy. Figure 3.1a shows the UV-Vis spectrum of the MHA-functionalized Ag@SiO₂ nanotriangles. The peak at 725 nm, shoulder at 490 nm, and peak at 330 nm can be ascribed to the in-plane dipole, in-plane quadrupole, and the out-of-plane quadrupole plasmon modes, respectively. TEM images were recorded for these samples, and are shown in Figure 3.1b. TEM shows the presence of a ~ 30 nm thick silica shell around the Ag nanotriangles.

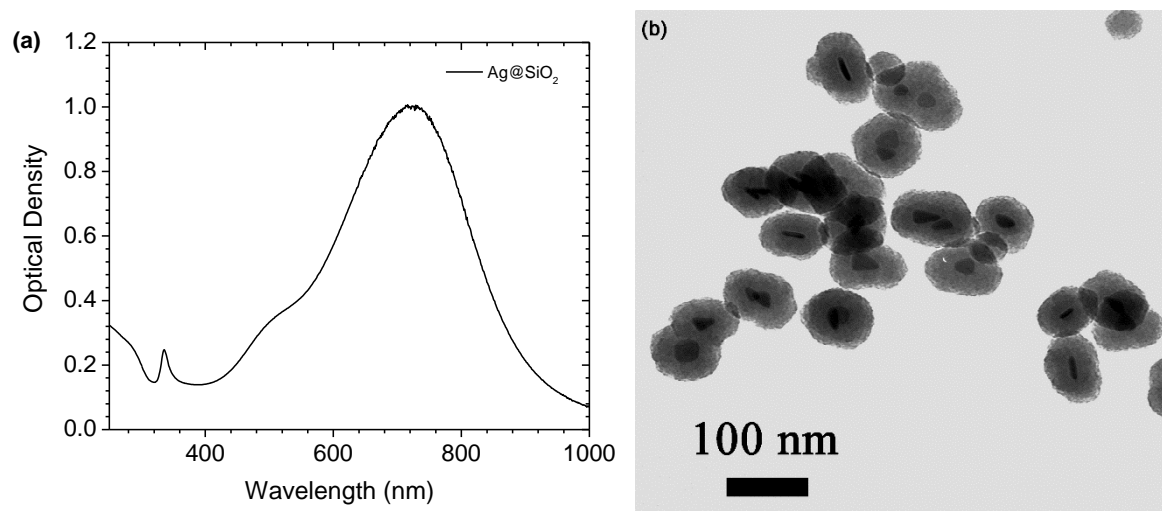


Figure 3.1. (a) UV-Vis spectrum of Au@SiO₂ nanotriangles suspended in EtOH (b) TEM image of as-synthesized triangular Ag@SiO₂ nanoparticles.

3.4.1. Thermal degradation study of Ag@SiO₂ using UV-Vis and TEM

After synthesizing the Ag@SiO₂ nanotriangles, they were subjected to different annealing temperatures in order to understand their thermal stability. The annealing temperatures were varied from 150 to 600 °C, in air or N₂ atmospheres. After annealing, the samples were redispersed in ethanol by sonication, characterized by UV-Vis and TEM, and compared with the samples before annealing. Figure 3.2 shows the normalized UV-Vis spectra of the Ag@SiO₂ samples before and after annealing in air (Figure 3.2a) and N₂ (Figure 3.2b). The plasmon bands of the air annealed Ag@SiO₂ nanotriangles were immediately and dramatically blue-shifted ($\lambda_{\text{LSPR}} \approx 420\text{-}440$ nm) compared to the as-synthesized nanotriangles ($\lambda_{\text{LSPR}} \approx 720$ nm). The magnitude of blue-shift depended on the annealing temperature, with the highest annealing temperature (600 °C) producing the most blue-shifted plasmon band ($\lambda_{\text{LSPR}} \approx 419$ nm). In contrast, the samples annealed in N₂ showed a more modest blue-shift. The peak corresponding to the LSPR in-plane dipole mode blue-shifts from 720 to 660 nm upon annealing at 150 °C, and blue-shifts further upon annealing at higher temperatures (615, 615, and 580 nm after annealing at 300, 450, and 600 °C, respectively).

An additional peak at *ca.* 440 nm also appears in the spectra of all post-annealed samples. In the case of triangular nanoparticles, the gradual blue-shifting of the plasmon peak is attributed to a rounding of the particle tips and the resulting formation of nanodiscs; however, the distinct peak at *ca.* 420-440 nm is typical of spherical Ag nanoparticles.¹ This suggests that the samples annealed in air are rapidly degraded into spherical byproducts, whereas the samples annealed in N₂ undergo a much more gradual morphology change.

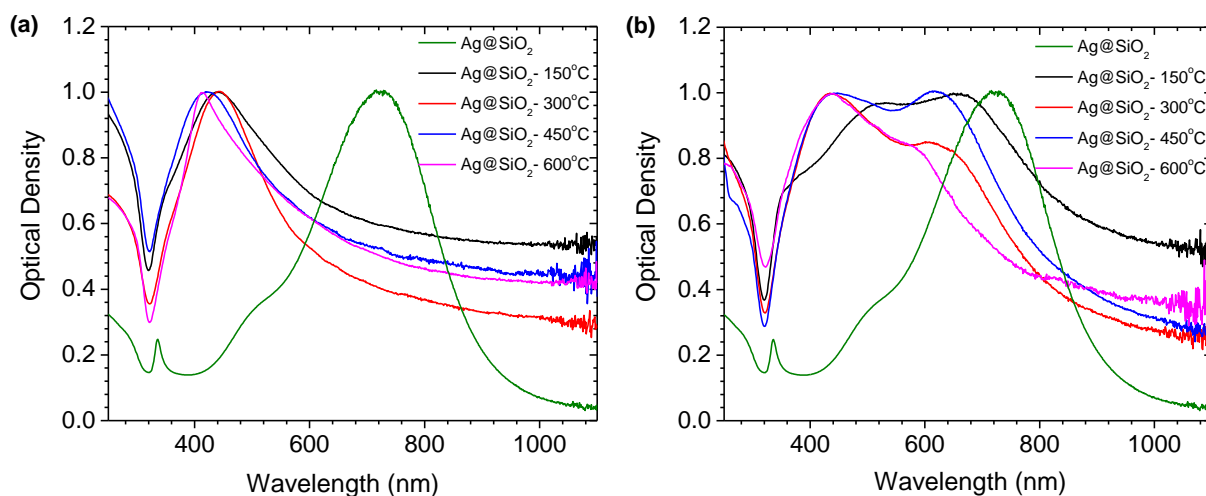


Figure 3.2. Normalized UV-Vis absorption spectra of Ag@SiO₂ nanotriangles after annealing in either an (a) air or (b) N₂ atmosphere.

To better understand these changes in particle morphology, we characterized the samples using TEM. Figure 3.3 shows the TEM images of Ag@SiO₂ nanotriangles after annealing in air (Figure 3.3a-d) and N₂ (Figure 3.3e-h) atmospheres. The nanotriangles that were annealed in air at 150 °C showed the presence of round Ag core particles surrounded by a number of smaller nanoparticles embedded in the silica shell (Figure 3.3a). Upon increasing the annealing temperature to 300 °C the size of the Ag core decreased further, in some cases leaving behind a hollow void in the silica shell. After annealing at either 150 or 300 °C, the Ag core was *ca.* 5 nm in diameter, and was surrounded by a large number of smaller particles (Figure 3.3a and b inset). These larger Ag nanoparticles at the core of the SiO₂ shell are assumed to be the remnants of the

original triangular Ag nanoparticles, while the smaller nanoparticles are formed from the material lost as the sharp tips decompose and fragment. After increasing the annealing temperature to 450 or 600 °C, the Ag cores completely disappear. At these temperatures, the triangular core was completely fragmented into small Ag nanoparticles, leaving behind a hollow silica sphere (Figure 3.3c-d). The size of these fragmented Ag nanoparticles was found to be relatively independent of temperature, with 450 °C ($d = 2.5 \pm 0.4$ nm) and 600 °C ($d = 2.3 \pm 0.4$ nm) producing similar sizes. These results are consistent with the UV-Vis data presented previously; in all cases, only relatively small, spherical nanoparticles are observed, in agreement with the plasmon bands located at 420-440 nm. The larger cores observed in Figure 3.3a and b would be expected to give rise to the plasmon bands at longer wavelengths ($\lambda_{\text{LSPR}} \approx 440$ nm, Figure 3.2a) than the smaller particles observed in Figure 3.3c and d ($\lambda_{\text{LSPR}} \approx 420$ nm, Figure 3.2a).

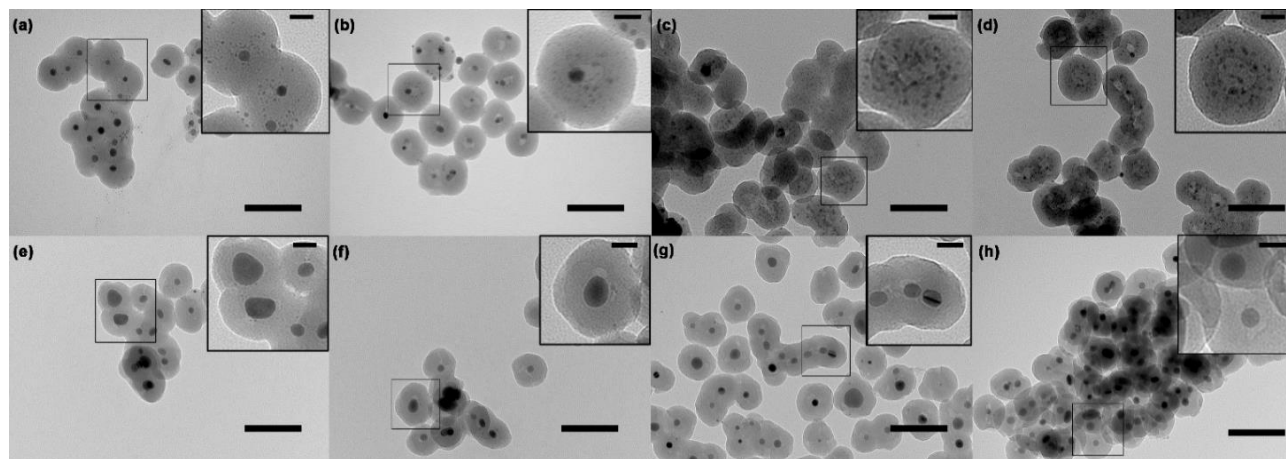


Figure 3.3. TEM images of the Ag@SiO₂ nanotriangles after annealing in either (a-d) air, or (e-h) N₂ atmospheres. The samples were annealed at: (a,e) 150 °C, (b,f) 300 °C, (c,g) 450 °C, and (d,h) 600 °C. The scale bars in the main images are 100 nm, while those in the insets are 20 nm.

The formation of hollow silica spheres has been observed previously by Lei *et al.* for spherical Ag@SiO₂ nanoparticles³⁷ and Kim *et al.*⁴⁴ for FeAuPd@SiO₂ nanoparticles after annealing the nanoparticles in air, which could be due to the metal diffusion from the core. However, in neither of these cases did the central core fragment into smaller particles. In the

present case, we hypothesize the formation of such small Ag nanoparticles could be the result of the size of the pores in SiO₂ around the Ag core. In order to better understand this phenomenon, we synthesized Ag nanotriangles on a SiO₂ support (SiO₂@Ag) and annealed them at 450 °C and 600 °C. Figure 3.4 shows the TEM images of the SiO₂@Ag nanoparticles after annealing. After annealing at 450 °C, spherical Ag nanoparticles were observed (Figure 3.4b) and the size (11.0 ± 3.5 nm) of these nanoparticles was found to be much larger than for those formed upon Ag@SiO₂ annealing (Figure 3.3c, $d \sim 2.5$ nm). Unlike the Ag@SiO₂ samples, for SiO₂@Ag there is no silica shell around the Ag nanotriangles to control the size of the particles formed after annealing. Upon increasing the annealing temperature to 600 °C, the SiO₂@Ag samples yielded smaller (7.5 ± 2.4 nm) nanoparticles (Figure 3.3c). However, in both cases, the Ag nanoparticles are still larger than those resulting from annealing of the Ag@SiO₂ samples. This indicates that, upon annealing the triangular Ag@SiO₂ core@shell nanoparticles, the silica shell restricts the ultimate size of the resulting Ag nanoparticles. All of the samples annealed in a N₂ atmosphere showed the presence of residual Ag cores in the TEM images (Figure 3.3e-h), regardless of annealing temperature. At low temperatures (150 °C), the core particle was only slightly rounded (Figure 3.3e), in keeping with the modest blue-shift observed in the UV-Vis spectrum (Figure 3.2b). The degree of rounding is correlated with the annealing temperature, with the samples annealed at the highest temperatures having the smallest and roundest Ag cores. Again, this agrees with the more pronounced blue-shift of the plasmon bands observed in these samples (Figure 3.2b). Unlike the samples annealed in air, no small particles were seen by TEM, indicating that the O₂ in the air is needed for the formation these small particles.

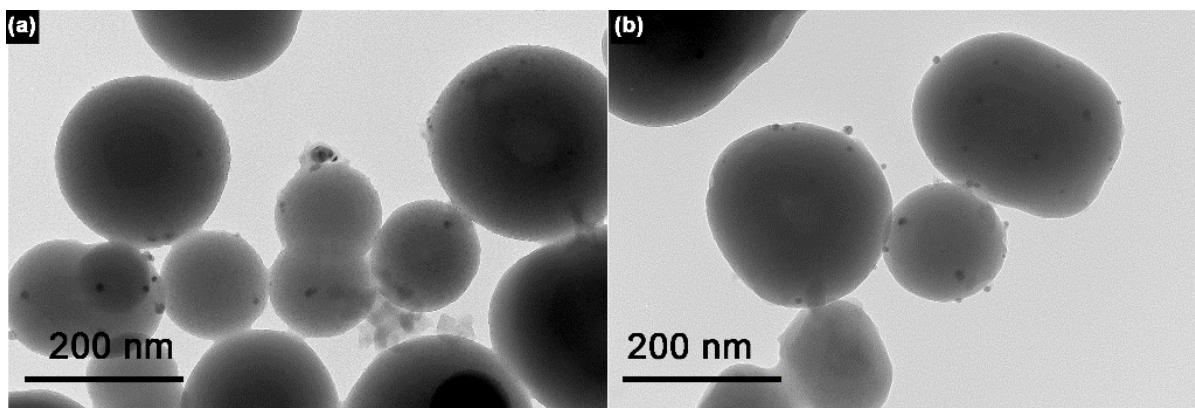


Figure 3.4. TEM images of SiO₂@Ag control samples annealed a) at 450 °C and (b) at 600 °C.

The thermal stability of the silver nanoparticles depends on the particle size and shape. Ag nanotriangles have a high aspect ratio, with (111) planes on the basal facets and either (110) or (100) planes on the edge facets.³⁰ As a result, the edges have a higher surface energy than the basal facets; hence they are less stable to corrosion. The vertices are highly unstable since at vertices the two high energy edge facets intersect. Hence, upon annealing the Ag@SiO₂ nanotriangles, the decomposition process begins with the tips. In the presence of air, we hypothesize that the Ag core interacts with atmospheric oxygen and oxidizes to Ag_xO.^{37, 45, 46} The atoms in the vertices are oxidized first; dissociation of the oxidized material leaves behind the circular nanoparticles observed in the cores of the SiO₂ particles (Figure 3.3a-b). The smaller nanoparticles observed throughout the SiO₂ particle are then presumably composed of the dissociated material that was lost from the particle tips. Upon increasing the annealing temperature, the Ag core further dissociates, leaving behind nothing but the smaller particles (Figure 3.3c-d). In the presence of a N₂ atmosphere, since there is no possibility of Ag oxidation, we noticed a different change in the morphology of the Ag nanotriangles. This could be attributed to the migration of atoms from the tips (highly unstable features) to the more stable basal planes. The resulting morphology after migration is a particle with rounded tips and a similar overall size (Figure 3.3e-f). This process becomes severe at higher annealing temperatures (Figure 3.3g-h), which can lead to a complete

rounding of the edges, and the deposition of a large number of atoms on the basal facets. This results in a pseudo-spherical nanoparticle, consistent with both the TEM images (Figure 3.3g-h) and the LSPR band at *ca.* 420 nm (Figure 3.2b). Such temperature dependent atomic migrations have been previously observed in modeling studies on Ag nanowires.³⁰

3.4.2. Thermal degradation study of Ag@SiO₂ using XANES and EXAFS analysis

Since UV-Vis spectroscopy and TEM provide no information on either the oxidation state or coordination environment of the resulting Ag@SiO₂ nanoparticles, we collected Ag *K*-edge X-ray absorption spectra. XANES spectroscopy is very specific to changes in valency, and EXAFS is specific to the coordination environment of the absorbing metal atoms. The Ag *K*-edge spectra of all the samples were compared with reference spectra of Ag-foil and Ag₂O standards. The XANES spectra of Ag@SiO₂ nanotriangles before and after annealing in air and N₂ are shown in Figure 3.5. Ag has a strong *K*-edge feature at 25514 eV which arises from dipole-allowed 2s to 5p transitions. The near edge features of all samples were similar to those of the reference Ag-foil spectra. However, the samples annealed in air showed a decrease in the intensities of the near-edge peaks compared to the reference Ag-foil spectrum. This decrease in the intensity of these peaks with an increase in annealing temperature is due to a decrease in the size of the Ag nanoparticle (resulting in a lower overall coordination number for the Ag atoms). Such changes were not seen in the case of the Ag@SiO₂ samples annealed in N₂. Regardless of annealing atmosphere and temperature, none of the samples showed spectral features matching those of the Ag₂O reference, which indicates the presence of little-to-no Ag₂O in the annealed samples.

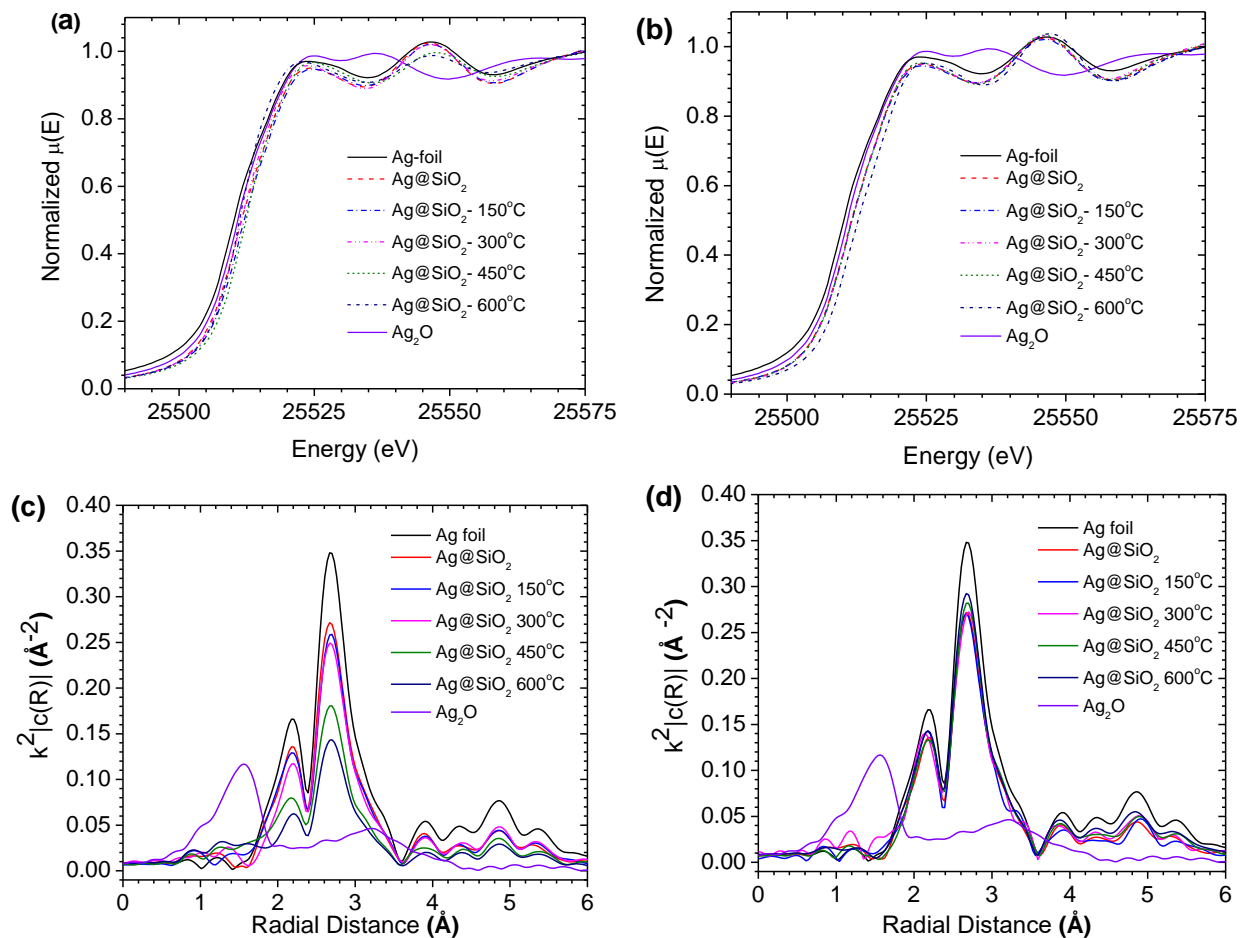


Figure 3.5. Ag *K*-edge (a,b) XANES and (c,d) FT-EXAFS spectra of Ag@SiO₂ nanotriangles annealed in (a,c) air and (b,d) N₂. All spectra were collected at room temperature.

We also performed an EXAFS analysis to study the changes in Ag coordination environment upon annealing the Ag@SiO₂ nanoparticles. The EXAFS region is very sensitive to the bonding environment around the scattering atom. To study this, Ag *K*-edge spectra of all the samples annealed in air and N₂ were plotted as the Fourier-transformed radial distribution function (FT-EXAFS) and the first coordination shell of Ag was fit using a Ag fcc model. Figure 3.5c and 3.3d show the experimental FT-EXAFS spectra of the Ag@SiO₂ samples in R space. All the samples showed peaks at 2.18 \AA and 2.67 \AA , which match well with the reference Ag foil spectra and are due to Ag-Ag first shell contributions. The Ag₂O bulk material standard spectra show a major peak at 1.56 \AA , which is due to the first shell Ag-O contribution. Although the Ag@SiO₂

nanoparticles were annealed in air, none of the spectra have a peak at 1.56 Å, indicating a lack of oxidation in the annealed samples (i.e., they are almost completely Ag(0)). However, the intensity of the peak corresponding to the first shell Ag-Ag contribution decreases as the annealing temperature is increased from 150 °C to 600 °C in air. The intensity of this peak in the FT-EXAFS spectra is directly proportional to the Ag-Ag coordination number (note that the spectra are collected at room temperature after annealing). Hence, for the samples annealed in air, there is a decrease in the average Ag-Ag coordination number with increasing annealing temperature; this is directly correlated with a decrease in the size of the particles, as for smaller particles a higher percentage of Ag atoms are under-coordinated on the particle surface. The samples annealed in N₂ showed much more modest changes in the intensity of the Ag-Ag peak, indicating relatively little change in the overall particle size upon annealing in N₂. This is in agreement with the TEM data, where the samples annealed at higher temperatures in air showed the presence of numerous small nanoparticles inside the silica sphere (Figure 3.3a-d), whereas for the samples annealed in N₂, only larger particles at the core of the SiO₂ shell were observed (Figure 3.3e-h).

To quantify these findings, EXAFS fitting was performed for all the samples using existing Ag crystallographic data (Fm-3m). Only the first shell single scattering path Ag_o-Ag₁ ($R_{\text{eff}} = 2.88$ Å, degeneracy = 12) was used as a model for fitting. The experimental EXAFS plot in R-space, along with the simulated EXAFS fitting of all the samples, is shown in Figure 3.6 and the corresponding fitting parameters are tabulated in Table 3.1. A decrease in the 1st shell Ag-Ag coordination number with an increase in the annealing temperatures was observed for the samples annealed in air. This implies a decrease in the average size of the particles with an increase in annealing temperature, which is in agreement with the observed formation of small Ag nanoparticles ($d \sim 2.5$ nm) and complete loss of the central Ag core at higher annealing

temperatures. Samples calcined at higher temperatures (450°C, 600°C) have low coordination numbers (6.6, 5.2), indicating the presence of very small particles with a large number of surface atoms. In the case of the samples annealed in N₂, only a small increase in the 1st shell Ag-Ag coordination number was observed, which is consistent with the migration of highly under-coordinated atoms from the tips of the triangles to the more stable basal planes, but an overall retention of the particle size. It is known that Ag is prone to oxidation at elevated temperatures; however, from the EXAFS analysis, there was no significant presence of Ag_xO after annealing in air. This indicates that any oxidation products must dissociate back to Ag and O₂. We postulate that upon annealing the Ag@SiO₂ nanotriangles in air, initially the vertices are oxidized to Ag_xO; this detaches from the triangle, leading to a rounding of the particle shape (Figure 3.7).

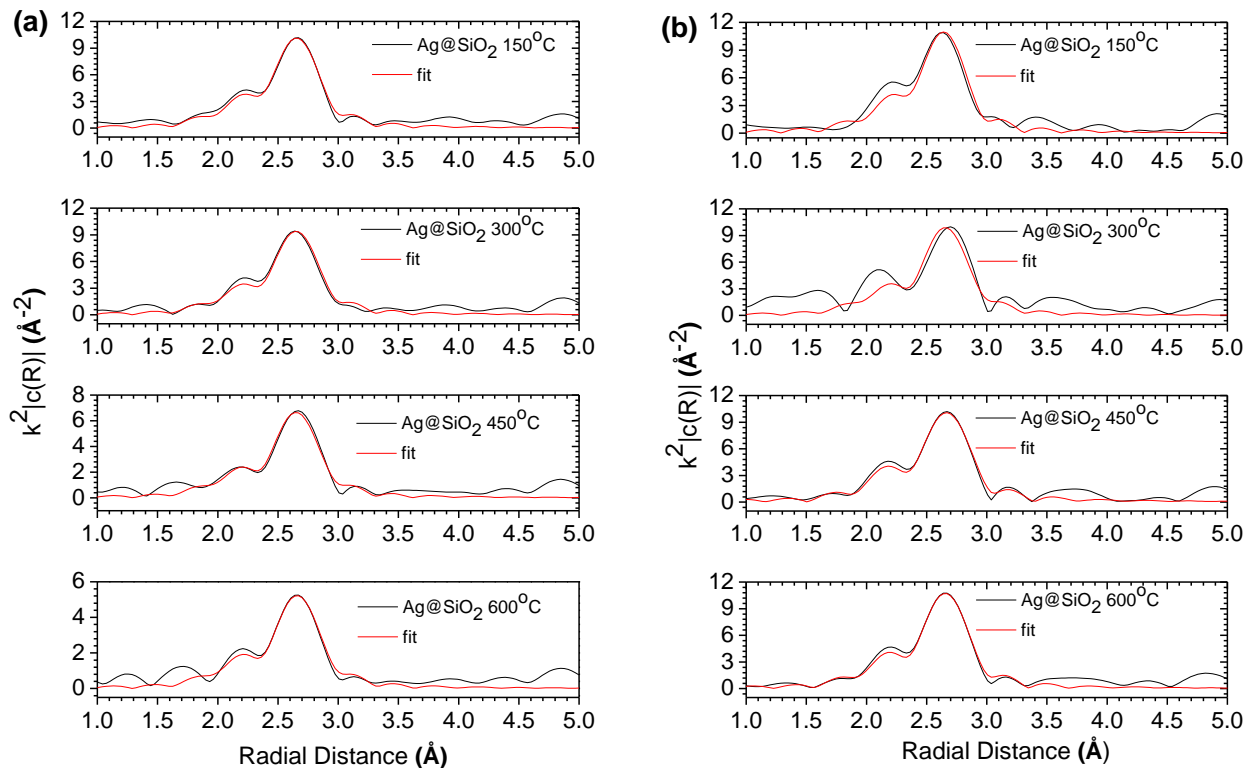


Figure 3.6. EXAFS fitting of Ag@SiO₂ nanotriangles annealed in (a) air and (b) N₂ at different temperatures. All spectra were collected at room temperature after annealing.

The dissociated Ag_xO then decomposes back into small Ag nanoparticles and O₂.^{37, 47} This oxidation and dissociation process depends on both the annealing temperature and atmosphere. By TEM, it can be observed that these small Ag nanoparticles are spread throughout the silica sphere. The silver that is lost from the nanotriangle tips clearly diffuses inside the silica shell (either as Ag_xO or metallic Ag), but due to the thick silica shell, has difficulty reaching the particle surface. In the case of samples annealed in N₂, these small Ag nanoparticles were not seen; in the absence of any oxidation/dissociation process, the observed changes in particle morphology are most likely due to atomic migration from less stable surfaces to more stable basal planes. A simplified mechanism of this thermal decomposition process is shown in Figure 3.7.

Table 3.1. EXAFS fitting parameters of Ag@SiO₂ nanotriangles annealed in air and N₂ at different temperatures, the amplitude factor for the fittings was kept at fixed value of 0.973

Ag@SiO ₂ Annealing Temperature	Air				N ₂			
	CN (Ag-Ag)	R/ Å (Ag-Ag)	σ ² / Å ²	E _o (shift) /eV	CN (Ag-Ag)	R/Å (Ag-Ag)	σ ² /Å ²	E _o (shift) /eV
RT	10.3 (6)	2.855 (4)	0.0102 (6)	2.0 (3)	N/A	N/A	N/A	N/A
150 °C	9.0 (5)	2.860 (4)	0.0102 (5)	1.9 (3)	9.1 (4)	2.853 (6)	0.0098 (6)	1.3 (3)
300 °C	8.8 (5)	2.858 (4)	0.0105 (6)	1.5 (3)	10.2 (6)	2.860 (6)	0.0111 (9)	1.4 (4)
450 °C	6.6 (3)	2.861 (4)	0.0109 (5)	0.8 (3)	10.0 (6)	2.860 (5)	0.0106 (6)	1.5 (3)
600 °C	5.2 (4)	2.863 (6)	0.0108 (8)	1.7 (4)	10.5 (6)	2.861 (4)	0.0106 (6)	0.9 (3)

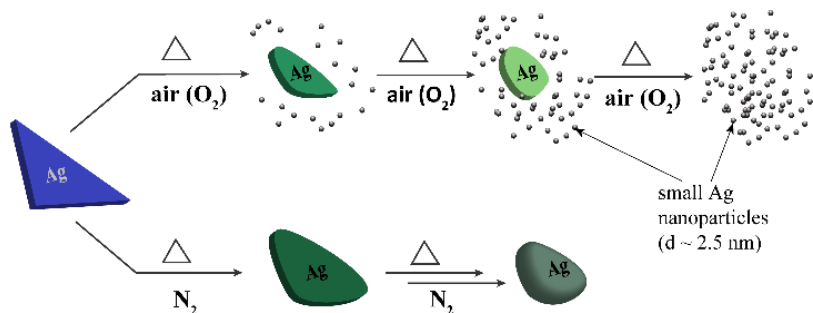


Figure 3.7. Proposed thermal degradation mechanism of Ag nanotriangles in air and N_2 . The silica shell is omitted for clarity.

3.5. Conclusions

Using a combination of UV-Vis spectroscopy, TEM and X-ray absorption spectroscopy, we have established a detailed mechanism for the thermal degradation of $Ag@SiO_2$ nanotriangles. Under all conditions studied, the triangular $Ag@SiO_2$ nanoparticles were found to be unstable, and displayed pronounced morphological changes. In the presence of air and at low annealing temperatures, truncation of the nanotriangles' tips was observed, and led to the formation of small nanoparticles surrounding the remaining Ag core. At higher temperatures the entire Ag core fragmented into these smaller nanoparticles. Our XANES and EXAFS analysis showed that these small particles are $Ag(0)$, and provided further evidence of a decrease in particle size. The samples annealed in N_2 yielded truncated nanotriangles (rounded particles) without the formation of any small nanoparticles. This suggested that the $Ag@SiO_2$ samples annealed in air first oxidize to Ag_xO and subsequently decompose back to $Ag(0)$. Understanding the mechanisms by which these unique nanomaterials degrade is the first step toward developing more stable compounds that could be exploited in a wide variety of plasmonic applications.

3.6. References

1. K. L. Kelly, E. Coronado, L. L. Zhao and G. C. Schatz, *J. Phys. Chem. C*, 2003, **107**, 668-677.
2. C. J. Murphy, T. K. Sau, A. M. Gole, C. J. Orendorff, J. Gao, L. Gou, S. E. Hunyadi and T. Li, *J. Phys. Chem. C*, 2005, **109**, 13857-13870.
3. E. Petryayeva and U. J. Krull, *Anal. Chim. Acta*, 2011, **706**, 8-24.
4. L. Lu, A. Kobayashi, K. Tawa and Y. Ozaki, *Chem. Mater.*, 2006, **18**, 4894-4901.
5. Y. C. Cao, R. Jin and C. A. Mirkin, *Science*, 2002, **297**, 1536-1540.
6. C. Gao, Z. Lu, Y. Liu, Q. Zhang, M. Chi, Q. Cheng and Y. Yin, *Angew. Chem., Int. Ed. Engl.*, 2012, **51**, 5629-5633.
7. E. Martinsson, M. M. Shahjamali, K. Enander, F. Boey, C. Xue, D. Aili and B. Liedberg, *J. Phys. Chem. C*, 2013, **117**, 23148-23154.
8. P. K. Jain, X. Huang, I. H. El-Sayed and M. A. El-Sayed, *Acc. Chem. Res.*, 2008, **41**, 1578-1586.
9. J. Sa, G. Tagliabue, P. Friedli, J. Szlachetko, M. H. Rittmann-Frank, F. G. Santomauro, C. J. Milne and H. Sigg, *Energy Environ. Sci.*, 2013, **6**, 3584-3588.
10. X. Zhou, G. Liu, J. Yu and W. Fan, *J. Mat. Chem.*, 2012, **22**, 21337-21354.
11. M. Murdoch, G. I. N. Waterhouse, M. A. Nadeem, J. B. Metson, M. A. Keane, R. F. Howe, J. Llorca and H. Idriss, *Nat. Chem.*, 2011, **3**, 489-492.
12. Z. Bian, T. Tachikawa, P. Zhang, M. Fujitsuka and T. Majima, *J. Am. Chem. Soc.*, 2013, **136**, 458-465.
13. J. Zhang, Q. Xu, Z. Feng, M. Li and C. Li, *Angew. Chem., Int. Ed. Engl.*, 2008, **47**, 1766-1769.

14. T. Balcha, J. R. Strobl, C. Fowler, P. Dash and R. W. J. Scott, *ACS Catal.*, 2011, **1**, 425-436.
15. M. K. Gangishetty, K. E. Lee, R. W. J. Scott and T. L. Kelly, *ACS Appl. Mater. Interfaces*, 2013, **5**, 11044-11051.
16. M. K. Gangishetty, R. W. J. Scott and T. L. Kelly, *Langmuir*, 2014, **30**, 14352-14359.
17. M. D. Brown, T. Suteewong, R. S. Kumar, V. D'Innocenzo, A. Petrozza, M. M. Lee, U. Wiesner and H. J. Snaith, *Nano Lett.*, 2011, **11**, 438-445.
18. H. A. Atwater and A. Polman, *Nat. Mater.*, 2010, **9**, 205-213.
19. M. A. Green and S. Pillai, *Nat. Photon.*, 2012, **6**, 130-132.
20. J. E. Millstone, G. S. Métraux and C. A. Mirkin, *Adv. Funct. Mater.*, 2006, **16**, 1209-1214.
21. K. Poorkazem, A. V. Hesketh and T. L. Kelly, *J. Phys. Chem. C*, 2014, **118**, 6398-6404.
22. A. P. Kulkarni, K. M. Noone, K. Munechika, S. R. Guyer and D. S. Ginger, *Nano Lett.*, 2010, **10**, 1501-1505.
23. M. M. Shahjamali, M. Salvador, M. Bosman, D. S. Ginger and C. Xue, *J. Phys. Chem. C*, 2014, **118**, 12459-12468.
24. K. E. Lee, A. V. Hesketh and T. L. Kelly, *Phys. Chem. Chem. Phys.*, 2014, **16**, 12407-12414.
25. B. Tang, S. Xu, J. An, B. Zhao, W. Xu and J. R. Lombardi, *Phys. Chem. Chem. Phys.*, 2009, **11**, 10286-10292.
26. L. Liu, C. A. Burnyeat, R. S. Lepsenyi, I. O. Nwabuko and T. L. Kelly, *Chem. Mater.*, 2013, **25**, 4206-4214.
27. Q. Zhang, J. Ge, T. Pham, J. Goebel, Y. Hu, Z. Lu and Y. Yin, *Angew. Chem., Int. Ed. Engl.*, 2009, **48**, 3516-3519.

28. B. Tang, S. Xu, X. Hou, J. Li, L. Sun, W. Xu and X. Wang, *ACS Appl. Mater. Interfaces*, 2013, **5**, 646-653.
29. B. Tang, J. An, X. Zheng, S. Xu, D. Li, J. Zhou, B. Zhao and W. Xu, *J. Phys. Chem. C*, 2008, **112**, 18361-18367.
30. E. Marzbanrad, G. Rivers, P. Peng, B. Zhao and N. Y. Zhou, *Phys. Chem. Chem. Phys.*, 2015, **17**, 315-324.
31. A. Volk, D. Knez, P. Thaler, A. W. Hauser, W. Grogger, F. Hofer and W. E. Ernst, *Phys. Chem. Chem. Phys.*, 2015, **17**, 24570-24575.
32. M. Á. Gracia-Pinilla, E. Pérez-Tijerina, J. A. García, C. Fernández-Navarro, A. Tlahuice-Flores, S. Mejía-Rosales, J. M. Montejano-Carrizales and M. José-Yacamán, *J. Phys. Chem. C*, 2008, **112**, 13492-13498.
33. Y. Yang, Q. Zhang, Z.-W. Fu and D. Qin, *ACS Appl. Mater. Interfaces*, 2014, **6**, 3750-3757.
34. C. Xue, X. Chen, S. J. Hurst and C. A. Mirkin, *Adv. Mater.*, 2007, **19**, 4071-4074.
35. P. Du, Y. Cao, D. Li, Z. Liu, X. Kong and Z. Sun, *RSC Advances*, 2013, **3**, 6016-6021.
36. D. Aherne, D. E. Charles, M. E. Brennan-Fournet, J. M. Kelly and Y. K. Gun'ko, *Langmuir*, 2009, **25**, 10165-10173.
37. Z. W. Lei, M. Liu, W. Ge, Z. P. Fu, K. Reinhardt, R. J. Knize and Y. Lu, *Appl. Phys. Lett.*, 2012, **101**, 083903.
38. Z. L. Wang, *J. Phys. Chem. C*, 2000, **104**, 1153-1175.
39. J. An, B. Tang, X. Zheng, J. Zhou, F. Dong, S. Xu, Y. Wang, B. Zhao and W. Xu, *J. Phys. Chem. C*, 2008, **112**, 15176-15182.
40. S. Chen, Z. Fan and D. L. Carroll, *J. Phys. Chem. C*, 2002, **106**, 10777-10781.

41. Q. Zhang, N. Li, J. Goebel, Z. Lu and Y. Yin, *J. Am. Chem. Soc.*, 2011, **133**, 18931-18939.
42. M. Newville, *J. Synchrotron Rad.*, 2001, **8**, 322-324.
43. B. Ravel and M. Newville, *J. Synchrotron Rad.*, 2005, **12**, 537-541.
44. Y. J. Kim, J. K. Choi, D.-G. Lee, K. Baek, S. H. Oh and I. S. Lee, *ACS Nano*, 2015, **9**, 10719–10728.
45. Q. Hua, A. Dimitri, G. Orest and S. M. Prokes, *Nanotechnology*, 2010, **21**, 215706.
46. M. Erol, Y. Han, S. K. Stanley, C. M. Stafford, H. Du and S. Sukhishvili, *J. Am. Chem. Soc.*, 2009, **131**, 7480-7481.
47. K. Chatterjee, S. Banerjee and D. Chakravorty, *Phys. Rev. B*, 2002, **66**, 085421.

CHAPTER 4

Panchromatic Enhancement of Light Harvesting Efficiency in DSSCs using Thermally Annealed Au@SiO₂ Triangular Nanoprisms

Mahesh K. Gangishetty, Robert W. J. Scott, and Timothy L. Kelly**

Department of Chemistry, University of Saskatchewan, 110 Science Place, Saskatoon, SK, S7N 5C9, Canada

In this work, the thermal stability of Au@SiO₂ nanotriangles and their plasmonic effects in DSSCs are discussed. It was observed that Ag@SiO₂ nanotriangles are not stable towards heating and the electrolyte, so Au@SiO₂ nanotriangles were used here. However, upon annealing a slight change in the morphology of Au was observed. This resulted in various shapes (truncated triangles and spheres) of Au nanoparticles. By integrating these Au nanoparticles in DSSCs, panchromatic light harvesting was achieved.

This chapter is a near-verbatim copy of work published in *Langmuir*, **2014**, 30, 14352. I performed all the experiments in this article. Also, the first draft of the manuscript was written by me and was revised by Prof. Tim Kelly and Prof. Robert Scott prior to publication.

4.1. Abstract

Plasmonic enhancement is an attractive method for improving the efficiency of DSSCs. Plasmonic materials with sharp features, such as triangular metal nanoparticles, show stronger plasmonic effects than their spherical analogues; however, these nanoparticles are also often thermally unstable. In this work, we investigated the thermal stability of Au@SiO₂ triangular nanoprisms by annealing at different temperatures. Morphological changes were observed at temperatures greater than 250 °C, which resulted in a blue shift of the LSPR. Annealing at 450 °C led to a further blue shift; however, this resulted in better overlap of the LSPR with the absorption spectrum of Black Dye. By introducing 0.05% (w/w) Au@SiO₂ nanoprisms into DSSCs, we were able to achieve a panchromatic enhancement of the light harvesting efficiency. This led to a 15% increase in the PCE, from $3.9 \pm 0.6\%$ to $4.4 \pm 0.4\%$.

4.2. Introduction

Noble metal nanoparticles are promising materials for a variety of applications, including photocatalysis,¹ photovoltaics² and biological imaging.³ In these materials, specific frequencies of light can drive a collective oscillation of the conduction electrons. This phenomenon is known as localized surface plasmon resonance, and is responsible for their unique optical and electronic properties.

Plasmonic metal nanoparticles (primarily Ag and Au) have been applied in variety of photovoltaic devices, including silicon-based solar cells,^{4,5} organic photovoltaics,^{6,7} and DSSCs.⁸⁻²⁰ They are able to enhance device light harvesting efficiency via resonant energy transfer from the metal nanoparticle to the nearby light absorber, which can occur in one of two ways.² First, plasmonic nanoparticles display strong resonant scattering at their LSPR wavelength; this

increases the effective optical path length within the device and leads to an increase in light absorption. The second possible mechanism is through an enhancement of the local electric field at the nanoparticle surface (the near-field effect); this increases the transition probability in the light absorber, again resulting in an increase in light absorption. Regardless of the exact mechanism, overlap of the nanoparticle LSPR band and the absorption spectrum of the semiconductor or dye is essential.¹⁷ To achieve this spectral overlap, the position of the LSPR can be tuned by changing the nanoparticle size and shape.²¹

Plasmonic enhancement has been particularly important in improving the LHE of DSSCs, which otherwise require thick TiO₂ photoanodes or light scattering layers to achieve sufficient levels of light absorption.^{15-17, 22} Ag and Au nanoparticles have been employed in DSSCs, and various nanoparticle shapes,^{8, 19, 23} sizes,¹² and structures¹⁷ have also been explored. One key factor in achieving a high enhancement of the LHE has been the use of anisotropic metal nanoparticles; since spherical Ag and Au nanoparticles typically absorb ~ 410 and 530 nm, respectively, they provide no benefit in the red-to-NIR portion of the spectrum. In contrast, anisotropic particles such as Au@TiO₂ polyhedra,¹⁹ Au@Ag₂S nanorods,²³ and TiO₂@Au@TiO₂ core@shell@shell nanostructures¹⁷ extend the range of plasmonic enhancements deeper into the visible region of the spectrum. In this respect, triangular metal nanoprisms are attractive materials; the presence of sharp features amplifies near-field effects, and their LSPR frequency is tunable throughout the visible-to-NIR region.²¹ Triangular Ag@SiO₂ nanoprisms have been used in DSSCs, although their chemical and thermal stability was modest.⁸

This lack of long-term stability is one of the major obstacles to using metal nanoprisms in DSSCs. In particular, silver nanoprisms exhibit poor stability toward oxidation processes.²⁴⁻²⁷ Recently, coating the nanoprism edges with a thin layer of gold improved stability with respect to

chemical etching.^{25, 28} However, the thermal stability of the nanoprisms also needs to be addressed. In DSSCs, as well as in photocatalytic applications, annealing TiO₂ nanoparticles at elevated temperatures (in the range of 450 to 500 °C) is necessary. This annealing is done to improve particle contacts (in the case of DSSCs)^{29, 30} or access the anatase structure (which is catalytically more active than the rutile phase).^{31, 32} Although there are some theoretical studies on the thermal stability of anisotropic gold nanoparticles,^{33, 34} there are only a few experimental reports of the thermal stability of highly anisotropic nanoparticles. Kan *et al.*^{35, 36} investigated the thermal stability of Au micro- and nanoplates and observed the fragmentation of edge facets and tips at temperatures exceeding 450 °C. However, it is not clear how encapsulation by metal oxide shells (e.g., SiO₂, TiO₂) affects the thermal stability of the Au core, and no investigations on the thermal stability of Au@SiO₂ nanoprisms particles have yet been reported.

In the present work, we addressed the thermal stability of triangular Au@SiO₂ nanoprisms, and studied their application in plasmon-enhanced DSSCs. We first synthesized Au@SiO₂ nanoprisms with various silica shell thicknesses and then annealed them in air at different temperatures ranging from 150 to 450 °C. Upon annealing at temperatures ≥ 250 °C, morphological changes were observed that resulted in a blue-shift of the LSPR band. However, the blue-shift was found to be advantageous in attaining the broad spectral overlap with the absorption spectrum of Black Dye. This in turn produced a panchromatic enhancement of the LHE from 400 to 800 nm, resulting in a 15% increase of the overall PCE.

4.3. Experimental Section

4.3.1. Materials

Hydrogen tetrachloroaurate(III) (HAuCl_4 , 99%), trisodium citrate (TSC, 99%), 16-mercaptohexadecanoic acid (90%), tetraethoxysilane (99%), titanium tetraisopropoxide ($\geq 97\%$), and deoxycholic acid were purchased from Sigma-Aldrich. Sodium thiosulfate ($\text{Na}_2\text{S}_2\text{O}_3 \cdot 2 \text{H}_2\text{O}$, 97%) was purchased from Fisher Scientific. Black Dye (N749) was purchased from Solaronix. All chemicals were used directly without any further purification, and aqueous solutions were prepared in Milli-Q water ($18.2 \text{ M}\Omega \cdot \text{cm}$).

4.3.2. Synthesis of triangular Au and Au@SiO₂ nanoparticles

Triangular gold nanoparticles were synthesized by following a literature procedure.³⁷ Briefly, aqueous HAuCl_4 (100 mL, 2 mM) was mixed with a freshly prepared aqueous $\text{Na}_2\text{S}_2\text{O}_3 \cdot 2 \text{H}_2\text{O}$ (120 mL, 0.5 mM) solution. After stirring the mixture for 9 min an additional amount of an aqueous $\text{Na}_2\text{S}_2\text{O}_3 \cdot 2 \text{H}_2\text{O}$ (50 mL, 0.5 mM) solution was added, followed by continued stirring for 1.5 h. The solution turned a deep purple color, after which the particles were isolated by centrifugation at 4000 rpm ($2218 \times g$'s) for 40 min.

The gold nanoparticles were then re-dispersed in 5 mM aqueous TSC solution, and functionalized with 16-mercaptohexadecanoic acid by adding an ethanolic MHA solution (1.25 mL, 18 mg/mL). The reaction mixture was stirred for 15 min, and then the nanoparticles were isolated by centrifugation at 4000 rpm ($2218 \times g$) for 40 min. The MHA functionalized nanoparticles were then re-dispersed in various concentrations of ethanolic TEOS solution (25 mL) and stirred overnight in the presence 0.6 M *N,N*-dimethylamine.

4.3.3. Thermal annealing studies

The Au@SiO₂ nanoparticles were annealed at various temperatures (150, 250, 350 and 450 °C) in air using a Lindberg/Blue M furnace. Samples were heated at a rate of 10 °C/min and the dwell time was 15 min.

4.3.4. Fabrication of DSSCs

DSSCs were fabricated according to literature procedures.^{8, 30} FTO (TEC 8, Hartford Glass Co., 8-10 Ω/sq) was used as a substrate for both working and counter electrodes. To prepare the working electrode, a compact TiO₂ layer was coated on FTO by pre-treatment with aqueous TiCl₄ solution (40 mM, 70 °C) for 30 min. A thin film of TiO₂ paste, which was synthesized by the hydrothermal method,³⁰ was doctor bladed onto the TiCl₄ pre-treated FTO. The TiO₂ film was sintered at 450 °C in air for 30 min and the film thickness was measured using a KLA Tencor D-120 Stylus profilometer, which was calibrated using a 4.474 μm reference sample (VLSI Standard Incorporated, KTS-4.5 QS). The film was then post-treated with aqueous TiCl₄ (40 mM, 70 °C) for 15 min and annealed again at 450 °C in air for 30 min. After cooling to 80 °C, the film was immersed for 48 h in an ethanolic solution of 0.2 mM Black Dye (N749, Solaronix) and 20 mM DCA. The counter electrode was made by drop casting a H₂PtCl₆ solution (50 mM in *iso*-propanol) on FTO, followed by annealing at 380 °C for 30 min. The working and counter electrodes were then fused together using a Surlyn gasket (Meltonix 1170-25, Solaronix). The I⁻/I₃⁻ electrolyte (Iodolyte AN-50, Solaronix) was injected into the device through pre-drilled holes in the counter electrode.

4.3.5. Characterization

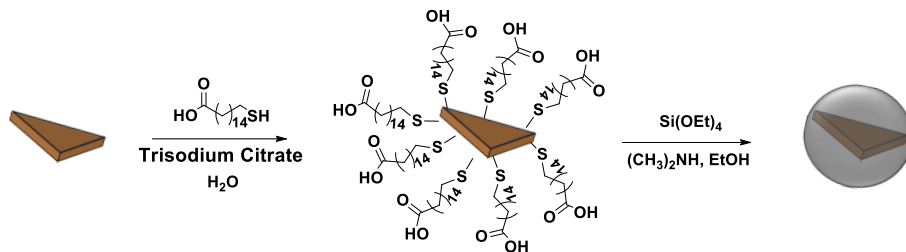
UV/Vis/NIR spectra were measured using a Varian Cary 6000i UV-Visible spectrophotometer. TEM was carried out on a Philips CM10 microscope operating at 100 kV. TEM samples were prepared by drop casting the ethanolic solution of nanoparticle on a carbon-coated 300 mesh Cu grid.

J-V curves were measured using a Keithley 2400 source-measure unit. A 450 W solar simulator (Sol3A, Oriel Instruments) was used to produce Air Mass 1.5 global simulated sunlight ($100 \text{ mW}\cdot\text{cm}^{-2}$). The incident light was calibrated to one sun intensity using a silicon reference cell (91150V, Oriel Instruments). The device active area was defined as 0.196 cm^2 using a black anodized aluminum aperture mask. IPCE spectra were recorded using a QE-PV-SI system (Oriel Instruments) in DC mode. The system was equipped with a 300 W xenon arc lamp, filter wheel, and monochromator. The IPCE spectra were calibrated to a silicon reference photodiode (71674, Oriel Instruments).

4.4. Results and Discussion

Gold nanoprisms were synthesized by reducing hydrogen tetrachloroaurate(III) with freshly prepared sodium thiosulfate.³⁷ This synthetic procedure reproducibly yielded significant (~20%) population of spherical and triangular Au nanoparticles, both of which can be observed in the TEM image (Figure 4.1a). The average diameter of the spherical nanoparticles was found to be $22 \pm 4 \text{ nm}$ and the triangular nanoparticles showed a broad particle size distribution. Figure 4.1b represents the particles size distribution of triangular nanoparticles, which shows the large population of triangular nanoparticles has an edge length of 50 to 70 nm. The UV-Vis spectrum of the as-synthesized Au nanoparticles (Figure 4.2), shows two peaks at 534 and 852 nm. The peak

at 534 nm is assigned to the spherical Au nanoparticles, and the peak at 852 nm corresponds to the in-plane dipole mode of the triangular nanoprisms.³⁸ To grow the silica shell, the nanoparticles were functionalized with MHA, which acts a linker between the Au nanoparticles and the silica shell. Au@SiO₂ nanoparticles were then synthesized by following a modified Stober process (Scheme 4.1).



Scheme 4.1. Synthesis of Au@SiO₂ nanoprisms.

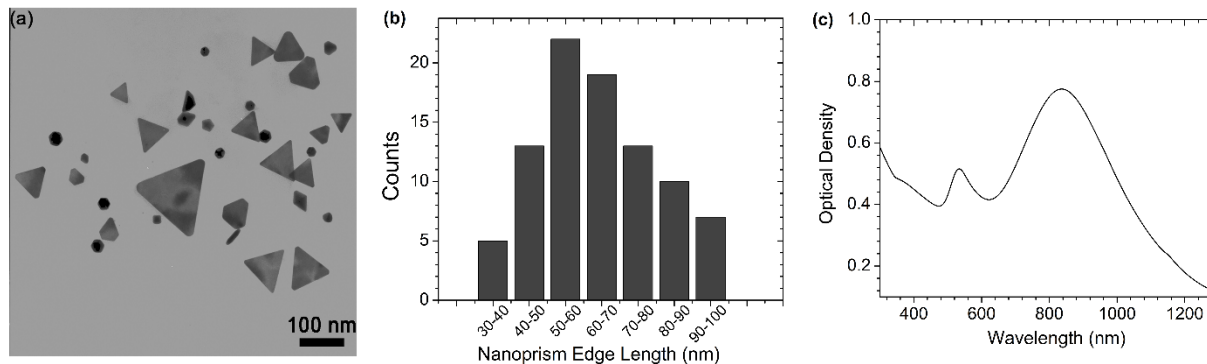


Figure 4.1. (a) TEM image, (b) size distribution, and (c) UV-Vis spectrum of the as-synthesized Au nanoprisms.

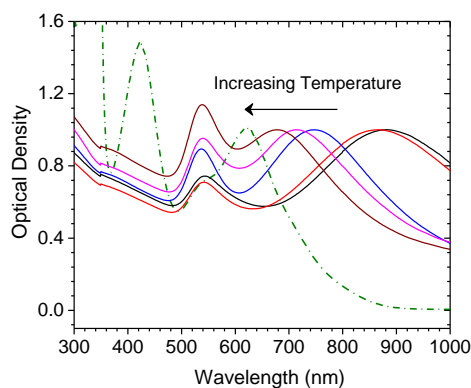


Figure 4.2. Normalized UV-Vis spectra of Au@SiO₂ nanoparticles after annealing at indicated temperatures. As-prepared (black), 150 °C (red), 250 °C (blue), 350 °C (pink), 450 °C (purple) and the absorption spectrum of Black Dye (dashed green).

In this synthesis, the thickness of the silica shell was tuned by changing the concentration of TEOS in the reaction mixture. Au@SiO₂ nanoparticles with shell thicknesses ranging from 8 ± 1 nm to 29 ± 3 nm were synthesized (Figure 4.3). In all cases, an increase in the ratio of spherical nanoparticles to triangular nanoprisms was observed. As a result, the intensity of the peak at 534 nm increased relative to that at 852 nm. At very low concentrations of TEOS (0.46 mM), incomplete, non-uniform silica shell growth was observed on the triangular nanoprisms, although the spherical nanoparticles displayed more complete shell growth (Figure 4.3a). Complete silica shell formation was achieved only at TEOS concentrations above 0.92 mM (Figure 4.3b-f). Further increases in the TEOS concentration led to a corresponding increase in the silica shell thickness. The SiO₂ shell formation is also reflected in the UV-Vis spectra (Figure 4.4). As the TEOS concentration is increased, there is a progressive red-shift in the position of the peak at 854 nm (corresponding to the triangular nanoprisms). This red-shift is attributed to an increase in the dielectric environment as the thickness of the silica shell is increased.⁸ In contrast, only a very slight red-shift was observed for the LSPR peak at 534 nm. The local field generated by the triangular nanoprisms is highly concentrated at the tips of the triangle, whereas spherical nanoparticles show relatively weak near-field effects.³⁹ As a result, the field generated by the triangular nanoprisms is very sensitive to the small changes in the surrounding dielectric medium, as compared to that of the spherical nanoparticles. After reaching a silica shell thickness of 23 ± 3 nm, the rate of change in the LSPR peak position was reduced (Figure 4.4b). At this thickness much of the near-field is already enclosed by the SiO₂ shell, and does not extend into the surrounding medium. After reaching a thickness of 29 ± 3 nm, the local field generated by the Au nanoprisms is almost entirely located within the silica shell, and the influence of the external dielectric environment on the LSPR is greatly attenuated.

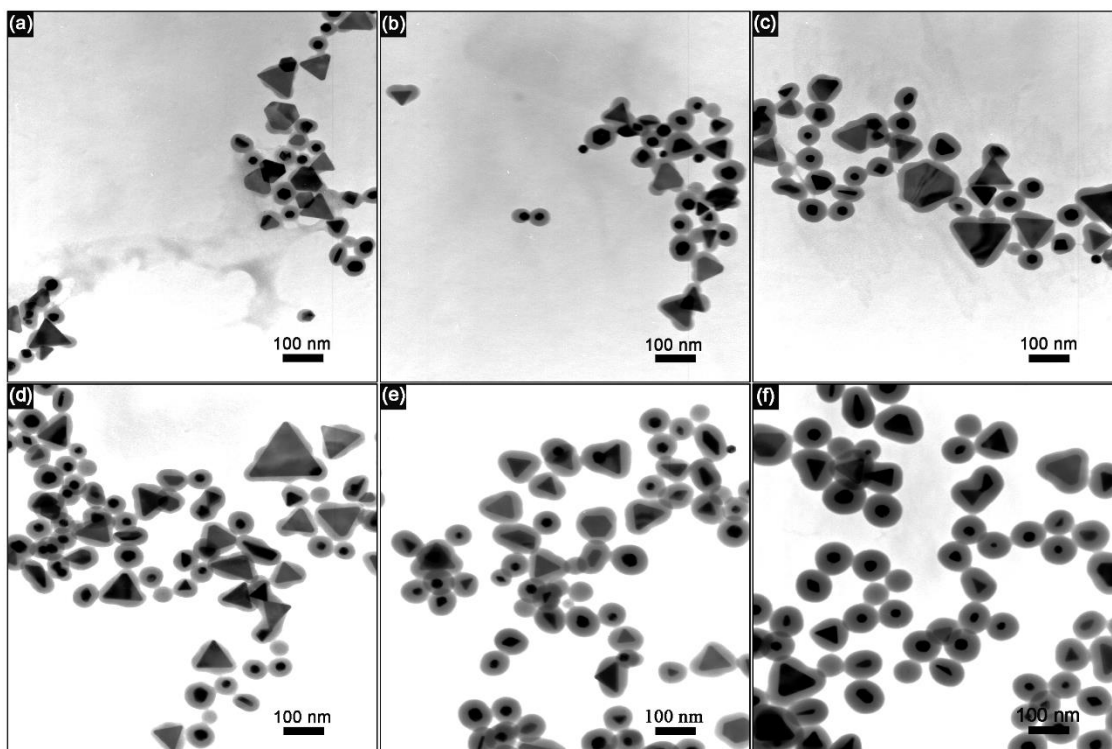


Figure 4.3. TEM images of Au@SiO₂ nanoparticles synthesized using different concentrations of TEOS: (a) 0.46 mM, (b) 0.92mM, (c) 1.38 mM, (d) 1.84mM, (e) 2.76 mM, and (f) 4.6 mM.

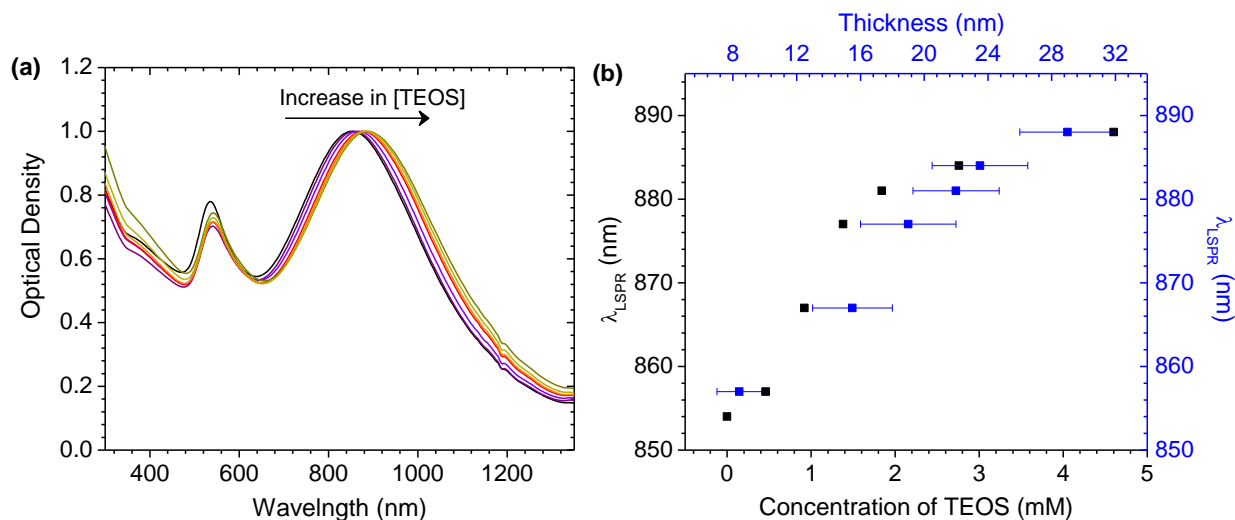


Figure 4.4. (a) Normalized UV-Vis spectra of Au nanoparticles functionalized with 16-mercaptohexadecanoic acid (black line), and Au@SiO₂ nanoparticles synthesized using different concentrations of TEOS: 0.46 mM, 0.92 mM, 1.38 mM, 1.84 mM, 2.76 mM and 4.6 mM. The spectra normalized to the maximum optical density (b) LSPR peak position (λ_{LSPR}) as a function of both TEOS concentration and SiO₂ shell thickness.

4.4.1. Thermal degradation of Au@SiO₂ nanoparticles

Before we introduced the Au@SiO₂ nanoparticles into DSSCs, their thermal stability at different temperatures was studied. Au@SiO₂ nanoparticles with a 23 ± 3 nm thick silica shell were employed in both the thermal stability studies and DSSC fabrication. Because the silica shell does not completely enclose the nanoparticle near-field, these nanoparticles are expected to show two plasmonic effects, near-field enhancements, and resonant scattering. In addition, the 23 ± 3 nm thick silica shell is sufficient to protect the metal nanoparticles from the corrosive action of the iodide electrolyte.⁴⁰ The as-synthesized Au@SiO₂ nanoparticles were isolated by centrifugation and dried overnight. They were annealed at temperatures of 150, 250, 350 and 450 °C in air for 15 minutes. The annealed nanoparticles were re-dispersed in ethanol, and characterized by TEM and UV-Vis spectroscopy. Figure 4.5 shows the UV-Vis spectra of the Au@SiO₂ nanoparticles before and after annealing. The LSPR peak at 880 nm corresponds to the in-plane dipole mode of the triangular nanoprisms, was blue-shifted as the annealing temperature was increased. The blue-shift was modest at 150 °C, but was very pronounced (~ 150 nm shift) for temperatures ≥ 250 °C.

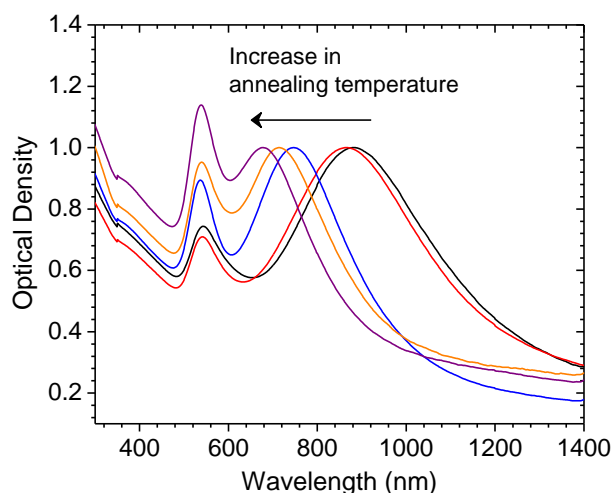


Figure 4.5. Normalized UV-Vis spectra of Au@SiO₂ nanoparticles after annealing at different temperatures, as-prepared (black line), 150 °C (red line), 250 °C (blue line), 350 °C (orange line), 450 °C (purple line). The spectra were normalized to the in-plane dipole plasmon peak (second peak of each spectrum).

The position of the LSPR depends on the morphology of the plasmonic nanoparticles. In general, the nanoprism edges are enclosed by high surface energy facets ((110) and (100) planes),⁴¹ and thus show the least stability.³³ Upon annealing at high temperatures, truncation of the nanoprism vertices can occur and this leads to the formation of disc-like nanoparticles.⁸ This structured evolution is responsible for the blue-shift of the LSPR peak at 880 nm. The formation of rounded or truncated nanoprisms was observed in the TEM images (Figure 4.6). At lower annealing temperatures (i.e., 150 °C), a significant (~60%) population of triangular nanoprisms was observed (Figure 4.6a), whereas the truncation of nanoprisms was observed at temperatures of 250 °C and above. This truncation became more pronounced at higher temperatures, resulting in a larger blue-shift. After annealing at 450 °C, the temperature required to sinter TiO₂ photoanodes in DSSCs, a large population of disc-like or spherical nanoparticles was observed in addition to the remaining triangular nanoprisms (Figure 4.6d). This is consistent with the large blue-shift observed in this sample. However, the intensity of the peak at 532 nm increased with annealing temperature. This is due to the formation of a larger population of spherical nanoparticles from the truncated portions of the triangular nanoprisms. This increase in the relative population of the spherical nanoparticles was also observed by TEM (Figure 4.6). In the case of the spherical nanoparticles no such morphological changes were observed due to the absence of such high energy facets (sharp tips). As such, the position of the LSPR band (532 nm) was unchanged upon annealing (Figure 4.5). From these studies, it is clear that the Au nanoparticles can survive annealing at 450 °C. The silica shell plays a key role in preventing nanoparticle aggregation and coalescence that might otherwise be expected to occur at these elevated temperatures.

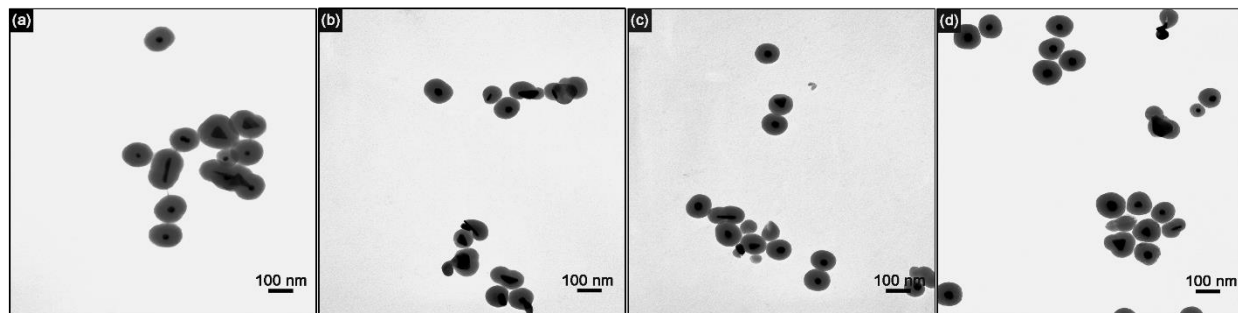


Figure 4.6. TEM images of Au@SiO₂ nanoparticles after annealing at different temperatures in air, (a) 150 °C, (b) 250 °C, (c) 350 °C, (d) 450 °C.

4.4.2. Overlap between the UV-Vis spectra of the dye and the Au@SiO₂ nanoparticles

Owing to its low energy absorption onset, we chose the commonly-used Black Dye (N749) to fabricate DSSCs.⁴² Since the plasmonic nanoparticles cannot generate photocurrent on their own, there must be spectral overlap between the LSPR band and the dye absorption spectrum in order to produce plasmonic enhancement. By tuning the LSPR wavelength into the region of dye absorption, more efficient energy transfer from the nanoparticle to the dye can be achieved, resulting in an increased LHE. Given the morphological changes observed in the Au@SiO₂ nanoparticles upon thermal annealing, we first evaluated the degree of spectral overlap between the nanoparticles and the absorption spectrum of Black Dye as a function of annealing temperature.

Figure 4.2 shows the absorption spectra of both Black Dye and the Au@SiO₂ nanoparticles annealed at various temperatures. The absorption spectrum of the dye shows two strong peaks at 420 and 650 nm, with relatively weak absorption from 750 nm onwards. In comparison, the as-synthesized Au@SiO₂ nanoparticles have substantially red-shifted spectra, with two pronounced peaks at 532 and 880 nm. After annealing, the in-plane dipole mode at 880 nm was blue-shifted into the region of dye absorption. This shift became more pronounced with higher annealing temperatures, increasing the overlap with the Black Dye absorption spectrum. After annealing at

450 °C, the nanoparticles showed excellent overlap with the absorption spectrum of the dye. The shorter wavelength regions of the dye spectrum were effectively covered by the LSPR of the spherical nanoparticles, while the longer wavelengths were in turn covered by the annealed nanoprisms. The mixture of nanoparticles provided better spectral coverage than could be achieved through the use of either spherical nanoparticles or triangular nanoprisms alone. In order to better quantify these effects, we calculated the overlap integral by integrating the product of the dye and Au@SiO₂ absorption spectra from 200 to 1000 nm (Figure 4.7). The intensity of the product spectra increases with increasing annealing temperature, reflecting the blue-shift of the in-plane dipole LSPR band. This indicates that the overlap between the LSPR of the nanoparticles and absorption spectrum of dye is improving as the morphology of the nanoparticles changes. The particles annealed at 450 °C showed the most effective overlap with the dye absorption spectrum, suggesting that annealing nanoparticles at 450 °C is advantageous to their application in plasmon-enhanced DSSCs. The overlap integral increased with annealing temperature, as shown in Figure 4.7b.

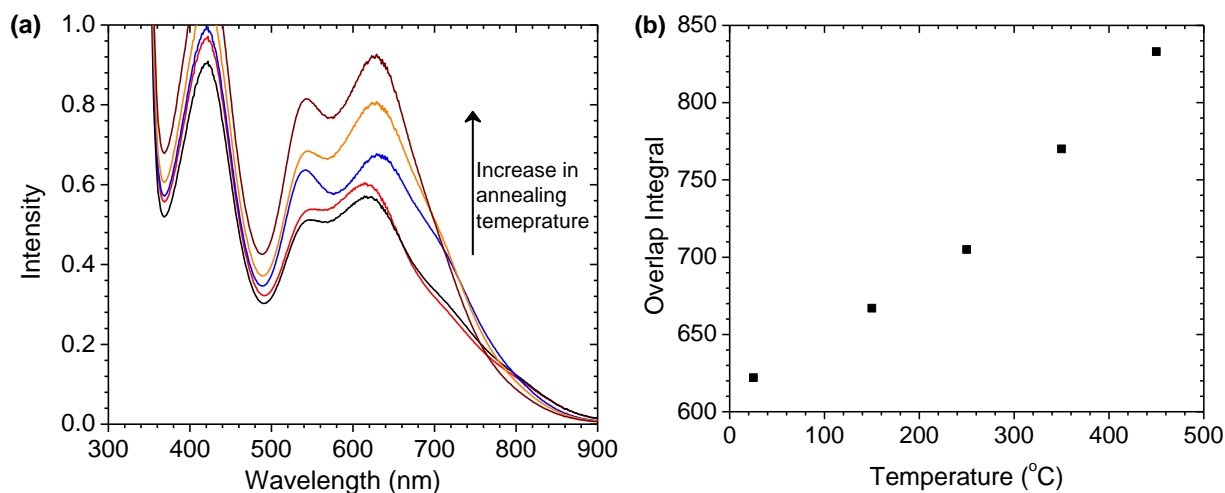


Figure 4.7. (a) Product of the dye absorption spectrum and the LSPR bands of the Au@SiO₂ nanoparticles: as-synthesized (black line), and after annealing at 150 °C (red line), 250 °C (blue line), 350 °C (orange line), and 450 °C (purple line). (b) Overlap integral (area under the curve in (a)) as a function of annealing temperature.

4.4.3. Device characteristics

DSSCs were fabricated according to published procedures.⁸ TiO₂ nanoparticles were synthesized using a hydrothermal sol-gel process, and used to make a TiO₂ paste. Plasmonic devices were made by blending various amounts (0.009% and 0.05% w/w) of Au@SiO₂ nanoparticles with the TiO₂ paste. For comparison, control devices were also prepared using a pure TiO₂ paste without any Au@SiO₂ nanoparticles. The TiO₂ paste was doctor bladed onto FTO to achieve 4-5 μm thick active layers. Control and plasmonic devices were fabricated, and the average device characteristics are tabulated in Table 4.1. The average PCE of the control devices was 3.9 ± 0.6%, whereas the device with 0.009% (w/w) Au@SiO₂ loading showed an average PCE of 4.5 ± 0.6%. The plasmonic devices with a 0.05% (w/w) Au@SiO₂ loading had an average PCE of 4.4 ± 0.4%. A 15% increase in PCE was achieved by introducing Au@SiO₂ nanoparticles into the DSSC. Compared to previous reports of plasmonic enhancement using spherical gold nanoparticles, the Au@SiO₂ loading used here is substantially lower while still achieving a substantial increase in efficiency.^{13, 17, 19} In order to statistically validate these results, we carried out a series of pairwise *t*-tests between the efficiencies of the controls and the plasmon-enhanced devices, and the results are tabulated in Table 4.2. The *p* value is < 0.05 for each set of plasmonic devices when compared to the controls, indicating with > 95% confidence that there is a significant difference between the PCE of the control and plasmon-enhanced cells. Similar *t*-tests showed no significant difference between the thickness of the various sets of devices (95% confidence), indicating any increase in PCE did not arise from an increase in photoanode thickness (Table 4.3).

Table 4.1. Average V_{oc} , J_{sc} , FF, and PCE, along with their standard deviations, for DSSCs with different Au@SiO₂ loadings.

Au@SiO ₂ (% w/w)	V_{oc} (V)	J_{sc} (mA/cm ²)	FF (%)	PCE (%)	Number of devices
0.0	0.60 ± 0.02	9 ± 1	71 ± 1	3.9 ± 0.6	34
0.009	0.61 ± 0.02	10 ± 2	71 ± 2	4.5 ± 0.6	9
0.05	0.62 ± 0.03	10.3 ± 0.8	71 ± 1	4.4 ± 0.4	14

Table 4.2. t-test for PCE (pairwise, two-tailed, assuming unequal variances).

	0 % (w/w)	0.009% (w/w)	0% (w/w)	0.05% (w/w)
Mean	3.9	4.5	3.9	4.4
Variance	0.4	0.3	0.4	0.1
Observations	34	9	34	14
Hypothesized Mean Difference	0		0	
df	13		41	
t Stat	-2.60		-3.57	
P(T<=t) one-tail	0.011		0.00046	
t Critical one-tail	1.77		1.68	
P(T<=t) two-tail	0.022		0.00093	
t Critical two-tail	2.16		2.02	

The average device performance parameters are tabulated in Table 4.1. There is no significant change in either V_{oc} or fill factor upon addition of the Au@SiO₂ nanoparticles to the DSSCs; however, there was a substantial increase in the J_{sc} of the plasmonic devices compared to

the controls. The control devices had an average J_{sc} of 9 ± 1 mA/cm², whereas the plasmonic devices had average J_{sc} values of 10 ± 2 mA/cm² and 10.3 ± 0.8 mA/cm² for the 0.009% and 0.05% loadings, respectively. This enhancement in J_{sc} is the driving force behind the observed increase in PCE, since the changes in FF and V_{oc} for the plasmonic devices were negligible

Table 4.3. t-test for active layer thickness (pairwise, two-tailed, assuming unequal variances).

	0 % (w/w)	0.009% (w/w)	0% (w/w)	0.05% (w/w)
Mean	4.56	4.78	4.56	4.91
Variance	0.13	0.14	0.13	0.39
Observations	34	9	34	14
Hypothesized Mean Difference	0		0	
df	13		17	
t Stat	-1.69		-1.98	
P(T<=t) one-tail	0.058		0.032	
t Critical one-tail	1.77		1.74	
P(T<=t) two-tail	0.16		0.064	
t Critical two-tail	2.16		2.11	

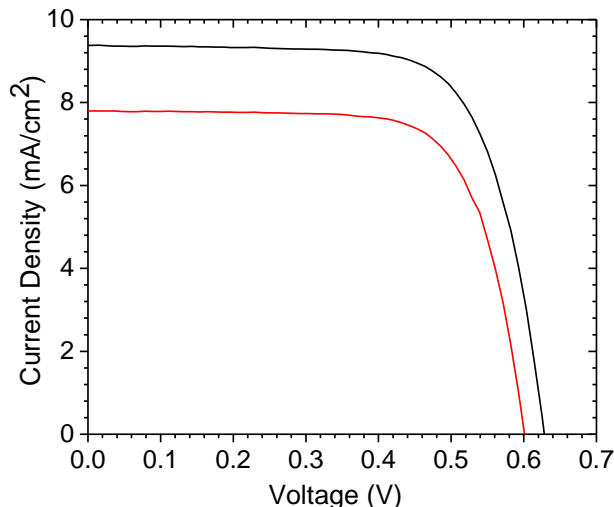


Figure 4.8. *J-V* curves of control (red line) and plasmon-enhanced (black line, 0.05% (w/w) Au@SiO₂) devices. In both cases, the active layer thickness was measured to be 4 μm. Here, the layer thickness was measured by profilometry.

Representative *J-V* curves for both control, and plasmon-enhanced (0.05 wt% Au@SiO₂) devices are shown in Figure 4.8. Both devices had a 4 μm thick active layer. The control device showed a V_{oc} of 0.60 V, a fill factor of 72%, and a J_{sc} of 7.8 mA/cm², producing a 3.4% PCE, whereas the device with a 0.05% (w/w) Au@SiO₂ nanoparticle loading showed a slight increase in V_{oc} to 0.63 V, a slight change in FF to 71% and a substantial increase in the J_{sc} to 9.4 mA/cm², leading to a PCE of 4.2%. To substantiate this increase in J_{sc} , the IPCE spectrum was measured for both devices (Figure 4.9a). Since the current density is the integral product of the photon flux and the IPCE, the increase in J_{sc} should also be reflected in the IPCE spectrum. As expected for DSSCs based on Black Dye, the IPCE spectra cover the entire visible spectrum (from 300 to 850 nm), with two sharp peaks at 350 and 420 nm, and a broad peak at 580 nm. Notably, the plasmonic device showed a higher IPCE over the broad range of 420 to 880 nm, as compared to the control. This broad panchromatic enhancement of the IPCE is due to the mixture of spherical and triangular Au@SiO₂ nanoparticles in the plasmonic DSSC. At longer wavelengths (~ 700 nm), the annealed nanoprisms are responsible for the observed increase in IPCE, while at shorter wavelengths (~ 500

nm) the spherical nanoparticles give rise to a similar enhancement. At ~ 600 nm, the differences in the IPCE spectra were the most pronounced, the IPCE of the plasmonic device was 32%, as opposed to only 28% for the control. This 4% increase was observed over the range of 490 to 660 nm, where there is maximum spectral overlap between the LSPR band and the Black Dye absorption spectrum (Figure 4.7a). Although the IPCE enhancement was extended to wavelengths above 800 nm, since the dye has a low extinction coefficient at these wavelengths, the absolute increase in IPCE was correspondingly reduced. At very short wavelengths (< 400 nm), a reduced IPCE was noticed for the plasmonic devices as compared to the controls. At these wavelengths, the dye absorption is off-resonance with LSPR of nanoparticles, and as a result there is negligible energy transfer from the nanoparticles to the dye. As a result, the Au@SiO₂ nanoparticles act as an insulator and hinder charge transport within the TiO₂ layer.⁸

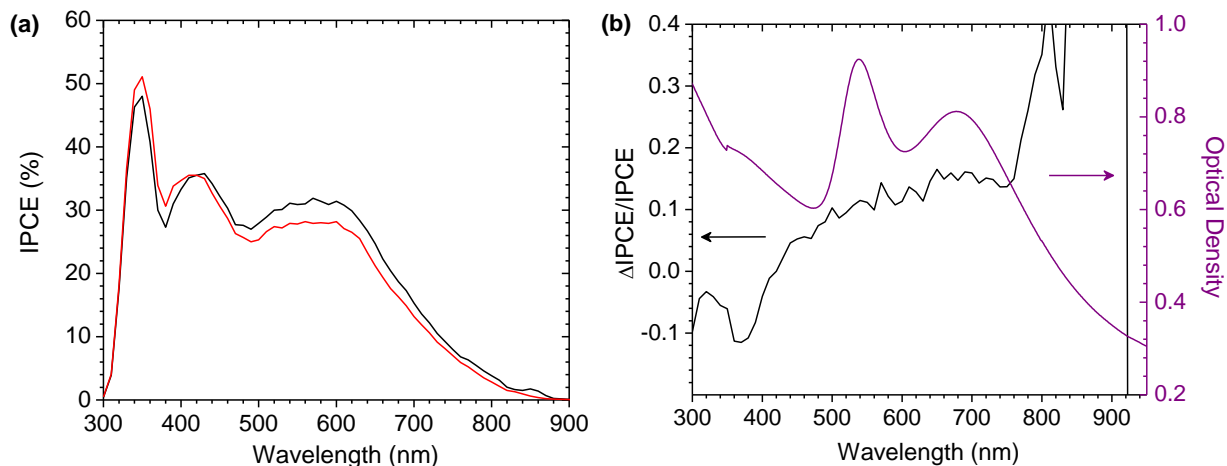


Figure 4.9. (a) IPCE spectra of control (red line) and plasmon-enhanced (black line, 0.05% (w/w) Au@SiO₂) devices. In both cases, the active layer thickness was measured to be 4 μ m. (b) Relative IPCE enhancement ($(IPCE_{Au@SiO_2} - IPCE_{control}) / IPCE_{control}$) spectrum (black line) for the data shown in (a) and the absorption spectrum of the Au@SiO₂ nanoparticles annealed at 450 °C (purple line).

To provide further evidence of the role of the Au@SiO₂ nanoparticles in any plasmonic enhancement, the relative increase in IPCE ($\Delta IPCE / IPCE_{control}$) was calculated. To a first approximation, it can be assumed that the carrier collection efficiency is unaffected by the presence

of the Au@SiO₂ nanoparticles, in which case the relative IPCE enhancement should be directly related to the spectrum of the Au@SiO₂ LSPR modes.¹⁰ From Figure 4.9b it can be seen that the $\Delta\text{IPCE}/\text{IPCE}_{\text{control}}$ spectrum shows a large positive increase in the range of 450 to 750 nm, where the LSPR bands of the spherical and triangular nanoparticles (annealed at 450 °C) are at their maximum. Above 750 nm, the decreasing S/N ratio of both IPCE spectra make the relative difference spectrum meaningless, while below 400 nm, the decrease in IPCE reflects the decrease in carrier collection efficiency as insulating SiO₂ nanoparticles are incorporated into the TiO₂ photoanode.

4.5. Conclusions

We synthesized a mixture of spherical and triangular Au@SiO₂ nanoparticles and evaluated their thermal stability by annealing at different temperatures. Morphological changes in the triangular Au@SiO₂ nanoprisms were observed at temperatures of 250 °C and higher, with the nanoprisms annealed at 450 °C displaying rounded or truncated corners. This produced a blue-shift of the in-plane dipole LSPR mode from 900 to 680 nm, increasing the spectral overlap with the absorption spectrum of Black Dye. By integrating 0.05% (w/w) Au@SiO₂ nanoparticles into DSSCs, a 15% increase in the PCE was observed, and the PCE enhancement was still observed even at very low gold loadings (0.009%). The increase in PCE was primarily due to an increase in J_{sc} , which was also reflected in the IPCE spectrum. In this study, we have clearly elucidated the importance of morphological changes that occur at the high temperatures required to sinter the TiO₂ photoanode, and further demonstrated that they provide an elegant and simple method for achieving panchromatic enhancement in the light harvesting efficiency of DSSCs.

4.6. References

1. X. Zhou, G. Liu, J. Yu and W. Fan, *J. Mat. Chem.*, 2012, **22**, 21337-21354.
2. H. A. Atwater and A. Polman, *Nat. Mater.*, 2010, **9**, 205-213.
3. P. K. Jain, X. Huang, I. H. El-Sayed and M. A. El-Sayed, *Acc. Chem. Res.*, 2008, **41**, 1578-1586.
4. D. Derkacs, S. H. Lim, P. Matheu, W. Mar and E. T. Yu, *Appl. Phys. Lett.*, 2006, **89**, 093103 - 093107.
5. S. Pillai, K. R. Catchpole, T. Trupke and M. A. Green, *J. Appl. Phys.*, 2007, **101**, 093105 - 093114.
6. L. Lu, Z. Luo, T. Xu and L. Yu, *Nano Lett.*, 2012, **13**, 59-64.
7. J. Yang, J. You, C.-C. Chen, W.-C. Hsu, H.-r. Tan, X. W. Zhang, Z. Hong and Y. Yang, *ACS Nano*, 2011, **5**, 6210-6217.
8. M. K. Gangishetty, K. E. Lee, R. W. J. Scott and T. L. Kelly, *ACS Appl. Mater. Interfaces*, 2013, **5**, 11044-11051.
9. H. Choi, W. T. Chen and P. V. Kamat, *ACS Nano*, 2012, **6**, 4418-4427.
10. J. Qi, X. Dang, P. T. Hammond and A. M. Belcher, *ACS Nano*, 2011, **5**, 7108-7116.
11. R. A. Naphade, M. Tathavadekar, J. P. Jog, S. Agarkar and S. Ogale, *J. Mater. Chem. A*, 2014, **2**, 975-984.
12. Q. Wang, T. Butburee, X. Wu, H. Chen, G. Liu and L. Wang, *J. Mater. Chem. A*, 2013, **1**, 13524-13531.
13. S. Wooh, Y.-G. Lee, M. N. Tahir, D. Song, M. Meister, F. Laquai, W. Tremel, J. Bisquert, Y. S. Kang and K. Char, *J. Mater. Chem. A*, 2013, **1**, 12627-12634.

14. S. W. Sheehan, H. Noh, G. W. Brudvig, H. Cao and C. A. Schmuttenmaer, *J. Phys. Chem. C*, 2012, **117**, 927-934.
15. N. C. Jeong, C. Prasittichai and J. T. Hupp, *Langmuir*, 2011, **27**, 14609-14614.
16. M. D. Brown, T. Suteewong, R. S. Kumar, V. D'Innocenzo, A. Petrozza, M. M. Lee, U. Wiesner and H. J. Snaith, *Nano Lett.*, 2011, **11**, 438-445.
17. X. Dang, J. Qi, M. T. Klug, P.-Y. Chen, D. S. Yun, N. X. Fang, P. T. Hammond and A. M. Belcher, *Nano Lett.*, 2013, **13**, 637-642.
18. Y. H. Jang, Y. J. Jang, S. T. Kochuveedu, M. Byun, Z. Lin and D. H. Kim, *Nanoscale*, 2014, **6**, 1823-1832.
19. W.-L. Liu, F.-C. Lin, Y.-C. Yang, C.-H. Huang, S. Gwo, M. H. Huang and J.-S. Huang, *Nanoscale*, 2013, **5**, 7953-7962.
20. M. A. Green and S. Pillai, *Nat. Photon.*, 2012, **6**, 130-132.
21. A. R. Tao, S. Habas and P. Yang, *Small*, 2008, **4**, 310-325.
22. S. D. Standridge, G. C. Schatz and J. T. Hupp, *J. Am. Chem. Soc.*, 2009, **131**, 8407-8409.
23. S. Chang, Q. Li, X. Xiao, K. Y. Wong and T. Chen, *Energy Environ. Sci.*, 2012, **5**, 9444-9448.
24. B. Tang, S. Xu, X. Hou, J. Li, L. Sun, W. Xu and X. Wang, *ACS Appl. Mater. Interfaces*, 2013, **5**, 646-653.
25. K. E. Lee, A. V. Hesketh and T. L. Kelly, *Phys. Chem. Chem. Phys.*, 2014, **16**, 12407-12414.
26. D. Aherne, D. E. Charles, M. E. Brennan-Fournet, J. M. Kelly and Y. K. Gun'ko, *Langmuir*, 2009, **25**, 10165-10173.
27. S. Chen and D. L. Carroll, *Nano Lett.*, 2002, **2**, 1003-1007.

28. M. M. Shahjamali, M. Salvador, M. Bosman, D. S. Ginger and C. Xue, *J. Phys. Chem. C*, 2014, **118**, 12459-12468.
29. D. Zhao, T. Peng, L. Lu, P. Cai, P. Jiang and Z. Bian, *J. Phys. Chem. C*, 2008, **112**, 8486-8494.
30. S. Ito, T. N. Murakami, P. Comte, P. Liska, C. Grätzel, M. K. Nazeeruddin and M. Grätzel, *Thin Solid Films*, 2008, **516**, 4613-4619.
31. J. Zhang, Q. Xu, Z. Feng, M. Li and C. Li, *Angew. Chem., Int. Ed. Engl.*, 2008, **47**, 1766-1769.
32. M. Murdoch, G. I. N. Waterhouse, M. A. Nadeem, J. B. Metson, M. A. Keane, R. F. Howe, J. Llorca and H. Idriss, *Nat. Chem.*, 2011, **3**, 489-492.
33. R. Huang, Y.-H. Wen, G.-F. Shao, Z.-Z. Zhu and S.-G. Sun, *RSC Advances*, 2014, **4**, 7528-7537.
34. A. S. Barnard, *Acc. Chem. Res.*, 2012, **45**, 1688-1697.
35. C. Kan, G. Wang, X. Zhu, C. Li and B. Cao, *Appl. Phys. Lett.*, 2006, **88**, 071904 - 071908.
36. C. Kan, X. Zhu and G. Wang, *J. Phys. Chem. C*, 2006, **110**, 4651-4656.
37. B. Pelaz, V. Grazu, A. Ibarra, C. Magen, P. del Pino and J. M. de la Fuente, *Langmuir*, 2012, **28**, 8965-8970.
38. K. L. Shuford, M. A. Ratner and G. C. Schatz, *J. Chem. Phys.*, 2005, **123**, 114713 - 114723.
39. K. L. Kelly, E. Coronado, L. L. Zhao and G. C. Schatz, *J. Phys. Chem. C*, 2002, **107**, 668-677.
40. S. D. Standridge, G. C. Schatz and J. T. Hupp, *Langmuir*, 2009, **25**, 2596-2600.
41. J. E. Millstone, S. J. Hurst, G. S. Métraux, J. I. Cutler and C. A. Mirkin, *Small*, 2009, **5**, 646-664.

42. J. Yum, E. Baranoff, S. Wenger, Md. K. Nazeeruddin and M. Grätzel, *Energy Environ. Sci.*, 2011, **4**, 842-857.

CHAPTER 5

Effect of CH₃NH₃PbI₃ Thickness on Device Efficiency in Planar Heterojunction Perovskite Solar Cells

*Dianyi Liu, Mahesh K. Gangishetty, and Timothy L. Kelly**

Department of Chemistry, University of Saskatchewan, 110 Science Place, Saskatoon, SK, S7N 5C9, Canada

This chapter investigates the optimum thickness of the perovskite layer for achieving the efficient light harvesting and efficient charge collection in perovskite solar cells. It provides a study on the fabrication of solution processed and vaped deposited perovskite layer.

This chapter is a near-verbatim copy of a paper published in *Journal of Material Chemistry, A*. **2014**, 2, 19873. I would like to acknowledge the contribution of Dr. Dianyi Liu in this work. This project was designed by Dr. Dianyi Liu and he fabricated and characterized all the perovskite solar cells. My contribution in this article is, X-ray diffraction studies, electrochemical impedance spectral analysis, studies on the hysteresis and fabrication some devices during the article revision process. The first draft of the manuscript was written by me and was revised by Prof. Tim Kelly prior to publication.

5.1. Abstract

Recent advances in the development of perovskite solar cells based on $\text{CH}_3\text{NH}_3\text{PbI}_3$ have produced devices with PCE of $> 15\%$. While initial work in this area assumed that the perovskite-based cells required a mesoporous TiO_2 support, many recent reports have instead focused on the development of planar heterojunction structures. A better understanding of how both cell architecture and various design parameters (e.g., perovskite thickness and morphology) affect cell performance is needed. Here, we report the fabrication of perovskite solar cells based on a ZnO nanoparticle electron transport layer, $\text{CH}_3\text{NH}_3\text{PbI}_3$ light absorber, and poly(3-hexylthiophene) (P3HT) hole transport layer. We show that vapor-phase deposition of the PbI_2 precursor film produces devices with performances equivalent to those prepared using entirely solution-based techniques, but with very precise control over the thickness and morphology of the $\text{CH}_3\text{NH}_3\text{PbI}_3$ layer. Optimization of the layer thickness yielded devices with efficiencies of up to 11.3%. The results further demonstrate that delicate balance between light absorption and carrier transport is required in these planar heterojunction devices, with the thickest perovskite films producing only very low PCEs.

5.2. Introduction

Perovskite-structured organometal halides (such as $\text{CH}_3\text{NH}_3\text{PbI}_3$) have recently revolutionized the field of organic-inorganic hybrid solar cells.¹⁻⁴ Their excellent optical and electronic properties, such as strong absorption bands that span the visible region^{5, 6} and long charge carrier diffusion lengths,⁶⁻¹⁰ make them ideal light absorbers in photovoltaic devices. In the past 5 years, the PCE of perovskite solar cells has increased dramatically – from less than 4% in 2009¹¹ to over 15% today,¹²⁻¹⁶ and estimates suggest that PCEs of over 20% are possible.³

Generally, these perovskite solar cells have been based on two different device architectures, (i) mesoscopic designs, and (ii) planar heterojunctions.² Mesoscopic designs evolved from the traditional DSSC structure, where the perovskite film is supported by an underlying mesoporous matrix of metal oxide nanoparticles. Since pioneering work by Kojima *et al.* in 2009,¹¹ where cells based on $\text{CH}_3\text{NH}_3\text{PbI}_3$ were shown to have PCEs of up to 3.8%, the performances of mesoscopic perovskite solar cells have improved rapidly. Optimization of the thickness of the mesoporous TiO_2 layer and a post-annealing treatment improved PCEs to 6.5%,¹⁷ and the adoption of spiro-OMETAD as a solid-state hole transfer material pushed PCEs nearly 10%.¹⁸ More recently, Snaith and coworkers demonstrated that charge injection into the mesoporous matrix is not a prerequisite for high power conversion efficiency; PCEs of > 10% were obtained when the n-type TiO_2 scaffold was replaced with an insulating Al_2O_3 analogue.¹⁹ While numerous other notable examples of mesoscopic perovskite solar cells have been reported,²⁰⁻³⁰ the most efficient devices (PCEs of \geq 15%) were achieved when either a two-step deposition method was used to prepare the perovskite material inside the TiO_2 matrix,¹² or modified TiO_2 layers were used as the electron selective contact.^{15, 16}

While many of the perovskite solar cells reported to date have successfully adopted the mesoscopic design, the high temperatures associated with sintering a TiO_2 mesoporous framework (> 400 °C) have spurred the development of alternative cell architectures. Several examples of perovskite solar cells with a planar heterojunction structure have been reported,^{14, 31-37} with encouraging results. While initial reports of cells based on a $\text{CH}_3\text{NH}_3\text{PbI}_3/\text{C}_{60}$ planar heterojunction showed relatively modest efficiencies of 3.9%,³¹ organolead halide perovskite/fullerene heterojunctions have achieved PCEs of up to 12%.^{32, 33} Recently, vapor-phase deposition techniques have also been used to prepare perovskite solar cells with the structure

ITO/TiO₂/CH₃NH₃PbI_{3-x}Cl_x/spiro-OMETAD/Ag; these prototypes displayed PCEs of up to 15.4%.¹³ We have also shown that planar heterojunction devices can be fabricated by the same two-step deposition procedure used by Burshka *et al.*, producing efficiencies of up to 15.7% on rigid substrates, and 10.2% on flexible supports.¹⁴ These devices are based on an ITO/ZnO/CH₃NH₃PbI₃/spiro-OMETAD/Ag structure, and are produced using solution-phase deposition techniques carried out at room temperature. The simplicity of the cell design and fabrication, when combined with their high performance and compatibility with flexible substrates, makes planar heterojunction perovskite solar cells a promising alternative to the original mesoscopic design.

One of the key variables in fabricating these devices is the thickness of the light harvesting perovskite layer. If the perovskite film is very thin, then the number of photons absorbed is low, resulting in low photocurrents; however, if very thick perovskite films are used, the efficiency of charge carrier extraction is low, and recombination becomes problematic. Mesoscopic cells that use TiO₂ photoanodes partially circumvent this issue by providing a large CH₃NH₃PbI₃ / TiO₂ interfacial surface area; electrons are therefore extracted from the perovskite throughout the entire thickness of the light harvesting layer. Previous studies have shown that the PCE of devices of this type show a relatively weak dependence on perovskite layer thickness, with optimized photoanode thicknesses of *ca.* 650 nm.⁹ In planar heterojunction devices, the situation becomes more complex. Recent work has shown that film thicknesses of 400 – 800 nm can be used to successfully prepare high-performance devices based on CH₃NH₃PbI_{3-x}Cl_x in both conventional^{7, 9, 38} and inverted³² architectures. The very long charge carrier diffusion lengths observed for CH₃NH₃PbI_{3-x}Cl_x (*ca.* 1000 nm)⁷ mean that film thicknesses comparable to those of mesoscopic devices can be used. This is not the case for the parent CH₃NH₃PbI₃ material, where the carrier diffusion lengths are an

order of magnitude lower.^{7,8} Previous reports of planar heterojunction cells based on $\text{CH}_3\text{NH}_3\text{PbI}_3$ have utilized perovskite layer thicknesses of only 100 – 350 nm,^{7, 14, 33-35} substantially thinner than those used in the chloride-doped analogues. Given the substantial differences in carrier diffusion lengths for these two perovskite compositions, a much deeper understanding of the role of film thickness and morphology on the efficiency of $\text{CH}_3\text{NH}_3\text{PbI}_3$ -based planar heterojunctions is required.

Here we report the fabrication of high performance perovskite ($\text{CH}_3\text{NH}_3\text{PbI}_3$) solar cells with a planar heterojunction structure, and elucidate the effect of perovskite film thickness and morphology on device efficiency. Perovskite films were deposited using a two-step deposition technique, with thermal evaporation used to prepare the PbI_2 precursor film. This approach circumvents issues with the solubility or viscosity of the PbI_2 precursor solution, which have previously complicated studies of this type. The evaporation of the PbI_2 precursor allows perovskite films of precisely tailored thickness to be produced. P3HT was used as the hole transport material, and devices with the structure $\text{ITO}/\text{ZnO}/\text{CH}_3\text{NH}_3\text{PbI}_3/\text{P3HT}/\text{Ag}$ were prepared. Optimization of the film thickness produced PCEs of up to 11.3%, which are among the highest ever reported for perovskite devices using a P3HT hole transport layer.

5.3. Experimental

5.3.1 Cell fabrication procedures

Solar cells were fabricated on pre-cleaned ITO-coated glass substrates with a sheet resistance of 20 Ω /square. First, a thin ZnO nanoparticle (~ 20 nm) layer was spin coated onto the substrate at 3000 rpm for 30 s; the ZnO nanoparticles were synthesized by following a literature procedure.¹⁴ The procedure was repeated three times to obtain a continuous smooth film. Then a

PbI₂ layer of given thickness was deposited on top of the ZnO layer by thermal evaporation at a base pressure of 2×10^{-6} mbar. The final thickness was experimentally determined by profilometry. Subsequently, the substrate was dipped into a solution of CH₃NH₃I in 2-propanol (10 mg/mL) for 3 min, then dried under a flow of clean air. For the solution PbI₂-based device, a PbI₂ solution (dissolved in *N,N*-dimethylformamide at a concentration of 460 mg/mL) was then spin coated on top of the ZnO layer at 3000 rpm for 15 s. After drying for several minutes in air, the substrate was dipped into a solution of CH₃NH₃I in 2-propanol (10 mg/mL) for 3 min. The P3HT-based hole transfer layer (20 mg of P3HT, 3.4 μ L of 4-*tert*-butylpyridine, and 6.8 μ L of a lithium-bis(trifluoromethanesulfonyl)imide (Li-TFSI) solution (28 mg Li-TFSI / 1 mL acetonitrile) all dissolved in 1 mL chlorobenzene) was then deposited by spin coating at 1000 rpm for 30 s. Finally, a 150 nm thick silver layer was deposited by thermal evaporation at a base pressure of 2×10^{-6} mbar. The completed devices were stored in a N₂-purged glovebox (< 0.1 ppm O₂ and H₂O).

5.3.2 Device characterization

The current-voltage curves of solar cells were measured inside the glovebox using a Keithley 2400 source-measure unit. The cells were illuminated by a 450 W Class AAA solar simulator equipped with an AM1.5G filter (Sol3A, Oriel Instruments) at a calibrated intensity of 100 mW/cm², as determined by a standard silicon reference cell (91150V Oriel Instruments). The effective area of the cell was defined to be 0.07065 cm² using a non-reflective metal mask. IPCE spectra were measured in air under short-circuit conditions using a commercial IPCE setup (QE-PV-Si, Oriel Instruments), which was equipped with a 300 W Xe arc lamp, filter wheel, and monochromator. Monochromated light was chopped at a frequency of 8 Hz and photocurrents measured using a lock-in amplifier. The setup was calibrated against a certified silicon reference

diode. Electrochemical impedance spectroscopy (EIS) measurements were carried out using a Solartron SI1260 Impedance/Gain-phase analyzer, under 1 sun AM1.5G illumination, by applying 0 V DC bias and a 5 mV voltage perturbation in the frequency range of 400 kHz to 0.1 Hz.

5.3.3 Thin film characterization

Film thicknesses were measured using a KLA Tencor profilometer. Absorption spectra were acquired on a Cary 6000i UV-vis-NIR spectrophotometer. Powder X-ray diffraction (pXRD) measurements were carried out using a PANalytical Empyrean X-ray diffractometer equipped with a Cu $K_{\alpha 1,2}$ X-ray source. The data were collected with a 0.02° step size (2θ). Scanning electron microscope (SEM) images were acquired on a JEOL 6010LV microscope; the images were collected at 15kV. Atomic force microscope (AFM) images were acquired on a Dimensions Hybrid Nanoscope system (Veeco Metrology Group). AFM data was collected in tapping mode (non-contact) with a scan rate of 1.97 Hz

5.4. Results and Discussion

5.4.1. Comparison of solution- and vapour-phase PbI_2 deposition

The thin films of $\text{CH}_3\text{NH}_3\text{PbI}_3$ used to fabricate the perovskite devices were prepared via the two-step deposition process described previously.^{12, 14, 39} As noted by Conings *et al.*,⁴⁰ tailoring the thickness of perovskite films prepared via spin coating is complicated by the low solubility of the PbI_2 precursor and the high viscosity of the precursor solution. We therefore used thermal evaporation³⁹ to prepare thin films of PbI_2 on ITO/ZnO substrates, rather than spin coating the PbI_2 from DMF solution. The films were then dipped in an isopropanol solution of methylammonium iodide in order to convert the PbI_2 to the organolead halide perovskite. The main advantage of this method is the thickness of the PbI_2 film (and therefore, the resultant perovskite layer) can be

precisely controlled and systematically varied from 50 to 330 nm, without any complications due to the limited solubility of the precursor; additionally, the solvent-free method of PbI_2 deposition may be useful in the future fabrication of tandem solar cells that include a perovskite component.

Before the influence of perovskite layer thickness and morphology could be investigated, it needed to be determined whether the change in PbI_2 deposition process would have any effect on the perovskite structure, morphology, or the performance of the resultant devices. As can be seen from the powder X-ray diffraction patterns of the PbI_2 and $\text{CH}_3\text{NH}_3\text{PbI}_3$ films (Figure 5.1), there are only minor differences in structure that arise as a result of the change in deposition process. Both PbI_2 films are poorly crystalline (as evidenced by the weak, broad diffraction peaks), and data are consistent with the 2H polytype, in keeping with previous reports of solution-prepared PbI_2 films.¹² After dipping both samples in the $\text{CH}_3\text{NH}_3\text{I}$ solution, both films are successfully converted into the corresponding perovskite. The diffraction patterns are consistent with the tetragonal phase of $\text{CH}_3\text{NH}_3\text{PbI}_3$.⁴¹ The morphology of the perovskite films was also compared by SEM (Figure 5.1). Both films consisted of a closely-packed collection of block-like perovskite crystallites, with at most only very subtle differences in crystallite shape and size.

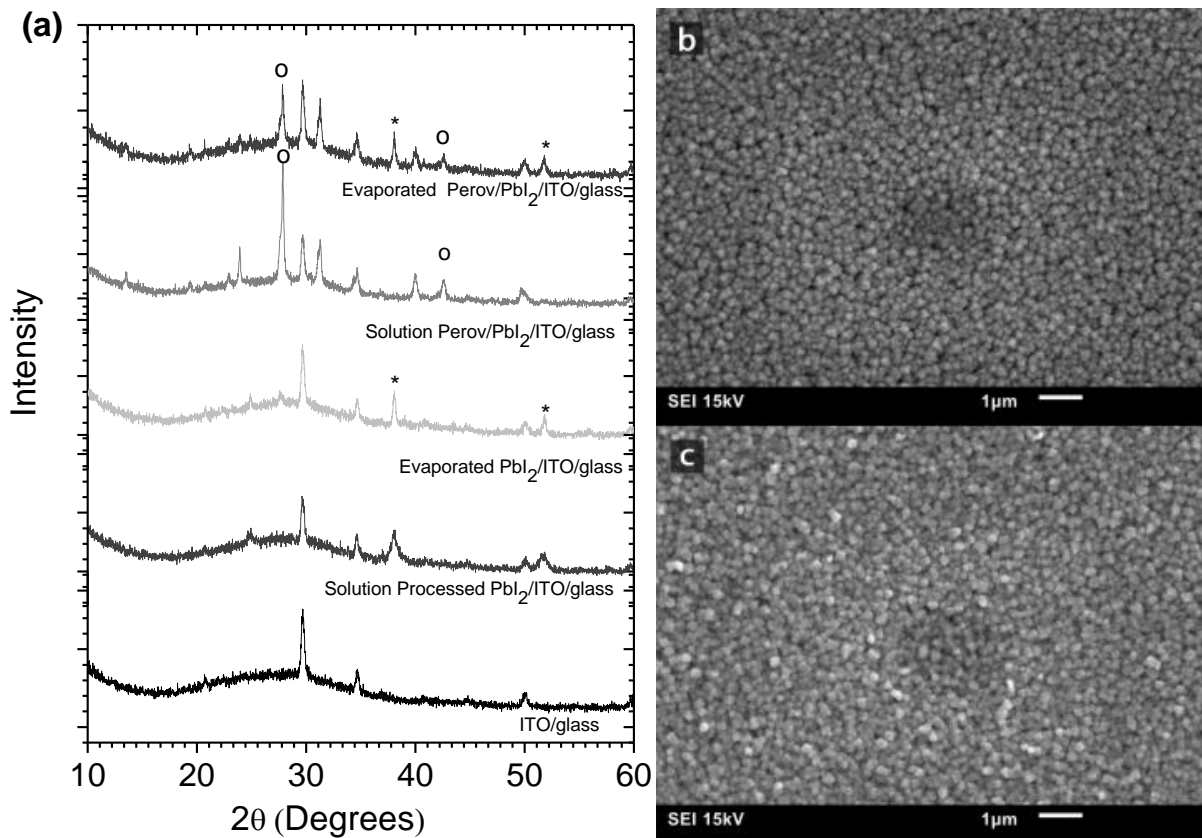


Figure 5.1. (a) Powder X-ray diffraction patterns of PbI_2 films deposited by spin coating (S- PbI_2) and thermal evaporation (E- PbI_2), and the corresponding $\text{CH}_3\text{NH}_3\text{PbI}_3$ films after dipping in methylammonium iodide solution. All films were deposited on ITO/glass substrates. The * denotes PbI_2 peaks and O denotes the characteristic peaks of $\text{CH}_3\text{NH}_3\text{PbI}_3$. (b) SEM micrograph of a perovskite film produced from a spin coated PbI_2 film; (c) SEM micrograph of a perovskite film produced from an evaporated PbI_2 film.

To gauge the effect of processing method on device efficiency, the perovskite films derived from both solution- and vapor-phase deposited PbI_2 were used to prepare planar heterojunction solar cells. In both cases, the thickness of the perovskite film was determined to be ≈ 300 nm. A thin (*ca.* 30 nm) ZnO nanoparticle layer on ITO was chosen as the electron-selective contact, and P3HT was used as the hole transport material. The J - V curves of all devices were measured under AM1.5G illumination, and those of the highest-performing cells are shown in Figure 5.2a. The results clearly indicate that the particular method of PbI_2 deposition has little effect on the overall PCE, the devices prepared using solution- and vapor-phase deposition techniques had PCEs of

11.8% and 11.3%, respectively. Both devices also had nearly identical open-circuit voltages ($V_{oc} = 0.95 \pm 0.01\text{V}$ and $0.94 \pm 0.01\text{ V}$) and similar fill factors (FF = 66.1% and 68.2%). The only notable difference between the two devices was a slightly higher short-circuit current density for the solution-processed device ($J_{sc} = 18.8\text{ mA}\cdot\text{cm}^{-2}$) compared to the one processed by thermal evaporation ($J_{sc} = 17.6\text{ mA}\cdot\text{cm}^{-2}$). The lower J_{sc} in the device fabricated from vapor-deposited PbI_2 is also reflected in the IPCE spectrum (Figure 5.2b). However, despite these small differences in J_{sc} , the difference in the overall PCE of devices constructed from both solution and vapor-deposited PbI_2 is quite minor. In order to ensure the reproducibility of our results, we fabricated and tested 34 separate devices using evaporated PbI_2 layers, and 29 separate devices using spin coated PbI_2 layers. The tabulated device performances are shown in Table 5.1. In this case, the average J_{sc} of the solution processed devices was found to be slightly higher ($17.1 \pm 1.1\text{ mA}/\text{cm}^2$) than that of the devices derived from evaporated PbI_2 films ($16.0 \pm 0.9\text{ mA}/\text{cm}^2$), suggesting that the differences in J_{sc} observed in Figure 5.2 simply reflect batch-to-batch variation in the perovskite layer, rather than any significant difference between the two fabrication processes. Similarly, the very small differences in V_{oc} and FF (and ultimately, PCE) for the two fabrication methods are well within their associated standard deviations, indicating that the two methods produce cells of similar performance.

Table 5.1. Device performance parameters for perovskite solar cells. ^aAverages derived from measurements on 29 separate devices. ^bAverages derived from measurements on 34 separate devices.

PbI₂ Deposition Method	V_{oc} (V)	J_{sc} (mA·cm⁻²)	FF (%)	PCE (%)	Best PCE (%)
Spin Coating^a	0.95 ± 0.01	17 ± 1	62 ± 4	10.0 ± 0.9	11.8
Thermal Evaporation^b	0.94 ± 0.02	16.0 ± 0.9	65 ± 4	9.7 ± 0.6	11.3

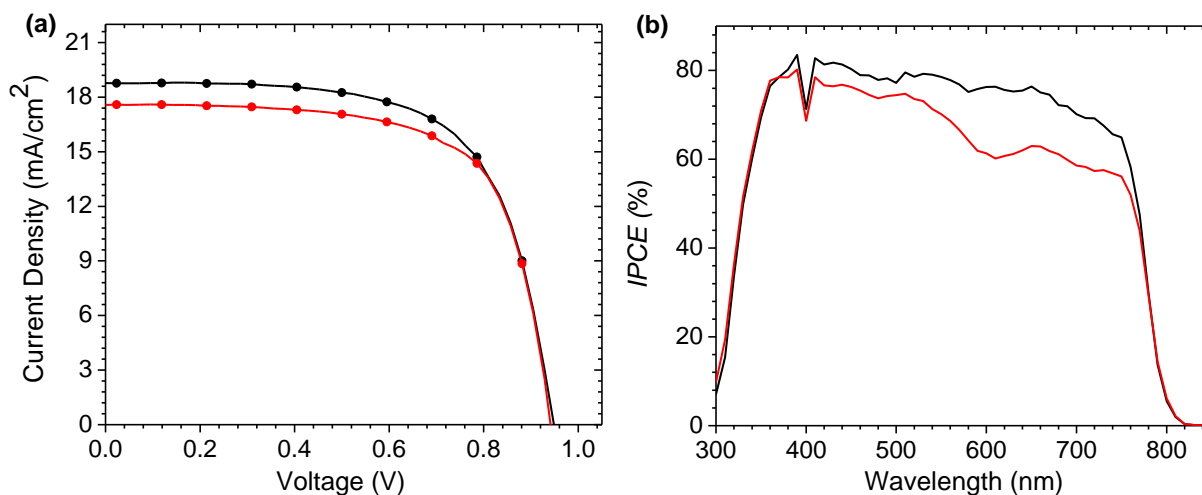


Figure 5.2. (a) *J-V* curves and (b) IPCE spectra for the highest-performing ITO/ZnO/CH₃NH₃PbI₃/P3HT/Ag devices prepared from both solution-processed (black line) and thermally evaporated (red line) PbI₂ films.

5.4.2. Effect of PbI₂ film thickness on CH₃NH₃PbI₃ composition and morphology

Having established that the evaporated PbI₂ films could be used to produce cells with PCEs identical to those produced using solution-based techniques, we next investigated the effect of PbI₂ film thickness on the composition, thickness, and morphology of the resultant perovskite layer. Lead iodide films were first deposited on glass substrates, and the thickness of the films was varied from 50 nm to 300 nm. The PbI₂ films were then dipped in an isopropanol solution of methylammonium iodide in order to produce perovskite films of varying thickness. The thickness of the perovskite film was found to increase linearly with the thickness of the PbI₂ precursor film, as shown in Figure 5.3. Measurements were carried out on multiple films of each thickness, and the process was found to be highly reproducible, as indicated by the small standard deviations associated with the profilometry measurements. In all cases, the thickness of the perovskite film was found to be approximately twice that of the PbI₂ precursor, in keeping with previous reports.³⁴ More quantitatively, a linear regression of the data obtained for the three thinnest films yields a slope of 2.1. This can be understood based on the volume changes that occur during the

intercalation of $\text{CH}_3\text{NH}_3\text{I}$ into the PbI_2 crystallites (Figure 5.4). The PbI_2 that is initially present in the film has a unit cell volume of 124 \AA^3 . Upon addition of $\text{CH}_3\text{NH}_3\text{I}$ and formation of the perovskite structure, the unit cell volume increases dramatically to 990 \AA^3 ; however, since the tetragonal phase of the perovskite contains four $\text{CH}_3\text{NH}_3\text{PbI}_3$ units within the unit cell, the molar volume of $\text{CH}_3\text{NH}_3\text{PbI}_3$ is calculated to be 248 \AA^3 . Comparing the molar volumes of PbI_2 and $\text{CH}_3\text{NH}_3\text{PbI}_3$, it can be seen that the volume occupied by the perovskite is almost exactly twice that of the PbI_2 precursor, which is in excellent agreement with the data shown in Figure 5.3a. However, for the thickest three films, the actual film thickness deviates from that predicted by the above arguments. Upon measuring the powder X-ray diffraction patterns of perovskite films of various thicknesses, it can be seen that this is related to the presence of residual unreacted PbI_2 in the film (Figure 5.5). For the thinnest films, the diffraction patterns indicate complete conversion to the perovskite; however, beginning at $\sim 300 \text{ nm}$ thick $\text{CH}_3\text{NH}_3\text{PbI}_3$ films, there is evidence of residual PbI_2 . As the film thickness increases, the relative amount of unreacted PbI_2 increases, in agreement with the data shown in Figure 5.3a. Figure 5.3b shows the absorption spectra of the perovskite films as a function of film thickness. All perovskite films exhibited a broad range of light absorption from 300 to 760 nm, with the optical density of the film increasing monotonically with film thickness. The linear increase in optical density demonstrates both the excellent control over film thickness provided by the evaporation of PbI_2 , and the overall consistency of the two-step deposition process.

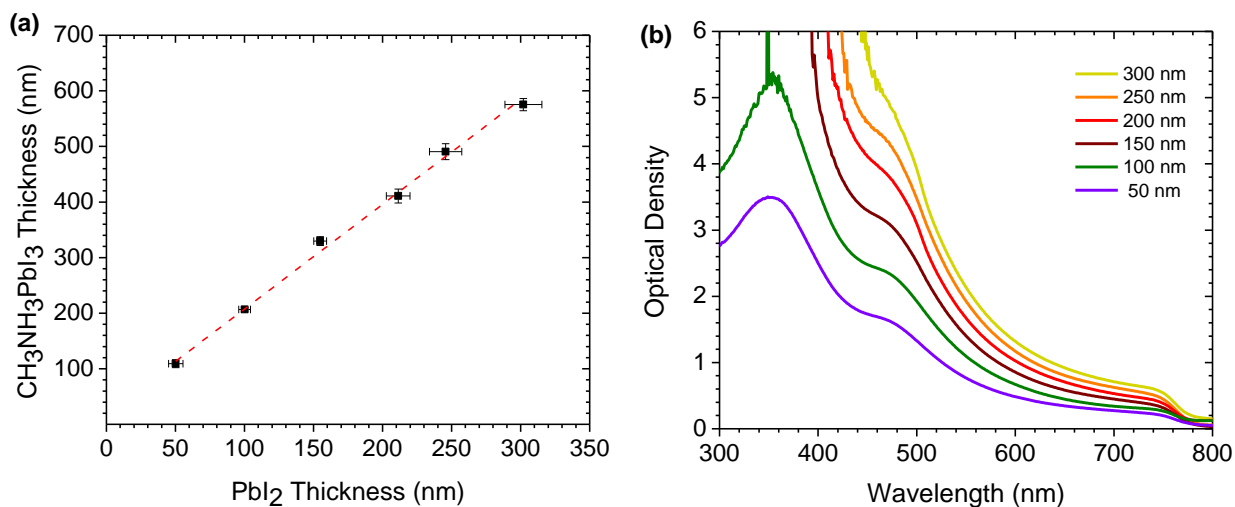


Figure 5.3. (a) Perovskite film thickness as a function of the thickness of the precursor PbI_2 film, as determined by profilometry; (b) Absorbance spectra of the films from (a). Error bars represent plus-or-minus one standard deviation from the mean.

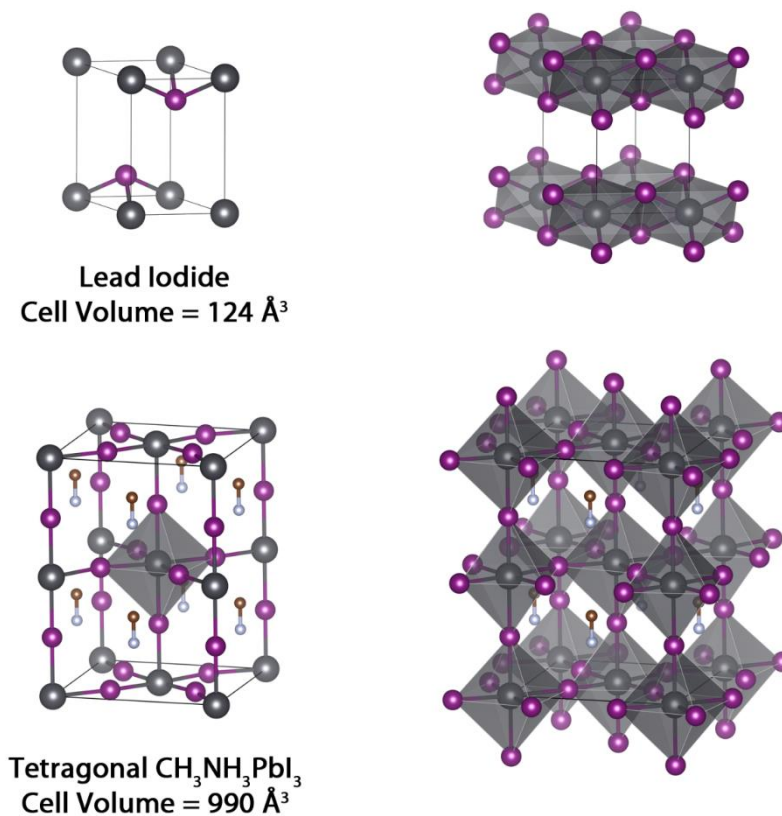


Figure 5.4. The unit cells and cell volumes of lead iodide and tetragonal $\text{CH}_3\text{NH}_3\text{PbI}_3$: Pb (grey), I (purple), C (brown) and N (grey). The unit cell of $\text{CH}_3\text{NH}_3\text{PbI}_3$ contains four $\text{CH}_3\text{NH}_3\text{PbI}_3$ units, and so the volume per $\text{CH}_3\text{NH}_3\text{PbI}_3$ repeat unit is 248 \AA^3 .

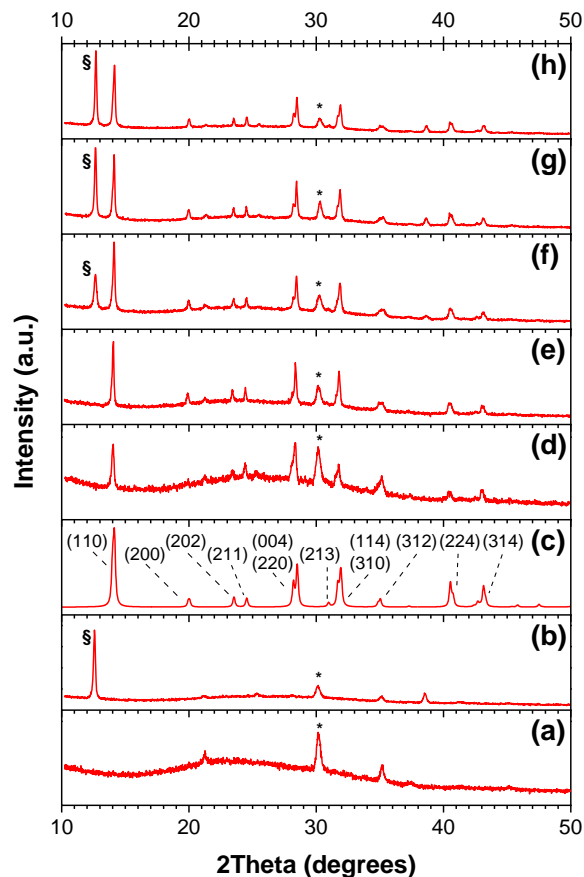


Figure 5.5. Powder X-ray diffraction patterns. All samples were prepared and measured on ITO/ZnO substrates. (a) Bare ITO/ZnO; (b) PbI_2 ; (c) Calculated diffraction pattern for the tetragonal phase of $\text{CH}_3\text{NH}_3\text{PbI}_3$ (peak widths arbitrarily broadened to $0.2^\circ 2\theta$). Where more than one reflection contributes to an unresolved peak, only the most intense reflection is labelled; (d) 61 nm $\text{CH}_3\text{NH}_3\text{PbI}_3$; (e) 200 nm $\text{CH}_3\text{NH}_3\text{PbI}_3$; (f) 280 nm $\text{CH}_3\text{NH}_3\text{PbI}_3$; (g) 400 nm $\text{CH}_3\text{NH}_3\text{PbI}_3$; (h) 560 nm $\text{CH}_3\text{NH}_3\text{PbI}_3$.

In order to understand how film thickness affects the morphology of the perovskite layer, both PbI_2 and $\text{CH}_3\text{NH}_3\text{PbI}_3$ films were evaluated by SEM (Figure 5.6). Figure 5.6a-c shows a top-down view of vapor-deposited PbI_2 films of *ca.* 50, 150 and 300 nm thickness. The 50 nm thick film was relatively smooth, with only very small nanocrystallites visible under the electron microscope. As the film thickness is increased to 150 nm, the PbI_2 crystallites begin to develop a flake-like texture, eventually becoming large nanoplates in the thickest films. After conversion to the perovskite (Figure 5.6d-f), the morphology of the films is substantially altered; the film is still

composed of a closely-packed collection of nanocrystallites, but the individual crystallites adopt a more block-like morphology, in keeping with the tetragonal perovskite unit cell. The same trend in morphology is also observed in the perovskite films. In the thinnest (*ca.* 110 nm) film, the block-like crystallites are small and densely packed, forming a film that, while not smooth, has very few gaps between the crystallites. As the perovskite film grows thicker, the individual nanocrystallites grow larger, in turn producing a rougher surface morphology. For the thickest (*ca.* 580 nm) film, many of the crystallites are over 100 nm in size, with equally large gaps between them; this produces a highly textured morphology.

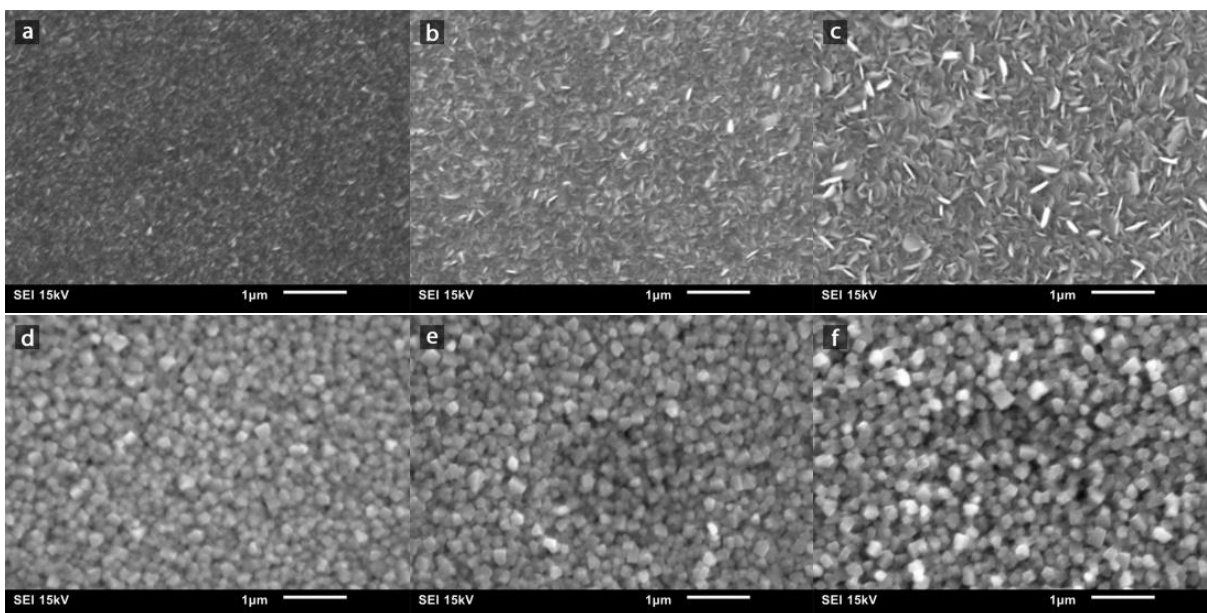


Figure 5.6. SEM images of (a-c) evaporated PbI_2 films and (d-f) the corresponding $\text{CH}_3\text{NH}_3\text{PbI}_3$ films after dipping in $\text{CH}_3\text{NH}_3\text{I}$. Films were (a) 50, (b) 150, (c) 300, (d) 110, (e) 330 and (f) 580 nm thick, as determined by profilometry.

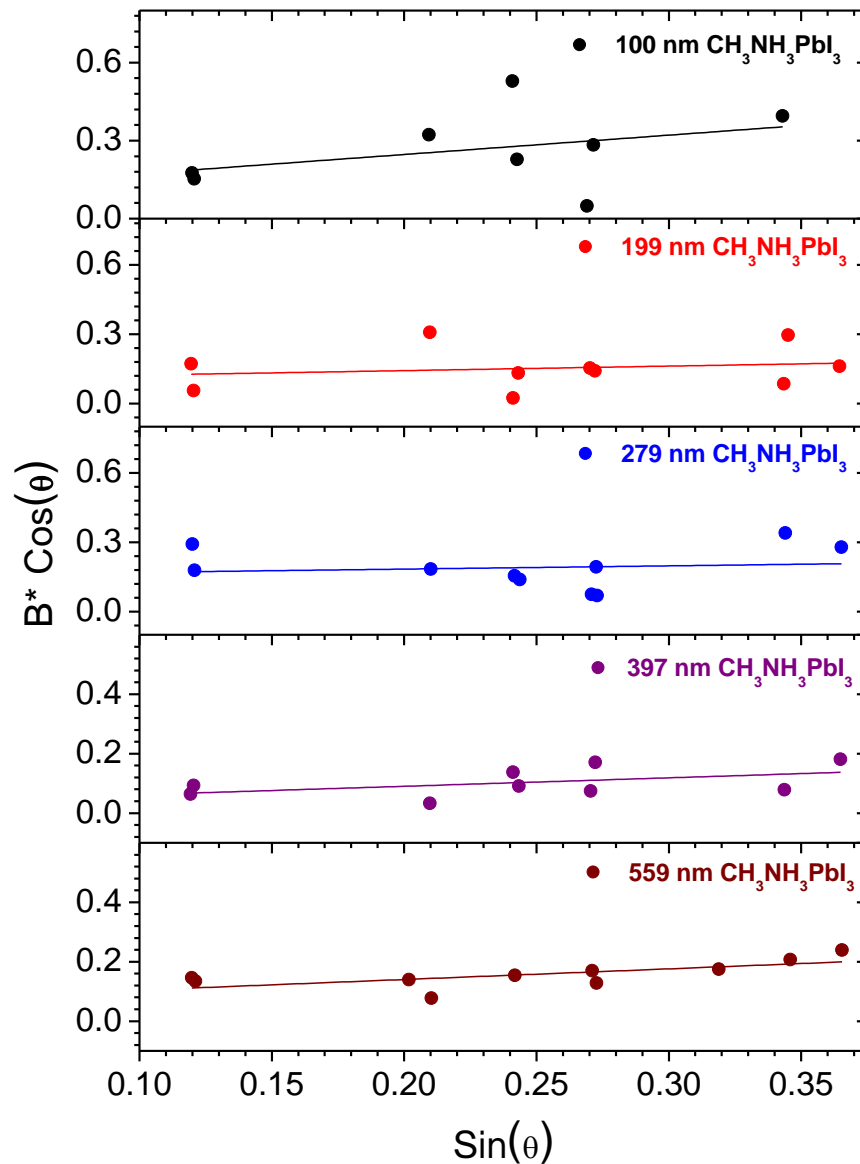


Figure 5.7. Williamson-Hall plots for $\text{CH}_3\text{NH}_3\text{PbI}_3$ films of various thicknesses.

In order to more quantitatively evaluate these trends, we plotted both the particle size (as measured by SEM) and the minimum grain size (as determined from a Williamson-Hall analysis of the pXRD data, Figure 5.7) as a function of perovskite layer thickness (Figure 5.8). As suggested by Figure 5.8, the average particle size increases as the perovskite layer is made thicker; however, this evolution in particle size is modest when compared to the pronounced morphological differences observed for the PbI_2 films (Figure 5.6). This suggests that a substantial degree of

structural reorganization occurs within the crystallites during the $\text{CH}_3\text{NH}_3\text{I}$ intercalation step, resulting in a highly crystalline perovskite film. This is supported by the Williamson-Hall analysis of the pXRD data, which separates out the effects of size and lattice strain on peak broadening (Figure 5.7). This analysis suggests that there is a slight dependence of the minimum grain size on the film thickness, with the thickest films having slightly larger crystalline domains than the thinnest samples. The degree of lattice strain is essentially negligible ($< 0.1\%$) for the majority of samples (Figure 5.8b). Combined with the excellent agreement between the observed $\text{CH}_3\text{NH}_3\text{PbI}_3$ thicknesses and those predicted based on the PbI_2 precursor thickness and the subsequent increase in molar volume, this suggests that the Pb^{2+} , I^- , and CH_3NH_3^+ ions are sufficiently mobile throughout the two-step deposition sequence to produce highly relaxed, crystalline films. This, in part, explains the excellent performance of the perovskite films fabricated using this technique.¹²

¹⁴ The one exception to this appears to be the thinnest films, which show a small amount of additional lattice strain, likely as a result of interactions with the underlying ZnO interface.

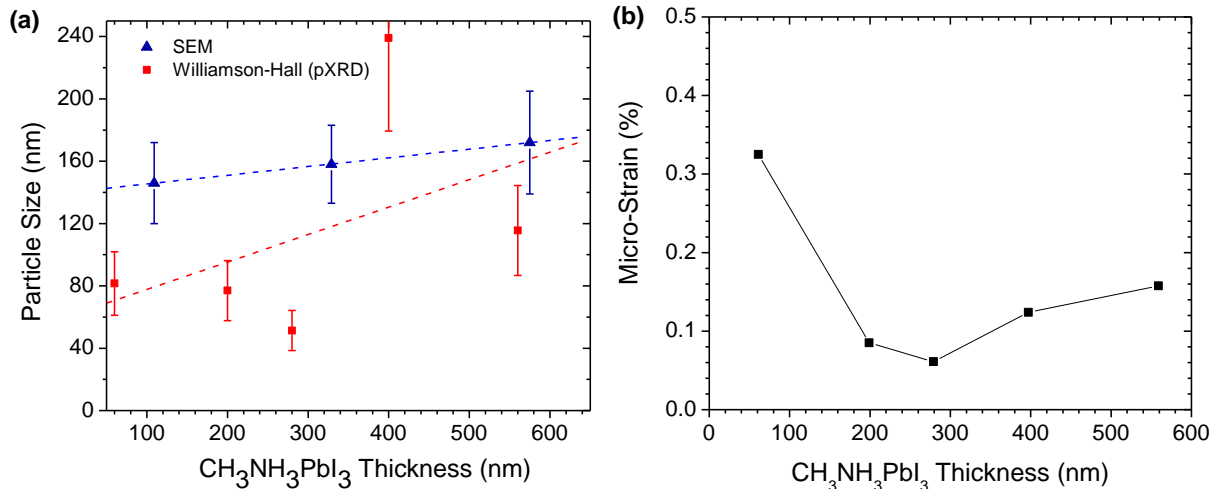


Figure 5.8. (a) Particle size as measured by SEM (blue triangles) and minimum grain size as determined by a Williamson-Hall analysis of powder X-ray diffraction data (red squares) as a function of perovskite layer thickness. The linear fits are a guide to the eye. (b) Microstrain (as calculated by a Williamson-Hall analysis of powder X-ray diffraction data) as a function of perovskite layer thickness.

Since both the change in particle/grain size and the associated changes in surface roughness have important implications for device performance, we further probed the surface roughness of the samples using atomic force microscopy (Figure 5.9). The root-mean-square surface roughness (R_{rms}) of the perovskite films was found to change with increasing film thickness; however, the thickest device (560 nm) showed a slightly higher root-mean-square surface roughness (49 nm) compared to rest of the devices. The implications that this observation has for device performance are discussed in more detail below.

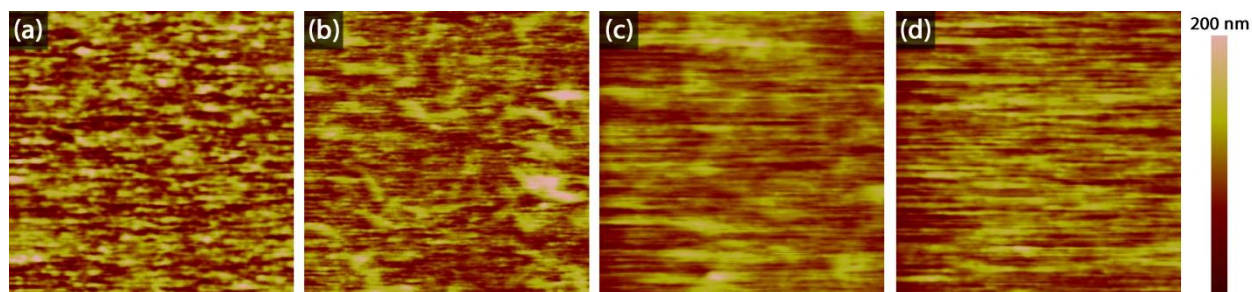


Figure 5.9. AFM images of $\text{CH}_3\text{NH}_3\text{PbI}_3$ films of various thicknesses on ITO/ZnO substrates: (a) 200 nm, (b) 280 nm, (c) 400 nm, and (d) 560 nm. All images were of a $15\ \mu\text{m} \times 15\ \mu\text{m}$ area. The samples had root-mean-squared surface roughnesses (R_{rms}) of: (a) 33, (b) 29, (c) 23, and (d) 49 nm, respectively.

5.4.3. Device performance as a function of perovskite film thickness

A number of ITO/ZnO/ $\text{CH}_3\text{NH}_3\text{PbI}_3$ /P3HT/Ag devices were fabricated at each of the perovskite thicknesses studied in Figure 5.3a, and changes in device performance correlated with the observed changes in the optical density and morphology of the perovskite film. The J - V curves and IPCE spectra of the highest performing devices at each thickness are shown in Figure 5.10, and V_{oc} , J_{sc} , FF and PCE are plotted as a function of perovskite film thickness in Figure 5.11. From the data, it is immediately apparent that device efficiency is strongly dependent on perovskite film thickness; both the thinnest and thickest perovskite films yield devices with PCEs of only 1-3%, while those with an optimal thickness of *ca.* 330 nm were found to have an average PCE of $9.4 \pm 0.6\%$, with the best device displaying a PCE of 11.3%. Based on the data in Figure 5.10 and 5.11,

the improvements in PCE with increasing perovskite thickness are due to two dominant factors. The first is a dramatic increase in both V_{oc} and FF as the thickness of the perovskite increases from 110 to 330 nm; based on the slopes of the corresponding J - V curves at J_{sc} , this is caused in large part by an increase in the shunt resistance (Table 5.2). The low shunt resistances observed in the thinnest films are entirely consistent with substantial recombination at the ZnO interface, which leads to the pronounced loss in V_{oc} . These losses are very similar to those observed in perovskite devices prepared via a one-step methodology,³⁸ where pin-hole shorts lead to low shunt resistances and open-circuit voltages. Given that the R_{rms} in these films is *ca.* 30 nm (Figure 5.9), and that the R_{rms} represents only one standard deviation in the sample height, there is statistically a very high likelihood of pin-hole short formation in the thinnest perovskite films. Increasing the film thickness prevents such contact, resulting in improvements to both FF and V_{oc} . These results are validated by electrochemical impedance spectroscopy measurements (Figure 5.12); fitting the Nyquist plots to an equivalent circuit used for other solid-state photovoltaic devices^{42, 43} shows that the thinnest devices have an extremely low recombination resistance (Table 5.3). This is entirely consistent with the low fill factors observed in these devices, and provides an explanation

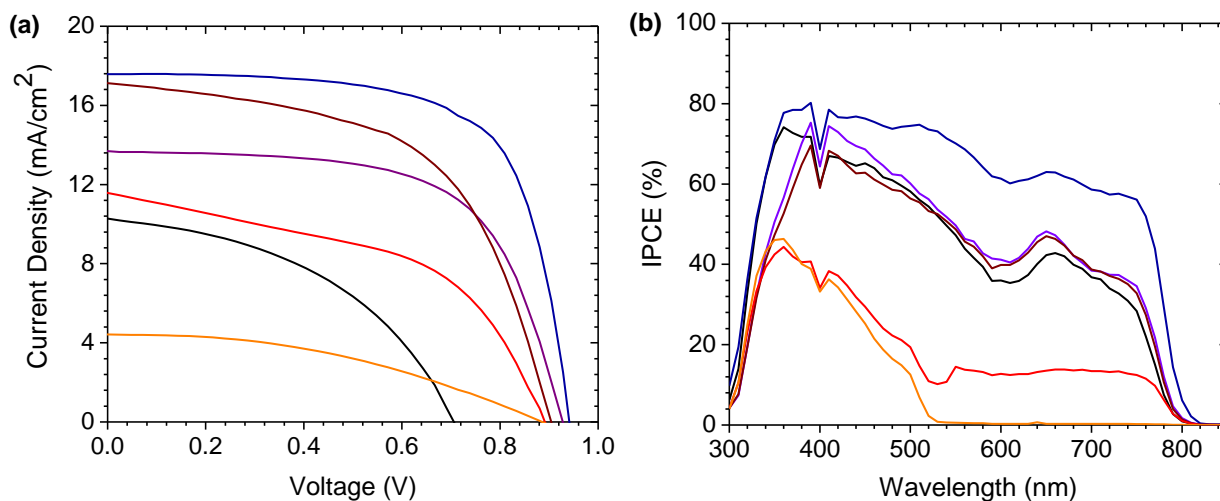


Figure 5.10. (a) J - V curves and (b) IPCE spectra for ITO/ZnO/CH₃NH₃PbI₃/P3HT/Ag devices with perovskite layers of 110 (black line), 210 (blue line), 330 (purple line), 410 (dark brown line), 490 (red line) and 580 nm (orange line).

for the losses observed in V_{oc} . As the perovskite thickness is increased, the recombination resistance increases accordingly, which is consistent with the concomitant rise in FF and V_{oc} . Very similar correlations have previously been observed between the recombination resistance and V_{oc} in planar heterojunction perovskite solar cells.⁴⁴

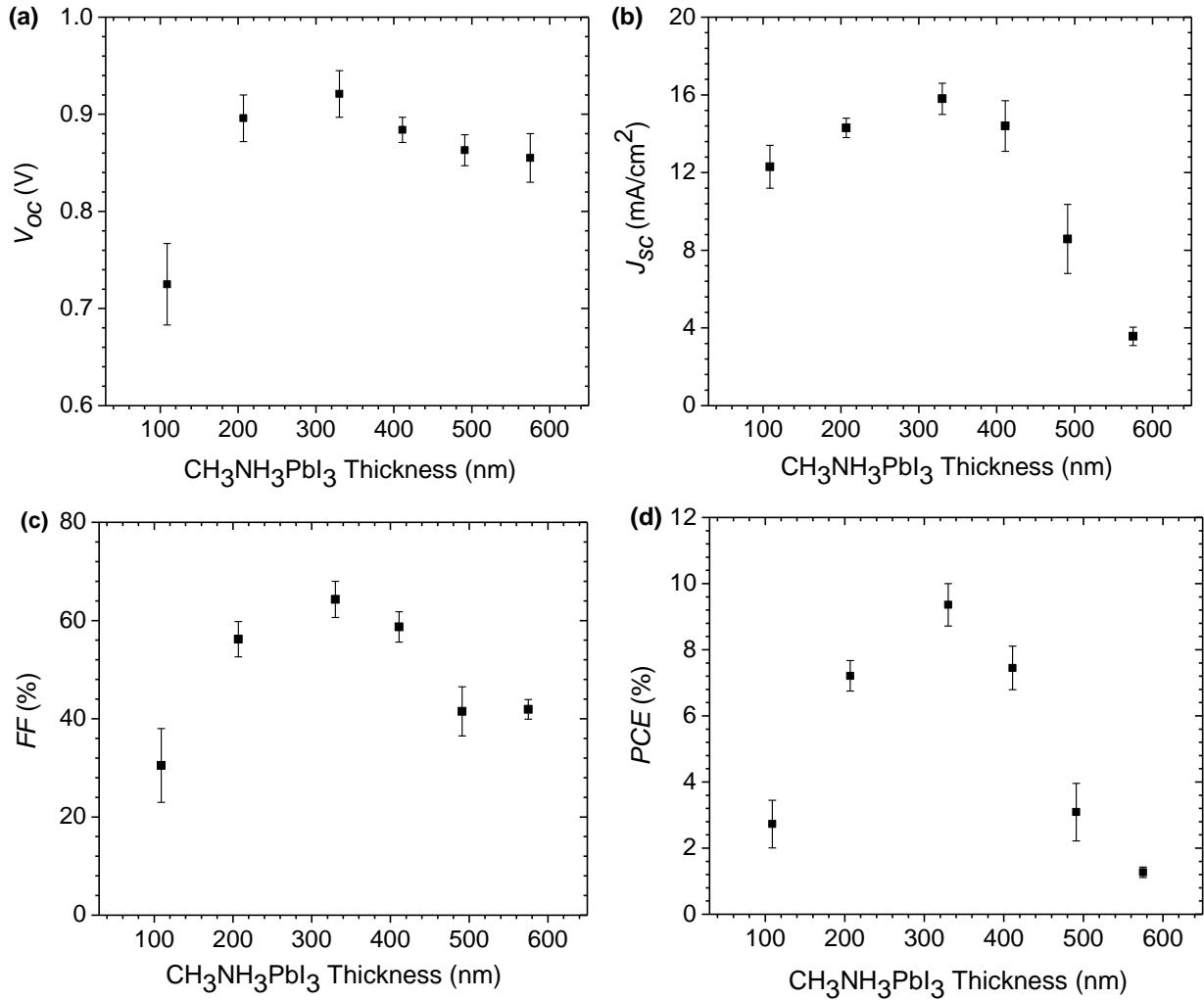


Figure 5.11. (a) Open circuit voltage, (b) short circuit current density, (c) fill factor and (d) PCE as a function of perovskite film thickness. Error bars represent plus-or-minus one standard deviation from the mean. Data are derived from measurements on 8, 17, 34, 12, 11 and 14 separate devices for 110, 210, 330, 410, 490, and 580 nm thick films, respectively.

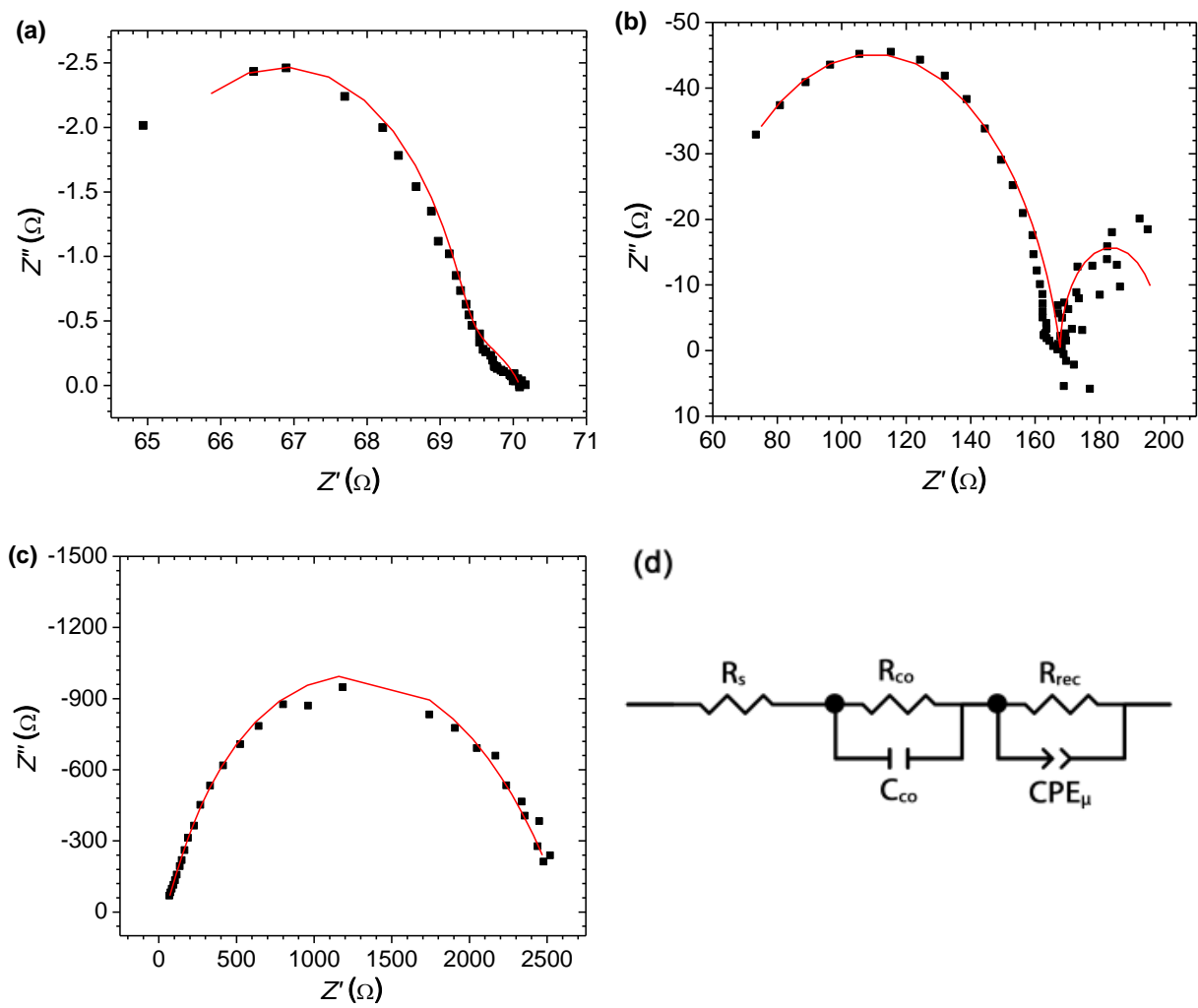


Figure 5.12. Nyquist plots for ITO/ZnO/CH₃NH₃PbI₃/P3HT/Ag devices with different CH₃NH₃PbI₃ thicknesses: (a) 110 nm, (b) 330 nm, (c) 580 nm. Experimental data (black squares) and theoretical fit (red line). (d) Equivalent circuit model used to fit the data.

The second factor leading to the observed increase in PCE is the steady increase in film optical density (Figure 5.3b) with increasing thickness. For the thinnest films studied, the light harvesting efficiency at longer wavelengths is relatively low: at 700 nm, only *ca.* 69% of the incoming light is absorbed (assuming a 4% reflection loss at the air/glass interface, and 100% reflection at the silver back-contact), and when combined with high levels of recombination, this results in an IPCE of only *ca.* 40%. As the film thickness is increased, the light harvesting efficiency increases steadily; for the optimum film thickness of 330 nm, approximately 86% of the

light at 700 nm is absorbed, leading to the stronger IPCE spectrum and improved J_{sc} . Since at this film thickness, only *ca.* 14% of the long wavelength light is lost to transmission, there is relatively little benefit to be realized from the use of thicker perovskite films.

For the devices with perovskite film thicknesses > 400 nm, the decline in device performance is particularly sharp. As the film thickness continues to increase, there is a significant increase in the series resistance of the devices (Table 5.2); the series resistance of the cells with the thickest perovskite layers is over an order of magnitude higher than for optimized devices. EIS measurements suggest that this is due to an increase in the contact resistance between the perovskite and interfacial layers (Table 5.3); since the ZnO/CH₃NH₃PbI₃ interface does not change as the perovskite thickness is increased, we ascribe this increase to changes in the CH₃NH₃PbI₃/P3HT interface. This may suggest that for the thickest films, the polymer hole-transport material has difficulty penetrating into the porous surface; this would lead to an increased contact resistance, and contribute to the higher series resistance of these devices. Additionally, as the thickness is increased, there is also a drop in the shunt resistance (Table 5.2). This may be related to the changing morphology of the perovskite layer; as the CH₃NH₃PbI₃/P3HT interface becomes rougher (Figure 5.6), there are also more opportunities for surface recombination to occur, and the efficiency is adversely impacted. Analogous behavior has been observed for perovskite solar cells with a high surface area ZnO/CH₃NH₃PbI₃ interface.⁴⁵ The combination of these two effects explains the observed drop in fill factor (64% to 42%).

Table 5.2. Average series (R_s) and shunt (R_{sh}) resistances for perovskite solar cells.

CH₃NH₃PbI₃ Thickness (nm)	R_s ($\Omega \cdot \text{cm}^2$)	R_{sh} ($\text{k}\Omega \cdot \text{cm}^2$)
110	170	0.22
210	13	3.0
330	8.0	4.0
410	12	0.42
490	41	0.24
580	110	1.2

Table 5.3. Tabulated fit parameters for the EIS data.

CH₃NH₃PbI₃ Thickness (nm)	R_s (Ω)	R_{co} (Ω)	C_{co} (F)	R_{rec} (Ω)	$CPE_{\mu-T}$ (F)	$CPE_{\mu-P}$
110	64	5	1×10^{-7}	1	2×10^{-3}	0.57
330	52	31	6×10^{-3}	116	9×10^{-8}	0.84
580	39	1250	2×10^{-7}	1323	9×10^{-7}	0.67

Even more striking than the changes to the V_{oc} and FF, however, is the dramatic loss (> 75%) in J_{sc} as the perovskite film thickness begins to exceed 400 nm. This is by far the largest contributor to the reduced efficiency of the thickest devices and is predominantly caused by the mismatch between the absorption depth of the perovskite and the carrier diffusion length. The electron and hole diffusion lengths for CH₃NH₃PbI₃ have been reported to be ~ 100 nm;^{7, 8} however, for the thickest (580 nm) devices, the perovskite film thickness significantly exceeds the diffusion lengths of the charge carriers. As such, carriers generated near the center of the film will recombine before reaching the electrodes. This is consistent with the sharp decrease in IPCE

observed for wavelengths > 500 nm (Figure 5.10b). For wavelengths < 500 nm, the perovskite absorbs very strongly (Figure 5.3b), and charge carriers are generated very close to the ZnO/CH₃NH₃PbI₃ interface; as such, a reasonable number of electrons can be collected by the ZnO electron-transport layer before they recombine. For wavelengths > 500 nm, the lower extinction coefficient means that charge carriers are generated deep in the interior of the perovskite film and are more than 100 nm away from either interface. As such, the carrier collection efficiency in this spectral region begins to approach zero, resulting in the very low short-circuit current densities that are observed. Additionally, the less-compact perovskite morphology observed in thicker films (Figure 5.6f) may result in poorer connectivity between adjacent crystallites, leading to a more tortuous pathway for carrier transport and a greater likelihood of recombination. Given the observed decrease in PCE, the increased light harvesting efficiency observed in the thicker films (96% at 700 nm for the thickest film, vs. 86% for the optimum thickness of 330 nm) is clearly insufficient to overcome these deleterious effects on carrier transport. This same argument would also hold true (although to a lesser degree) for the optimized perovskite film thickness of 330 nm. A large number of carriers would be generated in the innermost 130 nm of the perovskite film; since these are greater than an exciton diffusion length away from the electron- and hole-transport interfaces, many of these would be expected to recombine. However, given the good IPCE values achieved in these devices, this is clearly not the case. There are two possible explanations for this observation: (i) the carrier diffusion lengths are significantly longer than those originally reported by Stranks et al. and Xing et al.;^{7, 8} or, (ii) carrier extraction is facilitated by the high surface area CH₃NH₃PbI₃/P3HT interface. Although the measurements of Stranks et al. and Xing et al.^{7, 8} are fairly conservative estimates, we believe that the high surface area CH₃NH₃PbI₃/P3HT interface plays a key role in the high performance of these planar heterojunction devices. This can be

understood more quantitatively by considering the highest performance devices, which have a 330 nm thick perovskite layer. The first 130 nm of this film is within one charge carrier diffusion length of the ZnO interface,⁷ and carrier collection is not expected to be problematic. Similarly, holes can readily be extracted from the 110 nm closest to the P3HT interface.⁷ This leaves *ca.* 90 nm in the interior of the film that is too far away from either interface and thus would contribute significantly less to the photocurrent. However, AFM measurements indicate that the CH₃NH₃PbI₃/P3HT interface has a R_{rms} of 20-30 nm. Again, considering that the R_{rms} value represents the standard deviation of the sample height, the maximum peak-to-trough variation in the perovskite interface is closer to 60-90 nm. As a result, charge carriers can be extracted from much deeper within the perovskite film than would be the case if the CH₃NH₃PbI₃/P3HT interface were completely planar (Figure 5.13). Although there is still a very small section of the perovskite film that still does not contribute to the overall photocurrent in this model (< 30 nm), the discrepancy is quite small, and likely due to slightly longer charge carrier diffusion lengths in our films.

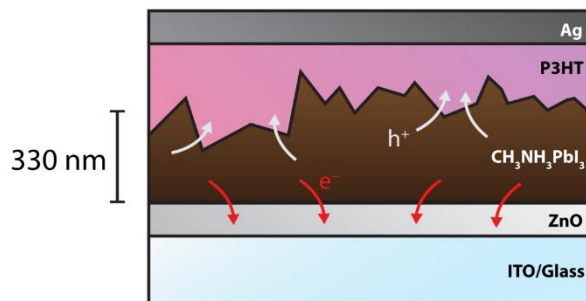


Figure 5.13. Schematic of the ITO/ZnO/CH₃NH₃PbI₃/P3HT/Ag devices tested in this work, showing the effect of the roughened CH₃NH₃PbI₃/P3HT interface on the hole-extraction efficiency.

Hysteresis in the J - V curve is now a well-known issue for perovskite solar cells,⁴⁶ and it results in a differential current response depending on the history of applied bias. In order to show that the trends observed⁷ in Figure 5.11 are the result of changes in film thickness (and not due to changes in hysteretic behaviour), we measured the J - V curves using both forward (short circuit

(SC) to forward bias (FB)) and reverse (forward-bias to short-circuit) scans for a series of representative devices (Figure 5.14). As with many planar heterojunction devices, the hysteresis is quite pronounced, with the reverse scan having a substantially higher efficiency (Figure 5.14a). However, the magnitude of the hysteresis was found to depend only very weakly on the thickness of the perovskite film (Figure 5.14b). This suggests that batch-to-batch variability in sample preparation has as much or more influence over the hysteresis than the film thickness. Therefore, while these results suggest that the absolute efficiencies of these devices are lower than might be expected from measurements of just the reverse scan, the overall trends in device performance (Figure 5.11) are actually due to changes in film thickness, and not due to changes in hysteretic behavior.

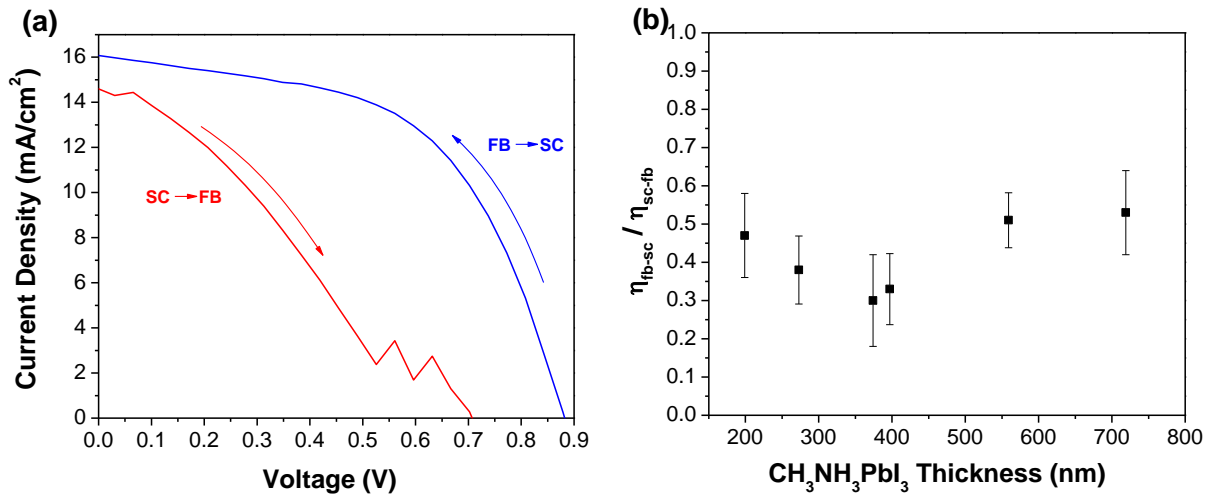


Figure 5.14. (a) J - V curves for a representative ITO/ZnO/CH₃NH₃PbI₃/P3HT/Ag device, measured from forward-bias (FB) to short-circuit (SC), and from short-circuit to forward-bias. (b) Ratio of the PCEs measured from FB to SC and from SC to FB as a function of perovskite film thickness. Measurements were the average of at least 6 devices, and the error bars represent plus or minus one standard deviation from the mean.

5.5. Conclusions

In summary, we have demonstrated that the thermal evaporation of PbI₂ films, in combination with a CH₃NH₃I treatment, is a highly reproducible method of preparing planar

heterojunction devices with very precise control over the perovskite film thickness. The optical properties and morphology of the perovskite films were measured as a function of film thickness, and the results correlated with changes in device performance. The improved light harvesting efficiency and reduced contact between electron- and hole-transport layers was found to improve the PCE and increase the recombination resistance for thicker films; however, once the film thickness significantly exceeded the carrier diffusion lengths in $\text{CH}_3\text{NH}_3\text{PbI}_3$, the efficiency declined sharply. At the optimum thickness of 330 nm, ITO/ZnO/ $\text{CH}_3\text{NH}_3\text{PbI}_3$ /P3HT/Ag devices were found to have PCEs of up to 11.3% when fabricated from evaporated PbI_2 layers, and 11.8% when prepared from solution-processed analogues; these efficiencies are among the highest reported for devices that use a P3HT hole-transport layer. It is expected that by better understanding the parameters that govern the efficiency of $\text{CH}_3\text{NH}_3\text{PbI}_3$ -based planar heterojunction devices, further improvements in device performance can be realized.

5.6. References

1. S. Kazim, M. K. Nazeeruddin, M. Grätzel and S. Ahmad, *Angew. Chem., Int. Ed.*, 2014, **53**, 2812-2824.
2. H. J. Snaith, *J. Phys. Chem. Lett.*, 2013, **4**, 3623-3630.
3. N.-G. Park, *J. Phys. Chem. Lett.*, 2013, **4**, 2423-2429.
4. N. Mohammad K, P. Gao and M. Grätzel, *Energy Environ. Sci.*, 2014, **7**, 2448-2463.
5. D. B. Mitzi, in *Prog. Inorg. Chem.*, John Wiley & Sons, Inc., 2007, pp. 1-121.
6. T. C. Sum and N. Mathews, *Energy Environ. Sci.*, 2014, **7**, 2518-2534.
7. S. D. Stranks, G. E. Eperon, G. Grancini, C. Menelaou, M. J. P. Alcocer, T. Leijtens, L. M. Herz, A. Petrozza and H. J. Snaith, *Science*, 2013, **342**, 341-344.
8. G. Xing, N. Mathews, S. Sun, S. S. Lim, Y. M. Lam, M. Grätzel, S. Mhaisalkar and T. C. Sum, *Science*, 2013, **342**, 344-347.
9. Y. Zhao and K. Zhu, *J. Phys. Chem. Lett.*, 2013, **4**, 2880-2884.
10. C. Wehrenfennig, G. E. Eperon, M. B. Johnston, H. J. Snaith and L. M. Herz, *Adv. Mater.*, 2014, **26**, 1584-1589.
11. A. Kojima, K. Teshima, Y. Shirai and T. Miyasaka, *J. Am. Chem. Soc.*, 2009, **131**, 6050-6051.
12. J. Burschka, N. Pellet, S. J. Moon, R. Humphry-Baker, P. Gao, M. K. Nazeeruddin and M. Grätzel, *Nature*, 2013, **499**, 316-319.
13. M. Liu, M. B. Johnston and H. J. Snaith, *Nature*, 2013, **501**, 395-398.
14. D. Liu and T. L. Kelly, *Nat. Photon.*, 2014, **8**, 133-138.

15. J. T.-W. Wang, J. M. Ball, E. M. Barea, A. Abate, J. A. Alexander-Webber, J. Huang, M. Saliba, I. Mora-Sero, J. Bisquert, H. J. Snaith and R. J. Nicholas, *Nano Lett.*, 2013, **14**, 724-730.
16. K. Wojciechowski, M. Saliba, T. Leijtens, A. Abate and H. J. Snaith, *Energy Environ. Sci.*, 2014, **7**, 1142–1147..
17. J.-H. Im, C.-R. Lee, J.-W. Lee, S.-W. Park and N.-G. Park, *Nanoscale*, 2011, **3**, 4088-4093.
18. H. S. Kim, C. R. Lee, J. H. Im, K. B. Lee, T. Moehl, A. Marchioro, S. J. Moon, R. Humphry-Baker, J. H. Yum, J. E. Moser, M. Grätzel and N. G. Park, *Sci Rep*, 2012, **2**, 591.
19. M. M. Lee, J. Teuscher, T. Miyasaka, T. N. Murakami and H. J. Snaith, *Science*, 2012, **338**, 643-647.
20. Z. Ku, Y. Rong, M. Xu, T. Liu and H. Han, *Sci. Rep.*, 2013, **3**, 3132.
21. W. A. Laban and L. Etgar, *Energy Environ. Sci.*, 2013, **6**, 3249-3253.
22. J. Shi, J. Dong, S. Lv, Y. Xu, L. Zhu, J. Xiao, X. Xu, H. Wu, D. Li, Y. Luo and Q. Meng, *Appl. Phys. Lett.*, 2014, **104**, 063901.
23. D. Bi, S.-J. Moon, L. Haggman, G. Boschloo, L. Yang, E. M. J. Johansson, M. K. Nazeeruddin, M. Grätzel and A. Hagfeldt, *RSC Advances*, 2013, **3**, 18762-18766.
24. J. H. Heo, S. H. Im, J. H. Noh, T. N. Mandal, C.-S. Lim, J. A. Chang, Y. H. Lee, H.-j. Kim, A. Sarkar, K. NazeeruddinMd, M. Grätzel and S. I. Seok, *Nat. Photon.*, 2013, **7**, 486-491.
25. J. H. Noh, S. H. Im, J. H. Heo, T. N. Mandal and S. I. Seok, *Nano Lett.*, 2013, **13**, 1764-1769.
26. J. M. Ball, M. M. Lee, A. Hey and H. J. Snaith, *Energy Environ. Sci.*, 2013, **6**, 1739-1743.
27. B. Cai, Y. Xing, Z. Yang, W.-H. Zhang and J. Qiu, *Energy Environ. Sci.*, 2013, **6**, 1480-1485.

28. E. Edri, S. Kirmayer, D. Cahen and G. Hodes, *J. Phys. Chem. Lett.*, 2013, **4**, 897-902.
29. N. Pellet, P. Gao, G. Gregori, T.-Y. Yang, M. K. Nazeeruddin, J. Maier and M. Grätzel, *Angew. Chem., Int. Ed.*, 2014, **53**, 3151-3157.
30. Y. Ogomi, A. Morita, S. Tsukamoto, T. Saitho, N. Fujikawa, Q. Shen, T. Toyoda, K. Yoshino, S. S. Pandey, T. Ma and S. Hayase, *J. Phys. Chem. Lett.*, 2014, **5**, 1004-1011.
31. J.-Y. Jeng, Y.-F. Chiang, M.-H. Lee, S.-R. Peng, T.-F. Guo, P. Chen and T.-C. Wen, *Adv. Mater.*, 2013, **25**, 3727-3732.
32. P. Docampo, J. M. Ball, M. Darwich, G. E. Eperon and H. J. Snaith, *Nat. Com.*, 2013, **4**, 2761.
33. O. Malinkiewicz, A. Yella, Y. H. Lee, G. M. Espallargas, M. Graetzel, M. K. Nazeeruddin and H. J. Bolink, *Nat. Photon.*, 2014, **8**, 128-132.
34. Q. Chen, H. Zhou, Z. Hong, S. Luo, H.-S. Duan, H.-H. Wang, Y. Liu, G. Li and Y. Yang, *J. Am. Chem. Soc.*, 2013, **136**, 622-625.
35. S. Sun, T. Salim, N. Mathews, M. Duchamp, C. Boothroyd, G. Xing, T. C. Sum and Y. M. Lam, *Energy Environ. Sci.*, 2014, **7**, 399-407.
36. A. Yella, L.-P. Heiniger, P. Gao, M. K. Nazeeruddin and M. Grätzel, *Nano Lett.*, 2014, **14**, 2591-2596.
37. C. Roldan-Carmona, O. Malinkiewicz, A. Soriano, G. Minguez Espallargas, A. Garcia, P. Reinecke, T. Kroyer, M. I. Dar, M. K. Nazeeruddin and H. J. Bolink, *Energy Environ. Sci.*, 2014, **7**, 994-997.
38. G. E. Eperon, V. M. Burlakov, P. Docampo, A. Goriely and H. J. Snaith, *Adv. Funct. Mater.*, 2013, **24**, 151-157.
39. K. Liang, D. B. Mitzi and M. T. Prikas, *Chem. Mater.*, 1998, **10**, 403-411.

40. B. Conings, L. Baeten, C. De Dobbelaere, J. D'Haen, J. Manca and H.-G. Boyen, *Adv. Mater.*, 2014, **26**, 2041-2046.
41. T. Baikie, Y. Fang, J. M. Kadro, M. Schreyer, F. Wei, S. G. Mhaisalkar, M. Graetzel and T. J. White, *J. Mater. Chem. A*, 2013, **1**, 5628-5641.
42. P. P. Boix, Y. H. Lee, F. Fabregat-Santiago, S. H. Im, I. Mora-Sero, J. Bisquert and S. I. Seok, *ACS Nano*, 2011, **6**, 873-880.
43. I. Mora-Seró, J. Bisquert, F. Fabregat-Santiago, G. Garcia-Belmonte, G. Zoppi, K. Durose, Y. Proskuryakov, I. Oja, A. Belaidi, T. Dittrich, R. Tena-Zaera, A. Katty, C. Lévy-Clément, V. Barrioz and S. J. C. Irvine, *Nano Lett.*, 2006, **6**, 640-650.
44. S. Chavhan, O. Miguel, H.-J. Grande, V. Gonzalez-Pedro, R. S. Sanchez, E. M. Barea, I. Mora-Sero and R. Tena-Zaera, *J. Mater. Chem. A*, 2014, **2**, 12754-12760.
45. M. H. Kumar, N. Yantara, S. Dharani, M. Graetzel, S. Mhaisalkar, P. P. Boix and N. Mathews, *Chem. Commun.*, 2013, **49**, 11089-11091.
46. H. J. Snaith, A. Abate, J. M. Ball, G. E. Eperon, T. Leijtens, N. K. Noel, S. D. Stranks, J. T.-W. Wang, K. Wojciechowski and W. Zhang, *J. Phys. Chem. Lett.*, 2014, **5**, 1511-1515.

CHAPTER 6

Effect of Relative Humidity on Crystal Growth, Device Performance and Hysteresis in Planar Heterojunction Perovskite Solar Cells

Mahesh K. Gangishetty, Robert W. J. Scott, and Timothy L. Kelly**

Department of Chemistry, University of Saskatchewan, 110 Science Place, Saskatoon, SK, S7N 5C9, Canada

In the previous project (*cf.* Chapter 5), the thickness of perovskite layer was optimized. However, the perovskite crystallites are smaller, and they are spread throughout the film with poor connectivity between each crystallite. It resists the efficient charge hopping from one crystallite to the other. This project investigates the growth of the crystallite to achieve the uniform perovskite layer by controlling the relative humidity in the atmosphere.

This chapter is a near-verbatim copy of a paper published in *Nanoscale*, **2016**, 8, 6300. I have solely performed all the experiments in this article. The first draft of the manuscript was written by me and it was revised by Prof. Tim Kelly and Prof. Robert Scott prior to publication.

6.1. Abstract

Due to the hygroscopic nature of organolead halide perovskites, humidity is one of the most important factors affecting the efficiency and longevity of perovskite solar cells. Although humidity has a long term detrimental effect on device performance, it also plays a key role during the initial growth of perovskite crystals. Here we demonstrate that atmospheric relative humidity plays a key role during the formation of perovskite thin films via the sequential deposition technique. Our results indicate that the RH has a substantial impact on the crystallization process, and hence on device performance. SEM and pXRD analysis show an increase in crystallite size with increasing humidity. At low RH, the formation of small cubic crystallites with large gaps between them is observed. The presence of these voids adversely affects device performance and leads to substantial hysteresis in the device. At higher RH, the perovskite crystals are larger in size, with better connectivity between the crystallites. This produced efficient planar heterojunction solar cells with low hysteresis. By careful control of the RH during the cell fabrication process, efficiencies of up to 12.2% are reached using P3HT as the hole-transport material

6.2. Introduction

Perovskite solar cells have attracted a great deal of interest in the field of solid state photovoltaics due to their large extinction coefficients and long charge carrier diffusion lengths.¹⁻
⁴ Within a period of 5 years, the efficiency of these devices has dramatically increased from 3.8% to 20.1%, making them one of the most promising alternatives to conventional silicon and CdTe technology.⁵⁻¹⁴

In the fabrication of high performance perovskite solar cells, the quality of the perovskite film plays a critical role.¹⁵ Recently, it was found that the presence of grain boundaries in the

perovskite film can affect not only the performance of the device, but also the amount of hysteresis observed in the J - V curves.^{16,17} As a result, a number of strategies for the production of high quality perovskite films have been reported, including the addition of chloride additives,¹⁷⁻²⁰ solvent engineering,¹³ and moisture^{6,21} and solvent annealing.²² By using the interdiffusion method, Hyeok *et al.* produced large perovskite crystallites, which led to state-of-the-art mesoscopic solar cells.¹² Nie *et al.*, by keeping the substrate above room temperature during the deposition process, were able to prepare high quality films containing millimeter scale perovskite crystallites with few grain boundaries.¹¹ This resulted in high performance, hysteresis-free devices with efficiencies of up to 18%. The importance of grain boundaries on the electronic properties of perovskite thin films was recently highlighted by recent work on perovskite single crystals; these studies suggest that the carrier diffusion lengths of $\text{CH}_3\text{NH}_3\text{PbI}_3$ single crystals are at least $2\ \mu\text{m}$,⁴ and may exceed $175\ \mu\text{m}$.¹

The formation of high quality perovskite films depends not only on the deposition process, but also on the atmospheric conditions present during crystal growth. Due to the highly hygroscopic nature of $\text{CH}_3\text{NH}_3\text{PbI}_3$, the RH is a key factor in both the growth and the degradation of perovskite crystals. Several research groups have observed that exposing perovskite films to high levels of moisture leads to degradation of the perovskite and the formation of hydrate phases;²³⁻²⁷ this in turn rapidly leads to device failure. Despite this problem, humidity has also been shown to have beneficial effects on the initial growth of perovskite films. Bass *et al.* observed that when $\text{CH}_3\text{NH}_3\text{PbX}_3$ ($X = \text{I}, \text{Br}$) powders were prepared under rigorously anhydrous conditions, the resulting powders showed very little long-range order; however, upon exposure to moisture, they immediately crystallized.²⁸ Similarly, by post-annealing perovskite films under a relative humidity of $30 \pm 5\%$, Zhou *et al.* were able to achieve uniform, crystalline, and pinhole-free

perovskite films.⁶ By increasing the relative humidity from 20% to 80% during the post-annealing step, further increases in the crystallinity of the perovskite films were observed.²¹ Spin coating the PbCl_2 and $\text{CH}_3\text{NH}_3\text{I}$ precursors under low RH conditions and subsequently annealing them under higher RH has also been shown to lead to improvements in long-range order and device performance.²⁹ However, all of these reports employed the single-step deposition method, where the effect of relative humidity was investigated during the post-annealing step. Analogous studies on the effect of humidity on films deposited *via* the two-step (sequential) deposition method^{30, 31} are lacking. Since the mechanism of crystal growth and subsequent film morphology are strongly dependent on the deposition method, the role of the RH during the sequential deposition of perovskite thin films needs to be addressed.

Here we demonstrate the effect of relative humidity on the growth of perovskite thin films deposited by the sequential deposition method. PbI_2 films were converted into $\text{CH}_3\text{NH}_3\text{PbI}_3$ inside a chamber of controlled RH, and larger perovskite crystallites were observed at higher RHs. This resulted in the formation of densely packed films with fewer grain boundaries, leading to an increase in device performance and a reduction in J - V curve hysteresis. By careful control of the RH, devices with PCEs of 12.2% were prepared using P3HT as the hole transport layer.

6.3. Experimental Section

6.3.1. Materials

Lead(II) iodide (99%), methylamine (37% in absolute ethanol), hydriodic acid (57% in H_2O), 4-*tert*-butylpyridine (96%) and lithium-bis(trifluoromethanesulfonyl)imide (99%) were purchased from Sigma-Aldrich. Poly(3-hexylthiophene) (electronic grade) and Ag pellets (99.99%) were purchased from Rieke Metals and Kurt J. Lesker, respectively. All commercial

reagents were used as received. Zinc oxide nanoparticles⁷ and methylammonium iodide³² were synthesized according to established procedures.

6.3.2. Device fabrication

Fabrication procedures for perovskite solar cells were similar to those outlined in our previous report.³³ ITO-coated glass substrates (Delta Technologies, $R_s = 15\text{-}25 \Omega/\text{sq}$) were cleaned by sequentially sonicating them for 30 min in 2% Extran 300 detergent and isopropanol, followed by drying under a stream of air. A thin layer of ZnO nanoparticles was spin coated at 3000 r.p.m. for 30 s using a 6 mg/mL colloidal ZnO NP solution in *n*-butanol. This procedure was repeated three times to produce a uniform 20 nm ZnO NP layer. A layer of PbI₂ (150 nm) was then deposited by thermal evaporation at a base pressure of 2×10^{-6} mbar. The PbI₂ films were then brought into a sealed atmospheric bag that was maintained at a constant RH (1 – 60%, Figure 6.1) and dipped in a solution of 10 mg/mL CH₃NH₃I in isopropanol for 3 min. After dipping, the substrates were dried by spinning at 3000 r.p.m. for 30 s, and then allowed to dry further inside the atmospheric bag for 10 minutes. A thin layer of P3HT-based hole transport material (20 mg of P3HT, 3.4 μL of 4-*tert*-butylpyridine, and 6.8 μL of a Li TFSI solution (28 mg Li-TFSI / 1 mL acetonitrile) all dissolved in 1 mL chlorobenzene) was spin coated at 1000 r.p.m. for 30 s under ambient conditions. Finally, a 50 nm thick Ag layer was deposited by thermal evaporation at a base pressure of 2×10^{-6} mbar.

6.3.3. Characterization

UV-Vis spectra were recorded on a Cary 6000 spectrophotometer. Scanning electron microscopy was carried out on a Hitachi SU8010 SEM operating at a 1.0 - 5.0 kV landing voltage. pXRD was performed on a PANalytical Empyrean diffractometer configured with a copper ($\lambda =$

1.54 Å) X-ray source. J - V curves were recorded in a N_2 -filled glovebox using a Keithley 2400 source-measure unit and a 450 W Class AAA solar simulator equipped with an AM1.5G filter (Sol3A, Oriel Instruments), at a calibrated intensity of 100 mW/cm^2 , as determined by a standard silicon reference cell (91150V, Oriel Instruments). The effective area of the device was defined as 0.0708 cm^2 using a non-reflective metal mask. IPCE spectra were measured in a N_2 -filled glovebox using a commercial IPCE setup (QE-PV-Si, Oriel Instruments). Monochromatic light was chopped at a frequency of 8 Hz and photocurrents measured using a lock-in amplifier.

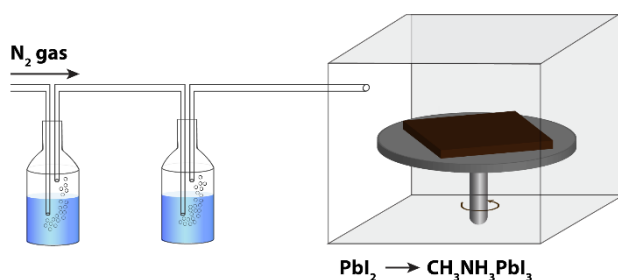


Figure 6.1. Schematic of the apparatus used to control the RH inside an atmospheric bag containing a spin coater. PbI_2 films are converted into $CH_3NH_3PbI_3$ by immersion in a solution of CH_3NH_3I , spin dried at 3000 r.p.m. for 30 s, and allowed to dry for a further 10 min.

6.4. Results and Discussion

6.4.1. Effect of humidity on perovskite crystal growth

In order to investigate the role of relative humidity in the growth of perovskite crystals during the sequential deposition process, an atmospheric bag of controllable RH was used (Figure 6.1). In this setup, dry N_2 was used as the carrier gas, and was flowed through a set of water bubblers into the atmospheric bag. A portable RH sensor was used to measure the humidity inside the bag, and the RH was controlled by adjusting the flow rate of the carrier gas. After achieving the desired humidity, the perovskite layer was deposited by the sequential deposition method. The device architecture used here is very similar to that described in our previous reports.^{7, 33} A thin

layer of ZnO was first deposited on ITO-coated glass, followed by a layer of PbI₂. In order to ensure the formation of reproducible PbI₂ films (and to eliminate any effect of varying humidity on the PbI₂ deposition step), the PbI₂ films were deposited by thermal evaporation. After deposition, the ITO/ZnO/PbI₂ films were brought into the atmospheric bag (which was maintained at the desired RH), and then immediately dipped into a solution of CH₃NH₃I. After 3 minutes of immersion, excess CH₃NH₃I solution was removed by spinning at 3000 r.p.m. for 30 s. The perovskite films were then allowed dry for a further 10 min inside the controlled RH environment. Perovskite films were prepared with RH ranging from 1% to 60%, and subsequently characterized by UV-Vis spectroscopy, pXRD and SEM. The absorption spectra of the films are shown in Figure 6.2a. The spectra are all qualitatively similar, consisting of intense absorption bands below 500 nm and a sharp band edge feature at 760 nm. With increasing RH, a small but steady increase in the optical density of the films is observed. At low RH (1%), the films were transparent and light brown in color, and as the RH increased, the films became both darker and more opaque (Figure 6.2b). Of all the samples studied, the perovskite films prepared at 60% RH showed the highest optical density across the entire visible spectrum. Further differences between the films become apparent at wavelengths close to the band edge (Figure 6.2a inset). All of the films showed a sharp decrease in the optical density, except the one prepared at 1% RH. Instead, it displayed a more gradual decay in the optical absorption, known as an Urbach tail.³⁴ This red tail in the optical absorption spectrum is attributed to electronic disorder within the film, and may be caused by the presence of trap states produced by the incomplete formation of the perovskite.^{17, 35}

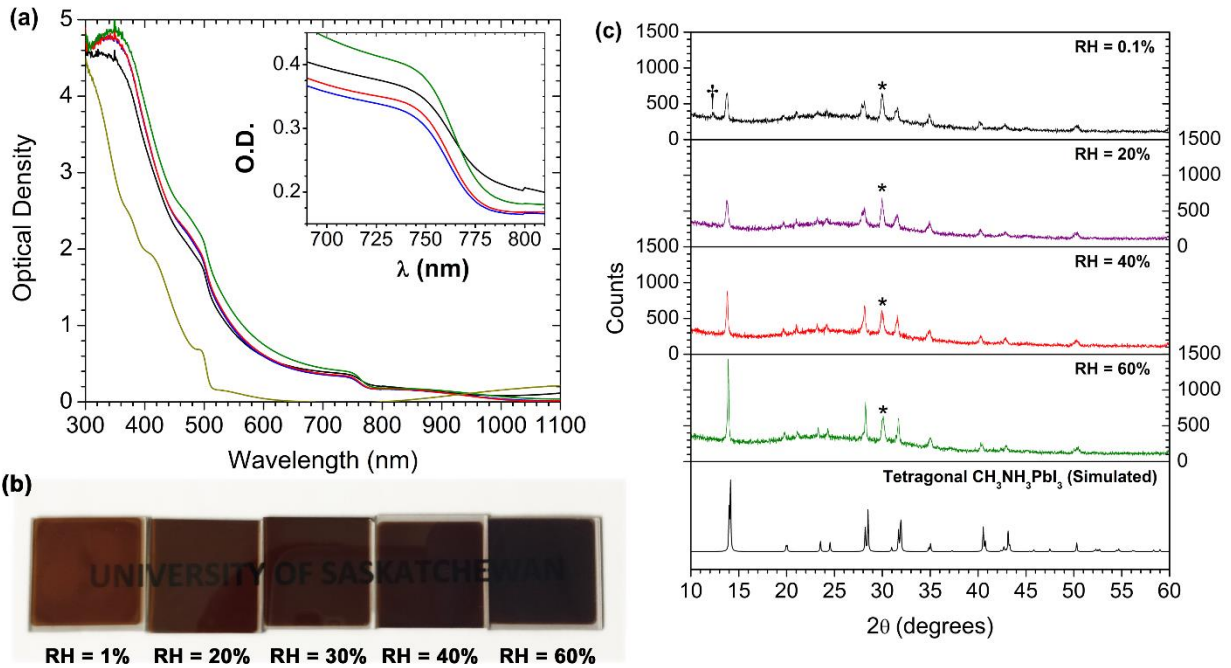


Figure 6.2 (a) UV-Vis absorption spectra for vapor deposited PbI_2 thin films (yellow line), and $\text{CH}_3\text{NH}_3\text{PbI}_3$ thin films prepared at 1% (black line), 33% (blue line), 40% (red line), and 60% (green line) RH. (b) Photographs of $\text{CH}_3\text{NH}_3\text{PbI}_3$ thin films prepared at various RH values. (c) Powder X-ray diffraction patterns for ITO/ PbI_2 / $\text{CH}_3\text{NH}_3\text{PbI}_3$ thin films prepared at various RH values. Peaks due to ITO and PbI_2 are marked with an asterisk (*) and dagger (†), respectively.

In order to understand the effect of RH on the crystallinity of the perovskite films, each of the samples was characterized by pXRD (Figure 6.2c). The diffraction pattern for all films agrees with the tetragonal structure of $\text{CH}_3\text{NH}_3\text{PbI}_3$.³⁶ The key differences observed between the samples are an increase in the intensity of the perovskite Bragg peaks (particularly the (110) and (220) reflections at *ca.* 14° and 28°), and a decrease in the peak width as the RH is increased. This indicates an increase in the size of the coherent scattering domains, suggesting the formation of larger crystallites at higher RH. Analysis of the (110) reflection by means of the Scherrer equation yielded minimum crystallite sizes of 25, 26, 40 and 61 nm for the films made at 0.1%, 20%, 40%, and 60% RH, respectively. Additionally, at the lowest (0.1%) RH, there is a weak peak corresponding to PbI_2 , indicating incomplete formation of the perovskite under this low humidity

condition. This is consistent with the presence of an Urbach tail in the absorption spectrum of this sample, and both the small crystallite size (with the associated increase in the number of surface states) and the residual PbI_2 may contribute to the observed electronic disorder.

These changes in crystallite size and film morphology were imaged by SEM. Figure 6.3 shows SEM images of both PbI_2 (Figure 6.3a) and perovskite films (Figure 6.3b – 6.3f). The vapor deposited PbI_2 film consisted of hexagonal flake-like structures (Figure 6.3a), in agreement with previous reports of thermally evaporated films.³³ Importantly, the SEM image of the perovskite film prepared at 1% RH showed small, cube-like crystallites with substantial empty space between them. As the RH increased to 20% RH, the film still appeared to consist of distinct cubic crystallites, but with improved connectivity between the grains. As the RH increased to 30% and above, the films became smoother and more planar, with fewer gaps between individual grains. As the RH increased further, there was a corresponding increase in the crystallite size, leading to more densely packed perovskite films. At the highest (60%) RH, the individual grains lost their distinctive cubic shape, and appeared more rounded; the edges of adjacent particles also appear to have fused together, providing much better connectivity within the film. These changes in crystallite size are consistent with the results of the Scherrer analysis of the pXRD data.

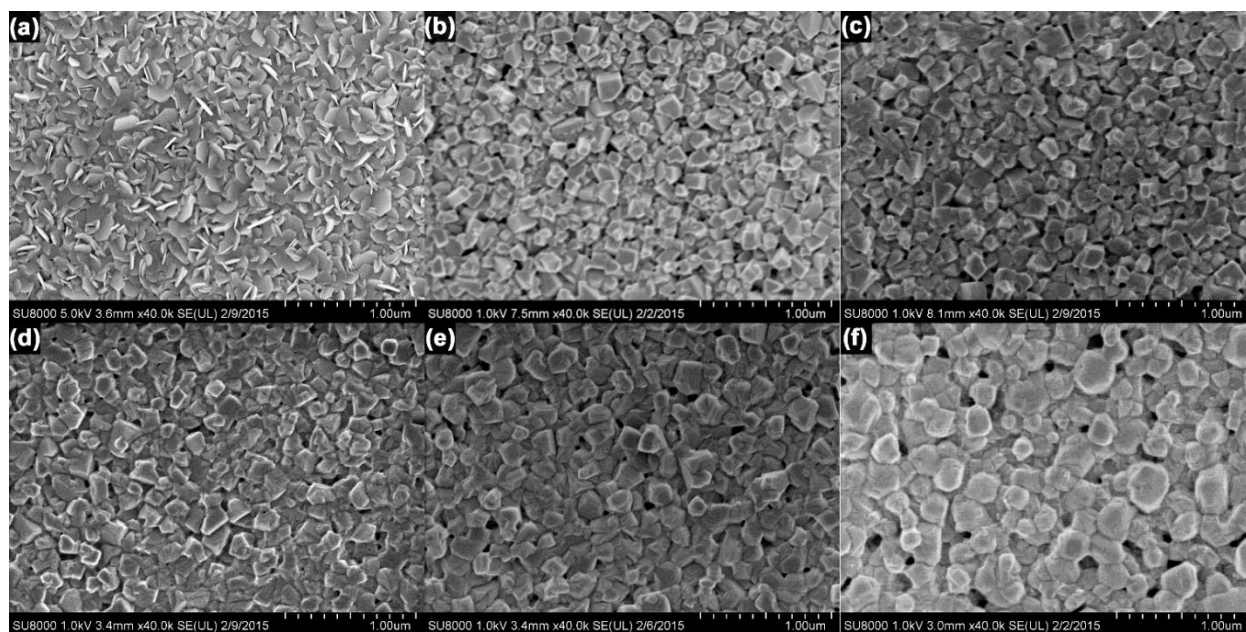


Figure 6.3. (a) SEM images of (a) PbI_2 , and $\text{CH}_3\text{NH}_3\text{PbI}_3$ films prepared at (b) 1%, (c) 20%, (d) 30%, (e) 40%, and (f) 60% RH.

From these analyses, it is evident that the RH has a substantial effect on the growth and crystallization of perovskite films. In the sequential deposition method, the intercalation of $\text{CH}_3\text{NH}_3\text{I}$ and the formation of $\text{CH}_3\text{NH}_3\text{PbI}_3$ starts at the surface of the PbI_2 crystallites immediately after immersion in the methylammonium iodide solution; however, ion diffusion within the bulk of the PbI_2 crystallites is relatively slow, and it takes several minutes for the conversion to $\text{CH}_3\text{NH}_3\text{PbI}_3$ to complete.³⁷ As a result, drying the film after 3 min is unlikely to result in the formation of well-ordered $\text{CH}_3\text{NH}_3\text{PbI}_3$ crystals. Additionally, given the insolubility of PbI_2 in isopropanol, the extent to which any one $\text{CH}_3\text{NH}_3\text{PbI}_3$ crystal can grow is limited by the size of its PbI_2 precursor. In the absence of other factors, this produces small, poorly crystalline perovskite grains that contain residual PbI_2 , entirely consistent with the data in Figure 6.2c. At this stage, the relative humidity around the perovskite film plays a crucial role in the growth of the crystals. In humid environments, water can be reversibly absorbed into the perovskite film, leading to the formation of hydrate phases.²³⁻²⁷ Ion diffusion in these less compact phases is expected to

be more facile; therefore, when the absorbed water eventually leaves the film, it leaves behind a higher quality crystal. This recrystallization process is conceptually similar to the solvent annealing procedures commonly employed in thin films of organic semiconductors.³⁸ Furthermore, the solubility of PbI_2 is much higher in water than in isopropanol, and the dissolution and recrystallization of grain edges may lead to the merging of adjacent grains within the film.²¹ This hypothesis is consistent with the rounding of the crystallite edges, the increase in grain size, and the improved inter-particle connectivity that are observed in Figure 6.3f.

6.4.2. Effect of humidity on device performance

After preparing perovskite films at various RH, the samples were removed from the atmospheric bag and assembled into complete devices. P3HT was used as the HTL, and was deposited under ambient laboratory conditions; a thin layer of Ag was then evaporated as the counter-electrode. J - V curves and incident photon-to-current efficiency spectra were measured in a N_2 -filled glovebox under AM1.5G illumination (Figure 6.4). Tabulated device performance parameters are shown in Table 6.1. The PCEs of the highest performance devices, as derived from the J - V curves, were 7.1, 9.0, 11.0, 12.2 and 10.0% for the devices prepared at 1, 20, 30, 40 and 60% RH, respectively. The efficiency of the highest performing device in this study (12.2%) is excellent for devices fabricated using P3HT as the HTL, and is likely limited by the hole mobility of P3HT, not by the quality of the perovskite film.^{33, 39} The increase in PCE with increasing RH can largely be attributed to changes in the film crystallinity and morphology. When the perovskite films are fabricated under dry conditions (1% RH), the films consist of small crystallites with numerous grain boundaries and poor inter-particle connectivity (Figure 6.3b). As a result, carrier transport within the film is poor, and the short-circuit current density is low. For the best devices, the J_{sc} increased from 14.2 mA/cm^2 (for the film prepared at 1% RH) to 18.9 mA/cm^2 when the

film was prepared at 40% RH. Similar trends are observed in the average device performance parameters (Table 6.1). At the same time, elimination of residual PbI_2 and growth in the average crystallite size is expected to reduce the number of trap states within the film, leading to the observed improvements in device fill factor as the RH is increased (Table 6.1).

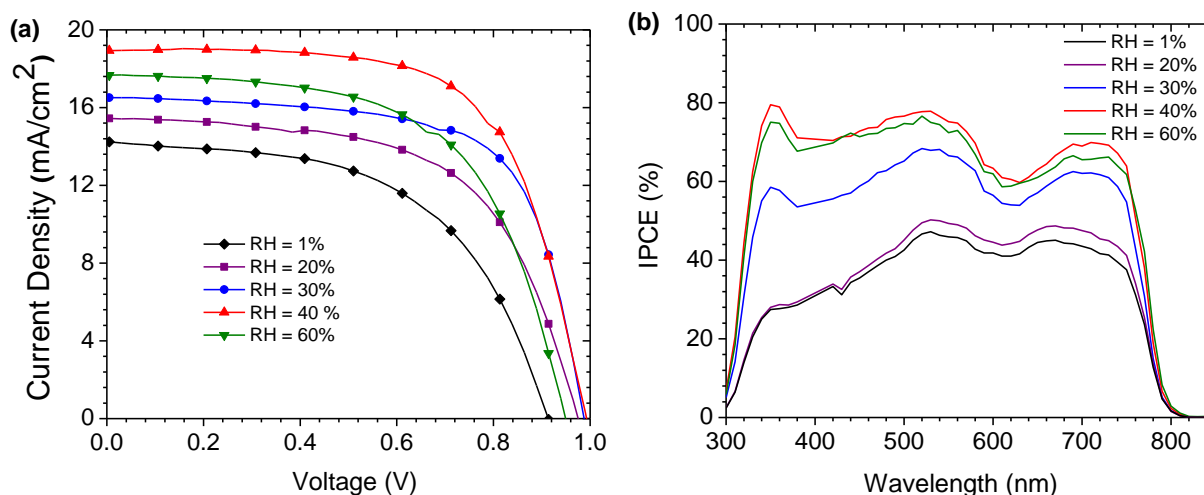


Figure 6.4 (a) J - V curves of the highest performance devices measured at a scan rate of 0.83 V/s. (b) IPCE spectra of the same devices.

In order to validate the trends in short-circuit current density (and hence PCE), IPCE spectra were measured for the best devices (Figure 6.4b). The J_{sc} values calculated by integrating the product of the AM1.5G photon flux and the IPCE spectra are in reasonable agreement with the J_{sc} values derived from the J - V curves (Table 6.1). As expected for devices based on $\text{CH}_3\text{NH}_3\text{PbI}_3$, all of the devices had broad IPCE spectra that spanned the range of 300 to 800 nm. The IPCE also increased with RH, which is consistent with the observed trends in J_{sc} . The most significant differences between the spectra, however, are the very pronounced changes in photon-to-current efficiency between 300 and 500 nm. In this wavelength range, the IPCE increases from *ca.* 30% in the devices prepared at 1% RH to a maximum of *ca.* 70% for those prepared at 40% RH. Yet despite these pronounced changes in IPCE, the light harvesting efficiency for all of the devices in

this range is *ca.* 95% (assuming a 4% loss due to reflection at the air/glass interface). This implies that the low IPCE for the devices made at low RH is due to charge carrier recombination, rather than transmission losses. Furthermore, due to the extremely high absorption cross section of $\text{CH}_3\text{NH}_3\text{PbI}_3$ in this wavelength range, most of these photons are absorbed by a thin perovskite layer at the $\text{ZnO}/\text{CH}_3\text{NH}_3\text{PbI}_3$ interface; this suggests that the recombination losses are most pronounced in this spatial region. Schlipf *et al.* used grazing incidence small angle X-ray scattering to evaluate the distribution of crystallite sizes within perovskite films prepared via the two-step deposition method.⁴⁰ Their results suggest that due to strain-induced fracturing of the growing perovskite crystals, smaller crystallites are produced closer to the substrate, with larger grain sizes at the surface of the film. Such a grain size distribution would produce a higher concentration of trap states close to the ZnO interface, and would explain the IPCE losses observed in the blue region of the spectrum (Figure 6.4b). This problem would be exacerbated in films prepared at low RH, where the grain sizes are smaller overall, and there is limited opportunity for recrystallization processes to occur. It should be noted that humidity-induced changes to the ZnO charge transfer resistance cannot be ruled out, and may also contribute to the changes in the IPCE spectra. Regardless, it is clear that the relative humidity has a dramatic effect on both perovskite crystal growth and device performance.

Table 6.1. Average device characteristics for perovskite solar cells measured at a scan rate of 0.1 V/s. Values shown in parentheses are for the highest performance devices measured at a scan rate of 0.83 V/s.

RH (%)	V_{oc} (V)	J_{sc} (mA/cm ²)	J_{sc} (mA/cm ²) from IPCE	FF	PCE (%)	PCE (%) from steady-state data
1	0.88 ± 0.03	12 ± 1 (14.2)	10.4	0.44 ± 0.04	4.6 ± 0.8 (7.1)	3.4
20	0.91 ± 0.04	13 ± 3 (15.4)	11.1	0.48 ± 0.07	6 ± 2 (9.1)	9.0
30	0.94 ± 0.03	15.2 ± 0.5 (16.5)	15.2	0.59 ± 0.05	9 ± 1 (11.0)	10.2
40	0.94 ± 0.03	17 ± 1 (18.9)	17.6	0.57 ± 0.04	9 ± 2 (12.2)	11.2
60	0.94 ± 0.01	16 ± 1 (17.6)	17.1	0.55 ± 0.02	8.2 ± 0.8 (10.0)	9.3

6.4.3. Effect of humidity on device hysteresis

One of the major concerns of perovskite solar cells is the hysteresis that is often observed in the J - V curves.^{16, 41-43} In order to quantify the amount of hysteresis in our devices, we measured the J - V curves at slow scan rates in both scan directions: forward bias-to-short circuit and short circuit-to-forward bias. Figure 6.5a shows both J - V curves for the best device made at 40% RH. Comparing the FB-SC scan in Figure 6.5a to a faster scan (0.83 V/s) in the same direction on the same device (Figure 6.4a), the J_{sc} and V_{oc} are similar, but the fill factor is reduced from 65% to 61% in the slower scan. This leads to a slight decrease in the PCE, from 12.2% to 11.3%. Changing the scan direction decreased the PCE further, to 10.0%. Although a relatively small effect, this clearly indicates the presence of hysteresis in the device. The J - V curves for the best devices prepared at other RH values are plotted in Figure 6.6, and the ratio of the PCEs measured from the forward (SC-FB) and reverse (FB-SC) scans (η_{fwd} / η_{rev}) is plotted as a function of RH (Figure 6.5b). The devices fabricated at 1% RH displayed the most pronounced hysteretic behavior.

Comparing the fast (Figure 6.4a) and slow (Figure 6.6a) scan rates, the device showed a decrease in both J_{sc} and FF, from 14.2 mA/cm² and 55% at 0.83 V/s, to 12.9 mA/cm² and 50% at 0.1 V/s, which leads to a decrease in PCE from 7.1% to 5.8%. Upon changing the scan direction at the slower scan rate, the efficiency drops further to 4.8%. As the RH during the film deposition step is increased, the degree of hysteresis in the devices drops substantially (Figure 6.5b). For the devices prepared at 60% RH (Figure 6.6e), the average ratio of the efficiencies obtained from forward and reverse scans is 96%, indicating very little dependence of the PCE on scan direction. It has been demonstrated that the hysteresis observed in perovskite solar cells can be caused by several factors: (i) trap states originating from either inherent defects in the perovskite or from grain boundaries,¹⁶ or (ii) contact resistance at either the ETL/CH₃NH₃PbI₃ or CH₃NH₃PbI₃/HTL interfaces.⁴³ The hysteresis observed in the devices prepared at low RH is likely caused by the numerous grain boundaries present in the film, which act as charge traps in the device. At higher RH, the increase in the size and connectivity of the crystallites reduces the number of trap states, and in turn a reduction in the device hysteresis is observed.

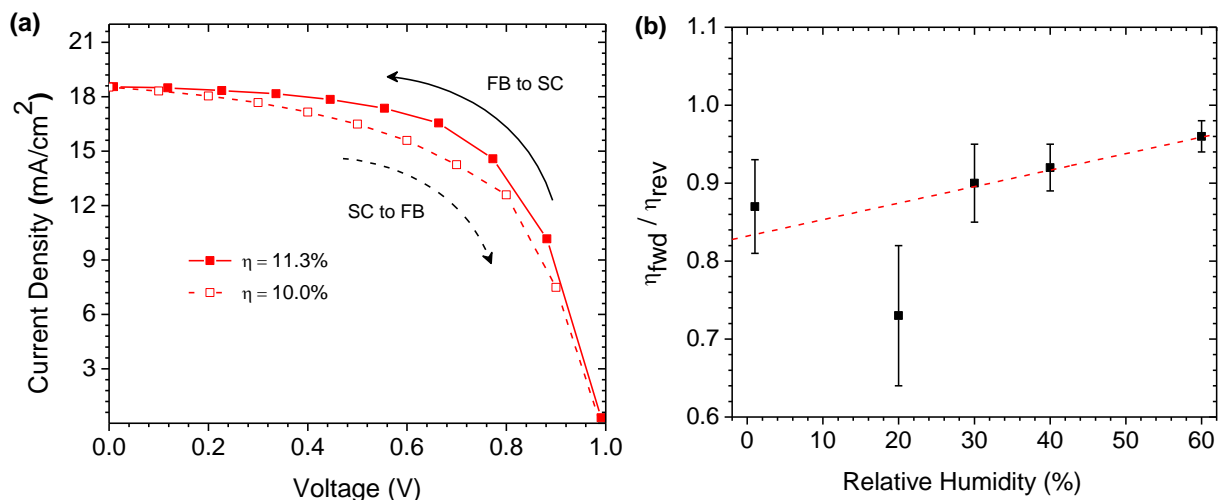


Figure 6.5. (a) J - V curves measured at 0.1 V/s for the best device prepared at 40% RH. (b) Ratio of PCEs determined from forward (SC-FB) and reverse (SC-FB) scans as a function of RH. The linear fit is a guide to the eye.

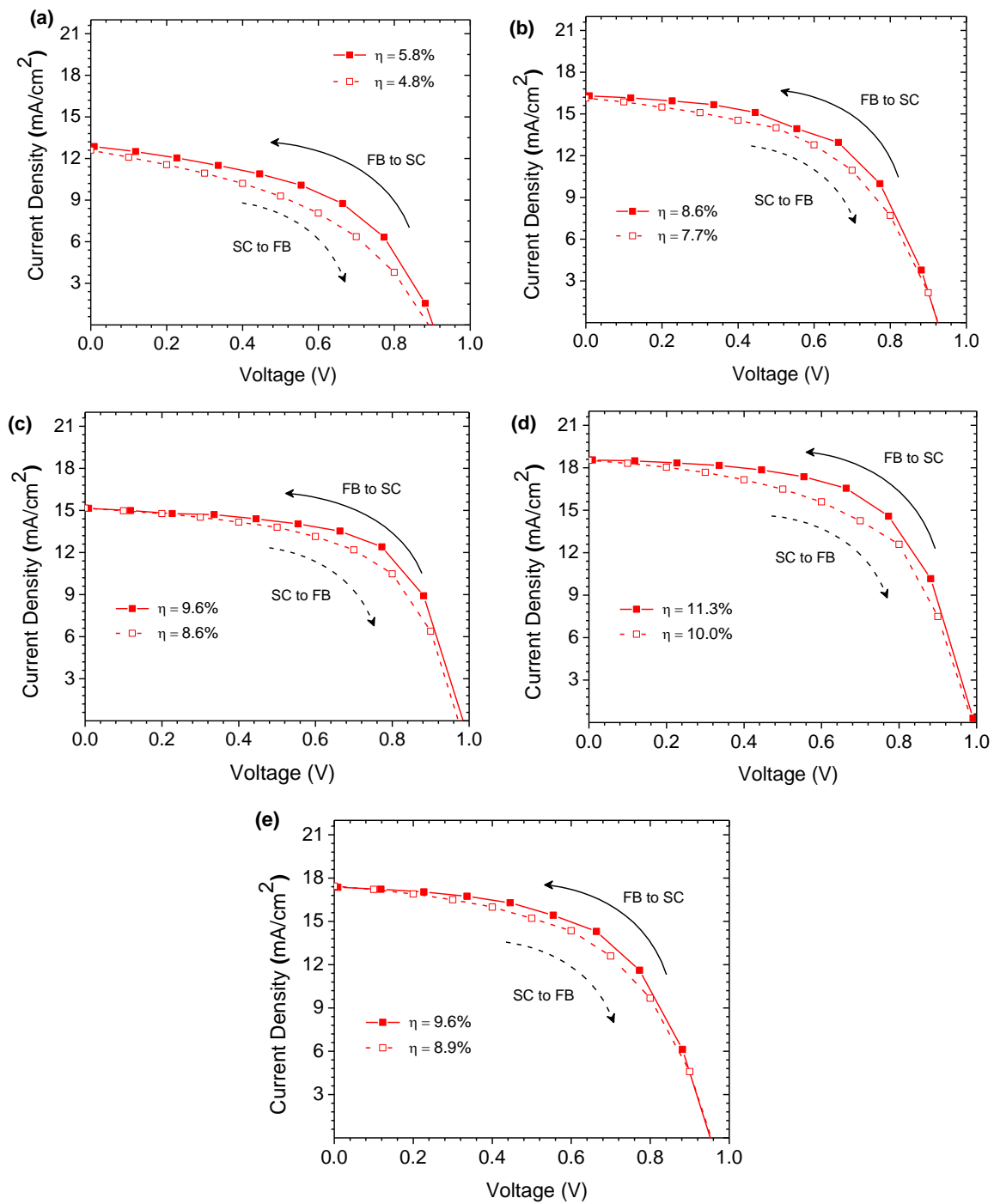


Figure 6.6. J–V curves measured at 0.1 V/s for devices prepared at: (a) 1%, (b) 20%, (c) 30%, (d) 40%, and (e) 60% RH.

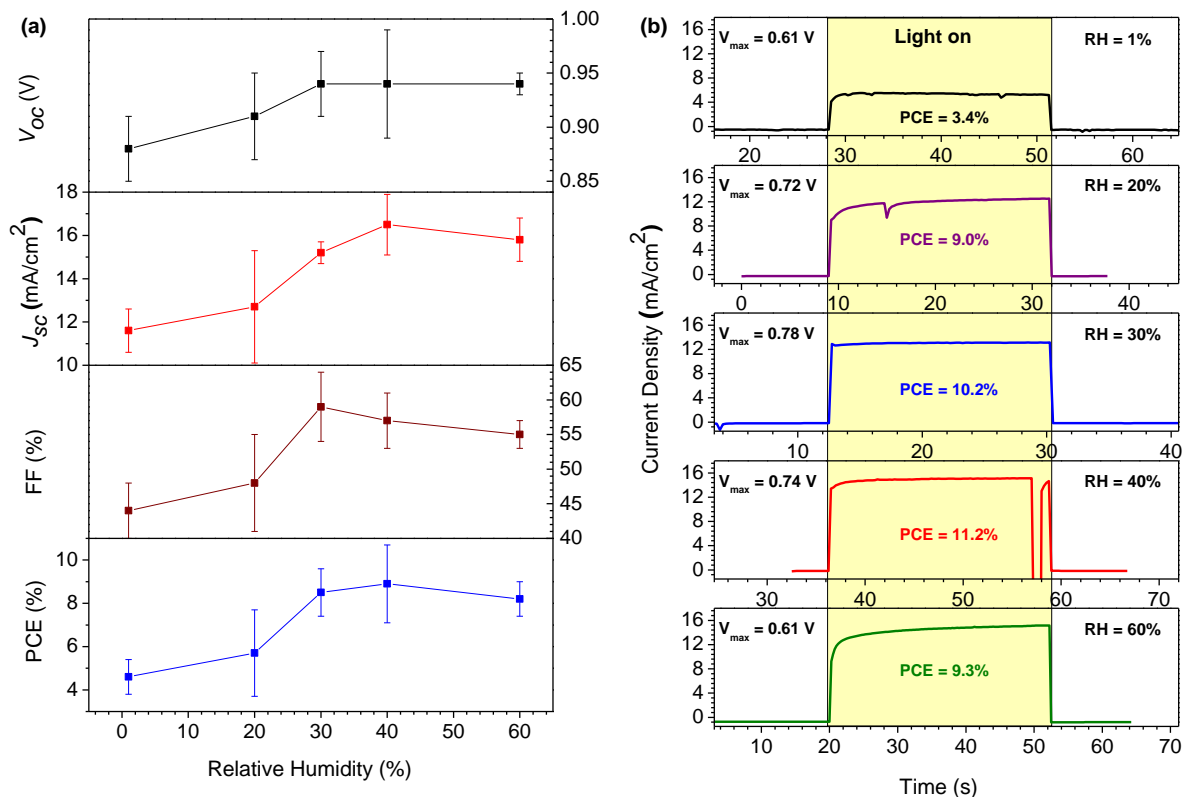


Figure 6.7. (a) Average device performance characteristics (measured at a scan rate of 0.1 V/s) as a function of relative humidity. Error bars represent plus or minus one standard deviation from the mean. (b) Steady-state current densities for representative devices at each relative humidity.

The average device characteristics as a function of relative humidity are plotted in Figure 6.7a. The key trends are an increase in J_{sc} and FF as the RH is increased, consistent with the elimination of grain boundaries and the crystal growth observed in the perovskite films. In order to further probe the degree of device hysteresis, and to evaluate the device performance under more realistic conditions, we recorded the steady-state power output for representative devices at each RH. The devices were kept at the maximum power point (as determined from the J - V curve) and the photocurrents were recorded as a function of time (Figure 6.7b). The stabilized PCE of the device made at 1% RH was found to be 3.4%, whereas it was measured to be 7.1% from the fast scan J - V curve (Figure 6.4a). This highlights the large degree of hysteresis observed in the device. For the devices prepared at 20% and above RH, however, the difference between the PCE obtained

from the J - V curves and the stabilized power output is more modest (Table 6.1). The best performing device in the current study (prepared at 40% RH) showed a stabilized PCE of 11.2%, which was much closer to the efficiency calculated from the J - V curve (12.2%); this reinforces the idea that the larger crystallite sizes observed in the perovskite layer lead to a reduction in the amount of device hysteresis.

6.5. Conclusions

In conclusion, we prepared perovskite films by the sequential deposition method in a controlled humidity environment. We found an increase in the crystallinity of the perovskite films with increasing RH. At low RH, the films consisted of small cubic crystals with large gaps between them; however, after increasing the RH, larger grains with better inter-particle connectivity were observed. These changes in film crystallinity and morphology have a pronounced effect on device performance, and films prepared at higher RH values produced devices with higher efficiencies and reduced device hysteresis. By carefully controlling the RH, we were able to achieve PCEs of up to 12.2% using P3HT as HTL. These results clearly demonstrate that careful control of all environmental parameters involved in the formation of perovskite films is necessary if reproducible fabrication procedures for perovskite solar cells are to be established.

6.6. References

1. Q. Dong, Y. Fang, Y. Shao, P. Mulligan, J. Qiu, L. Cao and J. Huang, *Science*, 2015, **347**, 967-970.
2. S. D. Stranks, G. E. Eperon, G. Grancini, C. Menelaou, M. J. P. Alcocer, T. Leijtens, L. M. Herz, A. Petrozza and H. J. Snaith, *Science*, 2013, **342**, 341-344.
3. G. Xing, N. Mathews, S. Sun, S. S. Lim, Y. M. Lam, M. Grätzel, S. Mhaisalkar and T. C. Sum, *Science*, 2013, **342**, 344-347.
4. D. Shi, V. Adinolfi, R. Comin, M. Yuan, E. Alarousu, A. Buin, Y. Chen, S. Hoogland, A. Rothenberger, K. Katsiev, Y. Losovyj, X. Zhang, P. A. Dowben, O. F. Mohammed, E. H. Sargent and O. M. Bakr, *Science*, 2015, **347**, 519-522.
5. A. Kojima, K. Teshima, Y. Shirai and T. Miyasaka, *J. Am. Chem. Soc.*, 2009, **131**, 6050-6051.
6. H. Zhou, Q. Chen, G. Li, S. Luo, T.-b. Song, H.-S. Duan, Z. Hong, J. You, Y. Liu and Y. Yang, *Science*, 2014, **345**, 542-546.
7. D. Liu and T. L. Kelly, *Nat. Photon.*, 2014, **8**, 133-138.
8. J. Burschka, N. Pellet, S. J. Moon, R. Humphry-Baker, P. Gao, M. K. Nazeeruddin and M. Grätzel, *Nature*, 2013, **499**, 316-319.
9. M. Liu, M. B. Johnston and H. J. Snaith, *Nature*, 2013, **501**, 395-398.
10. M. M. Lee, J. Teuscher, T. Miyasaka, T. N. Murakami and H. J. Snaith, *Science*, 2012, **338**, 643-647.
11. W. Nie, H. Tsai, R. Asadpour, J.-C. Blancon, A. J. Neukirch, G. Gupta, J. J. Crochet, M. Chhowalla, S. Tretiak, M. A. Alam, H.-L. Wang and A. D. Mohite, *Science*, 2015, **347**, 522-525.

12. J.-H. Im, I.-H. Jang, N. Pellet, M. Grätzel and N.-G. Park, *Nat. Nanotechnol.*, 2014, **9**, 927-932.
13. N. J. Jeon, J. H. Noh, Y. C. Kim, W. S. Yang, S. Ryu and S. I. Seok, *Nat. Mater.*, 2014, **13**, 897-903.
14. M. A. Green, K. Emery, Y. Hishikawa, W. Warta and E. D. Dunlop, *Prog. Photovolt: Res. Appl.*, 2015, **23**, 1-9.
15. S. D. Stranks, P. K. Nayak, W. Zhang, T. Stergiopoulos and H. J. Snaith, *Angew. Chem., Int. Ed.*, 2015, **54**, 3240-3248.
16. Y. Shao, Z. Xiao, C. Bi, Y. Yuan and J. Huang, *Nat. Com.*, 2014, **5**, 5784.
17. W. Zhang, M. Saliba, D. T. Moore, S. K. Pathak, M. T. Hörantner, T. Stergiopoulos, S. D. Stranks, G. E. Eperon, J. A. Alexander-Webber, A. Abate, A. Sadhanala, S. Yao, Y. Chen, R. H. Friend, L. A. Estroff, U. Wiesner and H. J. Snaith, *Nat. Com.*, 2015, **6**, 6142.
18. S. T. Williams, F. Zuo, C.-C. Chueh, C.-Y. Liao, P.-W. Liang and A. K. Y. Jen, *ACS Nano*, 2014, **8**, 10640-10654.
19. S. Colella, E. Mosconi, P. Fedeli, A. Listorti, F. Gazza, F. Orlandi, P. Ferro, T. Besagni, A. Rizzo, G. Calestani, G. Gigli, F. De Angelis and R. Mosca, *Chem. Mater.*, 2013, **25**, 4613-4618.
20. P.-W. Liang, C.-Y. Liao, C.-C. Chueh, F. Zuo, S. T. Williams, X.-K. Xin, J. Lin and A. K. Y. Jen, *Adv. Mater.*, 2014, **26**, 3748-3754.
21. J. You, Y. Yang, Z. Hong, T.-B. Song, L. Meng, Y. Liu, C. Jiang, H. Zhou, W.-H. Chang and G. Li, *Appl. Phys. Lett.*, 2014, **105**, 183902.
22. Z. Xiao, Q. Dong, C. Bi, Y. Shao, Y. Yuan and J. Huang, *Adv. Mater.*, 2014, **26**, 6503-6509.

23. B. R. Vincent, K. N. Robertson, T. S. Cameron and O. Knop, *Can. J. Chem.*, 1987, **65**, 1042-1046.
24. F. Hao, C. C. Stoumpos, Z. Liu, R. P. H. Chang and M. G. Kanatzidis, *J. Am. Chem. Soc.*, 2014, **136**, 16411-16419.
25. J. Yang, B. D. Siempelkamp, D. Liu and T. L. Kelly, *ACS Nano*, 2015, **9**, 1955-1963.
26. J. A. Christians, P. A. Miranda Herrera and P. V. Kamat, *J. Am. Chem. Soc.*, 2015, **137**, 1530-1538.
27. A. M. A. Leguy, Y. Hu, M. Campoy-Quiles, M. I. Alonso, O. J. Weber, P. Azarhoosh, M. van Schilfgaarde, M. T. Weller, T. Bein, J. Nelson, P. Docampo and P. R. F. Barnes, *Chem. Mater.*, 2015, **27**, 3397-3407.
28. K. K. Bass, R. E. McAnally, S. Zhou, P. I. Djurovich, M. E. Thompson and B. C. Melot, *Chem. Commun.*, 2014, **50**, 15819-15822.
29. H. Gao, C. Bao, F. Li, T. Yu, J. Yang, W. Zhu, X. Zhou, G. Fu and Z. Zou, *ACS Appl. Mater. Interfaces*, 2015, 9110-9117.
30. N. Yantara, D. Sabba, F. Yanan, J. M. Kadro, T. Moehl, P. P. Boix, S. Mhaisalkar, M. Grätzel and C. Grätzel, *Chem. Commun.*, 2015, **51**, 4603-4606.
31. K. Liang, D. B. Mitzi and M. T. Prikas, *Chem. Mater.*, 1998, **10**, 403-411.
32. J. H. Im, C. R. Lee, J. W. Lee, S. W. Park and N. G. Park, *Nanoscale*, 2011, **3**, 4088-4093.
33. D. Liu, M. K. Gangishetty and T. L. Kelly, *J. Mater. Chem. A*, 2014, **2**, 19873-19881.
34. S. De Wolf, J. Holovsky, S.-J. Moon, P. Löper, B. Niesen, M. Ledinsky, F.-J. Haug, J.-H. Yum and C. Ballif, *J. Phys. Chem. Lett.*, 2014, **5**, 1035-1039.
35. J. Kim, S.-H. Lee, J. H. Lee and K.-H. Hong, *J. Phys. Chem. Lett.*, 2014, **5**, 1312-1317.

36. C. C. Stoumpos, C. D. Malliakas and M. G. Kanatzidis, *Inorg. Chem.*, 2013, **52**, 9019-9038.
37. Y. Wu, A. Islam, X. Yang, C. Qin, J. Liu, K. Zhang, W. Peng and L. Han, *Energy Environ. Sci.*, 2014, **7**, 2934-2938.
38. K. C. Dickey, J. E. Anthony and Y. L. Loo, *Adv. Mater.*, 2006, **18**, 1721-1726.
39. J. Xiao, J. Shi, H. Liu, Y. Xu, S. Lv, Y. Luo, D. Li, Q. Meng and Y. Li, *Adv. Energy Mater.*, 2015, **5**, 1401943-1401950.
40. J. Schlipf, P. Docampo, C. J. Schaffer, V. Körstgens, L. Bießmann, F. Hanusch, N. Giesbrecht, S. Bernstorff, T. Bein and P. Müller-Buschbaum, *J. Phys. Chem. Lett.*, 2015, **6**, 1265-1269.
41. E. L. Unger, E. T. Hoke, C. D. Bailie, W. H. Nguyen, A. R. Bowring, T. Heumuller, M. G. Christoforo and M. D. McGehee, *Energy Environ. Sci.*, 2014, **7**, 3690-3698.
42. H.-S. Kim and N.-G. Park, *J. Phys. Chem. Lett.*, 2014, **5**, 2927-2934.
43. H. J. Snaith, A. Abate, J. M. Ball, G. E. Eperon, T. Leijtens, N. K. Noel, S. D. Stranks, J. T.-W. Wang, K. Wojciechowski and W. Zhang, *J. Phys. Chem. Lett.*, 2014, **5**, 1511-1515.

CHAPTER 7

Improving the Rates of Pd-Catalyzed Reactions by Exciting the Surface Plasmons of AuPd Bimetallic Nanotriangles

Mahesh K. Gangishetty^a, Adriana M. Fontes^b, Marcos Malta^b, Timothy L. Kelly^{a}, Robert W. J. Scott^{a*}*

^aDepartment of Chemistry, University of Saskatchewan, 110 Science Place, Saskatoon, SK, S7N 5C9, Canada.

^bInstituto de Química, Universidade Federal da Bahia, Campus Ondina, Salvador (BA), Brazil.

This chapter focuses on light harvesting for heterogeneous Pd catalysis using plasmonic Au nanotriangles. Here, the synthesis of AuPd nanotriangles and their catalytic activity towards Suzuki coupling and hydrogenation reactions are discussed. The reactions were performed in both light and dark conditions. Upon illumination, the nanotriangles showed enhanced rates of the reaction. In Suzuki reactions, the control experiments showed that the enhancement is primarily due to the plasmonic heating effect. However, there could be a contribution from plasmonic hot electron injection effects. In the hydrogenation reactions, the enhancement depends only on plasmonic heating effect.

This manuscript is in preparation. The work is done in collaboration with Adriana Fontes, and I would like to acknowledge her contribution. She synthesized AuPd nanotriangles and performed a hydrogenation reaction on 2-methy-3-butene-1-ol in presence and absence of the light. My contribution to the paper is the design, synthesis, and characterization of triangular AuPd nanotriangles and also, I performed all the Suzuki coupling reactions. The first draft of the manuscript was written by myself and is in revisions stage with Prof. Tim Kelly and Prof. Robert Scott.

7.1. Abstract

Gold nanoparticles exhibit unique optical properties due to surface plasmon oscillations when they interact with light. By utilizing their optical properties, the rates of many chemical reactions have been improved in the presence of visible light. Their properties are highly tunable based on the size and shape of the nanoparticle. Here, we have used anisotropic AuPd bimetallic nanotriangles to improve the rates of Pd-catalyzed reactions in the presence of visible light. We synthesized AuPd core-shell bimetallic nanotriangles and performed Suzuki cross-coupling and hydrogenation reactions in light and dark conditions. Upon illuminating AuPd nanotriangles with an array of green LEDs (power ~ 500 mW), an enhanced catalytic activity of palladium was observed. In order to understand the relative contributions of individual plasmonic effects, such as plasmonic hot electron transfer and plasmonic heating effects, the reaction temperatures were monitored, and careful control experiments were run at different temperatures. Our results indicated that the enhancement in the rate of these Pd-catalyzed reactions is primarily due to the plasmonic heating effect.

7.2. Introduction

Plasmonic nanoparticles have been extensively studied as light harvesting materials in various applications such as photovoltaics,¹⁻⁴ biotechnology,⁵ catalysis,⁶ and surface-enhanced Raman spectroscopy.⁷ In particular, employing their light trapping properties to drive chemical transformations is an emerging field.⁶ Upon interacting with certain frequencies of light, the metal nanoparticles show unique optical properties due to the collective oscillation of their conduction band electrons. This phenomenon is called localized surface plasmon resonance. The optical characteristics of plasmonic nanoparticles are tunable based on the size and the shape of the

nanoparticle.⁸ The energy accumulated in these oscillating surface plasmons can be used in several ways to accelerate the rates of chemical reactions. This energy can be either directly used to drive a chemical reaction,^{6, 9} or it can be transferred to an existing catalyst such as a semiconducting metal oxide (e.g., TiO₂, CeO₂) or a metal (e.g., Cu, Pd, and Ni) nanoparticle.^{4, 10-13} Among these catalysts, enhancing the activity of Pd nanoparticles using solar energy is attractive since Pd nanoparticles are known to catalyze many organic reactions, including C-C bond forming reactions. Also, these heterogeneous Pd catalysts can be easily recovered from the reaction mixture and reused for several reaction cycles. Recently, by using plasmonic metal nanoparticles, the rates of Pd-catalyzed reactions such as cross-coupling,^{14, 15} hydrogenation,¹⁶⁻¹⁹ and oxidation reactions²⁰⁻²² have been improved, and it has been found that the bimetallic nanoparticles show superior activity compared to the pure metals.^{23, 24} The most studied bimetallic catalysts in plasmon-enhanced Pd-catalyzed reactions are AuPd bimetallic nanoparticles. Here, the Au/Pd ratio has shown to be critical for both preserving the Au plasmonic properties as well as the catalytic activity of Pd.²⁴ In addition to this, the power of incoming light also plays a key role in the plasmonic enhancement.^{15, 24}

It has been demonstrated that two plasmonic effects contribute to the enhancement of Pd-catalytic activity; these two effects are plasmonic local heating effects, and plasmonic hot electron transfer.^{14, 15, 24} After the excitation of surface plasmons, they can decay non-radiatively *via* generation of hot electrons in the metal nanoparticles. The energy of these hot electrons is either redistributed among the ground state electrons through electron-electron scattering or dissipated in the form of heat by electron-phonon scattering.^{4, 25, 26} The heat generated by the metal nanoparticles can increase the temperature at their surface up to 500 °C.⁶ In a colloidal solution of metal nanoparticles, this local heat dissipates into the solution and increases the overall

temperature of the bulk solution. This plasmonic photothermal effect has been found to accelerate the rates of many Pd-catalyzed reactions when bimetallic AuPd nanoparticles are employed.^{15, 27, 28} In addition to this, plasmonic hot electron transfer from Au to Pd in AuPd alloys can also contribute to improving the rates of the reactions.^{24, 29} It has been demonstrated that in AuPd nanoparticles, the Fermi energy levels of Au and Pd are close to each other (Pd is 5.0 eV, and Au is 4.7 eV).³⁰ Upon exciting the surface plasmons in Au, the hot electrons can easily be transferred from Au to Pd. As a result of this transfer, the number of active catalytic sites on Pd increases, and this improves the overall rate of the reaction.¹⁴ Such hot electron transfer from Au to Pd was described by recording a single particle photoluminescence (PL) spectra from an Au-Pd nanorod and an Au nanorod.³¹ The authors observed a decrease in the PL intensity for the AuPd nanorod compared to the Au nanorod, which was attributed to hot electron transfer from Au to Pd. Further, by using a TiO₂ spacer between Au and Pd in an AuPd nanoparticle, Wang *et al.* controlled the electron transfer from Au to Pd. This resulted in a decrease in the conversion of a Suzuki reaction compared to AuPd without any spacer.¹⁵ However, the difference in conversion was very low, and it also depended on the power of the incoming light. Another study, with the help of DFT calculations, reported that the hot electrons generated in AuPd nanoparticles are directly transferred to the adsorbed molecules and drive the chemical transformation.¹⁴

All these plasmonic effects rely heavily on the power of the incoming light as well as on the morphology of the metal nanoparticle. Various morphologies of Au and Ag nanoparticles such as nanorods,^{15, 31, 32} nanowheels,²⁸ nanocages¹⁹ and spherical nanoparticles^{14, 18, 24, 33} have been used to enhance the catalytic activity of palladium. Here, we employed plasmonic Au nanotriangles to harvest light in order to photophysically improve the rate of Pd-catalyzed reactions. Due to the presence of sharp features, the nanotriangles are expected to show strong

plasmonic effects compared to other shapes.^{34, 35} Also, due to the plate-like morphology of a nanotriangle, the number of active sites (i.e., surface area) available for catalytic reactions to take place is higher compared to a spherical nanoparticle. By using AuPd bimetallic nanotriangles, we performed Suzuki cross-coupling and hydrogenation reactions in both dark and light conditions. The reactions performed in the light showed higher conversions compared to the ones carried out in the dark. The mechanism of this plasmonic enhancement was investigated by performing several control experiments. Our results indicate that the enhancements in the rates of both Suzuki and hydrogenation reactions upon illumination are mainly due to plasmonic heating effects. Further stability studies show that the sharp-featured triangles are unstable, and after two cycles of Suzuki reactions their catalytic activity is severely compromised.

7.3. Experimental Section

7.3.1. Materials

Hydrogen tetrachloroaurate(III) (99%), 4-iodobenzoic acid, and 2-methyl-3-buten-2-ol (98%) were purchased from Sigma-Aldrich. Potassium tetrachloropalladate (99%), cetyltrimethylammonium chloride (96%) and all the boronic acids used for Suzuki reactions were purchased from Alfa Aesar. Potassium iodide and sodium hydroxide were purchased from Fisher Scientific. All chemicals were used directly without any further purification, and aqueous solutions were prepared using Milli-Q water (18.2 M Ω ·cm).

7.3.2. Characterization

TEM images were collected using a HT7700 TEM operating at 100 kV. TEM samples were prepared by drop casting nanoparticle solutions onto a carbon-coated 300 mesh Cu TEM grid (Electron Microscopy Sciences). UV-vis spectra were measured using a Varian Cary

50 Bio UV–vis spectrophotometer with an optical path length of 1 cm. ^1H NMR spectra were collected by using a Bruker Avance 500 MHz spectrometer.

7.3.3. Methods

Synthesis of Au nanotriangles. Au nanotriangles were synthesized by following a literature procedure.³⁶ Briefly, aqueous CTAC (16.0 mL, 0.10 M) was dissolved in 20.0 mL Milli-Q water in a 250 mL Erlenmeyer flask. To this solution, aqueous solutions of KI (0.75 mL, 0.1 M), HAuCl_4 (0.80 mL, 25.4 mM) and NaOH (0.20 mL, 0.10 M) were added sequentially. At each addition, the solution was stirred manually by shaking the flask. Aqueous ascorbic acid (1.0 mL, 0.064 M) was then added, and then immediately, an aqueous NaOH (0.20 mL 0.10 M) solution was injected rapidly into the reaction mixture, while simultaneously shaking the flask. Finally, the entire mixture was kept undisturbed for 15 min until the solution became dark blue in color. This dark blue solution was centrifuged at 5500 rpm (4194 g) for 30 min, and then the supernatant was decanted. The Au nanotriangles were collected by redispersing the pellet in water.

Synthesis of AuPd nanotriangles. A concentrated Au nanotriangle solution (15 mL, optical density = 4.5 at 610 nm) was dispersed in aqueous CTAC (30 mL, 0.010 M) in an Erlenmeyer flask. To this mixture, an aqueous K_2PdCl_4 (2.0 mL, 0.010 M) solution was added while stirring the solution, which was maintained at 40 °C using a hot water bath. After 10 min of stirring, aqueous ascorbic acid (2.0 mL, 0.040 M) was added, the flask was covered, and the stirring was continued for 8 h at 40 °C by covering the flask with parafilm. Finally, this solution was centrifuged at 5500 rpm (4194 g) for 30 min, and the AuPd bimetallic nanotriangles were collected by decanting the supernatant. The AuPd nanotriangles were then dispersed in water.

7.3.4. Catalytic reactions

Suzuki cross-coupling reactions. In a model cross-coupling reaction, 0.5 mmol of p-iodobenzoic acid and 0.6 mmol of phenylboronic acid were taken up in a mixture of 8.0 mL of Milli-Q water and 2 mL of ethanol. To this mixture, 2.0 mmol of K_2CO_3 dissolved in 2.0 mL of water was added. The solution was mixed well to dissolve all of the reactants. Next, 2.0 mL of the as-synthesized AuPd nanotriangle solution (optical density = 4.5 at 532 nm) was added. The final optical density of the nanotriangles in the resulting solution was ~0.75 at 532 nm. This reaction was performed both with and without light illumination. At each hour, 200 μ L aliquots of the reaction mixture were collected, the reaction was quenched with 200 μ L of concentrated H_2SO_4 , and the products were extracted with dichloromethane. The solvent was evaporated in a stream of air, and the leftover solids were dissolved in $CDCl_3$ and characterized by 1H NMR. The rest of the cross-coupling reactions were performed in a similar way except for the number of moles of K_2CO_3 in the reaction mixture. For reactants containing an acid functional group, we used 2.0 mmol of K_2CO_3 ; 1.0 mmol of K_2CO_3 was used otherwise. Also, the conc. H_2SO_4 was added only when the reactants contained carboxylic acid groups, otherwise the reaction mixture was directly extracted into dichloromethane.

Hydrogenation of 2-methyl-3-buten-2-ol. In a 1 L round bottom flask, 3.0 mL of AuPd nanotriangle solution (optical density ~ 0.70 at 532 nm) was added, and the flask was sealed tight using a septum. The flask was then purged with hydrogen gas for 20 minutes; the flask was then filled with H_2 gas until the flask reached an initial pressure of 1.4 atm. The pressure in the flask was measured by a differential pressure manometer (Extech Instrument, Model #407910), and for all hydrogenation reactions the same initial pressure was maintained. The AuPd nanotriangle solution was then stirred under hydrogen for 30 minutes. Then 2-methyl-3-buten-2-ol (0.10 mL)

was injected into the flask. Similar to the cross-coupling reactions, hydrogenation reactions were performed in both light and dark conditions. For the ^1H NMR analysis, an aliquot of 100 μL of the reaction mixture was collected every 20 minutes and was directly extracted in of 500 μL CDCl_3 .

7.4. Results and Discussion

7.4.1. AuPd bimetallic nanotriangles

Au nanotriangles were synthesized via a literature procedure, which is a competitive process involving both reduction/oxidative etching of Au in the presence of CTAC as a stabilizing agent.³⁶ Here, ascorbic acid was used as the reducing agent and potassium iodide acts as an oxidative etchant in the presence of air. To synthesize the AuPd bimetallic nanotriangles, K_2PdCl_4 was reduced onto the as-synthesized Au nanotriangles using ascorbic acid as a reducing agent. These Au and AuPd nanotriangles were then characterized by UV-Vis spectroscopy and TEM; the results are shown in Figure 7.1. In the UV-Vis spectrum, the Au nanotriangles show a broad plasmon peak at 605 nm with a shoulder at 534 nm. The plasmon peak at 605 nm is attributed to the in-plane dipole mode,³⁷ while the shoulder at 534 nm is likely due to the presence of spherical Au nanoparticles.^{2, 36} Upon coating with Pd, a *ca.* 60 nm blue shift in the plasmon peak was observed. This might be due to some surface alloying between Au and Pd.³⁸ The morphologies of the Au and AuPd nanotriangles were confirmed by TEM analysis (Figure 7.1b-d). Figure 7.1b shows the presence of a large population of Au nanotriangles; the average edge length of these nanotriangles was found to be \sim 40 nm. However, the sample also contains *ca.* 10% of quasi-spherical Au nanoparticles along with the nanotriangles. Figure 7.1c shows a TEM image of the AuPd nanotriangles, and a higher resolution TEM image is shown in Figure 7.1d. The Z-contrast difference in the TEM images of AuPd (Figure 7.1c and 7.1d) indicates the spatial distribution of

Au and Pd within the nanotriangle; the lighter regions are the Pd shell, and the darker region corresponds to the Au core. The Pd shells of the AuPd nanotriangles are polycrystalline, and thus, the resulting AuPd nanotriangles appear textured with unevenly distributed Au and Pd sites on their surface. A similar morphology was observed in AuPd nanowheels due to the Pd alloying with Au.²⁸ The morphology likely occurs due to Pd deposition at multiple sites on each particle, which may be due to defects in the CTAC coating on the surface of the Au nanotriangles.³⁹ For catalytic purposes, the polycrystalline nature of the Pd shell may be favorable as the available surface area of the Pd catalyst would be substantially higher than perfect epitaxial core-shell structure.

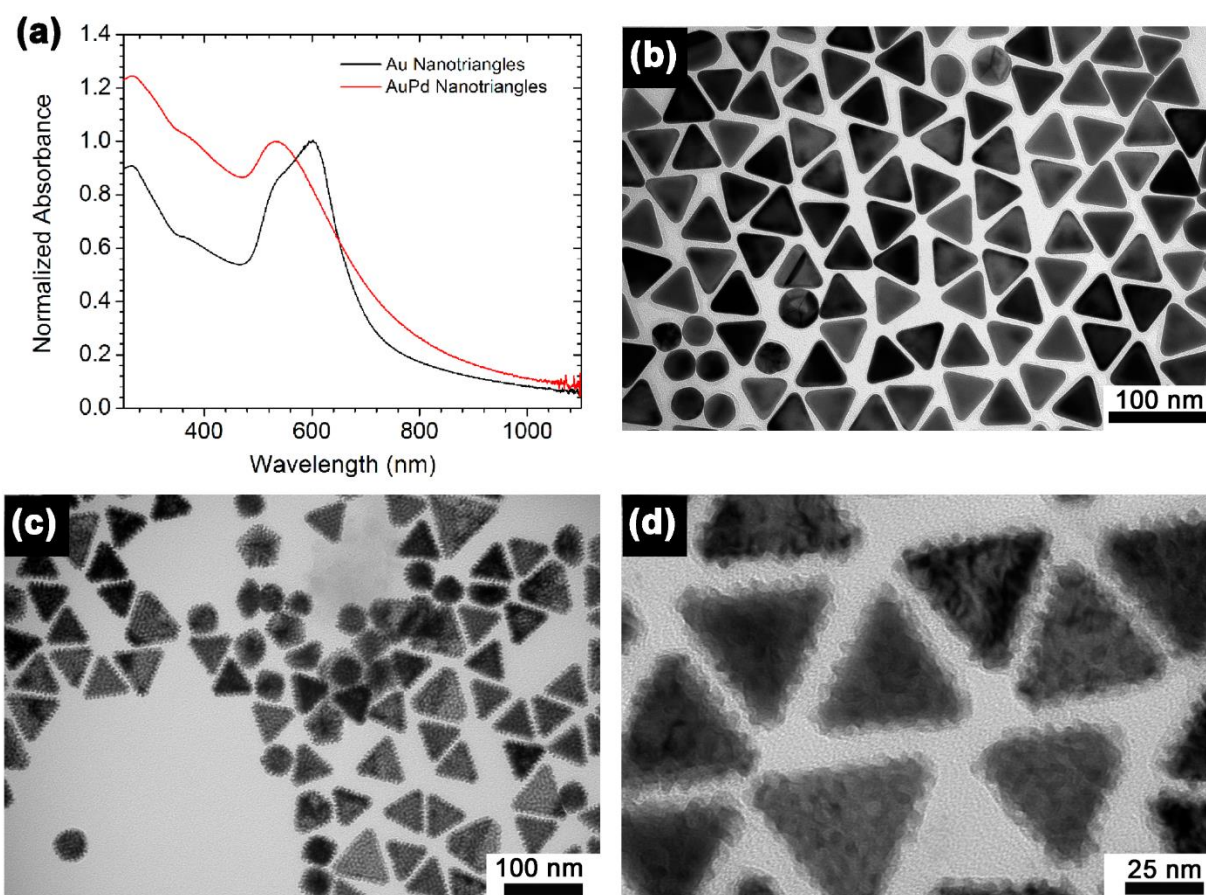


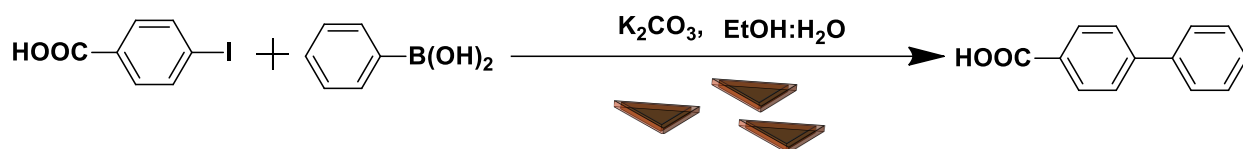
Figure 7.1. (a) Normalized UV-Vis spectra of Au and AuPd bimetallic nanotriangles; the spectra are normalized to the maximum of the plasmon band. TEM images of (b) as-synthesized Au nanotriangles, (c) AuPd bimetallic nanotriangles and (d) magnified image of AuPd nanotriangles.

7.4.2. Plasmon enhanced Suzuki-coupling reactions

After confirming the morphology of the AuPd nanotriangles, they were used to catalyze Suzuki cross-coupling reactions. The reactions were performed both with and without light illumination. For the dark reactions, the reaction flasks were covered with aluminum foil; for the light reactions, the flasks were illuminated with an array of green LEDs (power ~500 mW) (Figure 7.2a). The green light source was chosen to match the wavelength (534 nm) of the AuPd plasmon band (Figure 7.1a). The spectrum of green LED source is shown in Figure 7.3 At this wavelength, the surface plasmons of both the triangular and spherical AuPd will be excited. The light source setup is shown in Figure 7.2a; it contains an array of 8 green LEDs mounted on each heat sink, and four of these heat sinks are assembled in such a way that a 25 mL flask can be placed in the center and receive 360° illumination.

To investigate the plasmonic effect of AuPd nanotriangles on the Suzuki cross-coupling reaction, we chose to study a model reaction between p-iodobenzoic acid and phenylboronic acid, as shown in Scheme 7.1. This reaction was performed in both dark and light illumination, and the reaction kinetics were monitored by ^1H NMR. The percent conversions were calculated from the ^1H NMR spectra, and are plotted against time interval (Figure 7.2b). The cross-coupling reaction performed in the light showed significantly higher conversions compared to the dark reactions. For example, after 1 h of reaction time, the light reaction had proceeded to ~40% conversion, whereas the dark reaction had proceeded to only ~23% conversion. With an increase in time, the difference in conversion between the light and dark reactions was more pronounced. After 5 h of reaction time, the light reaction showed *ca.* 35% higher conversion compared to the dark. At the same time, the temperature of both the reaction mixtures was measured. We noticed a rise in the final temperature of the light reaction from 25 °C (the initial temperature of the reaction flask) to

37 °C, while the dark reaction showed no change in the final temperature. To determine if this increase in temperature was due to the presence of AuPd nanotriangles or due to light-induced heating of the solvent, we illuminated water with and without AuPd nanotriangles. After illuminating both flasks for 1 h, an increase in temperature from 25 °C to 37 °C was observed for the flask containing AuPd nanotriangles, whereas the flask containing only water showed only a 2 °C rise in temperature. This clearly confirms that the AuPd nanotriangles are the cause of the temperature increase; this is due to the plasmonic local heating generated by non-radiative plasmon decay (electron-phonon scattering).²⁷



Scheme 7.1. Schematic representation of a model Suzuki reaction used to test the AuPd nanotriangles as catalysts.

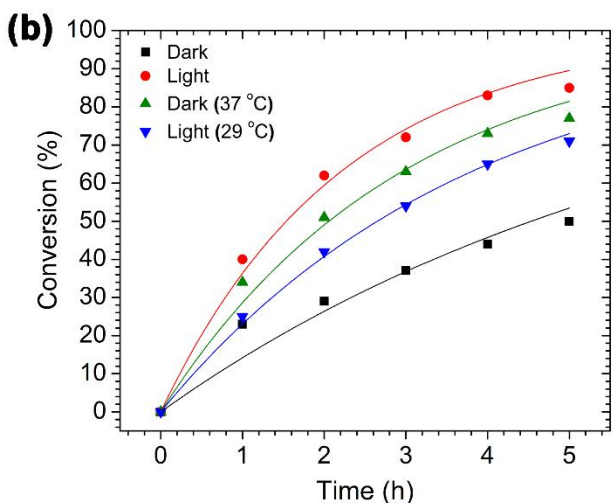
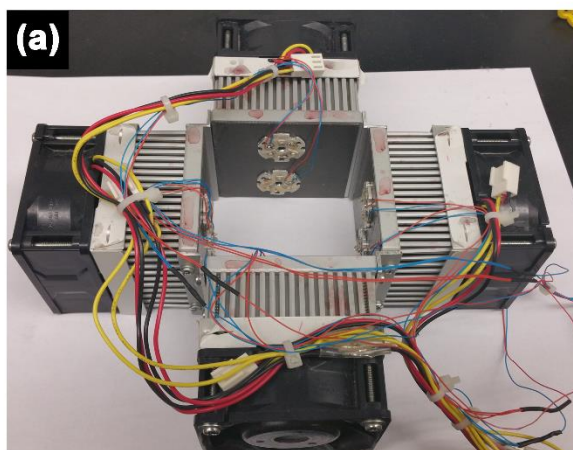


Figure 7.2. a) The LED light source with an array of green LEDs mounted on heat sinks, b) percent conversions calculated from ¹H NMR are plotted against time; the reaction is between p-iodobenzoic acid and phenylboronic acid. The green triangles indicate the control dark reaction performed in a hot water bath and the inverted blue triangles indicate the light reaction performed in a 25 °C water bath. The solid lines are a best-fit using a first-order kinetic model.

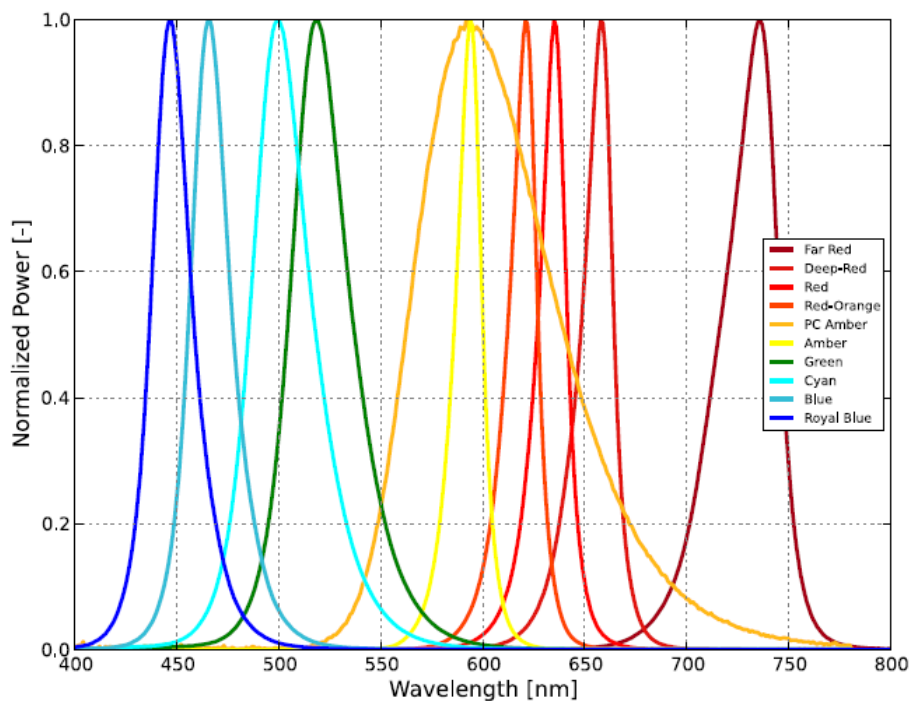


Figure 7.3. The normalized power vs wavelength for several LEDs including green LED source that was used to study the plasmonic catalysis. This is taken from the seller's (LUXEON) website.

To determine how significant a role this plasmonic heating effect has on the overall enhancement of the reaction rate, we performed a control reaction in the dark using a hot water bath to maintain the temperature of the reaction mixture at 37 °C (the same temperature reached by the light reaction flask). The reaction progress was monitored hourly by ^1H NMR, and the conversion plotted in Figure 7.2b. The light reaction still showed higher conversions compared to the dark reaction run at 37 °C, although the final temperatures of both the reaction mixtures were same (37 °C). However, the difference in conversion is only 9% after 5 h of the reaction time; this is much lower compared to the previous case (35%). From these results, it is clear that the rate of reaction is accelerated by the excitation of the AuPd surface plasmon modes. The effect of plasmonic excitation is also similar to that of conventional heating in improving the overall rate. To further support these conclusions, another Suzuki reaction was performed; this time the temperature of the light reaction flask was fixed at 25 °C using a water bath. After 5 h, this reaction

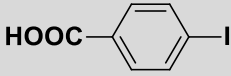
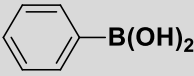
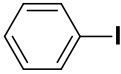
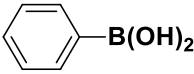
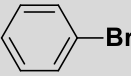
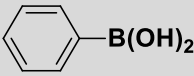
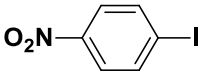
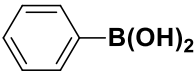
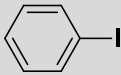
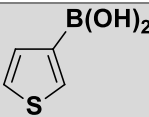
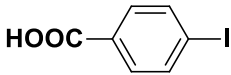
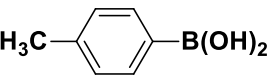
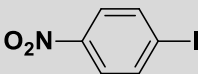
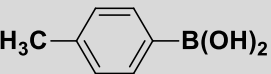
showed significantly higher conversion (*ca.* 20%) than the dark reaction. However, the final temperature increased to 29 °C (even though the reaction flask was in a 25 °C water bath). This slight rise in temperature perhaps may be due to direct photothermal heating of both the solvent and water bath, or simply insufficiently large thermal mass in cooling the bath.

In addition to the plasmonic heating effect, many reports have observed that plasmonic hot electron transfer contributes to the rate of a cross-coupling reaction.^{14, 15} In all of these reports, a high power laser source was used to excite the Au nanoparticle surface plasmons, whereas, in the current study, we used a relatively low power (~500 mW) and unfocused LED light source. The generation of plasmonic hot electrons is highly dependent on the power of the excitation light source.^{40, 41} The low power LEDs used here are likely insufficient to produce a significant population density of hot electrons; hence, the contribution of these hot electrons in improving the overall rate of the reaction is low. Nonetheless, the dark control reactions underperformed the light reactions even when both were run at the same temperature. It is therefore possible that there is a minor contribution from plasmonic hot electron transfer to the overall enhancement.

We extended our studies to examine the effect of different aryl halides and different boronic acids. The results for various substrates are shown in Table 7.1. In all cases, the reactions performed in the light showed an average of ~20% higher conversion compared to those carried out in the dark. A large difference in the conversions between the light and dark reactions was observed when aromatic iodides were used as substrates. Particularly in the case of entry 4, where nitro-substituted aryl iodide (*p*-iodonitrobenzene) was reacted with phenylboronic acid, the difference in conversion was very high. This difference was slightly higher even when compared to the other reactions where other aryl iodides were reacted with the same boronic acid (entries 1 and 2). The light reaction in entry 4 showed complete conversion, and the dark reaction showed a

decreased conversion compared to entries 1 and 2. The presence of an electron-withdrawing group such as $-\text{NO}_2$ on an aryl halide generally improves the rate of oxidative addition (typically the rate determining step) in Suzuki reactions. It is possible that the further acceleration of the reaction in the light could be coming from plasmonic hot electron transfer. However, the exact reason why this nitro-group is showing a positive effect on the light reaction and a negative effect on the dark reaction is unclear. On the other hand, the difference in conversions was lower when the same halide (p-iodonitrobenzene) was reacted with methyl-substituted phenylboronic acid (entry 7); the difference in conversion between light and dark was very low. Here, due to the presence of an electron-donating methyl group on the boronic acid, both the light and dark reactions showed almost complete conversions, resulting in less of a difference between them. Interestingly, in the case of entry 5, where 2-thiopheneboronic acid was used, the reaction showed almost double the conversion in the presence of light as opposed to the dark. Generally, sulfur-containing (thiophene-based) substrates have been shown to poison the Pd catalyst and cause low yields in cross-coupling reactions.⁴² They often need either high catalyst loadings or elevated temperatures to achieve good yields. In such reactions, the use of plasmonic nanoparticles might be a promising way of improving the overall conversions, while keeping the catalyst loading to a minimum. Finally, among all of the reactions, the aryl bromide substrate (entry 3) showed the lowest overall conversion, regardless of whether or not the reaction was illuminated. This can be due to the poor leaving ability of bromides as compared to iodides.

Table 7.1. Percent conversions measured by ^1H NMR for different Suzuki reactions performed in both the dark and the light.

Entry	Aryl halide	Boronic acid	Time	Conversion (Light)	Conversion (Dark)
1			3 h	92%	73%
2			3 h	85%	71%
3			3 h	34%	30%
4			3 h	100%	63%
5			2 h	57%	25%
6			2 h	100%	91%
7			2 h	100%	89%

The substrate to catalyst loading ratio for all reactions was 2.5: 0.002 mmol. The initial reaction temperature was 25 °C, and the solvent was a 80:20 mixture of water and ethanol.

7.4.3. Catalyst stability and recyclability

The main advantage of employing nanoparticles in catalysis is that the catalyst can easily be separated from the reaction mixture and reused for several reaction cycles. To test the recyclability of the AuPd nanotriangles, we first characterized them after a Suzuki coupling reaction between p-iodobenzoic acid and phenylboronic acid. Figure 7.4a shows the UV-Vis spectra of the AuPd nanotriangles before and after the Suzuki reaction. The spectra were recorded

for the AuPd nanotriangles used in the model cross-coupling reactions shown in Figure 7.2b. After completion of the reaction, the AuPd nanotriangles were collected by centrifuging the reaction mixture and then redispersed in a volume of water equivalent to the initial volume of the reaction mixture. A slight decrease in the intensity of the plasmon peak at 532 nm was observed after the reaction (Figure 3a). This suggests a slight decrease in the population of AuPd nanotriangles after the reaction. From the TEM analysis (Figure 7.4c), it was observed that some of the nanotriangles had aggregated after one reaction cycle. As a result of this aggregation, the nanotriangles tended to settle at the bottom of the reaction flask upon keeping the flask undisturbed for several days. We are uncertain as to why aggregation might be occurring in this system, but we believe it is due to the loss of their surface stabilizer (CTAC) during the Suzuki coupling reaction. A control experiment showed that the aggregation is not light-induced, and no such aggregation was seen for the hydrogenation system discussed below.

Using the same reactants that were used in the model Suzuki reaction between *p*-iodobenzoic acid and phenylboronic acid, we studied the catalyst recyclability over three reaction cycles in the presence of light. After each cycle, the AuPd nanotriangles were purified by centrifugation and then reused by dispersing them in the same amount of the reaction mixture. After 3 h of reaction, the percent conversion was calculated from the ^1H NMR spectrum, and the data is plotted against cycle number (Figure 7.4b). In cycle 1, after 3 h of reaction, *ca.* 70% conversion was observed, and the final temperature of the reaction flask was 37 °C. In cycle 2, the final temperature was slightly decreased slightly to 35 °C, and the percent conversion was reduced to *ca.* 50%. The reduction in conversion may be due to the decrease in the number of available active sites since, the nanoparticles are aggregated after the reaction (Figure 7.4c). In the 3rd cycle, the reaction yielded only 1% conversion and a final temperature of 31 °C; this could be due to the

almost complete destruction of the nanotriangles as the color of the solution substantially became lighter after redispersing the nanotriangles for the 3rd reaction cycle.

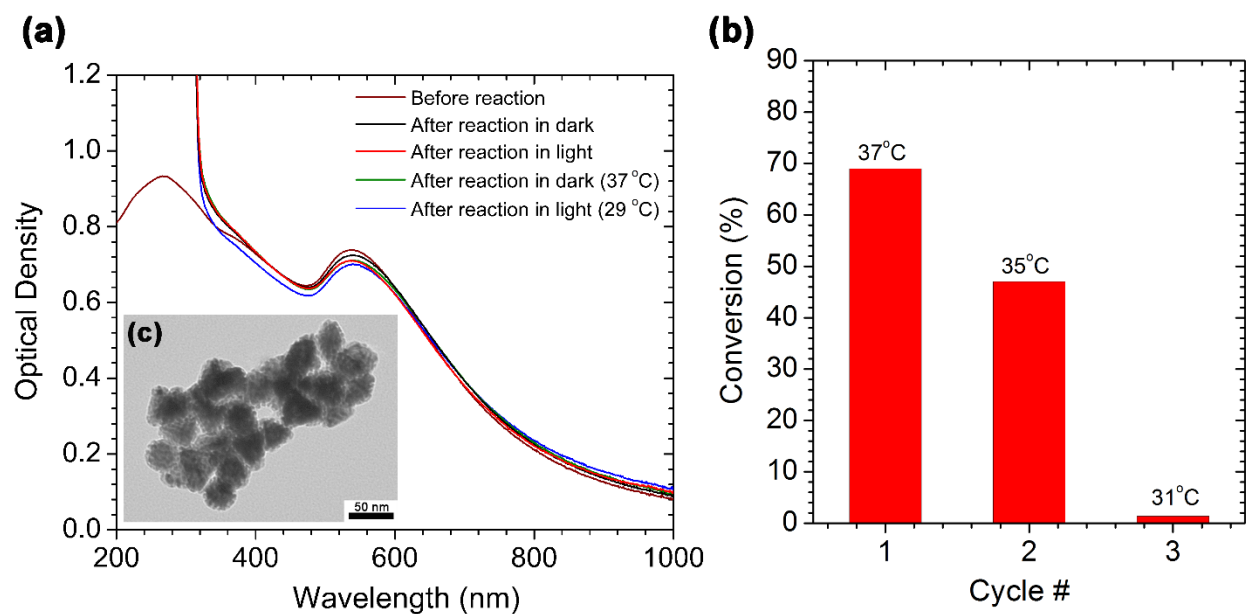


Figure 7.4. (a) UV-Vis absorption spectra of AuPd nanotriangles before and after cross-coupling reactions performed between p-iodobenzoic acid and phenylboronic acid. (b) Recyclability of AuPd nanotriangles and final temperature of the same coupling reaction performed under light illumination, and (c) TEM image showing aggregation of the AuPd nanotriangles, recorded after one cycle of the light reaction.

7.4.4. Plasmon enhanced hydrogenation reaction

To determine if the plasmonic properties of AuPd nanotriangles can be used to drive other Pd-catalyzed reactions, we studied the hydrogenation of 2-methyl-3-buten-2-ol using the nanotriangles as the catalyst. The reactions were performed in both the presence and absence of light illumination. We used the same LED source (Figure 7.2b) to irradiate the reaction mixture in the light reaction. Here, we used a larger (1 L) round-bottom flask to maintain an excess of H₂ gas for the hydrogenation reaction. The AuPd nanotriangles were added to the flask, and an excess of H₂ gas was supplied. Before injecting the substrate (2-methyl-3-buten-2-ol) into the flask, the flask was stirred to homogenize the solution. At 20 min intervals, the reaction was sampled and analyzed by ¹H NMR and the percent conversions are plotted against time (Figure 7.5). At each time

interval, the light reaction showed significantly higher conversions compared to the dark reaction. For example, after 20 min, the light reaction had proceeded to 42% conversion, whereas the dark reaction showed only 18% conversion. The difference became more pronounced as the reaction proceeded. Similar to the plasmon enhanced Suzuki reactions, an increase in the temperature of the light reaction (from 23 °C to 30 °C) was observed. However, the magnitude of the temperature increase was not as significant as in the Suzuki reactions. This is most likely due to the slightly lower AuPd catalyst loading, which was nearly 4 times lower compared to the Suzuki reaction. Again, to understand the role of plasmonic heating in the enhancement of the hydrogenation reaction, a control dark reaction was performed by heating the flask to 30 °C in a conventional hot water bath (i.e., the same temperature reached by the light reaction). After 120 min of reaction time, the control dark reaction showed almost same conversion as the light reaction (Figure 7.5). This is in contrast to the Suzuki reactions, where the light reaction showed slightly higher conversions (~9%) compared to the control dark reaction (Figure 7.2a). The fact that similar conversions are observed in both reactions (light and dark at 30 °C) clearly suggests that the enhancement is due to plasmonic heating effects alone. If other plasmonic effects contributed significantly to the improvement, the light reaction would show higher conversions compared to the high-temperature dark reaction. Similar results have been reported in the literature;^{43, 19} Long *et al.*, observed no contribution for the plasmonic hot electron effect in the hydrogenation of styrene.⁴³

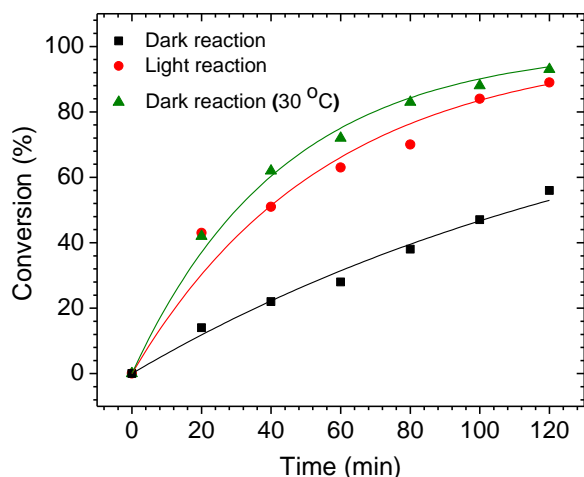


Figure 7.5. Percent conversion of hydrogenation reactions performed on 2-methyl-3-buten-2-ol using AuPd nanotriangles in the presence and absence of light. The black squares show the reaction performed at 23 °C under ambient conditions, the red circles show the reaction performed under illumination that achieved a final temperature of 30 °C, and the green triangles show the dark reaction performed at 30 °C using hot water bath. The solid lines are a best-fit using a first-order kinetic model.

Since it has been shown that Au nanoparticles alone can catalyze the hydrogenation reaction (although it requires high temperatures),^{41, 44} we also attempted to perform the same hydrogenation reaction using pure Au nanotriangles as the catalyst. No product formation was observed in either the light or dark conditions. This confirmed that the Pd is the active site on the AuPd catalyst for the hydrogenation reactions. Another possible mechanism to drive the hydrogenation reactions is by plasmonic hot electron transfer; however, to achieve the dissociation of H₂ by hot electrons generated on Au, a high power incoming light source (on order of W/cm²) is required.⁴¹ The LED light source used in the current study was likely not enough to produce sufficiently hot electrons, and no activity of Au was seen for this hydrogenation reaction.

7.5. Conclusions

In conclusion, we have synthesized triangular AuPd nanoparticles and employed them to improve the rates of Suzuki coupling and hydrogenation reactions. Upon exciting the surface

plasmons in AuPd nanotriangles using green LEDs (whose wavelength was near the maximum of the plasmon band), an improvement in the rates of Suzuki and hydrogenation reactions was observed. Our results revealed that the enhancement in the rate of reaction is mainly due to the contribution of plasmonic heating effects, with at most a minor contribution from plasmonic hot electron transfer. We have investigated the recyclability of these catalysts; we found that the catalyst survived for 2 cycles of Suzuki reactions. TEM showed aggregation AuPd nanotriangles causing a reduction in the catalytic activity. This study clearly demonstrates that a plasmonic enhancement in the rates of Pd-catalyzed reactions can be observed even by using a low power and unfocused LED light source, and that, at these low powers, there is only plasmonic photothermal effect contributing to the rate enhancement.

7.6. References

1. M. K. Gangishetty, K. E. Lee, R. W. J. Scott and T. L. Kelly, *ACS Appl. Mater. Interfaces*, 2013, **5**, 11044-11051.
2. M. K. Gangishetty, R. W. J. Scott and T. L. Kelly, *Langmuir*, 2014, **30**, 14352-14359.
3. H. A. Atwater and A. Polman, *Nat. Mater.*, 2010, **9**, 205-213.
4. C. Clavero, *Nat. Photon.*, 2014, **8**, 95-103.
5. J. N. Anker, W. P. Hall, O. Lyandres, N. C. Shah, J. Zhao and R. P. Van Duyne, *Nat. Mater.*, 2008, **7**, 442-453.
6. S. Linic, U. Aslam, C. Boerigter and M. Morabito, *Nat. Mater.*, 2015, **14**, 567-576.
7. L. Guerrini and D. Graham, *Chem. Soc. Rev.*, 2012, **41**, 7085-7107.
8. K. L. Kelly, E. Coronado, L. L. Zhao and G. C. Schatz, *J. Phys. Chem. C*, 2002, **107**, 668-677.
9. M. J. Kale, T. Avanesian and P. Christopher, *ACS Catal.*, 2014, **4**, 116-128.
10. P. Wang, B. Huang, Y. Dai and M.-H. Whangbo, *Phys. Chem. Chem. Phys.*, 2012, **14**, 9813-9825.
11. R. Jiang, B. Li, C. Fang and J. Wang, *Adv. Mater.*, 2014, **26**, 5274-5309.
12. J. Li, S. K. Cushing, J. Bright, F. Meng, T. R. Senty, P. Zheng, A. D. Bristow and N. Wu, *ACS Catal.*, 2013, **3**, 47-51.
13. L. Liu, S. Ouyang and J. Ye, *Angew. Chem., Int. Ed.*, 2013, **125**, 6821-6825.
14. Q. Xiao, S. Sarina, A. Bo, J. Jia, H. Liu, D. P. Arnold, Y. Huang, H. Wu and H. Zhu, *ACS Catal.*, 2014, **4**, 1725-1734.
15. F. Wang, C. Li, H. Chen, R. Jiang, L.-D. Sun, Q. Li, J. Wang, J. C. Yu and C.-H. Yan, *J. Am. Chem. Soc.*, 2013, **135**, 5588-5601.

16. Q. Xiao, S. Sarina, E. R. Waclawik, J. Jia, J. Chang, J. D. Riches, H. Wu, Z. Zheng and H. Zhu, *ACS Catal.*, 2016, **6**, 1744-1753.
17. L.-B. Zhao, M. Zhang, Y.-F. Huang, C. T. Williams, D.-Y. Wu, B. Ren and Z.-Q. Tian, *J. Phys. Chem. Lett.*, 2014, **5**, 1259-1266.
18. Z. Liu, Y. Huang, Q. Xiao and H. Zhu, *Green Chem.*, 2016, **18**, 817-825.
19. X. Zhao, R. Long, D. Liu, B. Luo and Y. Xiong, *J. Mater. Chem. A*, 2015, **3**, 9390-9394.
20. J. Cui, Y. Li, L. Liu, L. Chen, J. Xu, J. Ma, G. Fang, E. Zhu, H. Wu, L. Zhao, L. Wang and Y. Huang, *Nano Lett.*, 2015, **15**, 6295-6301.
21. Q. Xiao, Z. Liu, A. Bo, S. Zavier, S. Sarina, S. Bottle, J. D. Riches and H. Zhu, *J. Am. Chem. Soc.*, 2015, **137**, 1956-1966.
22. T. Jiang, C. Jia, L. Zhang, S. He, Y. Sang, H. Li, Y. Li, X. Xu and H. Liu, *Nanoscale*, 2015, **7**, 209-217.
23. S. Linic, P. Christopher and D. B. Ingram, *Nat. Mater.*, 2011, **10**, 911-921.
24. S. Sarina, H. Zhu, E. Jaatinen, Q. Xiao, H. Liu, J. Jia, C. Chen and J. Zhao, *J. Am. Chem. Soc.*, 2013, **135**, 5793-5801.
25. M. L. Brongersma, N. J. Halas and P. Nordlander, *Nat Nano*, 2015, **10**, 25-34.
26. W. R. Erwin, H. F. Zarick, E. M. Talbert and R. Bardhan, *Energy Environ. Sci.*, 2016, **9**, 1577-1601.
27. J. R. Adleman, D. A. Boyd, D. G. Goodwin and D. Psaltis, *Nano Lett.*, 2009, **9**, 4417-4423.
28. X. Huang, Y. Li, Y. Chen, H. Zhou, X. Duan and Y. Huang, *Angew. Chem., Int. Ed.*, 2013, **52**, 6063-6067.
29. Q. Xiao, S. Sarina, E. Jaatinen, J. Jia, D. P. Arnold, H. Liu and H. Zhu, *Green Chem.*, 2014, **16**, 4272-4285.

30. P. Verma, Y. Kuwahara, K. Mori and H. Yamashita, *J. Mater. Chem. A*, 2016, **4**, 10142-10150.
31. Z. Zheng, T. Tachikawa and T. Majima, *J. Am. Chem. Soc.*, 2015, **137**, 948-957.
32. M. Wen, S. Takakura, K. Fuku, K. Mori and H. Yamashita, *Catal. Today*, 2015, **242**, 381-385.
33. S. Zhang, C. Chang, Z. Huang, Y. Ma, W. Gao, J. Li and Y. Qu, *ACS Catal.*, 2015, **5**, 6481-6488.
34. E. Hao and G. C. Schatz, *J. Chem. Phys.*, 2004, **120**, 357-366.
35. K. L. Kelly, E. Coronado, L. L. Zhao and G. C. Schatz, *J. Phys. Chem. C*, 2003, **107**, 668-677.
36. L. Chen, F. Ji, Y. Xu, L. He, Y. Mi, F. Bao, B. Sun, X. Zhang and Q. Zhang, *Nano Lett.*, 2014, **14**, 7201-7206.
37. J. E. Millstone, S. Park, K. L. Shuford, L. Qin, G. C. Schatz and C. A. Mirkin, *J. Am. Chem. Soc.*, 2005, **127**, 5312-5313.
38. Y. Ding, F. Fan, Z. Tian and Z. L. Wang, *J. Am. Chem. Soc.*, 2010, **132**, 12480-12486.
39. M. Jaschke, H. J. Butt, H. E. Gaub and S. Manne, *Langmuir*, 1997, **13**, 1381-1384.
40. P. Dombi, A. Hörl, P. Rácz, I. Márton, A. Trügler, J. R. Krenn and U. Hohenester, *Nano Lett.*, 2013, **13**, 674-678.
41. S. Mukherjee, F. Libisch, N. Large, O. Neumann, L. V. Brown, J. Cheng, J. B. Lassiter, E. A. Carter, P. Nordlander and N. J. Halas, *Nano Lett.*, 2013, **13**, 240-247.
42. Y. Li, X. M. Hong, D. M. Collard and M. A. El-Sayed, *Org. Lett.*, 2000, **2**, 2385-2388.
43. R. Long, Z. Rao, K. Mao, Y. Li, C. Zhang, Q. Liu, C. Wang, Z.-Y. Li, X. Wu and Y. Xiong, *Angew. Chem., Int. Ed.*, 2015, **54**, 2425-2430.

44. T. Mitsudome and K. Kaneda, *Green Chem.*, 2013, **15**, 2636-2654.

CHAPTER 8

8.1. Summary

This thesis investigated various strategies for converting solar energy efficiently into electrical and chemical energy. To transform solar energy into electrical energy, two types of solar cells, DSSCs and perovskite solar cells were studied. In Chapter 2, the performance of DSSCs was successfully improved by employing plasmonic Ag@SiO₂ core-shell nanotriangles. The nanotriangles were designed to specifically target the red-to-NIR region, where the N719 dye absorbs weakly. Different quantities of these nanotriangles were embedded in the TiO₂ layer, and it was found that 0.05% (w/w) of the nanotriangles is the optimum loading for achieving the best efficiency. This loading resulted in a *ca.* 32% enhancement of the overall PCE; the enhancement was mainly due to an increase in the short-circuit current density. From the IPCE spectra, the same device (0.05 % (w/w) nanotriangles) showed a *ca.* 25% increase in photocurrent from the green photons (500-560 nm) compared to the control device (no nanotriangles). In the red-NIR region (600-750 nm) the photocurrent enhancement was *ca.* 10%. However, the Ag@SiO₂ nanotriangles were found to be unstable toward both the liquid iodide/triiodide electrolyte and the high temperatures used in the annealing process. At elevated temperatures, they broke down into very small spherical nanoparticles.

In the subsequent chapter (Chapter 3), the temperature induced transformation of nanotriangles to small nanoparticles was investigated by annealing the Ag@SiO₂ nanotriangles at different temperatures under air and N₂ atmospheres. In the presence of air and lower annealing temperatures, truncation of the Ag nanotriangles was observed. Upon increasing the temperature, they decomposed to small ~2 nm particles in the pores of the SiO₂ shell. By using X-ray absorption

spectroscopic studies (XANES and EXAFS), the resultant ~2 nm particles were found to be comprised of Ag⁰. This study suggested that, upon annealing Ag@SiO₂ in air, the core Ag nanotriangles are first oxidized to AgO or Ag₂O, which then decomposes back to form Ag and O₂. Here, the SiO₂ shell prevents the diffusion, aggregation, and coalescence of the resultant nanoparticles during the annealing process. This oxidation and decomposition mechanism was further confirmed by annealing the nanotriangles in a N₂ atmosphere. In the presence of only N₂, regardless of the annealing temperature, only truncation of the nanotriangles was observed and no formation of small particles was observed. Due to the lack of O₂, the oxidation and decomposition of the Ag nanotriangles did not take place.

To overcome this stability issue, Ag@SiO₂ nanotriangles were replaced by Au@SiO₂ nanotriangles in DSSCs. In Chapter 4, the Au@SiO₂ nanotriangles were used in DSSCs. Our results indicated that the Au@SiO₂ nanotriangles are relatively more stable to oxidation compared to the Ag@SiO₂ nanotriangles. However, at elevated temperatures (350-450 °C), a change in the morphology of the Au nanotriangles was observed. The resultant particles contained a mixture of truncated nanotriangles and spherical nanoparticles. Due to the presence of multiple shapes, the Au@SiO₂ system showed a broad SPR spectrum in the visible region. This eventually resulted in panchromatic light harvesting in a DSSC. By integrating 0.05% (w/w) of Au@SiO₂ nanotriangles into the DSSCs, a 15% enhancement in the PCE was observed. Devices showed a significant enhancement in PCE even at low (0.009% w/w) Au@SiO₂ loadings. Here, the thickness of the Au@SiO₂/TiO₂ layer was only ~3 μm; whereas, it was ~10 μm for Ag@SiO₂/TiO₂ that were studied in Chapter-1.

Another type of solar cell that was studied in this thesis is the perovskite solar cell. In Chapter 5, the effect of perovskite thickness on the device performance was successfully

elucidated. By physical vapor deposition of PbI_2 , different thicknesses of PbI_2 films were prepared. These PbI_2 films were then reacted with $\text{CH}_3\text{NH}_3\text{I}$ to prepared different thicknesses of $\text{CH}_3\text{NH}_3\text{PbI}_3$ perovskite films. The resulting thickness of the perovskite layer was almost double the thickness of its original PbI_2 film. By this method, perovskite layers with thicknesses ranging from 100 to 600 nm were prepared, and then the devices were fabricated. With an increase in thickness of the perovskite layer, the PCE increased and reached a maximum value for a device with a ~300 nm thick perovskite layer. Upon with a further increase in the thickness, a decrease in the PCE was observed. This trend was attributed to thinner perovskite layers producing low performance devices due to poor light absorption, whereas thicker layers suffered from charge carrier recombination and incomplete reaction of PbI_2 and $\text{CH}_3\text{NH}_3\text{I}$. The optimum perovskite thickness to balance efficient light absorption and effective charge carrier collection was found to be ~330 nm. The device with a ~330 nm thick perovskite layer produced the highest efficiency of 11.8%. However, all these devices suffered from severe hysteresis in the J - V curves regardless of the perovskite layer thickness, i.e. they showed very poor performance when changing the scan direction. This was attributed to the presence of a large number of grain boundaries in the perovskite layer. To minimize grain boundaries and to produce a more uniform perovskite layer, the growth of the perovskite crystallites was investigated by varying the atmospheric conditions. This was discussed in the subsequent chapter.

In Chapter 6, the role of atmospheric humidity on the growth of the perovskite crystallites and hence the performance of the final devices was investigated. By using an atmospheric bag, the relative humidity in the atmosphere was controlled from 20% to 60% during the growth of the perovskite. Our results from SEM analysis showed an increase in the crystallite size with an increase in the RH during the growth of the perovskite layer. At lower humidity conditions (1-30%

RH), the resulting film contained significant gaps between the perovskite crystallites, and the resulting devices showed poor performance with severe hysteresis in the *J-V* curves. With an increase in humidity to 40% and 60% RH, the perovskite produced was a uniform layer with well-connected crystallites. At 40% RH, a high performing and hysteresis-free device with a maximum efficiency of 12.2% was achieved. Upon scanning the device at a slow rate, it showed an efficiency of 11.3%. Also, stabilized currents were recorded for this device; from these current-transient measurements, the stabilized efficiency was determined to be 11.2%.

In the last part of the thesis, light energy was successfully utilized to improve the rates Pd-catalyzed reactions. To harvest the light for Pd-catalyzed reactions, plasmonic Au nanotriangles were employed in Chapter 7. The Au nanotriangle was coated with Pd to form bimetallic Au@Pd nanotriangles. These bimetallic nanotriangles were used for Suzuki cross-coupling and hydrogenation reactions. In the presence of light illumination with green LEDs, *ca.* 35% higher conversions in cross-coupling reactions was observed compared to dark conditions. Control experiments revealed that the enhancement in the rate of the Suzuki reaction was dominated by plasmonic heating effects as opposed to plasmonic hot electron injection. Plasmonic enhancement of cross-coupling was observed when different aryl halides and aromatic boronic acids are used in the reaction. However, the AuPd catalyst showed poor recyclability; it survived for only two cycles. This was attributed to the aggregation of the nanotriangles as evidenced from TEM analysis. The AuPd nanotriangles were also employed for the hydrogenation of methyl 2-butene-1-ol. Similar plasmonic enhancements were observed for hydrogenation reactions; upon light illumination, the hydrogenation reactions showed higher conversions. The enhancement was found to be due to plasmonic heating effects alone.

Finally, the major findings that are discovered in this dissertation are as follows. (1) By employing plasmonic Ag@SiO₂ nanotriangles in DSSCs, an enhancement in the light-harvesting efficiency was achieved in the desired region (red-NIR region). However, the Ag nanotriangles were unstable towards iodide redox couple and elevated temperature. Whereas, Au@SiO₂ nanotriangles were found to be more stable and ideal candidates for the plasmonic applications, where such harsh conditions are needed. (2) In perovskite solar cells, for balancing the light absorption and charge carrier collection, optimum thickness of the perovskite layer is important. Along with the thickness, atmospheric humidity was found to play a major role in producing the bigger perovskite crystallites and uniform perovskite layer. (3) Finally, AuPd plasmonic nanotriangles were found to be useful to improve the rate of cross-coupling and hydrogenation reactions by harvesting light. However, the AuPd catalyst employed in this study did not allow us to completely separate possible contributions of individual plasmonic effects such as plasmonic hot electron *vs.* plasmonic heating in the enhancement of the rate of the catalytic reactions.

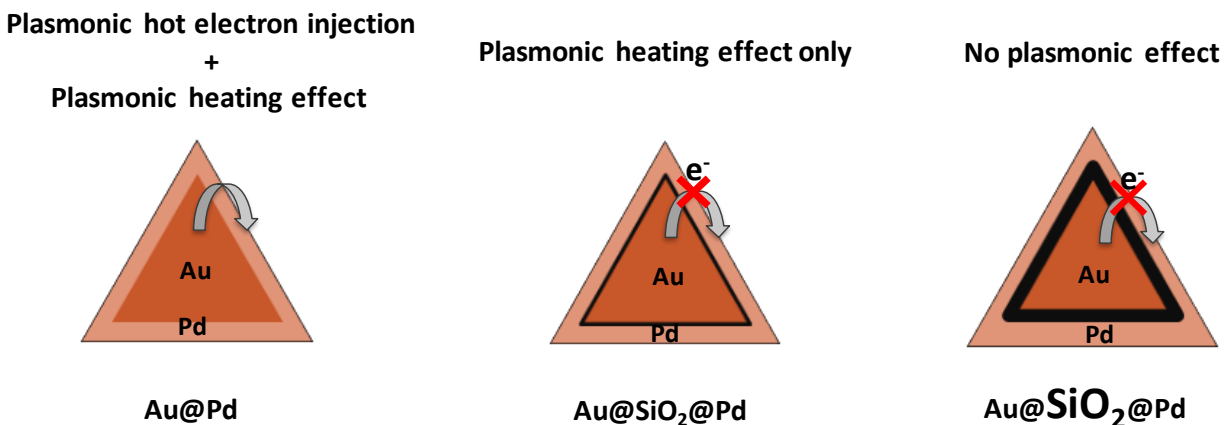
8.2. Future Outlook

Understanding the contributions of the various plasmonic effects in improving both the performance of a DSSC and the rate of a chemical reaction is still need to be addressed. In the case of DSSCs, although Chapter 2 aims at understanding the role of plasmonic near-field effect *vs.* plasmonic light scattering effect in improving the device efficiency, due to the instability of Ag@SiO₂ nanotriangles, the relative contributions were left unaddressed. In the case of cross-coupling reactions (Chapter 7), the higher rates in the presence of light illumination were attributed to plasmonic heating effects. However, even after maintaining the same temperatures in dark and light reactions, the light reactions showed slightly higher conversions compared to the dark ones for coupling reactions, indicating there could be some contribution of plasmonic hot electron

effects. As a part of the future work, a comprehensive study on the role of individual plasmonic effects in plasmonic enhancement is proposed, and possible strategies for addressing this are discussed in the following sections.

8.2.1. Plasmonic heating effects vs. plasmonic hot electron effects in Pd-catalyzed reactions

Plasmonic metal nanoparticles can enhance the activity of several existing catalysts by utilizing solar energy.¹⁻⁵ To improve the rates of Pd-catalyzed reactions, often Au cores are used as light-harvesting materials, as was shown in Chapter 7. The enhancement is either driven by plasmonic hot electron transfer from Au to Pd (and then to the substrate), or plasmonic heating effects.⁶⁻⁹ Untangling the contribution of one effect from the other is quite difficult when using bimetallic Au@Pd nanoparticles. However, by using a thin spacer such as SiO₂ between Au and Pd nanoparticle, the hot electron transfer from Au to Pd can be minimized.¹⁰ In this case, only plasmonic heating effects from the Au core will contribute to improving the rate of Pd-catalyzed reactions. With an increase in the thickness of SiO₂, the local heating generated can also be suppressed since the magnitude of local heating dramatically decreases as you move away from the surface of the nanoparticle.³ In this case, neither hot electron effects nor heating effects would contribute to the rate of Pd-catalyzed reactions, resulting in no net plasmonic effects on these reactions. By controlling the morphology of the plasmonic nanoparticle, the contribution of each plasmonic effect in the overall enhancement of the rate can be understood. Three different nanocatalysts are proposed as shown in the Scheme 8.1; these are Au@Pd bimetallic nanotriangles, and Au@SiO₂@Pd core-shell-shell nanotriangles with thin and thick SiO₂ shells, respectively.



Scheme 8.1. Representation of controlling the plasmonic hot electron effect vs plasmonic heating effect using three different types of nanoparticles.

8.2.1.1. Preliminary results on the synthesis and catalytic activity of Au@SiO₂@Pd core@shell@shell nanotriangles

For the synthesis of Au@SiO₂@Pd core@shell@shell nanotriangles, at first Au@SiO₂ core@shell nanotriangles are synthesized by using the method described in Chapter 4. To coat Pd nanoparticles on Au@SiO₂, a functionalizing agent 3(-aminopropyl)triethoxysilane (APTES) can be used.¹¹ Some preliminary experiments were already performed using this method, and the resultant nanoparticles were characterized by TEM. Figure 8.1a shows the adherence of Pd nanoparticles on Au@SiO₂ which has been modified with APTES. The thickness of SiO₂ was found to be around ~25 nm. However, upon performing a cross-coupling reaction between p-iodobenzoic acid and phenyl boronic acid using these Au@SiO₂@Pd catalysts in the presence of LED light source, the catalyst showed very poor (~3%) conversions after 5 h of the reaction (Figure 8.1b). This might be attributed to the poisoning of the Pd surface by APTES.

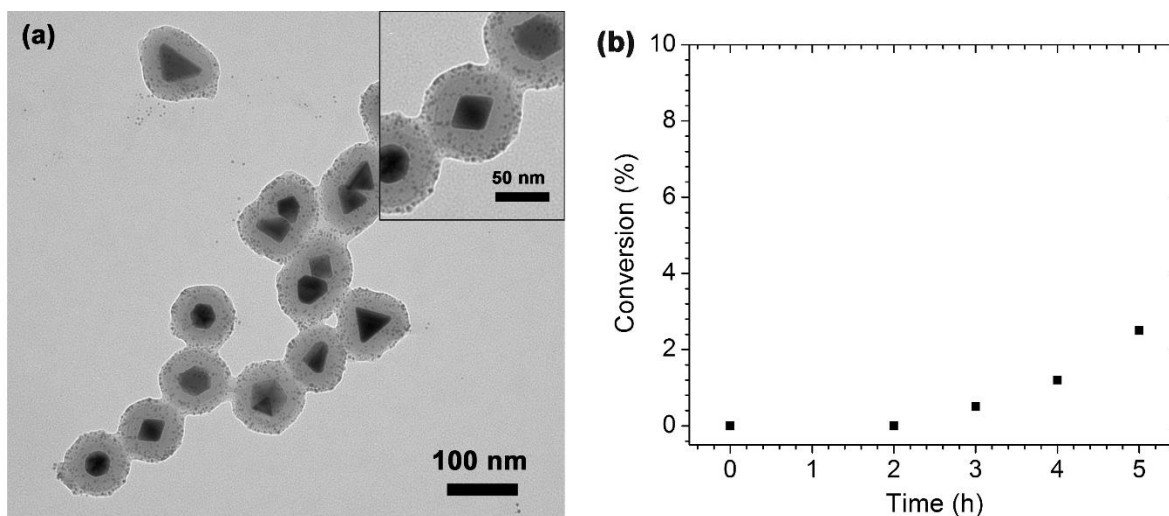


Figure 8.1. (a) TEM image of Au@SiO₂@Pd core-shell-shell nanoparticles, and (b) percent conversions of a cross-coupling reaction between p-iodobenzoic acid and phenyl boronic acid at ambient temperatures; substrate to catalyst loading ratio was (2.5mmol: 0.002mmol). The conversions are calculated from ¹H NMR

As an immediate goal of the future work, optimizing the synthetic procedure to overcome the Pd-poisoning by APTES is proposed. Several groups have used a similar synthetic method to immobilize the Pd on SiO₂, but still observed the catalytic activity of Pd.^{11, 12} Whereas, in our study, APTES is completely attenuating the Pd catalytic activity. This could be due to the high concentration of APTES used in the synthesis. Therefore, as a first step, the concentration of APTES will be optimized, and the catalytic activity of Pd will be studied. Also, there are other possible linkers such as Poly(ethylene-co-butylene)-b-poly(ethylene oxide) [P(E/B)-PEO] reported in the literature,¹³ in which reduced Pd²⁺ salts are reduced onto SiO₂ after functionalizing the SiO₂ with [P(E/B)-PEO], followed by calcination of the sample at 500°C to remove the linker. A similar method can be used as an alternative method for synthesizing Au@SiO₂@Pd. After the synthesis, the catalyst would be characterized by UV-Vis and TEM analysis. Then by using the model Suzuki coupling reaction discussed in Chapter 7, the contribution of individual plasmonic effects will be studied by tuning the thickness of SiO₂.

8.2.2. Plasmonic near-field effect vs plasmonic light scattering effect in DSSCs

As discussed earlier, there have been several mechanisms proposed for plasmon enhanced light harvesting in DSSCs and photocatalysis. In DSSCs, there are two major plasmonic effects which contribute to the enhancement of device efficiency; one is a plasmonic light scattering effect, and the other is plasmonic near-field effects.¹⁴⁻¹⁶ To study the contribution of each effect, one possible approach is using a variable thickness of the metal oxide shell (SiO_2) on the metal nanoparticle. If the shell thickness is very low, the metal nanoparticle is expected to show both near-field and light scattering effects. Whereas, with an increase in thickness, the metal nanoparticle tends to show only light scattering effect, since the near-field generated on the surface is attenuated by thick SiO_2 shell. It has been shown that the magnitude of near-field effect is highly dependent on the distance from the surface.¹⁷⁻¹⁹ Although Chapter 2 aims at studying the contributions of plasmonic effect by using Ag@SiO_2 nanotriangles of different SiO_2 thicknesses, the contribution of the relative plasmonic effects was left unstudied due to the instability of thin-shelled nanotriangles. However, in Chapter 4, the Au@SiO_2 nanotriangles were found to be stable; hence employing these stable Au@SiO_2 nanotriangles of the various shell (SiO_2) thicknesses in DSSCs can enable to elucidate the contribution of plasmonic effects.

For the synthesis of monodispersed Au nanotriangles, the method described in Chapter 7 will be used. After synthesizing the Au nanotriangles, the SiO_2 shells with various thicknesses will be coated by using a method discussed in Chapter 2 & 4. Each of these Au@SiO_2 nanotriangle materials would then separately be embedded in DSSCs to elucidate the role of individual plasmonic effects. The device fabrication method can be adopted from Chapter 2 and 4.

8.3. References

1. M. Xiao, R. Jiang, F. Wang, C. Fang, J. Wang and J. C. Yu, *J. Mater. Chem. A*, 2013, **1**, 5790-5805.
2. P. Christopher, H. Xin, A. Marimuthu and S. Linic, *Nat. Mater.*, 2012, **11**, 1044-1050.
3. S. Linic, U. Aslam, C. Boerigter and M. Morabito, *Nat. Mater.*, 2015, **14**, 567-576.
4. S. Linic, P. Christopher and D. B. Ingram, *Nat. Mater.*, 2011, **10**, 911-921.
5. P. Wang, B. Huang, Y. Dai and M.-H. Whangbo, *Phys. Chem. Chem. Phys.*, 2012, **14**, 9813-9825.
6. F. Wang, C. Li, H. Chen, R. Jiang, L.-D. Sun, Q. Li, J. Wang, J. C. Yu and C.-H. Yan, *J. Am. Chem. Soc.*, 2013, **135**, 5588-5601.
7. S. Zhang, C. Chang, Z. Huang, Y. Ma, W. Gao, J. Li and Y. Qu, *ACS Catal.*, 2015, **5**, 6481-6488.
8. P. Verma, Y. Kuwahara, K. Mori and H. Yamashita, *J. Mater. Chem. A*, 2016, **4**, 10142-10150.
9. X. Huang, Y. Li, Y. Chen, H. Zhou, X. Duan and Y. Huang, *Angew. Chem., Int. Ed.*, 2013, **52**, 6063-6067.
10. C. Wadell, T. J. Antosiewicz and C. Langhammer, *Nano Lett.*, 2012, **12**, 4784-4790.
11. X. Le, Z. Dong, Y. Liu, Z. Jin, T.-D. Huy, M. Le and J. Ma, *J. Mater. Chem. A*, 2014, **2**, 19696-19706.
12. Y. Wang, J. Liu, P. Wang, C. J. Werth and T. J. Strathmann, *ACS Catal.*, 2014, **4**, 3551-3559.
13. Z. Cao, H. Chen, S. Zhu, W. Zhang, X. Wu, G. Shan, U. Ziener and D. Qi, *Langmuir*, 2015, **31**, 4341-4350.

14. W. R. Erwin, H. F. Zarick, E. M. Talbert and R. Bardhan, *Energy Environ. Sci.*, 2016, **9**, 1577-1601.
15. H. A. Atwater and A. Polman, *Nat. Mater.*, 2010, **9**, 205-213.
16. M. A. Green and S. Pillai, *Nat. Photon.*, 2012, **6**, 130-132.
17. T. W. Hamann, R. A. Jensen, A. B. F. Martinson, H. Van Ryswyk and J. T. Hupp, *Energy Environ. Sci.*, 2008, **1**, 66-78.
18. D. D. Evanoff, R. L. White and G. Chumanov, *J. Phys. Chem. C*, 2004, **108**, 1522-1524.
19. K. L. Kelly, E. Coronado, L. L. Zhao and G. C. Schatz, *J. Phys. Chem. C*, 2002, **107**, 668-677.